



TECHNISCHE
UNIVERSITÄT
WIEN
Vienna | Austria



Dissertation

Multi-dimensional photothermal defect reconstruction in anisotropic media

carried out for the purpose of obtaining the degree of Doctor technicae (Dr. techn.), submitted at
TU Wien, Faculty of Mechanical and Industrial Engineering, by

Dipl.-Ing. Gregor Thummerer, BSc

Mat.Nr.: 11836784

under the supervision of

Priv.-Doz. Dipl.-Ing. Dr. Peter Burgholzer
Institute of Materials Science and Technology, E308

Vienna, August 2021

Reviewed by

.....
FH-Prof. Univ.-Doz. Mag. Dr. Günther Hendorfer
Institute of Experimental Physics
Johannes Kepler University

.....
Prof. Dr. rer. nat. habil. Marc Kreutzbruck
Institut für Kunststofftechnik
University of Stuttgart

This work was supported by the Austrian Federal Ministry
of Science, Research and Economy and the National
Foundation for Research, Technology and Development within
the framework of the Josef Ressel Center for Thermal NDE of
Composites.

I confirm, that going to press of this thesis needs the confirmation of the examination
committee.

Affidavit

I declare in lieu of oath, that I wrote this thesis and performed the associated research myself, using only literature cited in this volume. If text passages from sources are used literally, they are marked as such.

I confirm that this work is original and has not been submitted elsewhere for any examination, nor is it currently under consideration for a thesis elsewhere.

I acknowledge that the submitted work will be checked electronically-technically using suitable and state-of-the-art means (plagiarism detection software). On the one hand, this ensures that the submitted work was prepared according to the high-quality standards within the applicable rules to ensure good scientific practice "Code of Conduct" at the TU Wien. On the other hand, a comparison with other student theses avoids violations of my personal copyright.

City and Date

Signature

Acknowledgement

I feel very privileged for the opportunity to write my doctoral thesis within the Josef Ressel Center for Thermal NDE of Composites, which is embedded in the Research Group for Thermal Nondestructive Testing. Many people supported me during this time, which was very important for the progress of my doctoral thesis and in the following lines I would like to take the opportunity to say thank you.

I am very grateful to Peter Burgholzer, the supervisor of my doctoral thesis. Peter, thank you very much for your time, your explanations of scientific things and your quick answers. It is inspiring for me how you live science and research.

I would also like to thank my colleagues in the Research Group for Thermography and Non-Destructive Testing for their support with the measurement equipment and the very interesting discussions, both scientific and private.

I would especially like to thank the head of the Josef Ressel Center, Günther Mayr. Günther, thank you very much for the confidence, the development space and the very interesting discussions about the Virtual Wave Concept.

Furthermore, I would like to thank the scientific partners, especially Mathias Ziegler, Samim Ahmadi and Philipp Daniel Hirsch from the Bundesanstalt für Materialwissenschaften (BAM) and Markus Haltmeier from the University of Innsbruck. Thank you for the very interesting discussions on thermographic and inverse problems.

I would also like to thank the companies FACC, Engel and Ottronic for the financial support of the Josef Ressel Center for Thermal NDE of Composites, which was an important factor for the preparation of the present doctoral thesis

To my beloved wife Veronika and my beloved sons Theodor and Jonathan: thank you for your patience, inspiration and love during the preparation of my doctoral thesis. Veronika, thank you for organizing the everyday things of life so that I could focus on research and study.

Contents

Abstract	VI
Kurzfassung	VII
1 Introduction	1
1.1 Motivation	1
1.1.1 FRP components for aviation	2
1.1.2 Defects in FRP materials	3
1.1.3 Non-destructive testing of FRP components	3
1.2 Problem statement	4
1.3 Aim of this doctoral thesis	6
2 Thermographic signal processing	8
2.1 Experimental active IRT set-ups and limitations	8
2.1.1 Experimental set-ups	8
2.1.2 Limitations of active IRT	10
2.2 Local signal processing methods	12
2.3 Global signal processing methods	14
2.3.1 Inverse problem and regularization	15
2.3.2 One step IHCPs for defect characterization	17
2.3.3 Two step IHCP for defect characterization	18
3 Principles of the Virtual Wave Concept	19
3.1 First reconstruction step	19
3.1.1 The virtual wave signal in infinite bodies	21
3.1.2 The virtual wave signal in finite bodies	23
3.1.3 Discrete inverse problem	28
3.1.4 Arbitrary heating function	28

3.2	Second reconstruction step	30
3.3	Application of both reconstruction steps	32
4	Bibliography	34
5	Publications and Scientific contribution	45
5.1	Photoacoustic reconstruction from photothermal measurements including prior information	47
5.2	Photothermal image reconstruction in opaque media with virtual wave back-propagation	56
5.3	Photothermal testing of composite materials: Virtual wave concept with prior information for parameter estimation and image reconstruction	66
5.4	3D photothermal imaging of subsurface defects in composite materials	84
5.5	3D photothermal imaging of real subsurface defects in anisotropic media	95
5.6	Summary	103
5.7	Outlook	105
6	Curriculum Vitae	106

Abstract

To enable higher payloads, longer ranges and lower fuel consumption, the aviation industry is striving to reduce the weight of aircraft structures. This ambition has boosted the development of man-made composite structures, and today modern aircraft structures already consist of 50 percent fiber-reinforced polymers. Fiber-reinforced polymers are highly susceptible to impact damage, which significantly affects the mechanical properties of the composite structure. Impact damage can cause safety-critical subsurface defects such as delaminations in the composite structure. Advanced non-destructive testing methods such as active thermography are necessary to reveal safety critical defects. The industry requires reliable and fast non-destructive testing methods for economical part inspection. In principle, these requirements can be met by active thermography testing, which is also a contactless non-destructive testing method. However, a drawback of this method is the significant decrease in spatial resolution with increasing imaging depth, which results in blurred images. In addition, current active infrared thermography methods are lacking in 3D representation of subsurface defects or do not account for lateral heat flow.

In this thesis, a new approach for active thermography data evaluation, called the virtual wave concept, is extended for application to anisotropic materials and for photothermal temperature signals. Moreover, the degradation of spatial resolution with increasing imaging depth is partially compensated by incorporating prior information such as positivity and sparsity into the regularization procedure. In addition, a novel approach for the estimation of the anisotropic thermal diffusivity tensor is proposed, which enables the rectification of the anisotropic heat flux and a 3D visualization of subsurface defects in fiber-reinforced samples. The proposed 3D reconstruction method is applied to carbon fiber reinforced materials with artificial defects, represented by flat bottom holes, and to real defects, represented by delaminations. To summarize, this doctoral thesis presents a fast, easily interpretable 3D reconstruction tool for photothermal subsurface defect detection in anisotropic media.

Kurzfassung

Um höhere Nutzlasten, größere Reichweiten und einen geringeren Treibstoffverbrauch zu erzielen, ist die Luftfahrtindustrie bestrebt, das Gewicht von Flugzeugstrukturen zu reduzieren. Dieses Bestreben hat die Entwicklung von künstlichen Verbundstrukturen vorangetrieben, und heutzutage bestehen moderne Flugzeugstrukturen bereits zu 50 Prozent aus faserverstärkten Kunststoffen. Faserverstärkte Kunststoffe sind sehr anfällig für Schlagschäden, da diese die mechanischen Eigenschaften der Verbundstruktur erheblich beeinträchtigen. Schlagschäden können sicherheitskritische Defekte wie Delaminationen in der Verbundstruktur verursachen. Um sicherheitskritische Defekte zu detektieren, sind hochentwickelte zerstörungsfreie Prüfmethoden, wie beispielsweise die aktive Thermografie, notwendig. Zur wirtschaftlichen Bauteilprüfung benötigt die Industrie zuverlässige und schnelle zerstörungsfreie Prüfmethoden. Grundsätzlich können diese Anforderungen durch die Prüfung mittels aktiver Thermografie erfüllt werden, die zudem eine berührungslose zerstörungsfreie Prüfmethode darstellt. Ein Nachteil dieser Prüfmethode ist jedoch die deutliche Abnahme der örtlichen Auflösung mit zunehmender Abbildungstiefe, wodurch unscharfe Defektabbildungen entstehen. Zudem erlauben die existenten Rekonstruktionsverfahren der aktiven Thermografie, insbesondere bei anisotropen Materialien und unter der Berücksichtigung des lateralen Wärmeflusses, keine 3D Defektvisualisierung.

In dieser Arbeit wird ein neuer Ansatz zur aktiven Thermografie-Datenauswertung, das sogenannte virtuelle Wellenkonzept, für die Anwendung auf anisotrope Materialien und für photothermische Temperatursignale erweitert. Darüber hinaus wird die Abnahme der räumlichen Auflösung mit zunehmender Abbildungstiefe durch die Einbindung von Vorinformationen in das Regularisierungsverfahren, wie zum Beispiel Positivität und Sparsity (bezeichnet dünnbesetzte Matrizen), teilweise kompensiert. Zudem wird ein neuartiger Ansatz für die Bestimmung des anisotropen thermischen Diffusivitäts-Tensors vorgeschlagen, und ein mathematischer Zusammenhang dieses Tensors mit dem Tensor der virtuellen Schallgeschwindigkeiten hergeleitet. Mithilfe dieses Zusammenhanges kann der anisotrope Wärmefluss entzerrt werden, wodurch eine 3D Defektvisualisierung und Defektrekonstruktion in faserverstärkten Kunststoffen ermög-

licht wird. Das vorgeschlagene 3D Rekonstruktionsverfahren wird auf kohlenstofffaserverstärkte Materialien mit künstlichen Defekten, abgebildet durch Flachbodenbohrungen, und auf reale Defekte, abgebildet durch Delaminationen, angewendet. Zusammenfassend stellt diese Dissertation ein schnelles, leicht interpretierbares 3D Rekonstruktionswerkzeug zur photothermischen Defekterkennung in anisotrope Materialien vor.

1 Introduction

1.1 Motivation

Composite materials have a long tradition in the construction of aircraft structures. In the pioneering phase of aircrafts, the natural composite material wood was mainly used as it possessed appropriate mechanical properties and was much cheaper and easier to process than, for example, aluminum [1]. In the 1930s, however, aircraft composite structures were increasingly replaced by metal-based structures to enable higher flight speeds and payloads [2]. In the meantime however, polymer and fiber developments enabled the processing of fiber-reinforced polymers (FRP) with the following outstanding properties compared to metal-based structures [1, 3, 4]:

- high stiffness to weight ratio and high strength to weight ratio,
- corrosion resistance,
- possibility of tailored material properties.

The weight savings achieved by FRP composite structures enable higher payloads, longer ranges and lower fuel consumption [3]. Due to their favorable properties, composites started their comeback in the 1970s in the form of FRP structures, which are increasingly replacing the metal-based components of an civil aircraft [5]. Nowadays, FRP composites already account for more than 50% of modern civil aircraft structures [6].

During the manufacturing process and in service, different types of defects occur in FRP composites compared to metals, such as porosity or delamination. Especially impact damage is a great concern because it is often not detectable by visual inspection, but can introduce considerable damage in the form of e.g. delaminations which significantly affects the mechanical properties of the FRP materials. [3]

Consequently, fast and reliable non-destructive subsurface defect detection methods are necessary in order to reveal safety-relevant structure weaknesses rapidly and economically.

1.1.1 FRP components for aviation

FRP components typically consist of two phases, namely the matrix material, which represents the continuous phase, and the fiber material, which represents the reinforcement phase. The most common matrix materials used for aerospace components are thermosets such as epoxies, polyesters or vinyl esters. Fiber materials can be carbon, glass or aramid, for example. In modern aerospace manufacturing, preregs, fibers that are pre-impregnated with the matrix material, are commonly used. Preregs are available with a UD fiber orientation or different weave forms such as plain weave or satin weave. They are stacked in a defined manner to meet the required mechanical properties as illustrated in Figs. 1.1a) and 1.1b). Stacking of the preregs can be done either automatically or by hand lay-up. Especially for small quantities and complex components, hand lay-up is preferred to automatic lay-up for economic reasons. The lay-up consists not only of the preregs, but also of other constituents such as peel plies, release films, edge bleeders and breather material, and various bagging strategies are available. Once stacked, the prepreg collation or laminate is sealed in a vacuum bag, and after vacuum bagging, the laminate can be cured in an autoclave, for example. Autoclave curing is commonly used for high quality FRP components that are assembled into aircraft structures. [3]

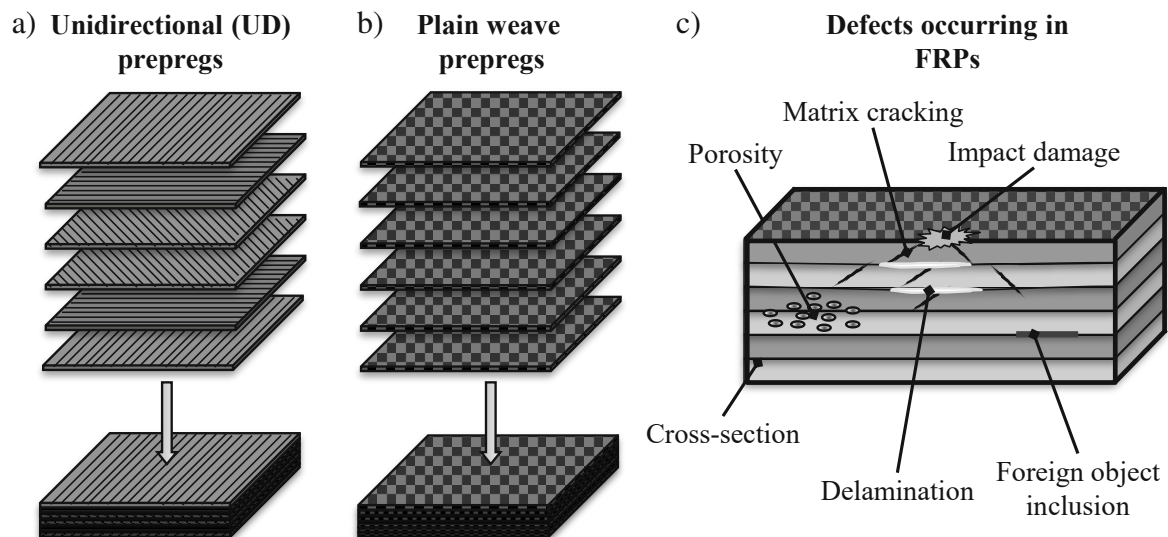


Figure 1.1: a) Stacking of UD prepreg layers and the corresponding laminate and b) stacking of plain weave prepreg layers and the corresponding laminate (inspired by Ref. [3]). c) Defects that can result from the manufacturing process or that can occur in service, for example, due to a bird strike (inspired by Ref. [7]).

1.1.2 Defects in FRP materials

During the manufacturing process and in service, many different defects can occur in the FRP components that affect their mechanical properties. Fig. 1.1c) shows some typical defects such as porosity, matrix cracks, delamination, foreign object inclusions or impact damage [7, 8].

While matrix cracking belongs to the microscale dimension, porosity belongs rather to the meso-scale dimension. Delamination and foreign object inclusions can be assigned to the meso-scale or macro-scale dimension. [9]

Porosity can be caused by gas inclusions in the manufacturing process. Foreign object inclusions, such as prepreg backing paper, can also be accidentally incorporated during the manufacturing process. Impact damage generated by a bird or lightning strike can cause matrix cracking and delamination which significantly impacts the mechanical properties of the FRP structure. Delaminations can also be introduced during manufacturing processes such as drilling or due to improper fastener mounting. [3]

1.1.3 Non-destructive testing of FRP components

In order to reveal safety-relevant defects in aircraft components, they have to be tested non-destructively by standardized methods. These components are tested not only after production, but also at specific maintenance intervals. The most commonly used non-destructive testing (NDT) imaging method in the aviation industry is ultrasonic testing (UT) [1]. Due to its long-term use and the corresponding experience with it, UT represents a robust and reliable method for multi-dimensional defect identification, detection, sizing and visualization. The main disadvantage of conventional UT is the need for a coupling agent to properly launch the ultrasonic waves into the sample, which can affect the sample [10]. This drawback and the change from metal-based to composite designs boosted the application of active infrared thermography (IRT) for the NDT of aircraft components. In contrast to UT, where acoustic wave propagation is observed, IRT monitors the heat diffusion process. Active IRT requires an active thermal excitation, i.e. a heating or cooling, of the sample under test (SUT), for instance, by a flash-lamp or a laser. The excitation energy is absorbed by the SUT initiating a heat diffusion process there. If the thermal diffusion process is disturbed by a subsurface defect with different thermophysical properties compared to the bulk material, this will affect the surface temperature signal that can be recorded using an infrared (IR) camera. Thermography testing is advantageous because it is a contactless method and due to the focal plane array of the IR camera, a huge measurement throughput is possible.

1.2 Problem statement

In recent years active IRT shows a trend from qualitative to quantitative defect detection. Qualitative defect detection methods have the benefit, that they allow fast data evaluation, but additional information about subsurface defects like size and depth cannot be extracted. This limits the application of active IRT for defect detection in aircraft components because uncertainties in the defect characterization corresponds with higher load tolerances, weights, and costs of the components [3].

One way to quantitatively locate and size defects is to solve an inverse heat conduction problem (IHCP). In contrast to UT, where the wave propagation is described by the time reversible wave equation, thermal wave propagation, which is described by the heat equation, is irreversible in time and hence a severely ill-posed inverse problem must be tackled. As shown in Fig. 1.2, for practical application, the forward solution is given by the measured surface temperature signal, which carries information about the structure of the subsurface of the SUT. The inverse problem is then, for example, to calculate the initial temperature signal and secondary boundary sources based on the measured temperature signal. Secondary boundary sources can result from defects and the back wall of the sample. To solve such a severely ill-posed inverse problem regularization tools, such as the truncated singular value decomposition (T-SVD), are necessary.

Solving a multi-dimensional IHCP is related to a large-scale problem. Consequently, its solution is computationally expensive [11]. For this reason, some research groups try to circumvent the solution of multi-dimensional IHCPs and use instead a 1D model or data driven evaluation methods for defect sizing and localization. These approaches work well for planar defects near the surface of isotropic samples, but may be inadequate for highly anisotropic samples and smaller and deeper defects because they do not account for lateral heat flow, thus preventing accurate defect sizing. In addition, the interpretation of results can be challenging compared to UT, as many thermographic evaluation methods such as the thermographic signal reconstruction (TSR) [12] only allow 2D defect visualization for a 3D SUT (see Fig. 1.2).

One possible approach to overcome these issues is the virtual wave concept (VWC), which is a two-step reconstruction procedure [13]. The intention of the VWC is to combine the advantages of UT and IRT to obtain a fast, non-contact and easily-interpretable reconstruction method. In a first step, the measured temperature signal obtained from an active IRT experiment is locally transformed (pixel by pixel) into a virtual wave signal. This virtual wave signal

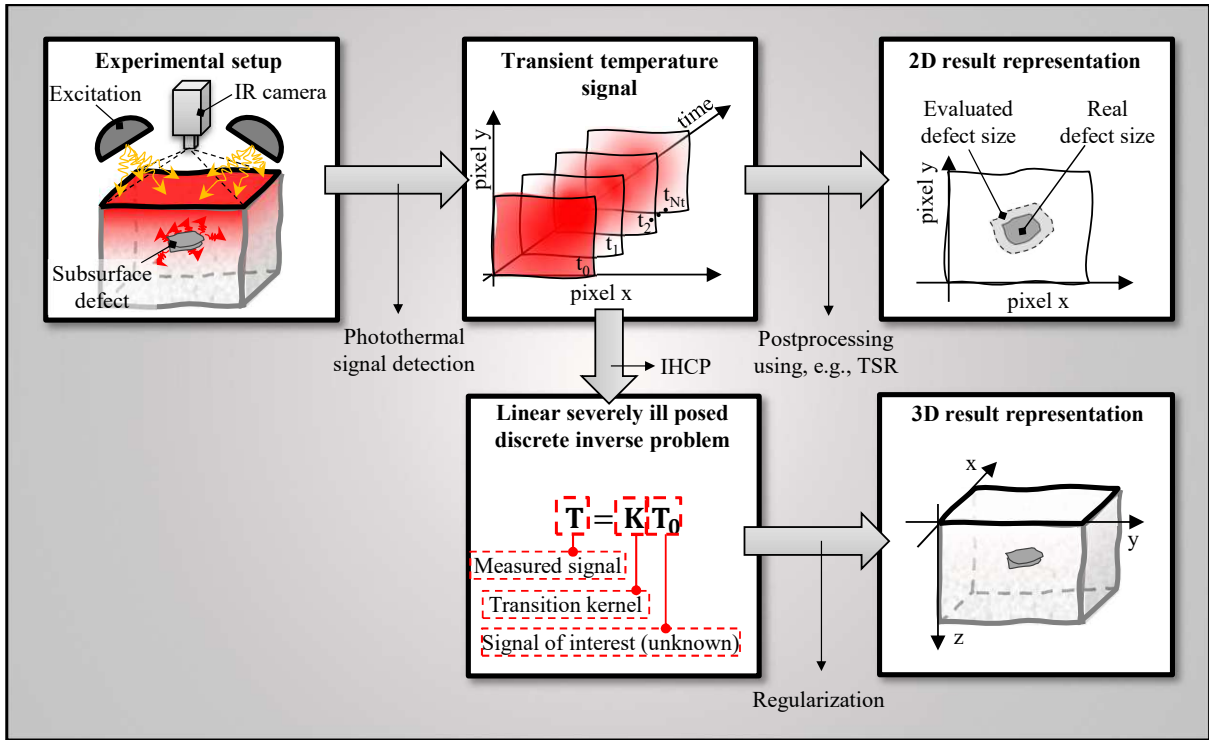


Figure 1.2: State-of-the-art subsurface thermographic reconstruction methods. 1D thermographic reconstruction method such as the TSR method do not take into account the lateral heat flow and allow only for a 2D defect representation. Solving an IHCP requires stabilization or regularization to obtain a useful solution and typically results in a large-scale problem which are computationally expensive.

obeys the standard wave equation, and hence in a second evaluation step, well known ultrasonic reconstruction methods, such as the time of flight (TOF) [14, 15] or the frequency/time domain aperture focusing testing (F/T-SAFT) algorithms [16, 17], can be used for defect localization. The current results of the VWC method for 3D defect imaging are very promising. However, the applicability of the VWC procedure is limited to date to isotropic samples and internal heat sources. The current state of the VWC technique is also schematically shown in Fig. 1.3a). Similar to an IHCP, the computation of the virtual wave field requires regularization to obtain a useful inverse solution. To date, only direct regularization methods such as T-SVD have been used. The problem with T-SVD is that no prior information, such as sparsity, can be included to compensate for the loss of information due to heat diffusion, which results in blurred images with increasing imaging depth. For this reason, as shown in Fig. 1.3a), after the second reconstruction step subsurface defects appear very blurry, which impedes accurate defect sizing.

1.3 Aim of this doctoral thesis

This doctoral thesis aims to complement the VWC procedure for 3D reconstruction and visualization of subsurface defects that are embedded in anisotropic materials such as CFRPs and for the pulse-echo configuration which is a very relevant practical active IRT set-up. To partially compensate for the degradation of the spatial resolution with increasing imaging depth, the iterative regularization method ADMM is implemented for the VWC evaluation procedure which enables the incorporation of prior information in the form of positivity and sparsity. Fig. 1.3b) shows schematically the further development of the VWC for the first and second reconstruction step. To rectify the anisotropic lateral heat flow, a novel thermal diffusivity tensor estimation procedure is proposed, and the second reconstruction step is modified, which enables the incorporation of the virtual speeds of sound in the principal directions. Moreover, a discretization criterion is proposed that drastically reduces the computational cost of the evaluation procedure, as indicated by the bars at the bottom of Fig.1.3, without affecting the quality of the defect imaging. The characteristics of the virtual wave signal, which is calculated from a distorted surface temperature signal and carries information about subsurface defects, are also discussed in detail.

The doctoral thesis is organized as follows: in Chapter 2 basic active IRT set-ups, some limitations of active IRT and state-of-the-art thermographic signal processing methods as well as the VWC are reviewed. Chapter 3 reviews the principles of the VWC by deriving the transformation of the temperature signal into a virtual wave signal and in terms of boundary conditions and noise filtering capabilities. Chapter 5 provides a short summary of the research papers and a discussion of the obtained results.

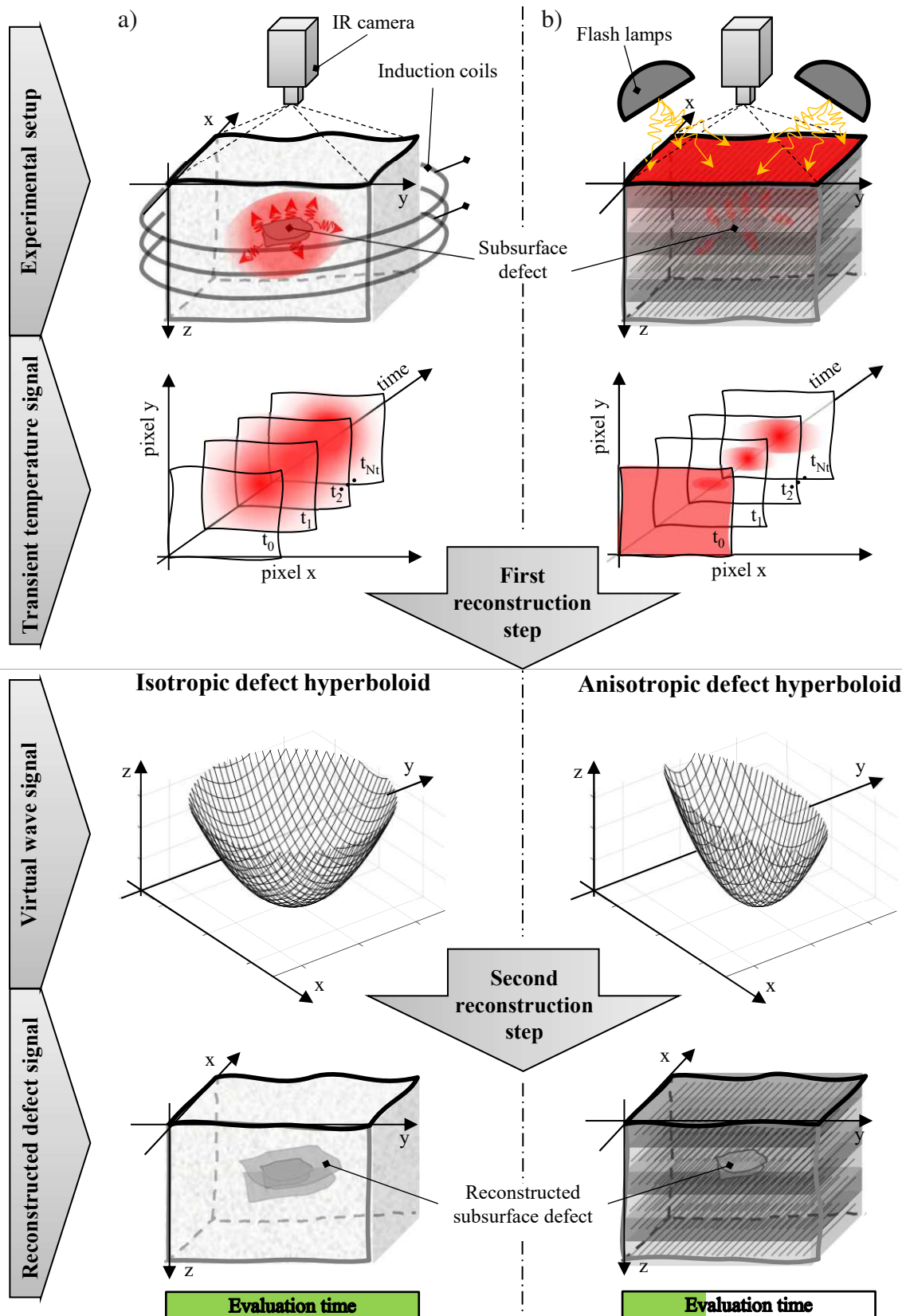


Figure 1.3: a) VWC for internal heat sources and isotropic media - current research state. b) Further development of the VWC to make it applicable for anisotropic media and photothermal testing for the practical most relevant pulse-echo configuration. To partially compensate for the degradation of the spatial resolution with increasing imaging depth prior information was incorporated in the regularization process. In this thesis also a discretization procedure was proposed which allows a fast and easy interpretable 3D defect reconstruction and visualization.

2 Thermographic signal processing

In contrast to UT, where acoustic wave propagation is analyzed, in active IRT heat diffusion or thermal wave propagation is observed. Compared to an acoustic wave, a thermal wave is strongly attenuated during propagation through the SUT. This attenuation is caused by the entropy production during the heat diffusion, which is equal to information loss [18]. Therefore, the thermal wave cannot be back-propagated like an acoustic wave. This fact leads to a significantly limited evaluability of raw active IRT data in terms of parameter estimation, defect localization and defect sizing. Thus, it is necessary to manipulate the raw IRT data by advanced signal processing methods. Another signal processing task is the compensation of, for example, non-uniform illumination or local variations in thermal emissivity or optical absorption [19].

Since in this doctoral thesis the subsurface defect detection is based on active IRT data, this chapter explains the main active IRT set-ups and discusses some experimental limitations. In addition, established and recent local and global thermographic signal processing methods for active IRT and their limitations are reviewed. In contrast to local thermographic signal processing methods, global thermographic signal methods take into account the lateral heat flow, which becomes particularly relevant for 3D defect visualization in anisotropic materials. Since the results and findings of this thesis are based on the global signal processing method VWC, special attention is given to this approach in Chapter 3.

2.1 Experimental active IRT set-ups and limitations

2.1.1 Experimental set-ups

Basic experimental set-ups for active IRT consisting of a SUT, an excitation source and an IR camera, are illustrated in Fig. 2.1. Figs. 2.1a) and 2.1b) show the configurations with an optical excitation in reflection and transmission mode, respectively. Typical optical excitation sources are flash lamps, halogen lamps and lasers. If the observed sample with thermophysical

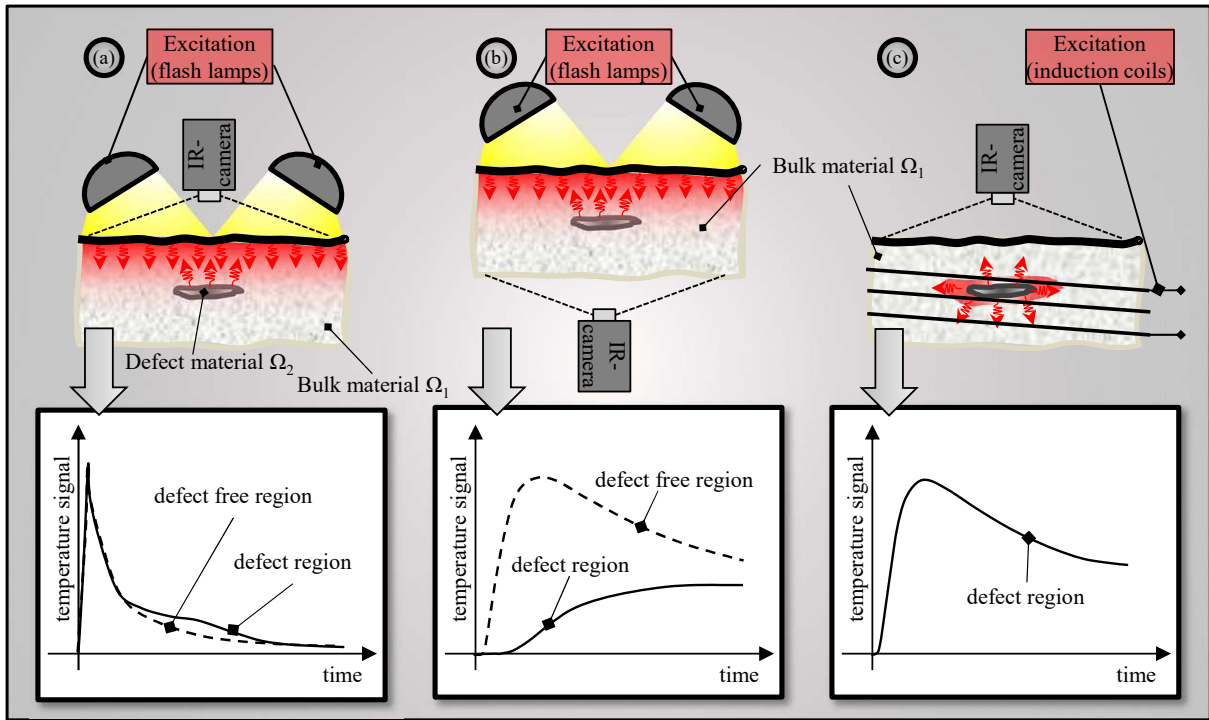


Figure 2.1: The most common active IRT scenarios and the corresponding characteristic transient surface temperature signals. Test scenario a) shows the reflection configuration and test scenario b) shows the transmission configuration. In these configurations, the heat is introduced at the surface of the opaque sample. c) shows an exemplary test scenario to generate internal heat sources via induction of eddy currents.

properties Ω_1 is optically opaque, the excitation energy is absorbed at the stimulated surface, which initiates thermal waves there that travel through the subsurface. If the thermal wave propagation is disturbed by a defect with thermophysical properties Ω_2 , which are unequal to Ω_1 , secondary thermal wave sources and sinks are introduced at the defect boundaries [20]. This results in a two-way heat diffusion and the corresponding spatial and temporal change of the surface temperature signal can be recorded with an IR camera. Conversely, in the transmission configuration, Fig. 2.1b), a one-way heat diffusion process is observed. The black boxes in Figs. 2.1a) and 2.1b), depict exemplary surface temperature signals in defect and defect-free regions for both reflection and transmission mode, where the SUT was heated by a temporally short optical pulse.

In contrast to Figs. 2.1a) and 2.1b), Fig. 2.1c) shows a thermography setup for generating internal heat sources in the SUT by inducing eddy currents. Here it is assumed that eddy currents can only be induced in Ω_2 , thus a reasonable thermal contrast between bulk and defect material can be achieved. Due to the internal heat source, thermal waves are initiated at the defect boundaries. They propagate through the sample and again cause a change in the surface temperature

signal which can be observed with an IR camera. The black box in Fig. 2.1c) shows an example of surface temperature signal in a defect region. Particularly in the case of semi-transparent and light-scattering samples, such as epoxy or biological tissue, light-absorbing subsurface structures, such as carbon fibers or blood vessels, can work as internal heat sources due to optical excitation. Another active IRT technique that can generate internal heat sources, is vibrothermography (VT). VT uses mechanical vibration which cause friction in a defect region leading to an energy conversion from mechanical to heat energy [21]. The heat energy again initiates a thermal wave that leads to a change in the surface temperature signal. Both external and internal heating or cooling can vary in space and time. Based on the temporal excitation, active IRT can be divided into pulsed thermography (PT) and Lockin Thermography (LT) which is also denoted as photothermal radiometry (PTR) [22]. More precisely, PTR describes a point-by-point photothermal imaging method (small evaluation range), while LT uses an IR camera for photothermal imaging (large evaluation range) [23]. While in PT the transient surface temperature signal response is observed after a temporally short excitation pulse, in LT the steady-state surface temperature signal response caused by a time-varying excitation is analyzed [22].




Several thermographic signal processing methods are based on a mathematical model in order to enable, for instance, parameter estimation or the localization and sizing of defects. Hence, the experimental set-up, i.e. initial and boundary conditions, must be designed in accordance with the underlying mathematical model.

2.1.2 Limitations of active IRT

As mentioned before, the spatial and temporal change of the surface temperature or, more precisely, the IR radiation signal can be detected with an IR camera. The main groups of IR detectors are represented by thermal detectors, such as bolometers, and photonic or quantum detectors. While bolometers use the change in resistance of semiconductor materials, quantum detectors use the internal photoelectric effect to characterize IR radiation. The advantages of thermal detectors compared to quantum detectors include that they are relatively cheap, cover a wide spectral range, and do not require cooling. Quantum detectors are advantageous because they offer good detectability and allow high imaging frequencies. However, each detector exhibits detector noise that results in a certain noise equivalent temperature difference (NETD) or temperature resolution of the IR camera. [24, 25]

The characterization of the camera noise is fundamental for a successful solution of an IHCP and therefore Beck et al. [26,27] formulated eight standard assumptions regarding measurement

Table 2.1: Resolution limits for PT data. Δ_ζ describes the resolution of a defect for early times $\hat{t} \ll \zeta^2/\alpha$ and near surface defect depths ζ , where α is the thermal diffusivity of the observed material and m is the frame number. The maximum depth resolution Δ_L , is calculated with the sample thickness L , the material density ρ , the specific heat capacity c_p , the energy Q and the ΔT_{NETD} which is a temperature equivalent to the IR camera noise [25]. δ_{res} describes the resolution of two lateral extended but axial infinitesimal small defects at a certain depth z and for a specific SNR.

Authors	Limit for:	Math. description	Sketch
Shepard et al. [30]	Early time/near surface	$\frac{\Delta_\zeta}{\zeta} = \frac{1}{2m}$	
Shepard et al. [30]	Late time/maximum depth	$\frac{\Delta_L}{L} = -\frac{\rho c_p L}{Q} \Delta T_{\text{NETD}}$	
Burgholzer et al. [29]	Axial defect separation	$\frac{\delta_{\text{res}}}{L} = \frac{z}{L} \frac{\pi}{\ln(\text{SNR})}$	

errors. Breitwieser et al. [28] verified these assumptions for IR cameras with a quantum detector based on the photon transfer technique with the result that they are not valid for the observed detectors. However, for a limited temperature range, the authors argued that the variance of the measurement signal can be considered constant which corresponds to white Gaussian noise. The temperature resolution and excitation signal lead to a certain signal-to-noise ratio (SNR) of the surface temperature signal, which limits the maximum defect depth and backwall resolution as well as the defect separation capability. Limits for defect separation [18, 29] and depth resolution as a function of NETD have been formulated specifically for PT testing, but for subsurface defects near the plane of observation, only the imaging frequency of the IR camera is the limiting parameter [30]. The limits, the corresponding mathematical descriptions and sketches are listed in Tab. 2.1. The derivation of the axial defect separation limit is based on a 1D heat diffusion process in a semi-infinite body. The near surface limit and the maximum depth limit are also based on a 1D heat diffusion process and their derivation is based on the following mathematical relationship [30]:

$$L = \sqrt{\pi \alpha t}, \quad (2.1)$$

where α is the thermal diffusivity and L is the sample thickness.

Another limitation of PT states that the defect diameter-to-depth ratio must be greater than two in order to detect the defect [22]. However, Almond and Pickering [31] found that this well-known rule of thumb for defect detection is incorrect. In an analytical study, they concluded

that the defect detection capability depends not only on the defect aspect ratio, but also on the input energy provided by the flash lamps.

2.2 Local signal processing methods

A simple and computationally inexpensive approach to improve the image quality and the defect visibility of PT data is to calculate a thermal contrast image. There exist various definitions of the thermal contrast, for instance, the running contrast, the standard contrast and the differential absolute contrast (DAC) [22, 32, 33]. The latter method is advantageous, because there is no need for predefining a sound area (defect-free region). Predefining a sound area is challenging because a priori defect locations in the observed sample are unknown. The DAC method was modified by Benitez et al. [34]. They introduced the sample thickness in the DAC modelling to extend the application for long periods after heating. Another prominent PT postprocessing method is the pulsed phase thermography (PPT). PPT aims to combine the advantages of PT and lockin thermography (LT), i.e. fast image recording is combined with a deeper probing and defect-sizing capability [35]. Using PPT the PT data is Fourier transformed, which enables the computation of an amplitude and a phase image [35, 36]. There exist several extensions of the original PPT processing. Galmich et. al [37], for instance, used a wavelet transform instead of the Fourier transform. Another modification, where PPT is combined with the thermographic signal reconstruction (TSR), was reported by Maldague et al. [38]. TSR is one of the most common postprocessing method for two-way heat diffusion. Commonly, the TSR method uses a polynomial fit to map the raw thermography signal, which introduces a considerable data compression because only the polynomial coefficients for each camera pixel location have to be stored to represent the measured temperature signal [12, 39]. Due to this, the non-thermal temporal noise produced by the IR camera can be significantly reduced and allows a simple data manipulation, for instance, differentiation [12]. Vavilov et. al [40, 41] proposed a phenomenological method called dynamic thermal tomography (DTT), which maps the sequential thermographic signal onto a maxigram and timegram. The maxigram reflects the maximal temperature signal and the timegram represents the corresponding optimal observation of each pixel. The timegram can be converted with a calibration function to estimate defect depths [42]. Similar to conventional thermal contrast methods, DTT processing requires the predefinition of a reference point. To circumvent this predefinition, thermal diffusivity estimates were supplemented to the classical DTT method [33].

To overcome the limitations of PT and LT in terms of maximum permissible exposure (MPE) and depth resolution, Tuli and Mulaveesala [43] and Mulaveesala et al. [44] proposed the use of linear frequency modulated (LFM) temporal thermal sample excitation for active IRT. LFM excitation requires lower excitation power compared to PT and, in contrast to conventional LT, thermal waves with multiple wavelengths are coupled into the SUT, which allows for an efficient testing procedure since no repetition with different excitation frequencies is needed to cover the entire sample thickness [45]. Similar to LT, phase images can be evaluated, which allows, for example, compensation for inhomogeneous illuminations or local variations of thermal emissivity or optical absorption [23, 43, 46]. The earliest work of such a photothermal wave system was published in 1986 by Mandelis et al. [47–49]. Tabatabaei and Mandelis [50] proposed the thermal wave radar (TWR), which uses an LFM for temporal thermal excitation and a special type of matched filter in the form of cross correlation (CC) technique for signal processing. In addition to the amplitude CC, they also evaluated the CC peak delay time, where the delay time corresponds to the delay between the photothermal excitation and the thermal response of the SUT. They found that by using TWR, a significantly higher SNR can be achieved, resulting in a significant enhancement of the depth resolution dynamic range compared to PTR [50]. In later work, Tabatabaei et al. [51] showed that phase CC evaluation is even more powerful than amplitude CC, but recommended that both CCs should be evaluated because they provide complementary information. TWR and thermal wave imaging was then applied and adapted by various research groups, for instance for bone diagnostics [52], non-destructive imaging of coatings and cracks [53, 54], or NDT of composite materials [55–58]. Based on the TWR idea, Tabatabaei and Mandelis [59, 60] proposed thermal coherence tomography (TCT), which allows the deconvolution of superimposed, axially discrete sources induced by binary phase-coded (BPC) modulation of the thermal excitation source. They demonstrated that the BPC excitation pattern reduces the side lobes of the CC peak while increasing the peak height in a turbid medium such as biological tissue. Kaiplavil and Mandelis modified TCT and reported a photothermal imaging method called truncated correlation photothermal coherence tomography (TC-PCT) that enables 3D visualization of subsurface features [61]. Contrary to TCT, TC-PCT cross-correlates the temporal thermal response signal caused by a chirped pulse excitation with a sliced reference chirp signal. This procedure results in a depth-resolved signature in which depth information is obtained in a pixel-wise manner based on the delay time. Tavakolian et al. [62, 63] proposed enhanced TC-PCT (eTC-PCT), which uses an optimized reconstruction algorithm and system instrumentation compared to TC-PCT, resulting in improved

axial and lateral resolution for visualization of 3D subsurface features. In recent studies, eTC-PCT has been used for non-destructive imaging of wood inlays [64] or non-invasive 3D in-vivo imaging of small animals [65].

2.3 Global signal processing methods

Local thermographic reconstruction methods do not consider lateral or multi-dimensional thermal diffusion, which may be sufficient for example in the case of homogeneous thermal excitation and defects close to the observation plane. For deeper subsurface defects with small lateral extension, multi-dimensional thermal diffusion must be considered to allow accurate defect sizing and localization as well as 2D/3D defect visualization, especially when they are embedded in anisotropic materials. Fig. 2.2 illustrates the aforementioned limitations of local thermographic signal processing methods. Figs. 2.2a-c) show a test setup with homogeneous thermal excitation, but only for the setup in Fig. 2.2a) the local processing is appropriate. Fig. 2.2c) shows an unsuitable test setup for the detection of vertical cracks. Such cracks provide an insufficient thermal barrier and therefore do not affect the plane thermal waves in-

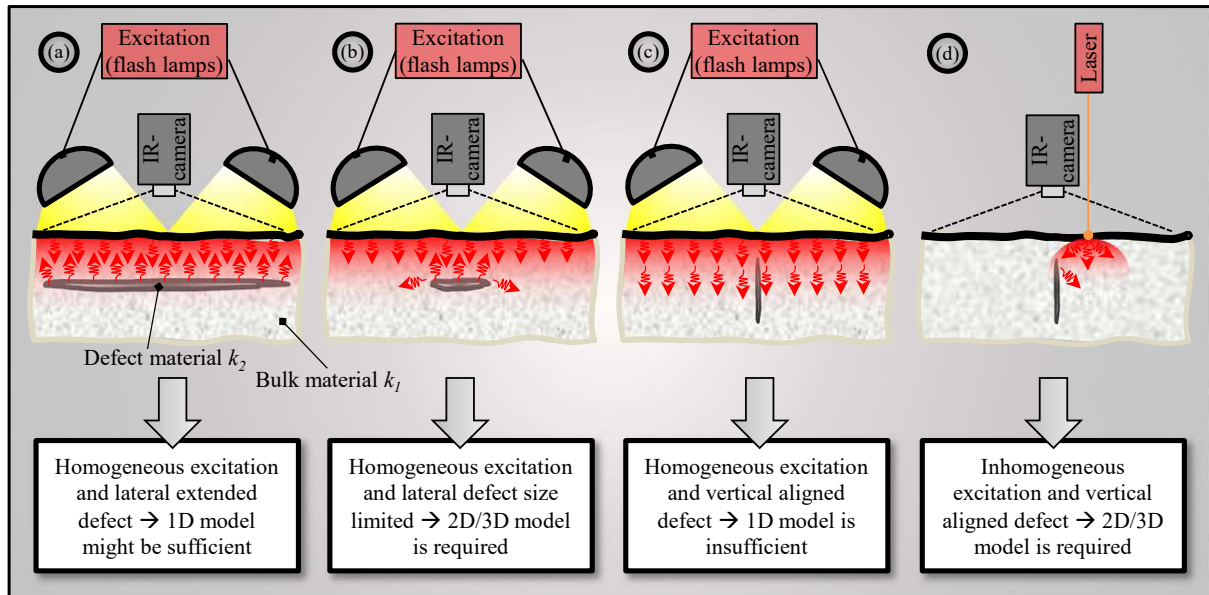


Figure 2.2: Limitations of 1D or local thermographic signal processing methods, explained on an optically opaque material. a-c) shows thermal excitation with flash lamps inducing a homogeneous plane thermal wave into the sample. However, only for a) local thermographic signal processing may be suitable, the others require global thermographic signal processing for accurate defect characterization. d) shows optical excitation with a laser, where only a limited surface area is thermally excited. This configuration also requires global thermographic processing for 3D defect visualization.

duced at the specimen surface. Consequently, there is no change in surface temperature and the crack is not detectable. Figs. 2.2b) and 2.2d) show configurations with spatially homogeneous and inhomogeneous thermal excitation, respectively. An inhomogeneous thermal excitation can be achieved, for instance, by a small laser spot. In both configurations, lateral heat diffusion must be considered for accurate defect sizing and localization. There are several methods that are based on a multi-dimensional heat diffusion model and a fitting procedure such as the Levenberg-Marquardt algorithm to characterize defects and to estimate the corresponding heat flux or initial temperature distribution [66]. Mendioroz et al. [67] for example, used VT data to estimate the defect dimensions, defect depth, and corresponding heat flux of rectangular vertical cracks by a fitting procedure. More recently, they used induction thermography data to characterize tilted cracks as well [68]. Only inverse problems stabilized by regularization are discussed in the following review, since this type of solution technique is used in this thesis for defect characterization.

2.3.1 Inverse problem and regularization

To overcome the limitations of local thermographic signal processing methods, an inverse heat conduction problem (IHCP) can be solved [27]. The IHCP requires forward modeling that accounts for the multi-dimensional heat flow, as shown in Fig. 2.3. There are several approaches, such as the separation of variables or the method of images, to solve the forward problem, i.e., the heat diffusion equation, to obtain the spatial and temporal temperature signal T [69, 70]. To solve the forward problem the boundary conditions, the initial temperature distribution, the defect dimensions and the material parameters such as the thermal conductivity k , the density ρ and the heat capacity c_p must be known a priori. Considering an inverse problem, the spatial and temporal temperature signal is known, but the a priori information is only partially available. Assuming, for example, that the initial and boundary conditions of a thermographic experiment and the material and geometry parameters of the SUT are known a priori, one can reconstruct the size and location of a subsurface defect by solving an inverse problem. An IHCP can be mathematically classified as a severely ill-posed inverse problem that is very sensitive to measurement errors, i.e., small errors in the measured data can lead to large errors for the inverse solution [71]. This is characteristic for IHCPs and can be explained by the entropy production during heat diffusion, which leads to highly attenuated thermal waves for the forward solution but to a high error amplification for the inverse problem. To overcome these issues and to obtain a useful inverse solution, stabilization or regularization methods are necessary [72]. Popular

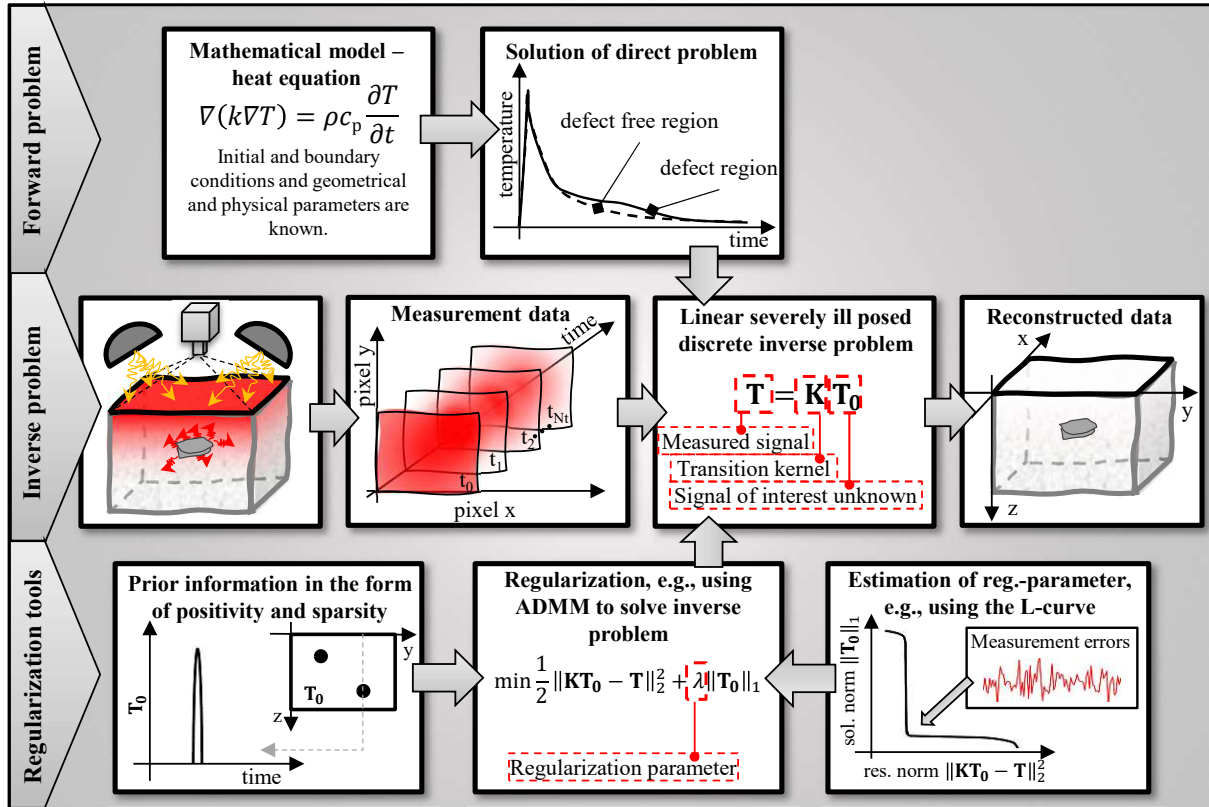


Figure 2.3: Process chain for solving a severely ill-posed inverse problem based on active IRT data and regularization (inspired by Ref. [76]). The process chain includes mathematical modeling by the heat equation with appropriate boundary and initial conditions. The derived model, thermographic measurements, and physical and geometric parameters are necessary to reconstruct subsurface defects using regularization. The regularization procedure requires the estimation of a regularization parameter and the inverse solution can be significantly improved by incorporating prior information.

regularization methods include truncated singular value decomposition (T-SVD), Tikhonov regularization, or alternating direction method of multipliers (ADMM), where each regularization method requires the determination of one or more regularization parameters [73, 74]. There are several methods for estimating regularization parameters, such as the Picard plot and the L-curve method, which is also visualized under regularization tools in Fig. 2.3 [72]. ADMM allows the incorporation of prior information in the form of positivity and sparsity [75]. Positivity assumes that the inverse solution has only positive data points and is applicable when the SUT is heated by, for example, flash lamps. Sparsity can be assumed when the SUT has few defects, resulting in a sparse inverse solution. Several publications consider IHCPs for estimating initial temperature distribution, boundary heat flux, or estimating geometric and physical parameters based on a measured temperature signal [27, 66, 77]. However, publications dealing with IHCPs for multi-dimensional subsurface defect localization, sizing, and visualization,

i.e. defect characterization, are rare. The following review focuses on such IHCPs and aims to highlight the characteristics of the different approaches. Thereby, direct or single-stage IHCPs are distinguished from the two-stage reconstruction method VWC.

2.3.2 One step IHCPs for defect characterization

Celorrío et al. [78] used lock-in VT to characterize vertical subsurface cracks that are embedded in an isotropic material. As mentioned earlier, in VT, mechanical energy is converted to heat energy due to friction at the defect boundaries and thus internal heat sources are induced. By forward modeling the heat diffusion problem, the authors obtained a Fredholm integral of the first kind and used Tikhonov and total variation (TV) regularization to solve the severely ill-posed inverse problem and to estimate the width, height, and depth of the subsurface defect. For this multi-dimensional defect reconstruction approach, Mendioroz et al. [21, 79] investigated the influence of the defect depth and established a resolution criterion. They found that their approach enables reconstruction of defects represented by internal heat sources with a minimum defect depth-to-width ratio of two. In a later work, Mendioroz et al. [80] modified their approach and used instead of a lock-in a burst excitation signal to thermally excite the sample. In this work, they analyzed the influence of different defect shapes, located at different depths, on the reconstruction quality. Especially for defects with discontinuous shapes and TV regularization, their results show that it is not possible to reconstruct a correct defect shape. Another approach for 3D reconstruction of internal heat sources or subsurface defects was proposed by Groz et al. [81]. In their forward modeling of the heat diffusion problem, the defect can be considered as a superposition of point sources, which is appropriate since the standard heat equation is linear. Experimentally, they realized the internal heat sources by a nickel-chromium wire embedded in polymer. A current was applied to the wire and, due to the Joule heating effect, electrical energy was converted to thermal energy, resulting in an internal heat source. To optimize the quality of the inverse solution, the authors performed a parameter study and analyzed the performance of different regularization methods. Holland and Schiefelbein [82] proposed a model-based inversion for pulsed thermography data in reflection configuration and anisotropic materials such as composites. Their model consists of multiple reflectors and the lateral size of the reflectors was modified according to depth to reduce the computational cost of the inversion procedure.

Each of the presented one-stage IHCPs for defect characterization is based on the method of images that uses smart positioning of the fundamental solution of heat conduction to fulfill

both sample and defect boundary conditions [83, 84]. Furthermore, these approaches are based on a lateral infinite and axial finite or semi-infinite body. Usually, depending on the spatial and temporal resolution of the surface temperature signal, such inversion approaches lead to a large-scale inverse problem that can be computationally expensive.

2.3.3 Two step IHCP for defect characterization

In 2017, Burgholzer et al. [13] proposed an alternative approach, called the virtual wave concept (VWC), for multi-dimensional defect reconstruction. Instead of the single-step reconstructions discussed in the last section, VWC involves two reconstruction steps. In the first step, an "acoustic" virtual wave signal is calculated from the measured surface temperature signal. The virtual wave signal fulfills the standard wave equation so that in the second step, established ultrasonic reconstruction methods such as TOF or F-SAFT can be used for defect reconstruction. While the surface temperature signal is temporally noise-filtered in the first step, spatial noise filtering is introduced in the second step. In contrast to the wave equation, the heat equation or diffusion equation describes an irreversible process. The first conversion of a diffusive (electromagnetic) wave signal to a non-diffusive wave signal was proposed by Lee et al. [85, 86] and Gershenson [87, 88] for geophysical applications. Later, Tamburrino et al. [89] used this conversion and presented applications for 3D eddy current testing based on theoretical and numerical results.

In the last few years VWC has also been used for parameter estimation and as a feature extraction method for machine learning approaches. For example, Mayr et al. [15] verified the accuracy of VWC in terms of sample thickness estimation. Plasser et al. [90] estimated the thermal diffusion time of CFRP materials in transmission and reflection configuration in order to evaluate the porosity of the corresponding samples. A hybrid approach that combines the temperature to virtual wave transformation with a deep learning approach was proposed by Kovacs et al. [91, 92]. They found that the VWC is an excellent method for feature extraction and due to this the training of the neural network can be significantly reduced compared to the direct transformation of surface temperature to initial temperature signal. In another study, VWC was combined with a thermographic super-resolution approach to overcome the resolution limit of active IRT [93–95].

3 Principles of the Virtual Wave Concept

This chapter reviews the principles of the VWC by deriving the transformation of the temperature signal into a virtual wave signal and in terms of boundary conditions and noise filtering capabilities. As already mentioned, the VWC is a two-step reconstruction procedure. In the first step the temperature signal $T(\mathbf{r}, t)$ is transformed locally (pixel by pixel) into a so-called virtual wave signal $T_{\text{virt}}(\mathbf{r}, t)$. The first reconstruction step eliminates the temporal noise, but the spatial noise is still present. In addition, only the axial boundary conditions can be considered in the first reconstruction step. The lateral boundary conditions and the heat flow from all directions are then separated and back-projected in the second evaluation step by applying, for example, ultrasonic reconstruction methods such as T-SAFT or F-SAFT.

3.1 First reconstruction step

In the sense of the VWC, the diffusive wave field is described by the heat equation [69]

$$\left(\Delta - \frac{1}{\alpha} \frac{\partial}{\partial t}\right) T(\mathbf{r}, t) = -\frac{1}{\alpha} T_0(\mathbf{r}) \delta(t). \quad (3.1)$$

The heat equation describes the thermal wave propagation or temperature signal $T(\mathbf{r}, t)$ in an isotropic or orthotropic solid as a function of the position vector $\mathbf{r} = (x, y, z)$ and the time t . The characteristic parameter for thermal wave propagation is the thermal diffusivity α which is assumed to be temperature-independent. When considering an orthotropic body, Eq. 3.1 also applies after a suitable coordinate transformation. However, the thermal diffusivity $\alpha = (\alpha_{11} \alpha_{22} \alpha_{33})^{1/3}$ is calculated with the thermal diffusivities in the principal directions [83]. The right-hand side of Eq. 3.1 depicts the source term. The temporal Dirac-Delta distribution $\delta(t)$ ensures that the initial temperature distribution $T_0(\mathbf{r})$ is introduced at $t = 0$. Δ is the Laplace operator that describes the second spatial derivatives of the temperature signal $T(\mathbf{r}, t)$. The virtual wave propagation $T_{\text{virt}}(\mathbf{r}, t)$ as a function of position vector \mathbf{r} and time t can be deduced

from the acoustic wave equation for pressure [96]

$$\left(\Delta - \frac{1}{c^2} \frac{\partial^2}{\partial t^2}\right) p(\mathbf{r}, t) = -\frac{1}{c^2} \frac{\partial}{\partial t} p_0(\mathbf{r}) \delta(t). \quad (3.2)$$

The photoacoustic wave pressure $p(\mathbf{r}, t)$ is also a function of position vector \mathbf{r} and time t , where c denotes the speed of sound, which is the characteristic parameter for pressure wave propagation. The right-hand side of Eq. 3.2 denotes the source term where the temporal Dirac-Delta distribution $\delta(t)$ ensures that the initial pressure signal $p_0(\mathbf{r})$ is spontaneously induced. To obtain the partial differential equation (PDE) for the virtual wave signal $T_{\text{virt}}(\mathbf{r}, t)$, the initial pressure signal $p_0(\mathbf{r})$ and the photoacoustic pressure signal $p(\mathbf{r}, t)$ for $t > 0$ are specified by [97]

$$p_0(\mathbf{r}) = c^2 \rho \beta T_0(\mathbf{r}) \quad (\text{for } t = 0) \quad \text{and} \quad p(\mathbf{r}, t) = c^2 \rho \beta T_{\text{virt}}(\mathbf{r}, t) \quad (\text{for } t > 0). \quad (3.3)$$

Here ρ denotes the material density and β is the thermal expansion coefficient. By substituting the relations of Eq. 3.3 into the acoustic wave equation for pressure, Eq. 3.2, the PDE for the virtual wave signal $T_{\text{virt}}(\mathbf{r}, t)$ can be written as follows [97]:

$$\left(\Delta - \frac{1}{c^2} \frac{\partial^2}{\partial t^2}\right) T_{\text{virt}}(\mathbf{r}, t) = -\frac{1}{c^2} \frac{\partial}{\partial t} T_0(\mathbf{r}) \delta(t). \quad (3.4)$$

Eq. 3.4 is also valid for orthotropic bodies after a coordinate transformation. In this case the virtual speed of sound $c = (c_{11}c_{22}c_{33})^{1/3}$ is computed with the virtual speeds of sound in the principal directions [98].

Comparing the parabolic heat equation Eq. 3.1 with the hyperbolic virtual wave equation Eq. 3.4, one can see that they are very similar and apart from the propagation parameters the main difference is given by the time derivatives. To obtain a mathematical relationship between surface temperature signal $T(\mathbf{r}, t)$ and virtual wave signal $T_{\text{virt}}(\mathbf{r}, t)$ one can temporally Fourier transform Eqs. 3.1 and 3.4. By a suitable substitution of the angular frequency $\omega \Rightarrow \tilde{\omega}$, a relation between temperature signal and virtual wave signal in the frequency domain can be obtained as shown in Fig. 3.1. This relation must be inverse Fourier transformed to obtain the corresponding relation in the time domain [13]:

$$T(\mathbf{r}, t) = \int_{-\infty}^{\infty} K(t, t') T_{\text{virt}}(\mathbf{r}, t') dt' \quad \text{with} \quad K(t, t') = \frac{c}{\sqrt{\pi \alpha t}} \exp\left(-\frac{c^2 t'^2}{4 \alpha t}\right) \quad \text{for } t > 0. \quad (3.5)$$

Eq. 3.5 can be classified as a Fredholm integral of the first kind, where t' is the integration

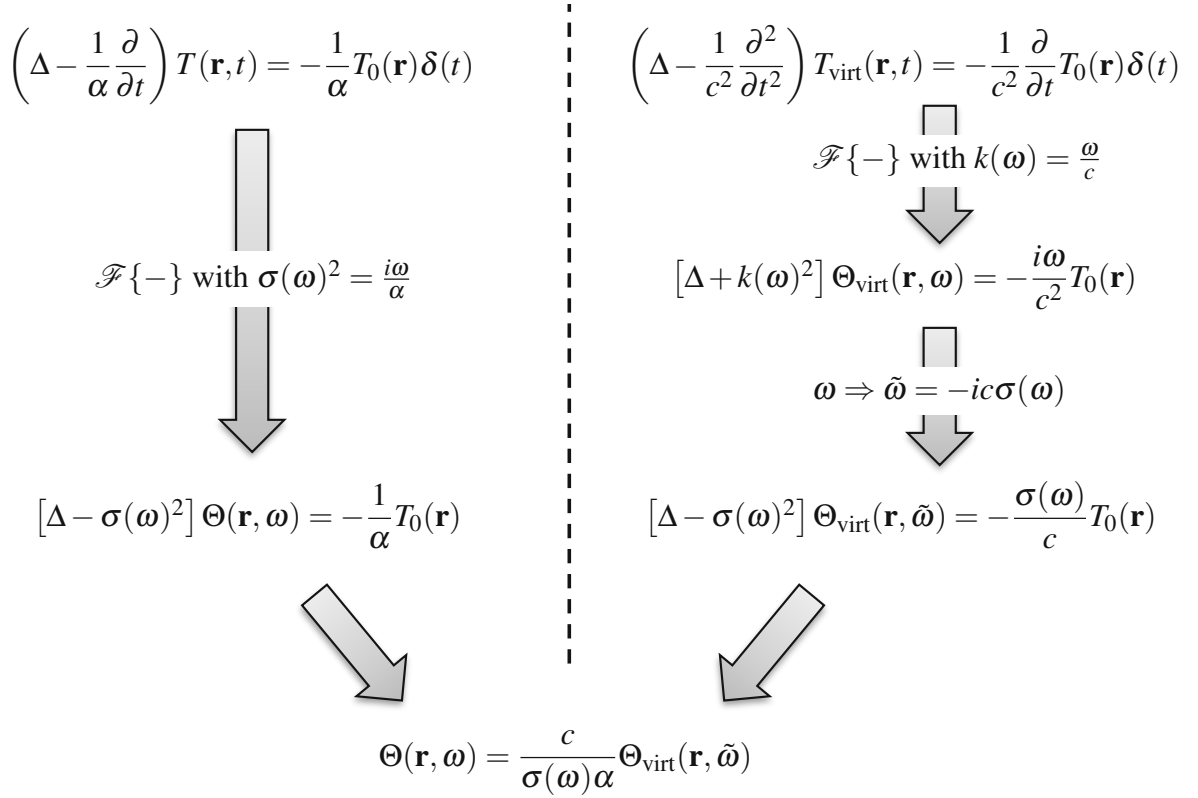


Figure 3.1: Derivation of the temperature signal $\Theta(\mathbf{r}, \omega)$ to virtual wave signal $\Theta_{\text{virt}}(\mathbf{r}, \tilde{\omega})$ conversion in the frequency domain using the heat equation Eq. 3.1 and the virtual wave equation Eq. 3.4 according to Ref. [13]. $\sigma(\omega)$ denotes the complex wave number, $k(\omega)$ denotes the real wave number, ω is the angular frequency, i is the imaginary number and $\mathcal{F}\{-\}$ is the temporal Fourier operator.

variable. The kernel $K(t, t')$ contains the characteristic parameters for thermal wave and virtual wave propagation and does not depend on the position vector \mathbf{r} . Thus, the surface temperature signal $T(\mathbf{r}, t)$ is transformed locally (pixel by pixel) into a virtual wave signal $T_{\text{virt}}(\mathbf{r}, t)$. [13]

3.1.1 The virtual wave signal in infinite bodies

Moreover, Eq. 3.5 is very similar to a 1D IHCP problem, which involves the fundamental solution of heat conduction. This can be seen by replacing ct' by the depth associated integration variable z' and by using the 1D virtual wave signal $T_{\text{virt}}(z, t') = 1/2T_0\delta(z - ct')$ for an infinite body (see Refs. [15, 99]) which yields:

$$T(z, t) = \int_{-\infty}^{\infty} \underbrace{\frac{c}{\sqrt{4\pi\alpha t}} \exp\left(-\frac{z'^2}{4\alpha t}\right)}_{\text{Fundamental solution of heat conduction}} \underbrace{T_0 \delta(z - z')}_{\text{Initial condition}} dz'. \quad (3.6)$$

Eq. 3.6 represents the Green's function solution equation (GFSE) for an initial condition (IC) that contains the fundamental solution of heat conduction and the IC (see for example Ref. [83]). Due to the IC, the initial temperature signal T_0 is introduced into the 1D infinite body by a point-like source. The VWC procedure for this case, with discrete data (see subsection 3.1.3), is visualized in Fig. 3.2, where the point-like source is introduced at the dimensionless depth $\hat{z} = z/\zeta$ with the detector to source distance ζ . The transient temperature signal is detected at the position $z = 0$. Based on the temperature signal, a virtual wave signal is obtained by calculating the inverse solution in Eq. 3.5. As can be seen, the initial temperature signal is approximately equivalent to the computed virtual wave signal. The small difference can be explained by the loss of information during heat diffusion, which can be partially compensated by including prior information such as positivity and sparsity in the regularization process.

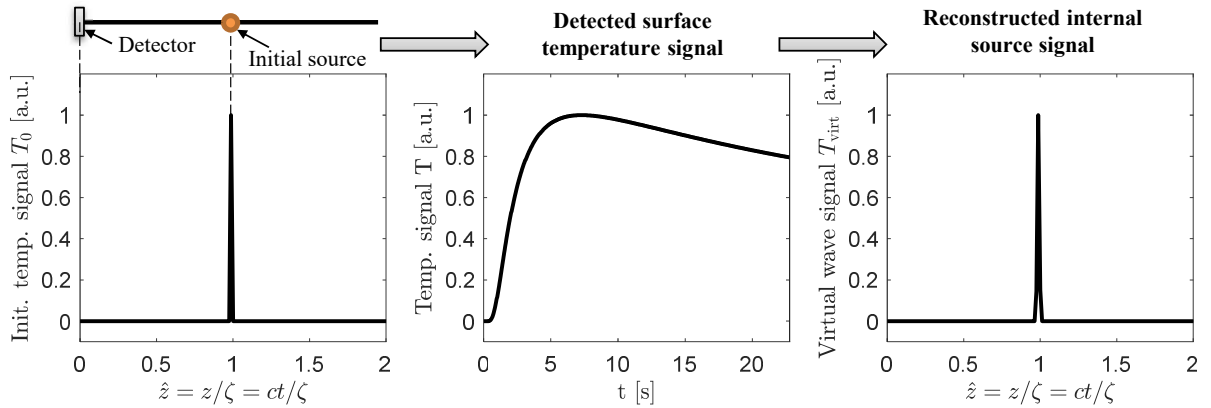


Figure 3.2: VWC processing for a 1D slab with infinite dimensions. The source is introduced at the dimensionless depth $\hat{z} = z/\zeta$ where the distance between source and detector is ζ . The detected temperature signal is converted to a virtual wave signal, which is equal to the initial source signal. Parameters: thermal diffusivity $\alpha = 3.2 \cdot 10^{-7} \text{ m}^2/\text{s}$; virtual speed of sound $c = \tilde{c}\Delta_z/\Delta_t$ with the dimensionless virtual speed of sound $\tilde{c} = 1$, the axial spatial resolution $\Delta_z = 2.7 \cdot 10^{-5} \text{ m}$ and the temporal resolution $\Delta_t = 0.023 \text{ s}$. The number of time steps for the surface temperature signal and the virtual wave signal was $N_t = 1000$ and $N_{\text{tv}} = 600$, respectively.

3.1.2 The virtual wave signal in finite bodies

For practical applications, the finite body assumption may be insufficient and therefore boundary conditions for the propagation of the thermal wave and the virtual wave must be considered. The conversion of the temperature signal into the virtual wave signal is independent of the position vector \mathbf{r} , and thus only boundary conditions in the axial direction are considered in the first reconstruction step for TOF evaluations.

Similar to heat conduction, where the Neumann and Dirichlet boundary conditions can be fulfilled by an appropriate positioning of mirror sources that are mathematically described by the fundamental solution of heat conduction [83], the characteristic virtual wave signal for these boundary conditions can be deduced via the fundamental solution of virtual wave propagation [15, 99]. This solution strategy, also known as the method of images, can be used to determine the Green's function for the semi-infinite, Neumann, and Dirichlet boundary conditions for both the temperature signal and the virtual wave signal. Then, using these Green's functions, the initial conditions, and the GFSE, one can calculate the corresponding temperature signal and virtual wave signal. A graphical representation of the method of images, following Ref. [83], is shown in Fig. 3.3. In that figure, the positioning of the sources and sinks that are represented by the fundamental solution of the virtual wave signal [99]

$$\mathcal{H}(z-z', t-\tau) = \begin{cases} \underbrace{\frac{1}{2c} \delta\left(t-\tau - \frac{z-z'}{c}\right)}_{\text{wave propagating to the right direction}} & \text{for } z-z' > 0 \\ \underbrace{\frac{1}{2c} \delta\left(t-\tau + \frac{z-z'}{c}\right)}_{\text{wave propagating to the left direction}} & \text{for } z-z' < 0 \end{cases}, \quad (3.7)$$

is shown for the boundary cases Z11, Z12, Z21, and Z22. The designation of the boundary cases is adopted from Ref. [83], where the numbers (1) and (2) denote Dirichlet and Neumann boundary cases, respectively. The letter Z indicates that the corresponding Green's function applies to the z coordinate, which in this work is equal to the depth coordinate. The first digit after the letter indicates the boundary condition on the front wall ($z=0$) and the second digit indicates the boundary condition on the back wall ($z=L_z$).

As shown in Fig. 3.3, the source is located at z' . For the boundary case Z11, the contribution of the boundaries at the front wall and the back wall must be zero, which requires the positioning of sinks and sources to satisfy the Dirichlet boundary conditions. To account for

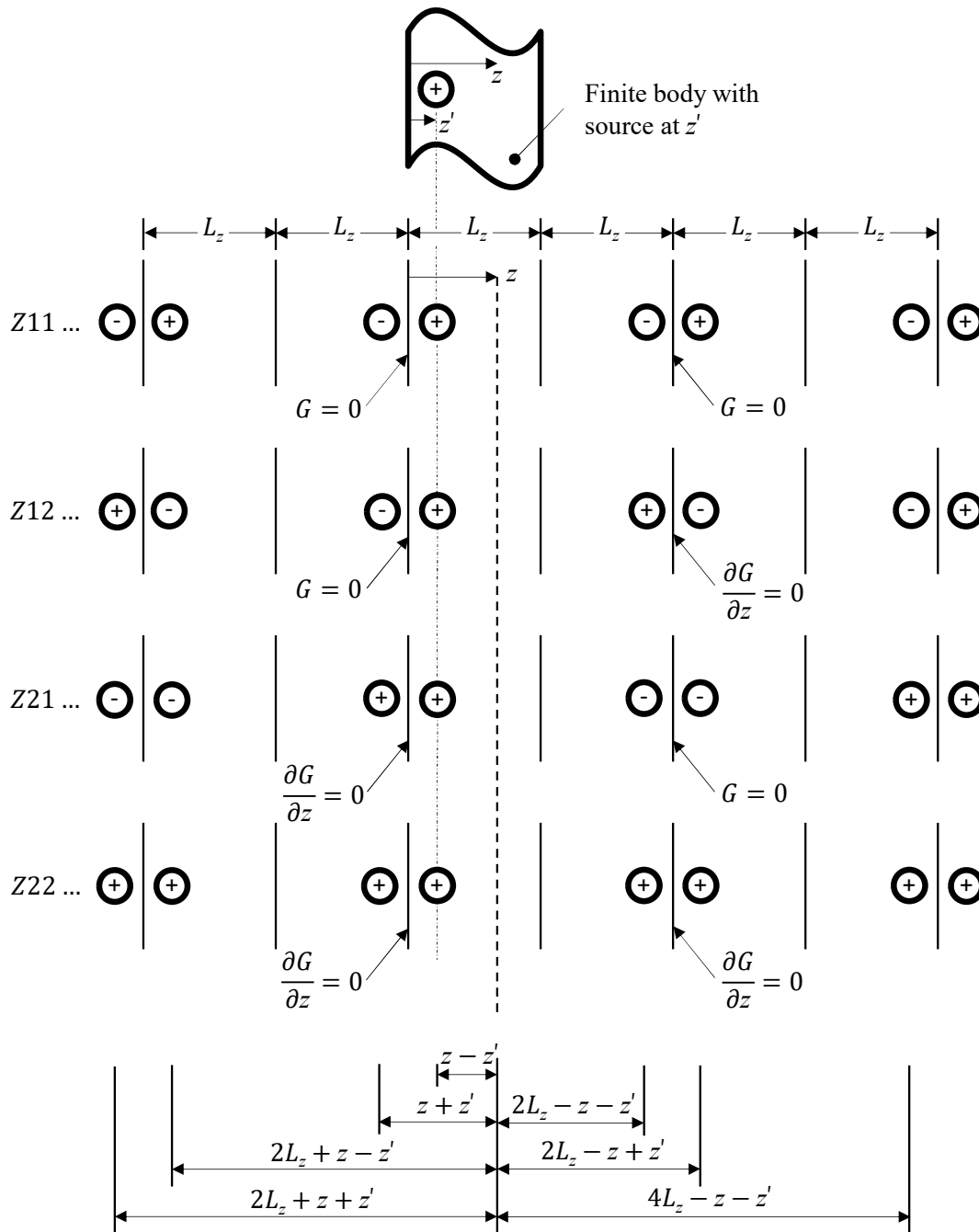


Figure 3.3: Method of images following Ref. [83]: Sources (+) and sinks (-) represented by the fundamental solution of the virtual wave signal are positioned in a defined manner to satisfy the corresponding boundary conditions. The various boundary cases are shown on the left-hand side, where (1) and (2) denote Dirichlet and Neumann boundary conditions, respectively. The first digit after the letter Z denotes the boundary condition on the front wall ($z = 0$) and the second digit denotes the boundary condition on the back wall ($z = L_z$).

the infinite reflections and transmissions at the front wall and back wall, the positioning of the mirror sources and sinks must be $2nL_z$ -periodically extended with the running variable n , where all sink or source locations are represented by the following equation [83]

$$\begin{aligned} 2nL_z + z + z' & \quad \text{for} \quad n = -\infty, \dots, -2, -1, 0, 1, 2, \dots, \infty \\ 2nL_z + z - z' & \quad \text{for} \quad n = -\infty, \dots, -2, -1, 0, 1, 2, \dots, \infty. \end{aligned} \quad (3.8)$$

Finally, all mirror sources and sinks are summed up and the final Green's function is shown in Tab. 3.1. The other boundary cases can be derived in an analogous way. The Green's functions for the different boundary cases are listed in Tab. 3.1, where non-physical boundary cases are also included, denoted by the digit 0. [83]

The results obtained with the method of images and the fundamental solution for the virtual wave signal are verified as an example in the pulse-echo configuration ($z = 0$) for the boundary cases Z21 and Z22 using VWC. Therefore, in a first step and according to Ref. [83], the 1D temperature signal is calculated for the corresponding boundary conditions using the GFSE for initial conditions. The observed rods and the boundary cases are schematically shown in Fig. 3.4a). The initial point source with thermal energy q_0 is introduced spontaneously at time $t = 0$ and $z = 0$. Thus, the initial condition is [15, 99]

$$T(z, t = 0) = \frac{q_0}{\rho c_p} \delta(z), \quad (3.9)$$

where ρ and c_p denote the density and the specific heat capacity, respectively. The Greens functions for heat conduction that applies for this boundary cases are [83]

$$G_{Z21}(z, t | z', \tau) = \frac{1}{\sqrt{4\pi\alpha(t-\tau)}} \sum_{n=-\infty}^{\infty} (-1)^n \left\{ \exp \left[\frac{(2nL_z + z - z')^2}{4\alpha(t-\tau)} \right] + \exp \left[\frac{(2nL_z + z + z')^2}{4\alpha(t-\tau)} \right] \right\} \quad (3.10)$$

$$G_{Z22}(z, t | z', \tau) = \frac{1}{\sqrt{4\pi\alpha(t-\tau)}} \sum_{n=-\infty}^{\infty} \left\{ \exp \left[\frac{(2nL_z + z - z')^2}{4\alpha(t-\tau)} \right] + \exp \left[\frac{(2nL_z + z + z')^2}{4\alpha(t-\tau)} \right] \right\}. \quad (3.11)$$

Using the GFSE for initial conditions and Eqs. 3.9-3.11 the temporal temperature signals for each depth position z can be calculated. Since in this case the pulse-echo configuration is

Table 3.1: Green's functions of the virtual wave signal for non-physical, Dirichlet, and Neumann boundary conditions derived via the method of images and the fundamental solution of the virtual wave signal. This presentation was originally adapted from Ref. [83] and presented in Ref. [99].

Case	Greens function
Z00	$\mathcal{H}(z-z', t-\tau) = \begin{cases} \frac{1}{2c} \delta\left(t-\tau - \frac{z-z'}{c}\right) & \text{for } z-z' > 0 \\ \text{wave propagating to the right direction} \\ \frac{1}{2c} \delta\left(t-\tau + \frac{z-z'}{c}\right) & \text{for } z-z' < 0 \\ \text{wave propagating to the left direction} \end{cases}$
Z10	$\mathcal{H}(z-z', t-\tau) - \mathcal{H}(z+z', t-\tau)$
Z20	$\mathcal{H}(z-z', t-\tau) + \mathcal{H}(z+z', t-\tau)$
Z11	$\sum_{n=-\infty}^{\infty} [\mathcal{H}(2nL_z + z - z', t-\tau) - \mathcal{H}(2nL_z + z + z', t-\tau)]$
Z12	$\sum_{n=-\infty}^{\infty} (-1)^n [\mathcal{H}(2nL_z + z - z', t-\tau) - \mathcal{H}(2nL_z + z + z', t-\tau)]$
Z21	$\sum_{n=-\infty}^{\infty} (-1)^n [\mathcal{H}(2nL_z + z - z', t-\tau) + \mathcal{H}(2nL_z + z + z', t-\tau)]$
Z22	$\sum_{n=-\infty}^{\infty} [\mathcal{H}(2nL_z + z - z', t-\tau) + \mathcal{H}(2nL_z + z + z', t-\tau)]$

observed the temporal temperature signals are evaluated at $z = 0$ and the corresponding signals are given by

$$T_{Z21}(z=0, t) = \frac{2q_0}{\sqrt{4\pi\alpha t}} \sum_{n=-\infty}^{\infty} (-1)^n \exp\left[\frac{(2nL_z)^2}{4\alpha t}\right] \quad (3.12)$$

$$T_{Z22}(z=0, t) = \frac{2q_0}{\sqrt{4\pi\alpha t}} \sum_{n=-\infty}^{\infty} \exp\left[\frac{(2nL_z)^2}{4\alpha t}\right]. \quad (3.13)$$

A graphical representation of the corresponding discrete temperature signals as a function of the Fourier number Fo is shown in Fig. 3.4b). The temperature signals were related to the adiabatic temperature $T_a = T_{Z22}(z = 0, Fo = 1)$. Then, the temperature signals were transformed into virtual wave signals by calculating the inverse of Eq. 3.5 using the regularization method ADMM. The resulting virtual wave signals as function of the dimensionless depth \hat{z} are shown in Fig. 3.4c). As can be seen, the positioning of the mirror sources (+) and mirror sinks (-) for both

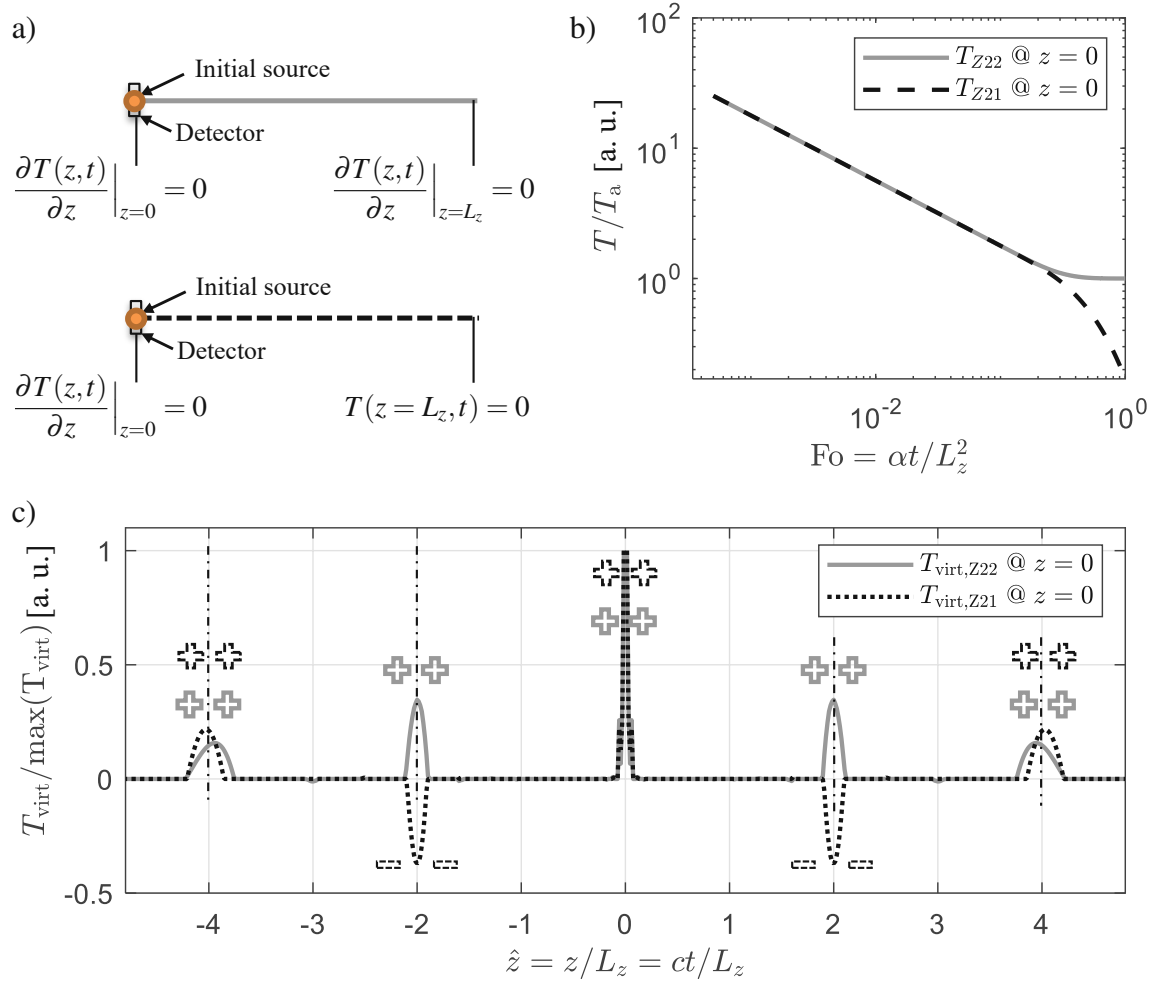


Figure 3.4: a) Rods with boundary cases Z22 and Z21, where the initial source is spontaneously introduced at $t = 0$ and $z = 0$. The detector is located at $z = 0$. b) Corresponding temperature signal for both cases on the double logarithmic scale. c) Virtual wave signal as function of dimensionless depth \hat{z} calculated using ADMM. As can be seen, the positioning of the mirror sources(+) and sinks(-), with $z' = 0$, corresponds to Fig. 3.3. Parameters: $n = \{-50, -49, \dots, 50\}$; $L_z = 2.7$ mm; thermal diffusivity $\alpha = 3.2 \cdot 10^{-7}$ m²/s; virtual speed of sound $c = \tilde{c}\Delta_z/\Delta_t$ with the dimensionless virtual speed of sound $\tilde{c} = 1$, the axial spatial resolution $\Delta_z = 2.7 \cdot 10^{-5}$ m and the temporal resolution $\Delta_t = 0.011$ s. The number of time steps for the surface temperature signal and the virtual wave signal was $N_t = 2000$ and $N_{tv} = 600$, respectively.

cases fits very well with the graphical representation of the method of images shown in Fig. 3.3. It is worth mentioning that the adiabatic boundary case Z22 consists only of sources. This is plausible, since no energy can be released at the boundaries and thus no "energy sink" must be included. For the boundary case Z21, mirror sinks must also be included to satisfy the boundary conditions at $z = L_z$. However, both virtual wave signals show a decrease in the source/sink amplitude and the corresponding full-half width. Ideally, these amplitudes should have infinitely high amplitudes and infinitesimally small full-half-width, as represented by the fundamental solution of the virtual wave signal (case Z00 in Tab. 3.1). The reason for the attenuation of the mirror sources/sinks with increasing depth or number of reflections and transmissions is the irreversibility resulting from small fluctuations in the temperature signal, which can only be partially compensated by including prior information in the regularization [29].

3.1.3 Discrete inverse problem

In practical applications the temperature data is discrete in space and time. Due to this Eq. 3.5 must be discretized, for example by the quadrature rule [73], which result in a linear matrix equation

$$\mathbf{T} = \mathbf{K}\mathbf{T}_{\text{virt}}. \quad (3.14)$$

with the matrix dimensions $\mathbf{T} \in \mathbb{R}^{N_t \times q}$, $\mathbf{K} \in \mathbb{R}^{N_t \times N_{\text{tv}}}$ and $\mathbf{T}_{\text{virt}} \in \mathbb{R}^{N_{\text{tv}} \times q}$ [13, 100]. In Eq. 3.14 the discrete Fredholm integral was notated for one spatial cross-section with pixel number q . The number of time steps of the temperature signal and the virtual wave signal are N_t and N_{tv} , respectively. Using the discrete time steps $t_k = k\Delta_t$ and $t'_j = j\Delta_t$ with the running variables $k = \{0, 1, \dots, N_t - 1\}$ and $j = \{0, 1, \dots, N_{\text{tv}} - 1\}$, the components of the kernel K are given by [98]

$$K(k, j) = \frac{c\sqrt{\Delta_t}}{\sqrt{\pi\alpha k}} \exp\left(-\frac{c^2\Delta_t j^2}{4\alpha k}\right) = \frac{\eta}{\sqrt{\pi k}} \exp\left(-\frac{\eta^2 j^2}{4k}\right). \quad (3.15)$$

Here $\eta = c\sqrt{\Delta_t}/\sqrt{\alpha}$ is a dimensionless number that depends on the propagation parameters c and α and on the temporal resolution Δ_t .

3.1.4 Arbitrary heating function

The Fredholm integral in Eq. 3.5 is only valid for a temporal Dirac-Delta like excitation. However, due to the linear nature of the standard heat equation and standard wave equation, Eq.

3.5 can be convolved in time ($*_t$) with any transient heating signal $h(t)$ and the corresponding relationship for the continuous case is given by [97]

$$T_h(\mathbf{r}, t) = T(\mathbf{r}, t) *_t h(t) = \int_{-\infty}^{\infty} [K(t, t') *_t h(t')] T_{\text{virt}}(\mathbf{r}, t') dt'. \quad (3.16)$$

The discrete case, where the heating function is represented by the vector $\mathbf{h} \in \mathbb{R}^{N_t \times 1}$ can be written as [97]

$$\mathbf{T}_h = \mathbf{T} *_t \mathbf{h} = \mathbf{K}_h \mathbf{T}_{\text{virt}} \quad \text{with} \quad \mathbf{K}_h = \mathbf{K} *_t \mathbf{h}, \quad (3.17)$$

using Eq. 3.14. The inversion of the modified linear matrix equation Eq. 3.17, yields again the virtual wave signal for a Dirac-Delta excitation signal.

An application of the modified temperature signal to virtual wave signal conversion, which considers temporal arbitrary heating functions, is represented in Fig. 3.5. Fig. 3.5a) shows the heating function \mathbf{h} that is introduced at $z = 0$ in a 1D rod with adiabatic boundaries Z22 and length L_z as function of the Fourier number Fo. The corresponding temperature signal $\mathbf{T}_{h,Z22}$

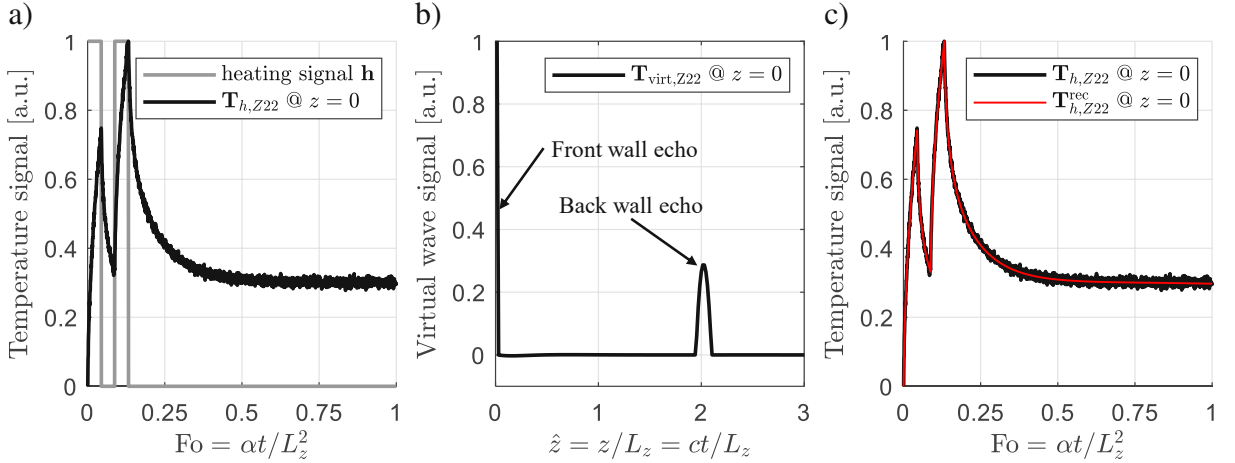


Figure 3.5: a) Simulated temperature signal based on an arbitrary temporal heating function \mathbf{h} that is superimposed with white Gaussian noise as function of the dimensionless Fourier number Fo. b) Corresponding virtual wave signal estimated using ADMM as regularization tool as function of the dimensionless depth \hat{z} . c) Visualization of the temporal noise filtering capability of the VWC. Parameters: $n = \{-50, -49, \dots, 50\}$; $L_z = 2.7$ mm; thermal diffusivity $\alpha = 3.2 \cdot 10^{-7}$ m²/s; virtual speed of sound $c = \tilde{c} \Delta_z / \Delta_t$ with $\tilde{c} = 1$, $\Delta_z = 2.7 \cdot 10^{-5}$ m and $\Delta_t = 0.011$ s. The number of time steps for the surface temperature signal and the virtual wave signal was $N_t = 2000$ and $N_{\text{TV}} = 600$, respectively.

which has been related to the maximum temperature signal $\mathbf{T}_{h,Z22}^{\max} = 3.348$ K and superimposed with white Gaussian noise with a standard deviation of $\sigma = 25$ mK, is observed at $z = 0$ (pulse-echo configuration). Based on the temperature signal the virtual wave signal is calculated by inversion of Eq. 3.17 using the regularization tool ADMM. As can be seen in Fig. 3.5b) the computed virtual wave signal $\mathbf{T}_{\text{virt},Z22}$ is again Dirac-Delta like with the initial source and the mirror source at the dimensionless depth $\hat{z} = 0$ and $\hat{z} = 2$, respectively. Fig. 3.5c) shows the noise filtering capability of the virtual wave concept. The filtered temperature signal $\mathbf{T}_{h,Z22}^{\text{rec}}$ was obtained via the matrix multiplication of the convolved discrete kernel \mathbf{K}_h and the virtual wave signal $\mathbf{T}_{\text{virt},Z22}$. In addition, one can see that the reconstructed filtered temperature slope $\mathbf{T}_{h,Z22}^{\text{rec}}$ fits the observed slope $\mathbf{T}_{h,Z22}$ very well.

3.2 Second reconstruction step

After the 1D temperature signal to virtual wave signal transformation either the sample thickness L_z can be estimated by the known axial thermal diffusivity α_{33} or vice versa using the virtual time of flight [15, 90]. However, subsurface defects in 2D and 3D geometries usually cause a 2D and 3D temperature signal which leads to a 2D and 3D virtual wave signal. The first reconstruction step of the VWC considers only local (pixel by pixel) thermal wave or virtual wave propagation, boundaries at the front wall and back wall and performs only a temporal noise-filtering. To separate the lateral heat flow from different directions and to take into account lateral boundary conditions and a spatial noise filtering ultrasonic reconstruction tools such as the T-SAFT and F-SAFT can be used. The second reconstruction step is discussed for one spatial cross-section y based on the T-SAFT method and graphics in Fig. 3.6. Figs. 3.6a) and Fig. 3.6b) show the observed virtual wave signal that results from a point-like defect and the region of interest (ROI) for the reconstruction of subsurface defects, respectively. Using T-SAFT, the relationship between a potential point scatterer $T_0(\mathbf{r}')$ at point \mathbf{r}' and the virtual wave signal $T_{\text{virt}}(\mathbf{r}, t)$, evaluated at the front wall (pulse-echo configuration), is given by [101]

$$T_0(\mathbf{r}') = T_0(x', y', z') = \iint_{S_M} T_{\text{virt}}(x, y, 0, t') dx dy \quad \text{with} \quad t' = \frac{2}{c} \sqrt{(x-x')^2 + (y-y')^2 + (z-z')^2}. \quad (3.18)$$

Point scatterers can be introduced at sample interfaces such as front-wall, back-wall and defects. To compute $T_0(\mathbf{r}')$, in the discrete case, a mesh grid (region of interest) must be defined by the

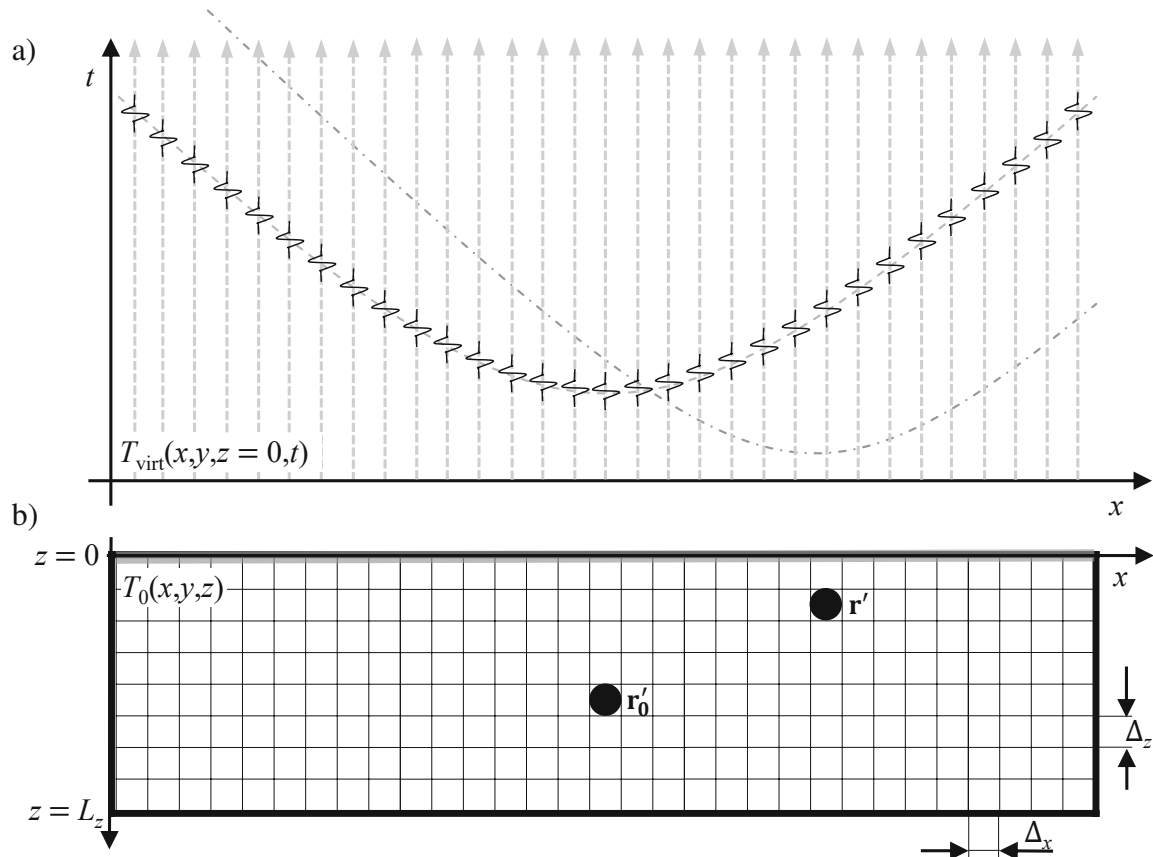


Figure 3.6: Sketch of T-SAFT reconstruction, which was adopted from Ref. [16]. a) B-scan of the virtual wave signal that consists of A-scans that are computed from the given temperature signal. b) Region of interest for the reconstruction of subsurface defects.

lateral (Δ_x , Δ_y) and axial spatial resolutions (Δ_z) corresponding to the lateral spatial resolution and the temporal resolution of the IR-camera.

In the discrete case, T-SAFT can be interpreted as a matched filter or trial and error method. In this procedure, each discrete mesh grid point $\mathbf{r}' = (x', y', z')$ yields a hyperbola and according to Eq. 3.18 the sum (discrete integral) along the hyperbola is evaluated. If the hyperbola of the observed mesh grid position is caused by a defect ($\mathbf{r}'_0 = \mathbf{r}'$), a high value is obtained and the resulting value is stored in the observed mesh grid position. The evaluation of each mesh grid point gives the final reconstruction $T_0(\mathbf{r}')$ of the region of interest. [16]

According to Ref. [16], T-SAFT and F-SAFT provide the same reconstruction result, but F-SAFT is much faster than T-SAFT [102] and therefore in this thesis the second reconstruction step is performed exclusively with F-SAFT. A disadvantage of the standard F-SAFT method is that it can only be applied to plane surfaces [102]. With F-SAFT, one can consider Dirichlet (sound transmitting) and Neumann (sound-reflecting) boundaries using the discrete sine and cosine-transforms, respectively.

3.3 Application of both reconstruction steps

In this subsection, an example result is presented where both reconstruction steps are involved. The results are based on an isotropic sample with adiabatic boundaries and a 2D transient temperature signal resulting from internal heat sources. In the first reconstruction step ADMM was used for regularization by minimizing the following cost function [75, 103]

$$\frac{1}{2} \|\mathbf{K}\mathbf{T}_{\text{virt}} - \mathbf{T}\|_2^2 + \lambda \|\mathbf{T}_{\text{virt}}\|_1 \quad \text{subject to} \quad \mathbf{T}_{\text{virt}} - \mathbf{z} = \mathbf{0}. \quad (3.19)$$

The letter λ denotes the regularization parameter and \mathbf{z} is an additional vector of variables [75].

Fig. 3.7 shows the results and indicates the evaluation procedure of VWC. In the left image the initial temperature signal \mathbf{T}_0 is illustrated. The resulting transient surface temperature signal \mathbf{T} is detected at $z = 0$ and reveals the diffusive nature of heat propagation which leads to blurred images. By calculating the inverse solution of Eq. 3.14, the detected surface temperature signal \mathbf{T} is transformed locally into a virtual wave signal \mathbf{T}_{virt} . The calculated virtual wave signal \mathbf{T}_{virt} also illustrates the defect depth feature extraction capability of the VWC. Comparing the

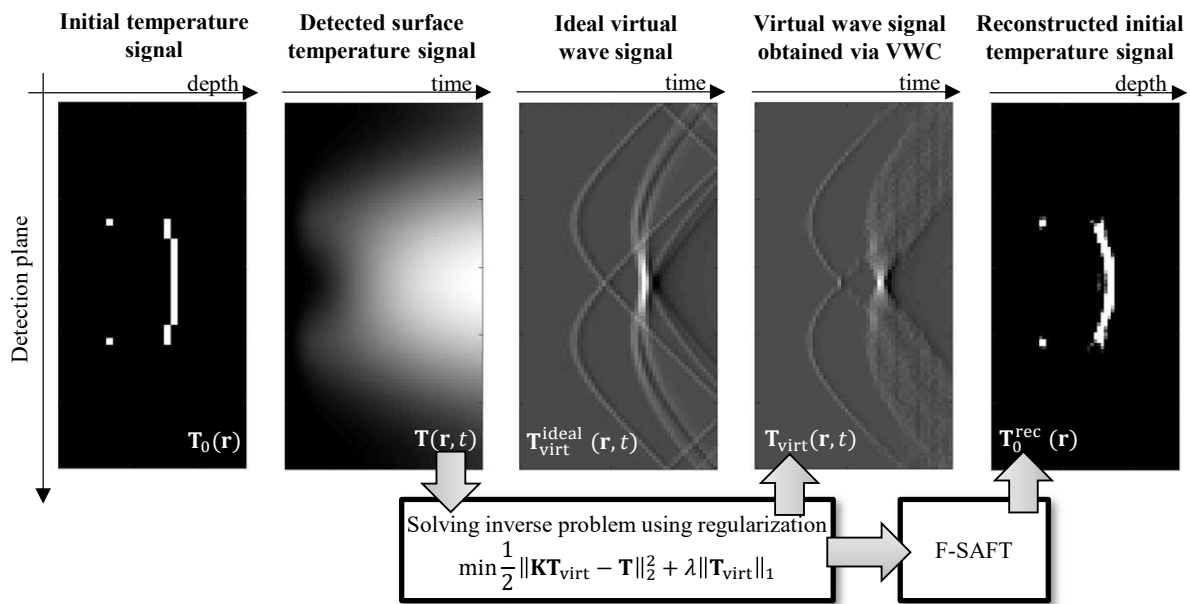


Figure 3.7: VWC processing for simulated 2D transient surface temperature data with adiabatic boundary conditions. To compute the virtual waves signal, the regularization tool ADMM was used. The second reconstruction step was performed with F-SAFT. Parameters: ROI = (Detection plane \times depth) = (10.8 mm \times 5.4 mm); thermal diffusivity $\alpha = 0.13 \cdot 10^{-6}$ m²/s; virtual speed of sound $c = \tilde{c} \Delta_z / \Delta_t$ with $\tilde{c} = 1$, $\Delta_z = 9.8 \cdot 10^{-5}$ m and $\Delta_t = 0.02$ s. The number of time steps for both the surface temperature signal and the virtual wave signal was $N_t = N_{tv} = 5000$.

"ideal" virtual wave signal $\mathbf{T}_{\text{virt}}^{\text{ideal}}$ obtained by directly solving the standard wave equation, with the virtual wave signal \mathbf{T}_{virt} one can see a high similarity between these signals. However, the loss of information due to entropy production during heat diffusion cannot be fully compensated by regularization even when using prior information in the form of positivity and sparsity and thus the deeper depth features of the calculated virtual wave signal \mathbf{T}_{virt} differ from the "ideal" virtual wave signal $\mathbf{T}_{\text{virt}}^{\text{ideal}}$. Since the calculated wave signal obeys the standard wave equation, ultrasonic reconstruction techniques, for instance F-SAFT, can be used in the second evaluation step to account for the lateral heat flow and to reconstruct the initial temperature signal and secondary boundary sources $\mathbf{T}_0^{\text{rec}}$. These secondary boundary sources can either originate from sample or defect boundaries.

The experimental surface temperature signals are superimposed with noise, and in this case F-SAFT also introduces spatial noise filtering, which significantly improves the SNR and defect detection capability.

4 Bibliography

- [1] C. Meola, S. Boccardi, G. Carlomagno, *Infrared Thermography in the Evaluation of Aerospace Composite Materials: Infrared Thermography to Composites*, Elsevier Science, 2016.
- [2] P. L. Jakab, Wood to metal: The structural origins of the modern airplane, *Journal of Aircraft* 36 (6) (1999) 914–918. doi:10.2514/2.2551.
- [3] F. C. Campbell, *Structural composite materials*, ASM Internat, Materials Park, Ohio, 2010.
- [4] R. M. Jones, *Mechanics of Composite Materials*, 2nd Edition, Chapman and Hall/CRC, Boca Raton, 2014.
- [5] C. Soutis, Fibre reinforced composites in aircraft construction, *Progress in Aerospace Sciences* 41 (2) (2005) 143–151. doi:10.1016/j.paerosci.2005.02.004.
- [6] J. Bachmann, X. Yi, H. Gong, X. Martinez, G. Bugada, S. Oller, K. Tserpes, E. Ramon, C. Paris, P. Moreira, Z. Fang, Y. Li, Y. Liu, X. Liu, G. Xian, J. Tong, J. Wei, X. Zhang, J. Zhu, S. Ma, T. Yu, Outlook on ecologically improved composites for aviation interior and secondary structures, *CEAS Aeronautical Journal* 9 (3) (2018) 533–543. doi:10.1007/s13272-018-0298-z.
- [7] F. Ciampa, P. Mahmoodi, F. Pinto, M. Meo, Recent advances in active infrared thermography for non-destructive testing of aerospace components, *Sensors (Basel, Switzerland)* 18 (2) (2018). doi:10.3390/s18020609.
- [8] M. Naebe, M. M. Abolhasani, H. Khayyam, A. Amini, B. Fox, Crack damage in polymers and composites: A review, *Polymer Reviews* 56 (1) (2016) 31–69. doi:10.1080/15583724.2015.1078352.

- [9] B. Wang, S. Zhong, T.-L. Lee, K. S. Fancey, J. Mi, Non-destructive testing and evaluation of composite materials/structures: A state-of-the-art review, *Advances in Mechanical Engineering* 12 (4) (2020) 168781402091376. doi:10.1177/1687814020913761.
- [10] D. Balageas, X. Maldague, D. Burleigh, V. P. Vavilov, B. Oswald-Tranta, J.-M. Roche, C. Pradere, G. M. Carlomagno, Thermal (IR) and other NDT techniques for improved material inspection, *Journal of Nondestructive Evaluation* 35 (1) (2016) 79. doi:10.1007/s10921-015-0331-7.
- [11] S. Gazzola, M. Sabaté Landman, Krylov methods for inverse problems: Surveying classical, and introducing new, algorithmic approaches, *GAMM-Mitteilungen* 43 (4) (2020) e202000017. doi:10.1002/gamm.202000017.
- [12] S. M. Shepard, Reconstruction and enhancement of active thermographic image sequences, *Optical Engineering* 42 (5) (2003) 1337. doi:10.1117/1.1566969.
- [13] P. Burgholzer, M. Thor, J. Gruber, G. Mayr, Three-dimensional thermographic imaging using a virtual wave concept, *Journal of Applied Physics* 121 (10) (2017) 105102. doi:10.1063/1.4978010.
- [14] J. P. Charlesworth, J. Temple, *Engineering Applications of Ultrasonic Time-of-flight Diffraction*, Ultrasonic inspection in engineering series, Research Studies Press, 2001.
- [15] G. Mayr, G. Stockner, H. Plasser, G. Hendorfer, P. Burgholzer, Parameter estimation from pulsed thermography data using the virtual wave concept, *NDT & E International* 100 (10) (2018) 101–107. doi:10.1016/j.ndteint.2018.09.003.
- [16] K.-J. Langenberg, *Ultrasonic Nondestructive Testing of Materials: Theoretical Foundations*, CRC Press, Hoboken, 2012.
- [17] D. Lévesque, A. Blouin, C. Néron, J.-P. Monchalain, Performance of laser-ultrasonic F-SAFT imaging, *Ultrasonics* 40 (10) (2002) 1057–1063. doi:10.1016/S0041-624X(02)00256-1.
- [18] P. Burgholzer, Thermodynamic limits of spatial resolution in active thermography, *International Journal of Thermophysics* 36 (9) (2015) 2328–2341. doi:10.1007/s10765-015-1890-7.

- [19] X. P. V. Maldague, P. O. Moore (Eds.), *Infrared and thermal testing*, 3rd Edition, Vol. 3 of *Nondestructive testing handbook*, American Society for Nondestructive Testing, Columbus, Ohio, 2001.
- [20] D. Almond, P. Patel, *Photothermal science and techniques*, 1st Edition, Vol. 10 of *Physics and its applications*, Chapman & Hall, London, 1996.
- [21] A. Mendioroz, R. Celorrio, A. Salazar, Characterization of rectangular vertical cracks using burst vibrothermography, *The Review of scientific instruments* 86 (6) (2015) 064903. doi:10.1063/1.4922464.
- [22] X. P. V. Maldague, *Theory and practice of infrared technology for nondestructive testing*, Wiley series in microwave and optical engineering, Wiley, New York, NY, 2001.
- [23] D. Wu, G. Busse, Lock-in thermography for nondestructive evaluation of materials, *Revue Générale de Thermique* 37 (8) (1998) 693–703. doi:10.1016/S0035-3159(98)80047-0.
- [24] X. P. V. Maldague, *Nondestructive Evaluation of Materials by Infrared Thermography*, Springer London, London, 1993. doi:10.1007/978-1-4471-1995-1.
- [25] V. Vavilov, D. Burleigh, *Infrared thermography and thermal nondestructive testing*, Springer, 2020.
- [26] J. V. Beck, K. J. Arnold, *Parameter estimation in engineering and science*, Wiley series in probability and mathematical statistics, Wiley, New York, 1977.
- [27] J. V. Beck, B. Blackwell, C. R. Saint Clair, *Inverse heat conduction: III-posed problems*, A Wiley-interscience publication, Wiley, New York, 1985.
- [28] S. Breitwieser, G. Zauner, G. Mayr, Characterization of mid-wavelength quantum infrared cameras using the photon transfer technique, *Infrared Physics & Technology* 106 (1) (2020) 103283. doi:10.1016/j.infrared.2020.103283.
- [29] P. Burgholzer, G. Mayr, G. Thummerer, M. Haltmeier, Linking information theory and thermodynamics to spatial resolution in photothermal and photoacoustic imaging, *Journal of Applied Physics* 128 (17) (2020) 171102. doi:10.1063/5.0023986.
- [30] S. M. Shepard, J. R. Lhota, T. Ahmed, Measurement limits in flash thermography, *SPIE Proceedings*, SPIE, 2009, p. 72990T. doi:10.1117/12.820062.

- [31] D. P. Almond, S. G. Pickering, An analytical study of the pulsed thermography defect detection limit, *Journal of Applied Physics* 111 (9) (2012) 093510. doi:10.1063/1.4704684.
- [32] D. A. González, C. Ibarra-Castanedo, M. Pilla, M. Klein, J. M. López-Higuera, X. Maldague, Automatic interpolated differentiated absolute contrast algorithm for the analysis of pulsed thermographic sequences, in: *Proceedings of the 2004 International Conference on Quantitative InfraRed Thermography*, QIRT Council, 2004. doi:10.21611/qirt.2004.014.
- [33] V. P. Vavilov, D. D. Burleigh, Review of pulsed thermal ndt: Physical principles, theory and data processing, *NDT & E International* 73 (1) (2015) 28–52. doi:10.1016/j.ndteint.2015.03.003.
- [34] H. D. Benítez, C. Ibarra-Castanedo, A. Bendada, X. Maldague, H. Loaiza, E. Caicedo, Definition of a new thermal contrast and pulse correction for defect quantification in pulsed thermography, *Infrared Physics & Technology* 51 (3) (2008) 160–167. doi:10.1016/j.infrared.2007.01.001.
- [35] X. Maldague, S. Marinetti, Pulse phase infrared thermography, *Journal of Applied Physics* 79 (5) (1996) 2694–2698. doi:10.1063/1.362662.
- [36] C. Ibarra-Castanedo, X. Maldague, Pulsed phase thermography reviewed, *Quantitative InfraRed Thermography Journal* 1 (1) (2004) 47–70. doi:10.3166/qirt.1.47-70.
- [37] F. Galmiche, Pulsed phased thermography with the wavelet transform, in: *AIP Conference Proceedings*, AIP, 2000, pp. 609–616. doi:10.1063/1.1306105.
- [38] X. Maldague, F. Galmiche, A. Ziadi, Advances in pulsed phase thermography, *Infrared Physics & Technology* 43 (3-5) (2002) 175–181. doi:10.1016/S1350-4495(02)00138-X.
- [39] S. M. Shepard, Advances in thermographic ndt, *SPIE Proceedings*, SPIE, 2003, p. 882. doi:10.1117/12.498157.
- [40] V. Vavilov, X. Maldague, J. Picard, R. L. Thomas, L. D. Favro, Dynamic thermal tomography: New NDE technique to reconstruct inner solids structure using multiple IR image processing, in: D. O. Thompson, D. E. Chimenti (Eds.), *Review of Progress in*

- Quantitative Nondestructive Evaluation, Springer US, Boston, MA, 1992, pp. 425–432. doi:10.1007/978-1-4615-3344-3_53.
- [41] V. Vavilov, V. Shiryaev, M. Kuimova, Time- and phase-domain thermal tomography of composites, *Photonics* 5 (4) (2018) 31. doi:10.3390/photonics5040031.
- [42] V. P. Vavilov, M. V. Kuimova, Dynamic thermal tomography of composites: A comparison of reference and reference-free approaches, *Journal of Nondestructive Evaluation* 38 (1) (2019) 40. doi:10.1007/s10921-018-0540-y.
- [43] S. Tuli, R. Mulaveesala, Defect detection by pulse compression in frequency modulated thermal wave imaging, *Quantitative InfraRed Thermography Journal* 2 (1) (2005) 41–54. doi:10.3166/qirt.2.41-54.
- [44] R. Mulaveesala, P. Pal, S. Tuli, Interface study of bonded wafers by digitized linear frequency modulated thermal wave imaging, *Sensors and Actuators A: Physical* 128 (1) (2006) 209–216. doi:doi.org/10.1016/j.sna.2006.01.004.
- [45] R. Mulaveesala, S. Tuli, Theory of frequency modulated thermal wave imaging for non-destructive subsurface defect detection, *Applied Physics Letters* 89 (19) (2006) 191913. doi:10.1063/1.2382738.
- [46] O. Breitenstein, W. Warta, M. C. Schubert, *Lock-in Thermography: Basics and Use for Evaluating Electronic Devices and Materials*, 3rd Edition, Vol. 10 of Springer Series in Advanced Microelectronics, Springer International Publishing, Cham, 2018. doi:10.1007/978-3-319-99825-1.
- [47] A. Mandelis, Frequency modulated FM time delay photoacoustic and photothermal wave spectroscopies. technique, instrumentation, and detection. part I: Theoretical, *Review of Scientific Instruments* 57 (4) (1986) 617–621. doi:10.1063/1.1138879.
- [48] A. Mandelis, L. M. L. Borm, J. Tiessinga, Frequency modulated FM time delay photoacoustic and photothermal wave spectroscopies. technique, instrumentation, and detection. part II: Mirage effect spectrometer design and performance, *Review of Scientific Instruments* 57 (4) (1986) 622–629. doi:10.1063/1.1138880.
- [49] A. Mandelis, L. L. M. Borm, J. Tiessinga, Frequency modulated FM time delay photoacoustic and photothermal wave spectroscopies. technique, instrumentation, and de-

- tection. part III: Mirage effect spectrometer, dynamic range, and comparison to pseudo-random-binary-sequence (prbs) method, *Review of Scientific Instruments* 57 (4) (1986) 630–635. doi:10.1063/1.1138881.
- [50] N. Tabatabaei, A. Mandelis, Thermal-wave radar: A novel subsurface imaging modality with extended depth-resolution dynamic range, *The Review of scientific instruments* 80 (3) (2009) 034902. doi:10.1063/1.3095560.
- [51] N. Tabatabaei, A. Mandelis, Thermal coherence tomography using match filter binary phase coded diffusion waves, *Physical review letters* 107 (16) (2011) 165901. doi:10.1103/PhysRevLett.107.165901.
- [52] S. Kaipilavil, A. Mandelis, Highly depth-resolved chirped pulse photothermal radar for bone diagnostics, *The Review of scientific instruments* 82 (7) (2011) 074906. doi:10.1063/1.3616140.
- [53] A. Melnikov, L. Chen, D. Ramirez Venegas, K. Sivagurunathan, Q. Sun, A. Mandelis, I. R. Rodriguez, Single frequency thermal wave radar: A next-generation dynamic thermography for quantitative non-destructive imaging over wide modulation frequency ranges, *The Review of scientific instruments* 89 (4) (2018) 044901. doi:10.1063/1.5016339.
- [54] A. Melnikov, K. Sivagurunathan, X. Guo, J. Tolev, A. Mandelis, K. Ly, R. Lawcock, Non-destructive thermal-wave-radar imaging of manufactured green powder metallurgy compact flaws (cracks), *NDT & E International* 86 (2017) 140–152. doi:10.1016/j.ndteint.2016.12.004.
- [55] R. Mulaveesala, S. Venkata Ghali, Coded excitation for infrared non-destructive testing of carbon fiber reinforced plastics, *Review of Scientific Instruments* 82 (5) (2011) 054902. doi:10.1063/1.3594551.
- [56] G. Silipigni, P. Burrascano, D. A. Hutchins, S. Laureti, R. Petrucci, L. Senni, L. Torre, M. Ricci, Optimization of the pulse-compression technique applied to the infrared thermography nondestructive evaluation, *NDT & E International* 87 (2017) 100–110. doi:10.1016/j.ndteint.2017.01.011.
- [57] V. Arora, R. Mulaveesala, A. Rani, A. Sharma, Digitised frequency modulated thermal wave imaging for non-destructive testing and evaluation of glass fibre reinforced

- polymers, *Nondestructive Testing and Evaluation* 34 (1) (2019) 23–32. doi:10.1080/10589759.2018.1546304.
- [58] S. Hedayatrasa, G. Poelman, J. Segers, W. van Paepegem, M. Kersemans, On the application of an optimized frequency-phase modulated waveform for enhanced infrared thermal wave radar imaging of composites, *Optics and Lasers in Engineering* 138 (2) (2021) 106411. doi:10.1016/j.optlaseng.2020.106411.
- [59] N. Tabatabaei, A. Mandelis, B. T. Amaechi, Thermophotonic radar imaging: An emissivity-normalized modality with advantages over phase lock-in thermography, *Applied Physics Letters* 98 (16) (2011) 163706. doi:10.1063/1.3582243.
- [60] N. Tabatabaei, A. Mandelis, Thermal coherence tomography: Depth-resolved imaging in parabolic diffusion-wave fields using the thermal-wave radar, *International Journal of Thermophysics* 33 (10-11) (2012) 1989–1995. doi:10.1007/s10765-012-1285-y.
- [61] S. Kaipilavil, A. Mandelis, Truncated-correlation photothermal coherence tomography for deep subsurface analysis, *Nature Photonics* 8 (8) (2014) 635–642. doi:10.1038/NPHOTON.2014.111.
- [62] P. Tavakolian, K. Sivagurunathan, A. Mandelis, Enhanced truncated-correlation photothermal coherence tomography with application to deep subsurface defect imaging and 3-dimensional reconstructions, *Journal of Applied Physics* 122 (2) (2017) 023103. doi:10.1063/1.4992807.
- [63] P. Tavakolian, S. Sfarra, G. Gargiulo, K. Sivagurunathan, A. Mandelis, Photothermal coherence tomography for 3-D visualization and structural non-destructive imaging of a wood inlay, *Infrared Physics & Technology* 91 (4) (2018) 206–213. doi:10.1016/j.infrared.2018.04.018.
- [64] P. Tavakolian, A. Mandelis, Perspective: Principles and specifications of photothermal imaging methodologies and their applications to non-invasive biomedical and non-destructive materials imaging, *Journal of Applied Physics* 124 (16) (2018) 160903. doi:10.1063/1.5044748.
- [65] P. Tavakolian, S. Roointan, A. Mandelis, Non-invasive in-vivo 3-D imaging of small animals using spatially filtered enhanced truncated-correlation photothermal

- coherence tomography, *Scientific reports* 10 (1) (2020) 13743. doi:10.1038/s41598-020-70815-3.
- [66] H. R. B. Orlande, *Thermal measurements and inverse techniques*, CRC Press, Boca Raton, 2017.
- [67] A. Mendioroz, A. Castelo, R. Celorrio, A. Salazar, Defect characterization from lock-in vibrothermography data, *International Journal of Thermophysics* 36 (5-6) (2015) 1208–1216. doi:10.1007/s10765-014-1679-0.
- [68] A. Mendioroz, L. Fuggiano, P. Venegas, I. S. de Ocariz, U. Galietti, A. Salazar, Characterizing subsurface rectangular tilted heat sources using inductive thermography, *Applied Sciences* 10 (16) (2020) 5444. doi:10.3390/app10165444.
- [69] H. S. Carslaw, J. C. Jaeger, *Conduction of heat in solids*, 2nd Edition, Clarendon, Oxford, 1959.
- [70] D. W. Hahn, M. N. Özışık, *Heat conduction*, 3rd Edition, Wiley, Hoboken, NJ, 2012. doi:10.1002/9781118411285.
- [71] H. W. Engl, M. Hanke-Bourgeois, A. Neubauer, *Regularization of inverse problems*, Vol. 375 of *Mathematics and its applications*, Kluwer, Dordrecht, 2000.
- [72] P. C. Hansen, *Rank-deficient and discrete ill-posed problems: Numerical aspects of linear inversion*, Vol. 4 of *SIAM monographs on mathematical modeling and computation*, Society for Industrial and Applied Mathematics (SIAM 3600 Market Street Floor 6 Philadelphia PA 19104), Philadelphia, Pa, 1998.
- [73] P. C. Hansen, *Discrete inverse problems: Insight and algorithms*, *Fundamentals of algorithms*, Society for Industrial and Applied Mathematics (SIAM 3600 Market Street Floor 6 Philadelphia PA 19104), Philadelphia, Pa., 2010.
- [74] S. Boyd, Distributed optimization and statistical learning via the alternating direction method of multipliers, *Foundations and Trends® in Machine Learning* 3 (1) (2010) 1–122. doi:10.1561/2200000016.
- [75] R. C. Aster, B. Borchers, C. H. Thurber, *Parameter estimation and inverse problems*, 3rd Edition, Elsevier, Amsterdam, Netherlands, 2019.

- [76] G. Mayr, Charakterisierung von porösen carbonfaserverstärkten Kunststoffbauteilen mit optisch angeregter Puls-Thermographie, Linz, Univ., Diss., 2016.
- [77] M. Özişik, H. R. B. Orlande, Inverse Heat Transfer: Fundamentals and Applications, Routledge, 2020.
- [78] R. Celorrio, A. Mendioroz, A. Salazar, Characterization of vertical buried defects using lock-in vibrothermography: Ii. inverse problem, Measurement Science and Technology 24 (6) (2013) 065602. doi:10.1088/0957-0233/24/6/065602.
- [79] A. Mendioroz, A. Castelo, R. Celorrio, A. Salazar, Characterization and spatial resolution of cracks using lock-in vibrothermography, NDT & E International 66 (1) (2014) 8–15. doi:10.1016/j.ndteint.2014.04.004.
- [80] A. Mendioroz, R. Celorrio, A. Cifuentes, L. Zatón, A. Salazar, Sizing vertical cracks using burst vibrothermography, NDT & E International 84 (1/2/3/4) (2016) 36–46. doi:10.1016/j.ndteint.2016.07.006.
- [81] M.-M. Groz, E. Abisset-Chavanne, A. Meziane, A. Sommier, C. Pradère, Three-dimensional reconstruction of thermal volumetric sources from surface temperature fields measured by infrared thermography, Applied Sciences 9 (24) (2019) 5464. doi:10.3390/app9245464.
- [82] S. D. Holland, B. Schiefelbein, Model-based inversion for pulse thermography, Experimental Mechanics 59 (4) (2019) 413–426. doi:10.1007/s11340-018-00463-2.
- [83] K. D. Cole, J. V. Beck, A. Haji-Sheikh, B. Litkouhi, Heat conduction using Green's functions, 2nd Edition, Series in computational and physical processes in mechanics and thermal sciences, CRC Press, Boca Raton, Fla., 2011.
- [84] P. Morse, H. Feshbach, Methods of Theoretical Physics: Types of fields, International series in pure and applied physics, McGraw-Hill, 1953.
- [85] K. H. Lee, G. Liu, H. F. Morrison, A new approach to modeling the electromagnetic response of conductive media, GEOPHYSICS 54 (9) (1989) 1180–1192. doi:10.1190/1.1442753.
- [86] K. H. Lee, G. Xie, A new approach to imaging with low-frequency electromagnetic fields, GEOPHYSICS 58 (6) (1993) 780–796. doi:10.1190/1.1443464.

- [87] M. Gershenson, Simple interpretation of time domain electromagnetic sounding using similarities between wave and diffusion propagation, SPIE Proceedings, SPIE, 1995, pp. 942–947. doi:10.1117/12.211388.
- [88] M. Gershenson, Synthetic aperture processing of electromagnetic sounding in conductive media, SPIE Proceedings, SPIE, 1999, pp. 326–332. doi:10.1117/12.365714.
- [89] A. Tamburrino, R. Fresa, S. S. Udpa, Y. Tian, Three-dimensional defect localization from time-of-flight/eddy current testing data, IEEE Transactions on Magnetics 40 (2) (2004) 1148–1151. doi:10.1109/TMAG.2004.824584.
- [90] H. Plasser, G. Mayr, G. Thummerer, G. Hendorfer, P. Burgholzer, Z. Major, Photothermal porosity estimation in CFRP by the time-of-flight of virtual waves, Journal of Non-destructive Evaluation 39 (4) (2020) 509. doi:10.1007/s10921-020-00722-0.
- [91] P. Kovács, B. Lehner, G. Thummerer, G. Mayr, P. Burgholzer, M. Huemer, Deep learning approaches for thermographic imaging, Journal of Applied Physics 128 (15) (2020) 155103. doi:10.1063/5.0020404.
- [92] P. Kovacs, B. Lehner, G. Thummerer, G. Mayr, P. Burgholzer, M. Huemer, A hybrid approach for thermographic imaging with deep learning, in: ICASSP 2020 - 2020 IEEE International Conference on Acoustics, Speech and Signal Processing (ICASSP), IEEE, 2020, pp. 4277–4281. doi:10.1109/ICASSP40776.2020.9053411.
- [93] P. Burgholzer, T. Berer, J. Gruber, G. Mayr, Super-resolution thermographic imaging using blind structured illumination, Applied Physics Letters 111 (3) (2017) 031908. doi:10.1063/1.4995410.
- [94] P. Burgholzer, T. Berer, M. Ziegler, E. Thiel, S. Ahmadi, J. Gruber, G. Mayr, G. Hendorfer, Blind structured illumination as excitation for super-resolution photothermal radiometry, Quantitative InfraRed Thermography Journal 17 (4) (2020) 268–278. doi:10.1080/17686733.2019.1655247.
- [95] S. Ahmadi, G. Thummerer, S. Breitwieser, G. Mayr, J. Lecompanion, P. Burgholzer, P. Jung, G. Caire, M. Ziegler, Multidimensional reconstruction of internal defects in additively manufactured steel using photothermal super resolution combined with virtual wave-based image processing, IEEE Transactions on Industrial Informatics 17 (11) (2021) 7368–7378. doi:10.1109/TII.2021.3054411.

- [96] L. V. Wang (Ed.), Photoacoustic imaging and spectroscopy, Vol. 144 of Optical science and engineering, CRC Press, Boca Raton, 2009.
- [97] P. Burgholzer, G. Stockner, G. Mayr, Acoustic reconstruction for photothermal imaging, *Bioengineering* (Basel, Switzerland) 5 (3) (2018). doi:10.3390/bioengineering5030070.
- [98] G. Thummerer, G. Mayr, P. Burgholzer, Photothermal testing of composite materials: Virtual wave concept with prior information for parameter estimation and image reconstruction, *Journal of Applied Physics* 128 (12) (2020) 125108. doi:10.1063/5.0016364.
- [99] Gregor Thummerer, Image reconstruction of defects using the virtual wave concept for pulsed thermography data, Master thesis, University of Applied Sciences Upper Austria, Wels (September/2018).
- [100] G. Thummerer, G. Mayr, P. Burgholzer, 3D photothermal imaging of subsurface defects in composite materials, *NDT & E International* 122 (2021) 102476. doi:10.1016/j.ndteint.2021.102476.
- [101] G. Thummerer, G. Mayr, P. D. Hirsch, M. Ziegler, P. Burgholzer, Photothermal image reconstruction in opaque media with virtual wave backpropagation, *NDT & E International* 112 (2020) 102239. doi:10.1016/j.ndteint.2020.102239.
- [102] A. Zimmer, *Abbildende zerstörungsfreie Prüfverfahren mit elastischen und elektromagnetischen Wellen*, Kassel, Univ., Diss., 2008.
- [103] G. Thummerer, G. Mayr, M. Haltmeier, P. Burgholzer, Photoacoustic reconstruction from photothermal measurements including prior information, *Photoacoustics* 19 (2020) 100175. doi:10.1016/j.pacs.2020.100175.

5 Publications and Scientific contribution

Current reconstruction methods for active thermography data, monitored in the pulse-echo configuration, are lacking in 3D localization and visualization of subsurface defects considering lateral anisotropic heat propagation. This work is based on a promising 3D reconstruction ap-



Figure 5.1: Scientific contribution.

proach called VWC and complements it in terms of anisotropic heat propagation observed by transient 3D temperature signals recorded in the pulse-echo configuration. Moreover, a novel method for estimating the anisotropic thermal diffusivity tensor based on the VWC is introduced. In addition, a discretization criterion is proposed that significantly speeds up the reconstruction process while maintaining the reconstruction quality. In summary, this work presents a fast, readily-interpretable and efficient multi-dimensional photothermal reconstruction method for anisotropic media developed in the course of four published peer-reviewed journal papers and one preprint with first authorship. An overview of the publications is shown in Fig. 5.1. The publications are presented below, preceded by a summary of the most important results and scientific contributions. Since the publications were prepared in collaboration with other authors, authorship credit is given in accordance with the CRediT taxonomy¹.

¹Brand, A., Allen, L., Altman, M., Hlava, M. and Scott, J. (2015), Beyond authorship: attribution, contribution, collaboration, and credit. *Learned Publishing*, 28: 151-155. <https://doi.org/10.1087/20150211>

5.1 Photoacoustic reconstruction from photothermal measurements including prior information

This work presents reconstructions of internal heat sources for 2D photothermal temperature signals. The goal of this work was to incorporate prior information in the form of positivity and sparsity to compensate for the degradation of spatial resolution that leads to blurred images of deeper structures. A test specimen was prepared with graphite rods embedded in epoxy resin at different depth positions. The graphite rods were thermally excited with a laser to introduce internal heat sources, which initiated a 2D thermal diffusion process. Simultaneously, the surface temperature signal was recorded with an IR camera. To incorporate prior information, the iterative regularization scheme ADMM was implemented for application within the VWC. The inclusion of the prior information sparsity is valid since typical test specimens have few defects. To include the prior information positivity, the Abel transform was used to project the bi-modal 2D virtual wave signal onto a positive data set and the linear inverse problem was adapted appropriately. To verify the benefits of including the prior information, the results obtained with ADMM were compared with those obtained with the direct regularization method T-SVD. Compared to ADMM, when using T-SVD, only the measurement errors represented by the temperature resolution of the IR camera can be used to estimate the regularization parameters, but prior information such as positivity and sparsity cannot be considered.

The main conclusion of this work is that prior information in the form of positivity and sparsity together with the iterative regularization tool ADMM can significantly improve the quality of the inverse solution, thus improving the localization of internal heat sources.

Authorship contribution statement

G. Thummerer: Conceptualization, Methodology, Software, Formal analysis, Validation, Investigation, Writing - original draft, Visualization. **G. Mayr:** Conceptualization, Methodology, Writing - review & editing, Project administration, Funding acquisition. **M. Haltmeier:** Software, Writing - review & editing. **P. Burgholzer:** Conceptualization, Methodology, Software, Formal analysis, Writing - original draft, Writing - review & editing, Supervision.



Research article

Photoacoustic reconstruction from photothermal measurements including prior information

G. Thummerer^{a,*}, G. Mayr^a, M. Haltmeier^b, P. Burgholzer^c^a Josef Ressel Centre for Thermal NDE of Composites, University of Applied Sciences Upper Austria, Wels, Austria^b Department of Mathematics, University of Innsbruck, Innsbruck, Austria^c RECENTD – Research Centre for Nondestructive Testing, Linz, Austria

ARTICLE INFO

Keywords:

Thermography
Photoacoustic PDE
Inverse problem
Regularization
Image reconstruction

ABSTRACT

Photothermal measurements with an infrared camera enable a fast and contactless part inspection. The main drawback of existing reconstruction methods is the degradation of the spatial resolution with increasing imaging depth, which results in blurred images for deeper lying structures. In this paper, we propose an efficient image reconstruction strategy that allows prior information to be included to overcome the diffusion-based information loss. Following the virtual wave concept, in a first step we reconstruct an acoustic wave field that satisfies the standard wave equation. Therefore, in the second step, stable and efficient reconstruction methods developed for photoacoustic tomography can be used. We compensate for the loss of information in thermal measurements by incorporating the prior information positivity and sparsity. Therefore, we combine circular projections with an iterative regularization scheme. Using simulated and experimental data, this work demonstrates that the quality of the reconstruction from photothermal measurements can be significantly enhanced.

1. Introduction

Photoacoustic (or optoacoustic) tomography uses thermoelastic expansion following a rapid temperature rise after the illumination of light absorbing structures within a semitransparent and turbid material, such as a biological tissue. Photothermal imaging belongs to the methods of active thermography and measures directly the increased temperature propagating by heat diffusion from the light absorbing structures to the surface of the sample. Both methods have the same optical absorption contrast and enable to detect hemoglobin, lipids, water and other light-absorbing chromophores, but with greater penetration depth than purely optical imaging modalities that rely on ballistic photons [1–3]. In photoacoustic tomography, the temporal evolution of the acoustic pressure field is sampled using an array of ultrasound detectors placed on the tissue surface or by moving a single detector across the detection surface. From the measured pressure signals, images of the optical absorption within the tissue can be reconstructed by time reversal and back projection methods or by solving an inverse source problem [3–5]. In photothermal imaging the surface temperature evolution is measured by an infrared camera.

The achievable spatial resolution for photoacoustic tomography and photothermal imaging degrades with imaging depth, which results in blurred images of deeper lying structures. Besides pure technical

limitations of the measurement equipment, the ultimate resolution limit has its origin in the second law of thermodynamics: scattering, dissipation or diffusion of the acoustic or “thermal” wave on its path through the sample causes entropy production, which is equal to the loss of information [6–8] (Fig. 1). As the information content of the reconstructed image strongly correlates with the spatial resolution, the higher entropy production from deeper lying structures causes a degradation in resolution. Overcoming the resolution limit due to entropy production is not trivial. Without taking into account additional knowledge or information about the sample, no mathematical reconstruction algorithm can compensate for this information loss, causing the degradation in resolution.

Super-resolution fluorescence imaging techniques, such as stochastic optical reconstruction microscopy (STORM) [9], photoactivated localization microscopy (PALM) [10], or super-resolution optical fluctuation imaging (SOFI) [11] utilize the fact that the localization of point sources (e.g. activated fluorescent molecules) is possible with a much higher accuracy than the width of the point spread function (PSF). Although the resolution in optical imaging has been greatly improved, there continues to be rapid advancements in the development of high resolution imaging methods also for many other imaging modalities. Localization microscopy was also used to achieve super-resolution in ultrasound imaging by using scattering microbubbles instead of

* Corresponding author.

E-mail address: Gregor.Thummerer@fh-wels.at (G. Thummerer).<https://doi.org/10.1016/j.pacs.2020.100175>

Received 6 November 2019; Received in revised form 31 January 2020; Accepted 8 March 2020

Available online 19 March 2020

2213-5979/ © 2020 The Authors. Published by Elsevier GmbH. This is an open access article under the CC BY-NC-ND license (<http://creativecommons.org/licenses/by-nc-nd/4.0/>).

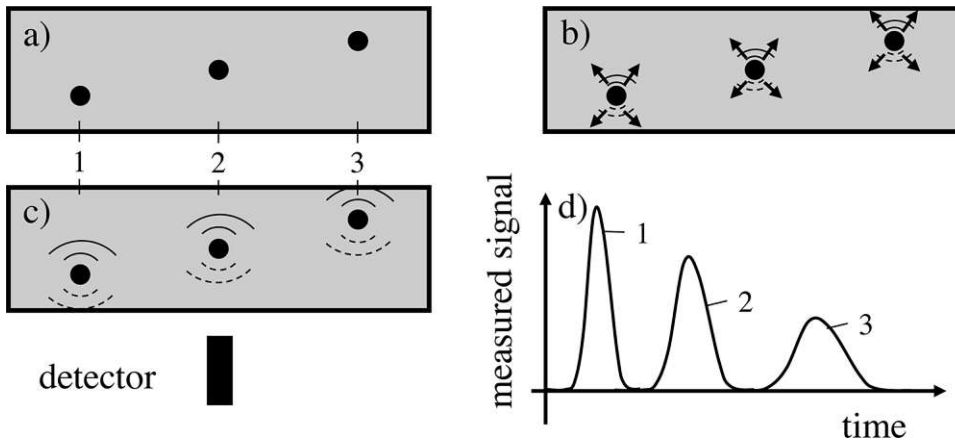


Fig. 1. Schematic sketch of the information loss from entropy production during scattering, dissipation, or diffusion. (a) Sample with sub-surface structure, which should be imaged; (b) propagation of the acoustic or “thermal” waves to the sample surface; entropy production determines the loss of information; (c) detection of signals at the sample surface; (d) measured signals at the detector surface as a function of time. Due to entropy production, the signal from the deeper structures has not only a smaller amplitude. They are also broadened compared to the signal from the structure just beneath the surface.

fluorescent molecules as point sources [12,13], and recently even for in vivo localization of single dyed droplets for photoacoustic tomography [14]. Ultrafast localization microscopy allows for super-resolution ultrasound imaging of vasculature in whole organs [15].

In the field of optics, it has been known since 2007 that optical diffusion in a strong scattering sample can be “inverted” by wavefront shaping [16]. Coherent photons from a laser scatter in a deterministic way (at least for a certain correlation time), which is measured pointwise. The resulting scattering matrix is used to change the light wave front, e.g. by a spatial light modulator in such a way that after diffusive scattering the light is focused. For heat diffusion, phonons are not coherent and the propagation of phonons is highly uncorrelated in time. Therefore, a “phonon scattering matrix” cannot be measured and used to invert heat diffusion in time. For photoacoustic imaging in a (quasi) diffusive regime a comprehensive overview about the advances in super-resolution imaging was recently given by Shi et al. [17].

The degradation of spatial resolution with increasing imaging depth in thermographic imaging could be circumvented by using structured heating, e. g. by structured illumination patterns. For super-resolution reconstruction out of numerous images with different illumination patterns, we have successfully proposed a non-linear iterative joint sparsity (IJOSP) algorithm [18,19].

These patterns can even be unknown, which is called blind structured illumination. We demonstrated this by imaging a line pattern and a star-shaped structure through a metal sheet with a resolution that was four times better than the resolution limit from entropy production [19]. The structured illumination was realized using parallel slits cut in an aluminum foil, where the excitation is carried out either by a flash lamp, which passes through the slits in the foil, or by a high-power laser with a line-shaped spot.

In this work, we demonstrate that even without structured illumination, just by taking into account prior information, such as positivity and sparsity of the heated structures inside the sample and using adequate iterative non-linear reconstruction algorithms, the increased blurring with imaging depth can be reduced significantly. Positivity comes from the fact that heating always causes a temperature increase. By converting the temperature signal into a virtual wave, which is a solution of the wave equation, positivity is not directly preserved for 2D and 3D wave propagation. An initially nonnegative acoustic signal will take negative values during propagation. In this work, we account for this issue by calculating the circular or spherical projections, which is in 2D the Abel transformation and in 3D the time integral of the virtual wave [20]. The circular and spherical projections preserve positivity of the initial source. For one data point the information gain by a positivity constraint would be only a factor of two, but for a signal with n data points this factor becomes 2^n , which can be large for higher n . More information could be gained by using also sparsity. Sparsity can often be assumed because defects, such as cracks in samples, are usually

sparse and also in biomedical imaging the sample consists of different types of tissues separated by “sparse” interfaces. The application of the virtual wave concept (VWC) with prior information for a high-resolution thermographic image reconstruction is shown using 2D experimental surface temperature data.

2. Virtual wave concept

The intention of the virtual wave concept is to reconstruct the initial temperature distribution $T_0(\mathbf{r})$ based on temporal temperature data $T(\mathbf{r}, t)$ measured at the sample surface (Fig. 2a, c). For this purpose, we transform $T(\mathbf{r}, t)$ locally into a virtual wave field $T_{\text{virt}}(\mathbf{r}, t)$ (Fig. 2d) in order to enable the application of efficient and stable photoacoustic image reconstruction methods. The reconstruction of the initial heat sources is imaged in Fig. 2e.

2.1. Forward problem

The direct or forward problem is analytically given by the heat equation

$$\left(\nabla^2 - \frac{1}{\alpha} \frac{\partial}{\partial t}\right) T(\mathbf{r}, t) = -\frac{1}{\alpha} T_0(\mathbf{r}) \delta(t). \quad (1)$$

The heat equation describes the heat diffusion process in a solid and hence the temperature distribution $T(\mathbf{r}, t)$ as function of position vector $\mathbf{r} = (x, y, z)$, where x, y, z are the Cartesian coordinates, and time t . α is the thermal diffusivity. The right hand side of Eq. (1) represents the source term. Herein, the temporal Dirac-Delta distribution $\delta(t)$ arranges that the spatial temperature distribution $T_0(\mathbf{r})$ is introduced at time $t = 0$. The heat equation can be classified as parabolic partial differential equation (PDE) and describes an irreversible process. Practically the forward problem is given by heating up the test specimen, e.g. by absorption of optical radiation or induction of eddy current and measuring the corresponding temporal temperature change at the surface. In Fig. 2a an exemplary initial temperature distribution is illustrated. The corresponding simulated surface temperature distribution $T(y, z = 0)$ is imaged in Fig. 2c.

The propagation of the virtual wave $T_{\text{virt}}(\mathbf{r}, t')$ is based on the acoustic wave equation for pressure [21]

$$\left(\nabla^2 - \frac{1}{c^2} \frac{\partial^2}{\partial t^2}\right) p(\mathbf{r}, t) = -\frac{1}{c^2} \frac{\partial}{\partial t} p_0(\mathbf{r}) \delta(t). \quad (2)$$

Herein, $p(\mathbf{r}, t)$ is the photoacoustic wave pressure, $p_0(\mathbf{r})$ is the initial pressure distribution and c is the speed of sound. We claim, that the following initial pressure and temperature distribution relation holds:

$$p(\mathbf{r}, t = 0) = p_0(\mathbf{r}) = c^2 \rho \beta T_0(\mathbf{r}) \quad \text{for } t = 0, \quad (3)$$

where ρ is the material density and β is the thermal expansion

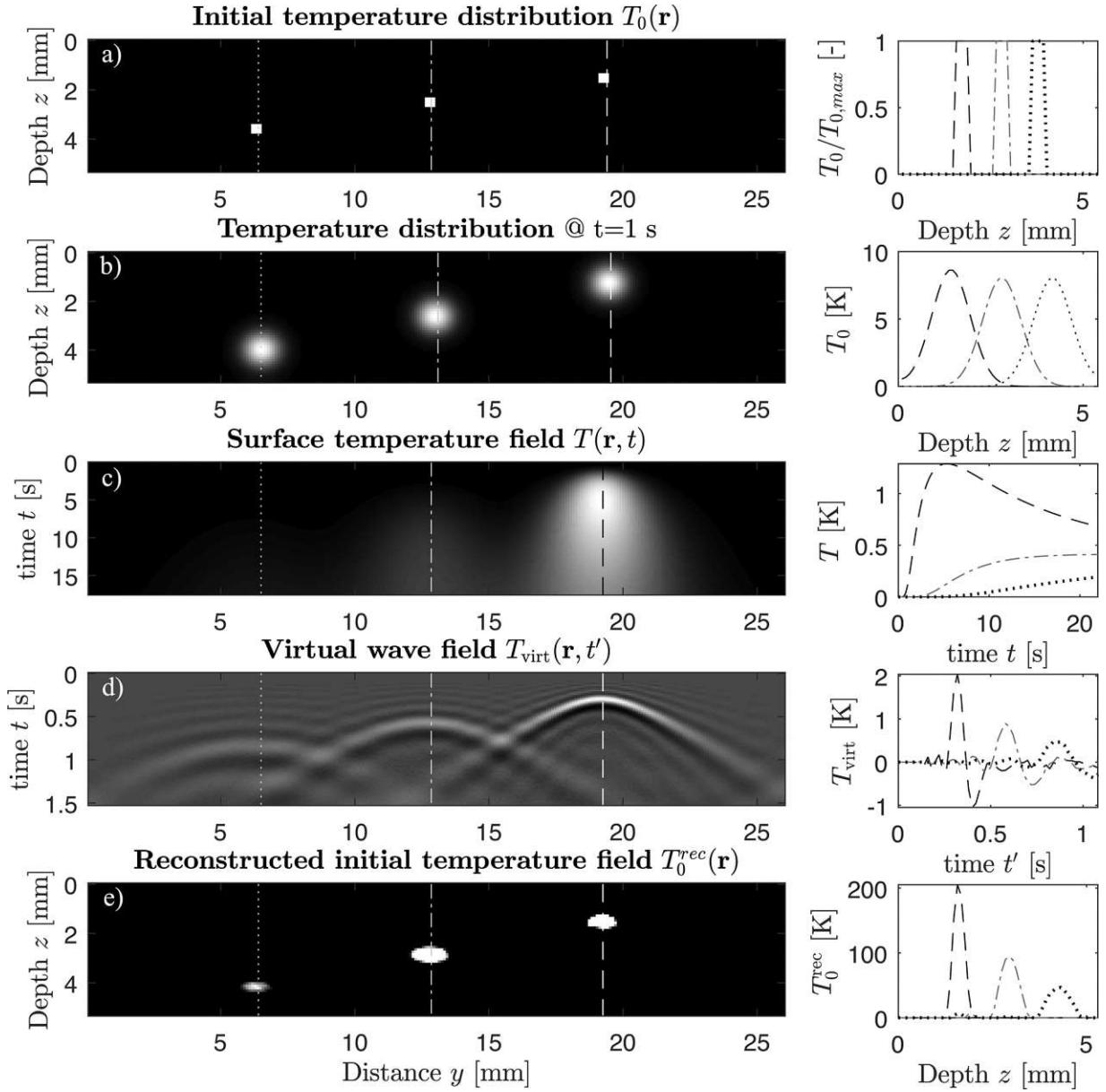


Fig. 2. Process steps of VWC based on simulated data with internal heat sources: (a) initial temperature distribution 2D (left) and 1D (right) at $y = \{6.5, 13, 19.5\}$ mm, (b) spatial temperature distribution at $t = 1$ s, (c) simulated surface temperature field, (d) virtual wave field and (e) reconstructed field.

coefficient of the observed material. Then we define a virtual wave field, where the above relationship is extended for times $t > 0$ by introducing the virtual time scale t' :

$$T_{\text{virt}}(\mathbf{r}, t') = \frac{p(\mathbf{r}, t)}{c^2 \rho \beta}. \quad (4)$$

By substituting Eqs. (3) and (4) into the acoustic wave equation for pressure, Eq. (2), the PDE for the virtual wave propagation yields:

$$\left(\nabla^2 - \frac{1}{c^2} \frac{\partial^2}{\partial t'^2} \right) T_{\text{virt}}(\mathbf{r}, t') = -\frac{1}{c^2} \frac{\partial}{\partial t'} T_0(\mathbf{r}) \delta(t'). \quad (5)$$

Herein, c is the virtual speed of sound and t' corresponds to the virtual time scale. The wave equation can be classified as hyperbolic PDE and is, in contrast to the heat equation, time reversible. The virtual wave exhibit wave properties such as wavefront propagation, reflection and refraction [22,23]. Frequency domain- synthetic aperture focusing technique (F-SAFT), a well known acoustic reconstruction method, is used to reconstruct the initial temperature distribution $T_0^{\text{rec}}(\mathbf{r})$. $T_0(\mathbf{r})$ is

again the initial temperature distribution.

2.1.1. Fredholm integral equation

According to Burgholzer et al. [24] the temperature distribution $T(\mathbf{r}, t)$, can be calculated based on the virtual wave field $T_{\text{virt}}(\mathbf{r}, t')$ and the kernel $K(t, t')$ for the same position vector \mathbf{r} , but different time scales t and t' :

$$T(\mathbf{r}, t) = \int_{-\infty}^{\infty} T_{\text{virt}}(\mathbf{r}, t') K(t, t') dt' \quad (6)$$

with

$$K(t, t') = \frac{c}{\sqrt{\pi \alpha t}} \exp\left(-\frac{c^2 t'^2}{4 \alpha t}\right) \quad t > 0. \quad (7)$$

The kernel, Eq. (7), contains the thermal diffusivity α and virtual speed of sound c , which are the characteristic parameters for heat and virtual wave propagation. Eqs. (6) and (7) are valid for a temporal Dirac-Delta like heating $h(t) = \delta(t)$ of the specimen. To obtain Eq. (7), we have to Fourier transform Eqs. (1) and (5) temporally. Due to the elimination of

the time derivatives one can find a relationship between temperature field and virtual wave field for the same position vector \mathbf{r} . Applying the inverse Fourier transformation on this relationship yields Eq. (6) and consequently Eq. (7). Due to the linear nature of wave and diffusion equation, Eq. (6) can be extended for any heating function $h(t)$ via temporal convolution [6]. The benefit of VWC compared to the direct solution of the inverse heat conduction problem (IHCP) comes with the application on multidimensional heat conduction problems. Here the VWC, in contrast to IHCP where the temporal and spatial components are treated simultaneously, solves for the temporal virtual wave field which yields the depth information such as defect depth, front wall and backwall. This first reconstruction step is then post processed by acoustic reconstruction methods where again the temporal information and the spatial components are respected.

3. Image reconstruction

3.1. Inverse problem

Our goal is to convert the measured or simulated temperature field into a so-called virtual wave field to enable the application of photoacoustic reconstruction methods. As mentioned previously, a consequence of entropy production during heat diffusion, characterized by the heat equation is that information is lost. Hence, calculating T_{virt} from T is a severely ill-posed inverse problem and regularization tools are necessary to calculate an appropriate regularized solution [25].

Usually, thermographic data is discrete in time and space. Hence, it is convenient to write Eq. (6) in discrete matrix form with $t_k = (k - 1)\Delta_t$ and $t'_j = (j - 1)\Delta_{t'}$

$$\mathbf{T} = \mathbf{K}\mathbf{T}_{\text{virt}} \quad (8)$$

The matrices have the subsequent dimensions: $\mathbf{T} \in \mathbb{R}^{m \times q}$, $\mathbf{K} \in \mathbb{R}^{m \times n}$ and $\mathbf{T}_{\text{virt}} \in \mathbb{R}^{n \times q}$ with $k = \{1, 2, \dots, m\}$ and $j = \{1, 2, \dots, n\}$. The variable $\ell = \{1, 2, \dots, q\}$, counts for the spatial extension in y . For a *Dirac-Delta* like heating function $h(t) = \delta(t)$, the components of the \mathbf{K} -matrix are calculated in the following manner:

$$\begin{aligned} K_{kj} &= \frac{\tilde{c}}{\sqrt{\pi\Delta_{F0}(k-1)}} \exp\left(-\frac{\tilde{c}^2(j-1)^2}{4\Delta_{F0}(k-1)}\right) \\ &= \frac{\eta}{\sqrt{\pi(k-1)}} \exp\left(-\frac{\eta^2(j-1)^2}{4(k-1)}\right). \end{aligned} \quad (9)$$

During calculation of the matrix elements K_{kj} the expression $(1/0)$ occurs for $k = 1$. Hence, the first row of the Kernel-matrix is set to zero: $\mathbf{K}(1, :) = \mathbf{0}$. In Eq. (9), the dimensionless numbers \tilde{c} , Δ_{F0} and η are defined as

$$\tilde{c} = \frac{c\Delta_{t'}}{\Delta_y}, \quad \Delta_{F0} = \frac{\alpha\Delta_{t'}}{\Delta_y^2}, \quad \eta = \frac{\tilde{c}}{\sqrt{\Delta_{F0}}}, \quad (10)$$

where \tilde{c} equates to the *Courant-Friedrichs-Levy* (CFL) number [26], Δ_{F0} is the discrete *Fourier* number [27] and η is the ratio of these dimensionless numbers.

3.1.1. Reduction to circular projections

The quality of the regularized solution, i.e. the solution of the virtual wave field can be enhanced if prior informations, such as positivity or sparsity, are available. Considering the temperature distribution based on a heating pulse, in all spatial dimensions, the temperature distribution is always positive with respect to the ambient temperature for each time step of the simulation or measurement data. In contrast to this, the virtual wave field is not positive for all spatial dimensions. Positivity of the virtual wave field can only be guaranteed if the reconstruction is based on a one dimensional heat conduction problem. Hence, the intention is to transfer the multidimensional virtual wave data, via circular projections into a positive data set in order to incorporate the additional condition positivity [20,28,29]. Therefore, we

consider the circular projection \mathbf{M}_{virt} which can be computed with the inverse Abel transformation of the two dimensional virtual wave field \mathbf{T}_{virt} :

$$\mathbf{M}_{\text{virt}} = \mathbf{A}^{-1}\mathbf{T}_{\text{virt}}. \quad (11)$$

Herein \mathbf{A}^{-1} is the inverse Abel transformation operator with respect to time. For the 3D wave equation, the Abel transformation is replaced by integration with respect to the temporal variable, which results in spherical projections of the initial 3D source [25, Appendix A].

Our goal is now to relate the positive data, i.e. the circular projected virtual wave signal \mathbf{M}_{virt} from Eq. (11) with the temperature signal \mathbf{T} . For this purpose, we recapitulate the temperature field of Eq. (8), that is based on an arbitrary heating function $h(t)$ represented by the vector \mathbf{h} :

$$\mathbf{T} = (\mathbf{K}*\mathbf{h})\mathbf{T}_{\text{virt}} = \tilde{\mathbf{K}}\mathbf{T}_{\text{virt}}. \quad (12)$$

Herein $(*)$ denotes the temporal convolution operator applied to the rows of \mathbf{K} . Performing the inverse operation of Eq. (11) and substituting this into Eq. (12) yields:

$$\mathbf{T} = \tilde{\mathbf{K}}\mathbf{T}_{\text{virt}} = \tilde{\mathbf{K}}\mathbf{A}\mathbf{M}_{\text{virt}} = \hat{\mathbf{K}}\mathbf{M}_{\text{virt}} \quad (13)$$

$$\text{with } \hat{\mathbf{K}} = \tilde{\mathbf{K}}\mathbf{A} = (\mathbf{K}*\mathbf{h})\mathbf{A}. \quad (14)$$

In any dimension, the circular means of a non-negative function are again non-negative. By solving Eq. (13) we can therefore incorporate the known non-negativity of the circular projections of \mathbf{T}_{virt} as prior knowledge when reconstructing \mathbf{M}_{virt} . In order to obtain the two-dimensional virtual wave field we can apply again the Abel transformation \mathbf{A} to the reconstructed virtual circular projections. We apply regularization tools to solve the inverse problems Eq. (8) and Eq. (13). For the inverse problem in Eq. (8) we use the truncated singular value decomposition (T-SVD) for regularization. To solve the inverse problem Eq. (13) we apply the alternating direction method of multipliers (ADMM).

3.1.2. Regularization

In this work we use the direct regularization method truncated T-SVD and the iterative regularization algorithm ADMM. For the sake of simplicity, the solution strategies are described for 1D temperature profiles of a single infrared camera pixel. The heat diffusion is still in 2D or 3D, where the described solution strategies are applied separately to each pixel location.

The solution using T-SVD approximates the least squares solution and its objective function is given by [30]

$$\text{minimize } \frac{1}{2} \|\mathbf{K}\mathbf{T}_{\text{virt}} - \mathbf{T}\|_2^2. \quad (15)$$

Formally we have for the virtual wave solution:

$$\mathbf{T}_{\text{virt}}^{\text{T-SVD}} = \sum_{i=1}^k \frac{\mathbf{u}_i^T \mathbf{T}}{\mu_i} \mathbf{v}_i. \quad (16)$$

Herein, k is the regularization parameter that is estimated using the discrete *Picard plot*, where the only prior information is the noise level. \mathbf{u}_i and \mathbf{v}_i are orthonormal column vectors of the matrices \mathbf{U} and \mathbf{V} , obtained via SVD.

To incorporate the prior information positivity and sparsity we apply the ADMM algorithm, which is an efficient iterative algorithm for constrained optimization. [31]. Using ADMM the prior information sparsity is respected, because we assume that the virtual wave field \mathbf{T}_{virt} is sparse. ADMM is a descendant of the *Douglas-Rachford splitting* method [32,33]. The idea is to split the objective function

$$\text{minimize } \frac{1}{2} \|\hat{\mathbf{K}}\mathbf{M}_{\text{virt}} - \mathbf{T}\|_2^2 + \lambda \|\mathbf{M}_{\text{virt}}\|_1 \quad (17)$$

into two parts in order to obtain separate problems that are easier to solve. Hence, the new problem is given by:

$$\text{minimize } f(\mathbf{M}_{\text{virt}}) + g(\mathbf{z}) \quad (18)$$

$$\text{with } f(\mathbf{M}_{\text{virt}}) = 1/2 \|\hat{\mathbf{K}}\mathbf{M}_{\text{virt}} - \mathbf{T}\|_2^2, g(\mathbf{z}) = \lambda \|\mathbf{M}_{\text{virt}}\|_1 \text{ and subject to } \mathbf{M}_{\text{virt}} - \mathbf{z} = \mathbf{0}. \quad (19)$$

Then we can form the *Lagrangian* with respect to Eqs. (18) and (19). To increase robustness, one adds a penalty term and an appropriate penalty parameter $\rho > 0$ to the *Lagrangian*. This approach gives the *augmented Lagrangian* and leads to the following iteration procedure to reconstruct \mathbf{M}_{virt} [31]:

$$\begin{aligned} \mathbf{M}_{\text{virt}}^{k+1} &: = (\hat{\mathbf{K}}^T \hat{\mathbf{K}} + \rho \mathbf{I})^{-1} [\hat{\mathbf{K}}^T \mathbf{T} + \rho(\mathbf{z}^k - \mathbf{u}^k)] \\ \mathbf{z}^{k+1} &: = S_{\lambda/\rho}(\mathbf{M}_{\text{virt}}^{k+1} + \mathbf{u}^k) \\ \mathbf{u}^{k+1} &: = \mathbf{u}^k + \mathbf{M}_{\text{virt}}^{k+1} - \mathbf{z}^{k+1}. \end{aligned} \quad (20)$$

$S_{\lambda/\rho}$ is a threshold operator. In order to enforce positivity, we apply soft thresholding only to the positive entries and set the negative entries to zero. λ is a regularization parameter that is determined by the L-curve method [34].

4. Experimental results

In this section we apply the VWC to pulse thermography data based on internal heat sources. Based on the physical parameters, the time resolution and the spatial resolution we can compute the kernel matrix for T-SVD. Further, using the Abel transformation, we introduce the prior information positivity. Then a comparison of the above presented regularization tools is given. Finally, we apply F-SAFT to reconstruct the initial temperature distribution. Since the information content of $\hat{\mathbf{K}}$ is higher than for \mathbf{K} we expect a significant improvement of the regularized solution for ADMM compared to T-SVD. The reconstruction of the internal heat sources is performed by F-SAFT.

4.1. Image reconstruction of internal heat sources

The test specimen is built up with graphite bars that are embedded in epoxy resin. The geometric dimensions are shown in Fig. 3a. The

graphite bars are heated by laser excitation, where the laser has a wavelength of 938 ± 10 nm. As one can see in the exemplary surface temperature profiles (Fig. 4a), the laser excitation causes a volumetric heating of the epoxy resin and a surface heating of the graphite bars. Hence, the epoxy resin behaves like a semi-transparent material for the corresponding laser excitation (see Fig. 3b). The maximum power of the diode laser is 250 W and the numerical aperture is 0.22. The raise time is smaller than $10 \mu\text{s}$ and the bandwidth is greater than 50 kHz. In the experiment the laser power was 250 W and the heating time was $t_h = 200$ ms. The spatial laser power distribution was homogeneous over the laser spot. The laser spot diameter was approximately 40 mm. The heated graphite bars work as internal heat sources. Simultaneously, the temperature evolution is measured on the surface of the test specimen using an infrared camera. The infrared camera has an image frequency of 106 Hz in full frame modus and the noise equivalent temperature difference (NETD) is smaller than 25 mK. This camera has a cooled indium antimony (InSb) sensor, that is sensitive in the spectral range of $3.0\text{--}5.1 \mu\text{m}$. In this spectral range the epoxy resin is opaque. Hence, we measure the temporal surface temperature at $z = 0$ and not the surface temperature of the graphite bars.

The spatial resolution is $\Delta_y = 0.098$ mm and the time resolution is $\Delta_t = 0.02$ s. Fig. 4a illustrates temporal temperature slopes for different position along the graphite bars. Fig. 4b shows spatial temperature distributions for $t = \{20, 30, 50\}$ s related to the corresponding maximum. For both images, the gray lines show the original data and the black lines the spatial mean value of three-hundred surface temperature slices normal to the graphite bars. As one can see, the deeper the steel rod, the lower the maximal temperature signal. This behavior is a consequence of the diffusive nature of the thermal wave.

Based on the measured surface temperature, we calculate a virtual wave field using T-SVD and ADMM. The thermal diffusivity $\alpha = 0.13e-6 \text{ m}^2/\text{s}$ was determined using the linear diffusivity fit (LDF) method [35]. The dimensionless speed of sound was set in the stable regime to $\tilde{c} = 1$. Using T-SVD we directly solve for the virtual wave field and set the benchmark for ADMM. Using ADMM, we then take into account the prior information, sparsity via the cost function Eq. (17)

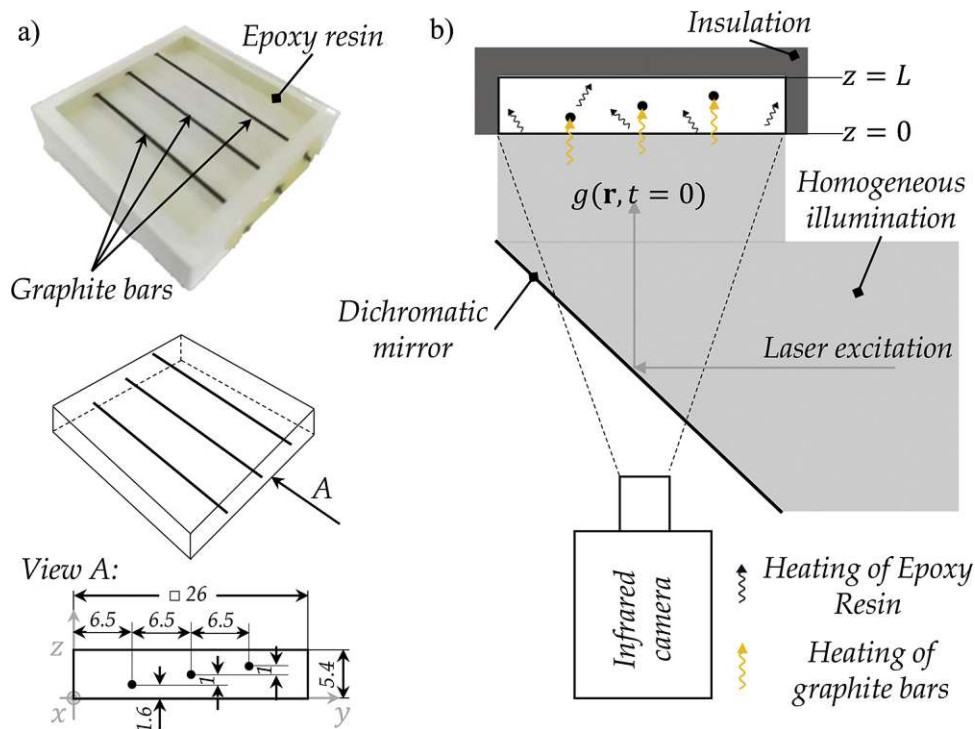


Fig. 3. (a) Test specimen built up with graphite bars, that are embedded in epoxy resin. (b) Principle sketch of the measurement set-up: The graphite bars are stimulated by laser excitation. The resulting change of the surface temperature is measured with an infrared camera.

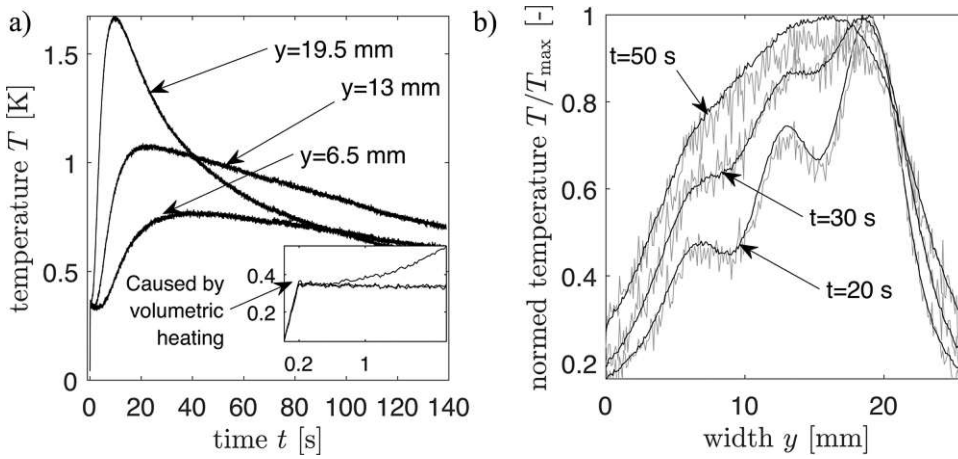


Fig. 4. (a) Temporal temperature distribution for several pixel positions. Because of the partially volumetric heating of the epoxy resin we have a sudden temperature increase at $t = 0$. (b) Spatial temperature distribution for several time stamps. The gray lines show the original data and the black lines the spatial mean value of three-hundred surface temperature slices normal to the graphite bars.

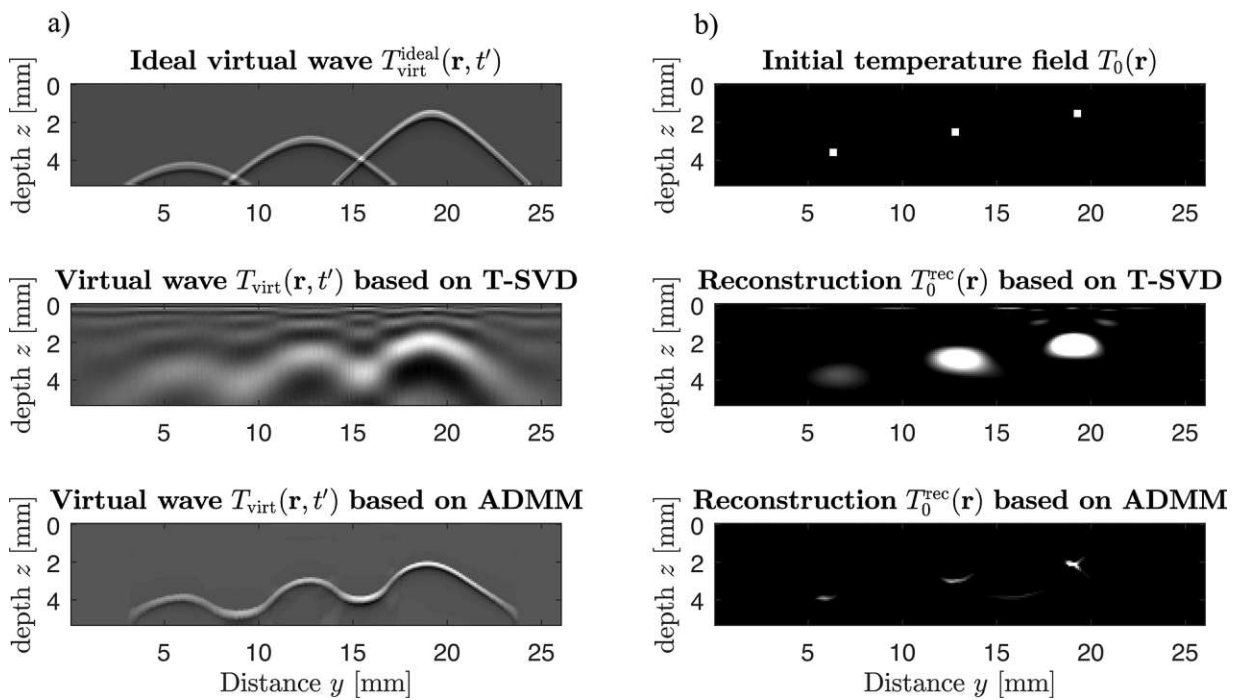


Fig. 5. (a) Comparison of the ideal virtual wave field to the reconstructed wave fields applying F-SAFT and ADMM. (b) Comparison of the initial temperature distribution and the reconstructed initial temperature distributions using T-SAFT and ADMM.

and positivity is introduced by the Abel transformation. Consequently, we calculate the regularized solution for the circular projections \mathbf{M}_{virt} . To calculate the virtual wave field \mathbf{T}_{virt} we apply the Abel transformation to the circular projections \mathbf{M}_{virt} . The ideal virtual wave field and the virtual wave fields calculated by T-SVD and ADMM are illustrated in Fig. 5a. For the T-SVD, $k = 14$ singular values were respected. For the ADMM algorithm 40 iterations with a fixed penalty parameter $\rho = 0.0016$ and regularization parameter $\lambda = 7.58$ were performed. One can see, that the virtual wave field based on ADMM matches much better the ideal virtual wave field compared to T-SVD. As a consequence the image reconstruction of the internal heat sources based on ADMM exhibit a much better spatial resolution compared to T-SVD.

To highlight the process steps of VWC the result of ADMM regularization is again illustrated in Fig. 6. The left side of Fig. 6 show the results in 2D and the right side shows a 1D representation of the initial temperature field, the measured surface temperature field, the calculated virtual wave field applying ADMM, and the reconstructed initial temperature distribution applying F-SAFT. The 1D representations were obtained by evaluating the corresponding 2D fields at $y =$

$\{6.2, 12.85, 19.25\}$ mm (see different line styles). The evaluation at y differ from the simulation because of inaccuracy in the manufacturing of the specimen. Especially, for the 1D representation of the virtual wave, we see the characteristics of 2D wave propagation. Compared to the results obtained by simulation (Fig. 2e), the experimental results (Fig. 6d) show non-symmetric rods.

For simulated data we used a homogeneous material with a certain spatial initial temperature distribution (Fig. 2a). In the experiment we see an influence caused by the volumetric heating of the semi-transparent material that have different thermophysical properties (epoxy resin and graphite). Hence, we have some balancing processes at the interface of these two materials. Consequently, we expect that the non-proper heating in the experiment affect a symmetric reconstruction of the rods.

5. Conclusions

In this work an application of the VWC for thermographic image reconstruction based on multidimensional temperature data was

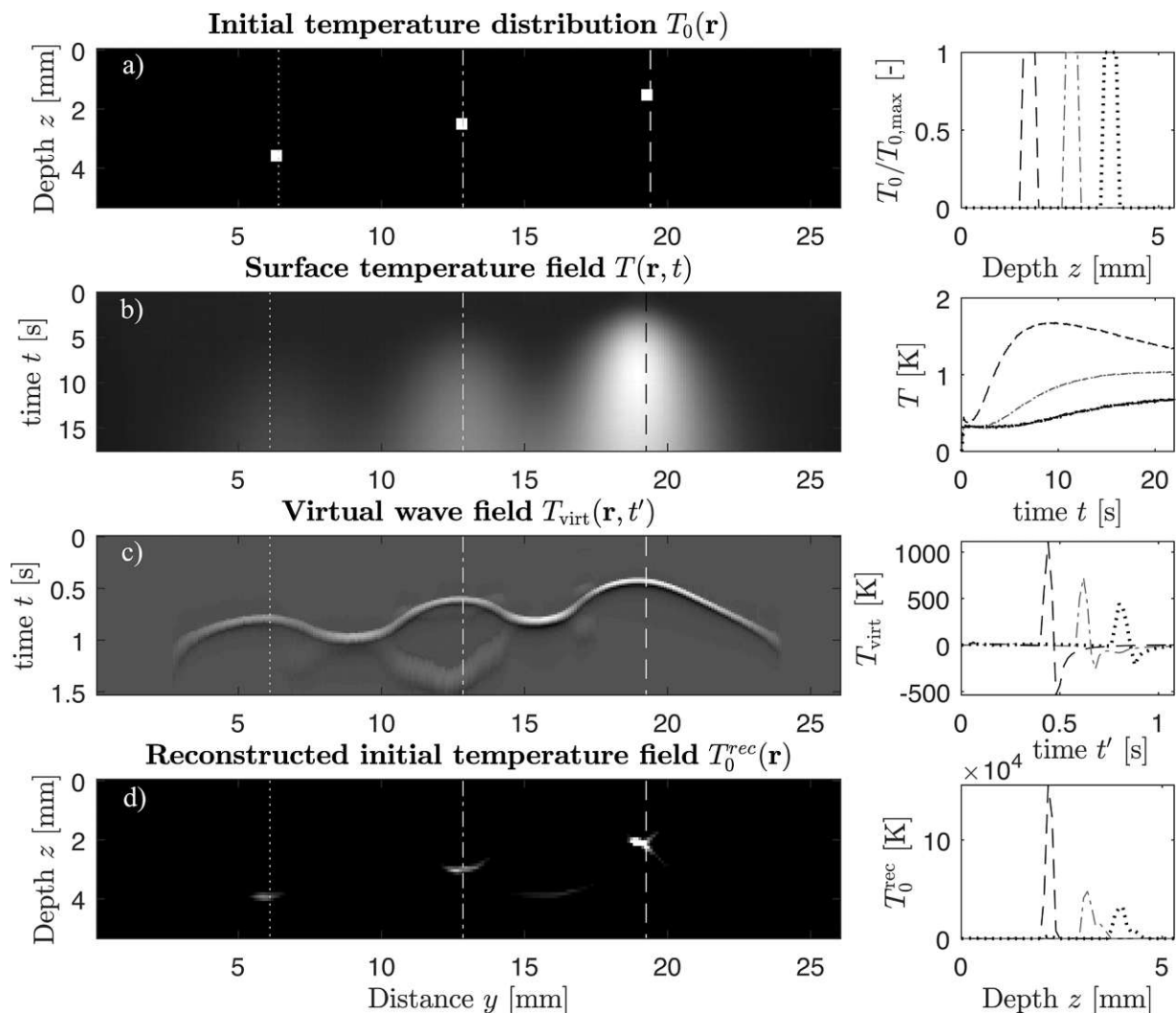


Fig. 6. Process steps of VWC based on measured data with internal heat sources: (a) initial temperature distribution 2D (left) and 1D (right) at $y = \{6.2, 12.85, 19.25\}$ mm, (b) measured surface temperature field, (c) virtual wave field and (d) reconstructed field.

shown. We emphasize that VWC is only meaningful and different to an IHCP when the reconstruction of defects is based on a multidimensional heat conduction problem. The main goal of this work was to illustrate that prior information significantly improves the regularized solution and, hence, the reconstructed field. Using T-SVD for regularization the information about measurement noise was considered in order to estimate the regularization parameter k . Using ADMM, the prior information positivity and sparsity were incorporated. For this purpose we reformulated the linear severely ill-posed inverse problem. The regularization and reconstruction results show that respecting more information about the data significantly increases the quality of the regularized solution. Due to the linearity of the heat and wave equation it is possible to employ VWC for thermo-tomography for the detection and characterization of cracks in isotropic and anisotropic media.

Conflict of interest

The authors declare that there is no conflict of interest.

Acknowledgments

The financial support by the Austrian Federal Ministry of Science, Research and Economy and the National Foundation for Research, Technology and Development is gratefully acknowledged. Furthermore,

this work has been supported by the project multimodal and in-situ characterization of inhomogeneous materials (MiCi), by the Federal Government of Upper Austria and the European Regional Development Fund (EFRE) in the framework of the EU-program IWB2020. Financial support was provided by the Austrian Research Funding Association (FFG) under the scope of the COMET programme within the research project "PhotonicSensing for Smarter Processes (PSSP)" (contract #871974). This programme is promoted by BMVIT, BMDW, the Federal State of Upper Austria and the Federal State of Styria, represented by SFG. The work of MH has been supported by the Austrian Science Fund (FWF) project P30747-N32.

References

- [1] R.A. Kruger, W.L. Kiser, D.R. Reinecke, G.A. Kruger, K.D. Miller, Thermoacoustic molecular imaging of small animals, *Mol. Imaging* 2 (2) (2003), <https://doi.org/10.1162/15353500200303109> 153535002003031.
- [2] P. Beard, Biomedical photoacoustic imaging, *Interface Focus* 1 (4) (2011) 602–631, <https://doi.org/10.1098/rsfs.2011.0028>.
- [3] L.V. Wang, S. Hu, Photoacoustic tomography: in vivo imaging from organelles to organs, *Science* 335 (6075) (2012) 1458–1462, <https://doi.org/10.1126/science.1216210>.
- [4] P. Burgholzer, G.J. Matt, M. Haltmeier, G. Paltauf, Exact and approximative imaging methods for photoacoustic tomography using an arbitrary detection surface, *Phys. Rev. E: Stat. Nonlinear Soft Matter Phys.* 75 (4 Pt 2) (2007) 46706, <https://doi.org/10.1103/PhysRevE.75.046706>.
- [5] P. Kuchment, L. Kunyansky, Mathematics of thermoacoustic tomography, *Eur. J.*

- Appl. Math. 19 (2) (2008) 31, <https://doi.org/10.1017/S0956792508007353>.
- [6] P. Burgholzer, G. Stockner, G. Mayr, Acoustic reconstruction for photothermal imaging, *Bioengineering* 5 (3) (2018), <https://doi.org/10.3390/bioengineering5030070>.
- [7] M. Esposito, C. van den Broeck, Second law and Landauer principle far from equilibrium, *EPL (Europhys. Lett.)* 95 (4) (2011) 40004, <https://doi.org/10.1209/0295-5075/95/40004>.
- [8] P. Burgholzer, Thermodynamic limits of spatial resolution in active thermography, *Int. J. Thermophys.* 36 (9) (2015) 2328–2341, <https://doi.org/10.1007/s10765-015-1890-7>.
- [9] M.J. Rust, M. Bates, X. Zhuang, Sub-diffraction-limit imaging by stochastic optical reconstruction microscopy (storm), *Nat. Methods* 3 (10) (2006) 793–795, <https://doi.org/10.1038/nmeth929>.
- [10] E. Betzig, G.H. Patterson, R. Sougrat, O.W. Lindwasser, S. Olenych, J.S. Bonifacio, M.W. Davidson, J. Lippincott-Schwartz, H.F. Hess, Imaging intracellular fluorescent proteins at nanometer resolution, *Science* 313 (5793) (2006) 1642–1645, <https://doi.org/10.1126/science.1127344>.
- [11] T. Dertinger, R. Colyer, G. Iyer, S. Weiss, J. Enderlein, Fast, background-free, 3D super-resolution optical fluctuation imaging (SOFI), *Proc. Natl. Acad. Sci. U. S. A.* 106 (52) (2009) 22287–22292, <https://doi.org/10.1073/pnas.0907866106>.
- [12] O.M. Viessmann, R.J. Eckersley, K. Christensen-Jeffries, M.X. Tang, C. Dunsby, Acoustic super-resolution with ultrasound and microbubbles, *Phys. Med. Biol.* 58 (18) (2013) 6447–6458, <https://doi.org/10.1088/0031-9155/58/18/6447>.
- [13] K. Christensen-Jeffries, R.J. Browning, M.-X. Tang, C. Dunsby, R.J. Eckersley, In vivo acoustic super-resolution and super-resolved velocity mapping using microbubbles, *IEEE Trans. Med. Imaging* 34 (2) (2015) 433–440, <https://doi.org/10.1109/TMI.2014.2359650>.
- [14] P. Zhang, L. Li, L. Lin, J. Shi, L.V. Wang, In vivo superresolution photoacoustic computed tomography by localization of single dyed droplets, *Light Sci. Appl.* 8 (2019) 36, <https://doi.org/10.1038/s41377-019-0147-9>.
- [15] C. Errico, J. Pierre, S. Pezet, Y. Desailly, Z. Lenkei, O. Couture, M. Tanter, Ultrafast ultrasound localization microscopy for deep super-resolution vascular imaging, *Nature* 527 (7579) (2015) 499–502, <https://doi.org/10.1038/nature16066>.
- [16] I.M. Vellekoop, A.P. Mosk, Focusing coherent light through opaque strongly scattering media, *Opt. Lett.* 32 (16) (2007) 2309–2311, <https://doi.org/10.1364/OL.32.002309>.
- [17] J. Shi, Y. Tang, J. Yao, Advances in super-resolution photoacoustic imaging, *Quant. Imaging Med. Surg.* 8 (8) (2018) 724–732, <https://doi.org/10.21037/qims.2018.09.14>.
- [18] T.W. Murray, M. Haltmeier, T. Berer, E. Leiss-Holzinger, P. Burgholzer, Super-resolution photoacoustic microscopy using blind structured illumination, *Optica* 4 (1) (2017) 17, <https://doi.org/10.1364/OPTICA.4.000017>.
- [19] P. Burgholzer, T. Berer, J. Gruber, G. Mayr, Super-resolution thermographic imaging using blind structured illumination, *Appl. Phys. Lett.* 111 (3) (2017) 31908, <https://doi.org/10.1063/1.4995410>.
- [20] P. Burgholzer, J. Bauer-Marschallinger, H. Grün, M. Haltmeier, G. Paltauf, Temporal back-projection algorithms for photoacoustic tomography with integrating line detectors, *Inverse Probl.* 23 (6) (2007) S65–S80, <https://doi.org/10.1088/0266-5611/23/6/S06>.
- [21] L.V. Wang, *Photoacoustic Imaging and Spectroscopy*, Vol. 144 of *Optical Science and Engineering*, CRC Press, Boca Raton, 2009.
- [22] L.J. Busse, Three-dimensional imaging using a frequency-domain synthetic aperture focusing technique, *IEEE Trans. Ultrason. Ferroelectr. Freq. Control* 39 (2) (1992) 174–179, <https://doi.org/10.1109/58.139112>.
- [23] D. Lévesque, A. Blouin, C. Néron, J.-P. Monchalin, Performance of laser-ultrasonic F-SAFT imaging, *Ultrasonics* 40 (10) (2002) 1057–1063, [https://doi.org/10.1016/S0041-624X\(02\)00256-1](https://doi.org/10.1016/S0041-624X(02)00256-1).
- [24] P. Burgholzer, M. Thor, J. Gruber, G. Mayr, Three-dimensional thermographic imaging using a virtual wave concept, *J. Appl. Phys.* 121 (10) (2017) 105102, <https://doi.org/10.1063/1.4978010>.
- [25] P.C. Hansen, *Discrete Inverse Problems: Insight and Algorithms*, *Fundamentals of Algorithms*, Society for Industrial and Applied Mathematics, Philadelphia, 2010.
- [26] S. Lecheler, *Numerische Strömungsberechnung: Schneller Einstieg in ANSYS CFX 18 durch einfache Beispiele*, fourth edition, Springer Vieweg, Wiesbaden, 2017.
- [27] C. Pozrikidis, *Fluid Dynamics: Theory, Computation, and Numerical Simulation*, Springer, New York and London, 2009.
- [28] D. Finch, M. Haltmeier, Rakesh, Inversion of spherical means and the wave equation in even dimensions, *SIAM J. Appl. Math.* 68 (2) (2007) 392–412, <https://doi.org/10.1137/070682137>.
- [29] G. Paltauf, R. Nuster, K. Passler, M. Haltmeier, P. Burgholzer, Optimizing image resolution in three-dimensional photoacoustic tomography with line detectors, *SPIE Proceedings* (2008) 685621, <https://doi.org/10.1117/12.763161>.
- [30] P.C. Hansen, *Rank-Deficient and Discrete Ill-Posed Problems: Numerical Aspects of Linear Inversion/Per Christian Hansen*, *SIAM Monographs on Mathematical Modeling and Computation*, SIAM, Philadelphia, PA, 1998.
- [31] R.C. Aster, B. Borchers, C.H. Thurber, *Parameter Estimation and Inverse Problems*, third edition, Elsevier, Amsterdam, 2018.
- [32] S. Boyd, Distributed optimization and statistical learning via the alternating direction method of multipliers, *Found. Trends Mach. Learn.* 3 (1) (2010) 1–122, <https://doi.org/10.1561/22000000016>.
- [33] J. Eckstein, W. Yao, Relative-error approximate versions of Douglas-Rachford splitting and special cases of the ADMM, *Math. Program.* 170 (2) (2018) 417–444, <https://doi.org/10.1007/s10107-017-1160-5>.
- [34] P.C. Hansen, Regularization tools: a matlab package for analysis and solution of discrete ill-posed problems, *Numer. Algorithms* 6 (1) (1994) 1–35, <https://doi.org/10.1007/BF02149761>.
- [35] G. Mayr, B. Plank, J. Sekelja, G. Hendorfer, Active thermography as a quantitative method for non-destructive evaluation of porous carbon fiber reinforced polymers, *NDT & E Int.* 44 (7) (2011) 537–543, <https://doi.org/10.1016/j.ndteint.2011.05.012>.



Gregor Thummerer studied mechanical engineering at the University of Applied Science Upper Austria both bachelor and master's degree. He is currently a Ph.D. student at the Technical University Vienna. He is a research associate at the Josef Ressel Center for Thermal Non-Destructive Evaluation of Composites at FH OÖ F&E GmbH. His main research interests are thermographic defect reconstruction and parameter estimation of composite materials.



Dr. Günther Mayr, born 1981, studied sensors and microsystems at the University of Applied Sciences Upper Austria, School of Engineering. After graduating, he worked as a research assistant at FH OÖ F&E GmbH. In 2015 he completed his dissertation at the Johannes Kepler University in the field of polymer science. Since January 2018, he is the head of the Josef Ressel Center for Thermal Non-Destructive Evaluation of Composites in Wels.



Markus Haltmeier received his Ph.D. degree in mathematics from the University of Innsbruck, Tyrol, Austria, in 2007, for research on computed tomography. He was then involved in various aspects of inverse problems as a research scientist with the University of Innsbruck, the University of Vienna, Austria, and the Max Planck Institute for Biophysical Chemistry, Göttingen, Germany. Since 2012, he is full professor with the Department of Mathematics, University of Innsbruck. His current research interests include inverse problems, signal and image processing, computerized tomography, and machine learning.



Peter Burgholzer received his Ph.D. in technical science from the Johannes-Kepler-University of Linz, Austria in 1993 with a thesis on X-ray texture measurements and anisotropy of aluminum. Since 1998 he has been lecturer at the University of Applied Sciences Upper Austria. From 2000 to 2010 he was head of the Sensor Technology Department of the Upper Austrian Research. His main working area is non-destructive testing with optical methods, especially laser ultrasound, photoacoustic imaging, and optical coherence tomography. In 2008 he could habilitate on the Technical University of Vienna in Non-Destructive Testing. Since January 2010 he is scientific director of the Christian Doppler Laboratory for Photoacoustic Imaging and Laser Ultrasonics and CEO of the Research Center for Non-Destructive Testing (RECENDT).

5.2 Photothermal image reconstruction in opaque media with virtual wave backpropagation

This publication demonstrates the application of the VWC for the reconstruction of subsurface defects using 2D photothermal temperature signals acquired in the pulse-echo configuration. As described in Paper 5.1, prior information in the form of positivity and sparsity was included in the iterative regularization tool ADMM to compensate for the degradation of spatial resolution for deeper defects. However, instead of considering internal heat sources and a one-way heat diffusion process, photothermal temperature signals obtained in the pulse-echo configuration were considered, involving a two-way heat diffusion process. Since test specimens are often accessible from only one side, the application of the VWC to photothermal temperature signals acquired in the pulse-echo configuration is of great practical relevance. This publication also contains a detailed analytical description of the Abel transform and its application to 2D photothermal temperature signals. For experimental validation, a metallic specimen with artificial defects at different depths and isotropic material properties was 3D printed using a cobalt-chromium powder. To improve the thermal energy absorption at the sample surface, the sample was coated with a diamond-like carbon. The opaque sample was thermally excited using a vertical-cavity surface-emitting laser (VCSEL) array. Simultaneously, the resulting surface temperature signal was recorded with an IR camera.

The incorporation of prior information in the form of positivity and sparsity together with ADMM and subsequent evaluation with the ultrasonic reconstruction method F-SAFT enabled the detection of subsurface defects with a defect width-to-defect depth ratio of up to 0.52.

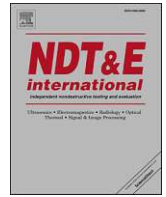
Authorship contribution statement

G. Thummerer: Conceptualization, Methodology, Software, Formal analysis, Validation, Investigation, Writing - original draft, Visualization. **G. Mayr:** Conceptualization, Methodology, Writing - review & editing, Visualization, Project administration, Funding acquisition. **P.D. Hirsch:** Validation, Investigation, Writing - original draft. **M. Ziegler:** Writing - review & editing. **P. Burgholzer:** Writing - review & editing, Supervision.



Contents lists available at ScienceDirect

NDT and E International

journal homepage: <http://www.elsevier.com/locate/ndteint>

Photothermal image reconstruction in opaque media with virtual wave backpropagation

G. Thummerer^{a,*}, G. Mayr^a, P.D. Hirsch^b, M. Ziegler^b, P. Burgholzer^c

^a Josef Ressel Centre for Thermal NDE of Composites, University of Applied Sciences Upper Austria, 4600, Wels, Austria

^b Bundesanstalt für Materialforschung und -prüfung (BAM), 12200, Berlin, Germany

^c RECENDT - Research Centre for Nondestructive Testing, 4040, Linz, Austria

ARTICLE INFO

Keywords:

Thermography
Photothermal Technique
Virtual wave concept
Image reconstruction

ABSTRACT

Thermographic reconstruction of defects that lie in the bulk of a sample is a difficult task because entropy production during heat diffusion leads to information loss. To reconstruct defects one has to solve an inverse heat conduction problem. The quality of the reconstruction is closely related to the information content of the observed data set that is reflected by the decreasing ability to spatially resolve a defect with growing defect depth. In this work we show a 2D reconstruction of rectangular slots with different width-to-depth ratios in a metallic sample. For this purpose, we apply the virtual wave concept and incorporate positivity and sparsity as prior information to overcome the diffusion-based information loss partially. The reconstruction is based on simulated and experimental pulse thermography data. In the first reconstruction step, we compute a virtual wave field from the surface temperature data. This allows us, in the second step, to use ultrasonic backpropagation methods for image reconstruction.

1. Introduction

In recent decades the number of industrial applications of the non-destructive testing method active thermography has significantly grown [1,2]. For active thermography the specimen is stimulated, e.g. by a flash lamp, laser or induction of eddy current, to obtain a temperature rise compared to the initial state. This change in temperature or more precisely the change in electromagnetic radiation in the infrared regime, is then detected on the surface of the specimen using an infrared (IR)-camera. Since defects like, e.g. cracks, have different physical properties compared to the bulk material of the specimen they can be detected. The advantages of active thermography are that large components can be quickly tested due to the focal plane array of the IR-camera. The specimen can also be inspected contactless, and the resulting images are readily assessable by non-experts.

The detected surface temperature fulfils the diffusion equation. Here, the disadvantage of thermography becomes visible. The heat diffusion equation describes an irreversible process that is characterized by entropy production, that is directly connected to information loss [3]. This loss of information is responsible for the thermal detection limit. For a spatially homogeneous and temporally Dirac-delta-like heating of a specimen there exists a basic rule for the thermal detection limit that

states: The defect diameter-to-depth ratio must be greater than 2 [1,4]. Otherwise, the defect cannot be detected reliably.

In state-of-the-art thermal NDE methods, a one-dimensional (1D) thermal model is used for depth estimation and in some cases for the characterization of the thermal resistance between the bulk material and the defect [5,6]. These 1D approaches become inaccurate for defect visualization when the inspected objects have a complex shape or the defects have a finite or irregular boundary, taking into account that the anisotropic heat conduction of composites amplifies these effects [7]. To overcome these problems, Kaipilavil and Mandelis [8] reported a depth-resolved photothermal imaging modality, the so-called truncated-correlation photothermal coherence tomography (TC-PCT), which enables a 3D visualization through the deconvolution of thermal responses from axially discrete sources. This improves the depth resolution to overcome image blurring limitations [9]. Another approach for more accuracy regarding the effects of lateral heat diffusion is the solution of the multi-dimensional heat conduction equation for a model-based image reconstruction [10]. Several studies use the finite-element method for the numerical solution of the heat conduction problems to realize the defect reconstruction [11–13]. Thermographic image reconstruction based on analytical solutions of the temperature field is applied for buried heat sources [14] and also for defects in

* Corresponding author.

E-mail address: gregor.thummerer@fh-wels.at (G. Thummerer).

<https://doi.org/10.1016/j.ndteint.2020.102239>

Received 30 October 2019; Received in revised form 7 February 2020; Accepted 17 February 2020

Available online 22 February 2020

0963-8695/© 2020 The Authors. Published by Elsevier Ltd. This is an open access article under the CC BY license (<http://creativecommons.org/licenses/by/4.0/>).

composite materials [15]. The multi-dimensional thermal wave field modelling always results in large-scale reconstruction problems, which are computationally intensive and severely ill-posed. To partly compensate for the information loss and to improve the quality of the multidimensional reconstruction, Burgholzer et al. introduced a new approach for thermographic imaging, the so-called virtual wave concept (VWC) [16]. The idea of VWC is to transform the surface temperature detected by an IR-camera into a virtual wave field. The first applications of a transformation of the diffusive electromagnetic wave into a wave field was shown by Lee et al. [17,18] and Gershenson [19] for geophysical applications. While the surface temperature fulfils the diffusion equation, the virtual wave field obeys the wave equation. In contrast to the diffusion equation, the wave equation describes a reversible process. Due to this fact, reconstruction methods well known from ultrasonic testing can be employed for 3D thermographic imaging. Thus, in principle VWC is a two-step inverse process. The first inverse problem is severely ill-posed due to information loss that is equal to the entropy production during heat diffusion.

To enhance the quality of the inverse solution one can introduce prior information, such as positivity and sparsity [20,21]. In contrast to the 1D virtual wave field, the 2D acoustic virtual wave exhibits negative data points with respect to time, hence the additional information positivity is not direct applicable. For one IR-camera pixel the information gain incorporating positivity is only a factor of two, but if we consider the n -pixel of the camera we have an information gain of 2^n . In order to apply positivity, these data sets have to be transformed. For 3D this is readily done by spherical projections that correspond to a time integral of the 3D virtual wave. In 2D, the Abel transformation or circular projection has to be applied in order to increase the information content for the regularization process [22,23]. Note, in the discrete case positivity is introduced by a simple matrix multiplication using the Abel-trafo matrix which has full rank. Hence, the inverse of the Abel-trafo matrix exists. Moreover, the prior information sparsity is introduced, because usually we have only a few defects in practise related specimens, e.g. delaminations or cracks. Consequently, we have only a few point scatterers which leads to a sparse virtual wave field. Sparsity is introduced by an appropriate formulation of the objective function using L_1 norm minimization.

In this work we show 2D reconstructions of rectangular slots in a metallic sample with different defect width-to-depth ratios. An overview of the process steps using VWC for a 2D reconstruction problem is illustrated in Fig. 1. In the first section we give an overview of the regularization and reconstruction tools used. We show how additional information can be incorporated into the regularization process. Moreover, we discuss the link between the virtual wave field and its projection on positive data points. Heat conduction simulations with the Finite Element Method (FEM) and experimental investigations based on pulsed thermography measurements are used to validate the modified virtual wave concept.

2. Virtual wave concept

Referring to the virtual wave concept (VWC), one can compute the multidimensional temperature distribution $T(\mathbf{r}, t)$ based on so-called virtual waves $T_{\text{virt}}(\mathbf{r}, t')$ for the same position vector \mathbf{r} but different time scales t and t' , respectively. According to Ref. [16], the formal relationship is given by a Fredholm integral of the first kind:

$$T(\mathbf{r}, t) = \int_{-\infty}^{\infty} K(t, t') T_{\text{virt}}(\mathbf{r}, t') dt' \quad (1)$$

$$\text{with } K(t, t') = \frac{c}{\sqrt{\pi at}} \exp\left(-\frac{c^2 t'^2}{4at}\right) \text{ for } t > 0.$$

$K(t, t')$ is the transformation kernel between temperature and virtual waves. It contains the characteristic parameters thermal diffusivity α

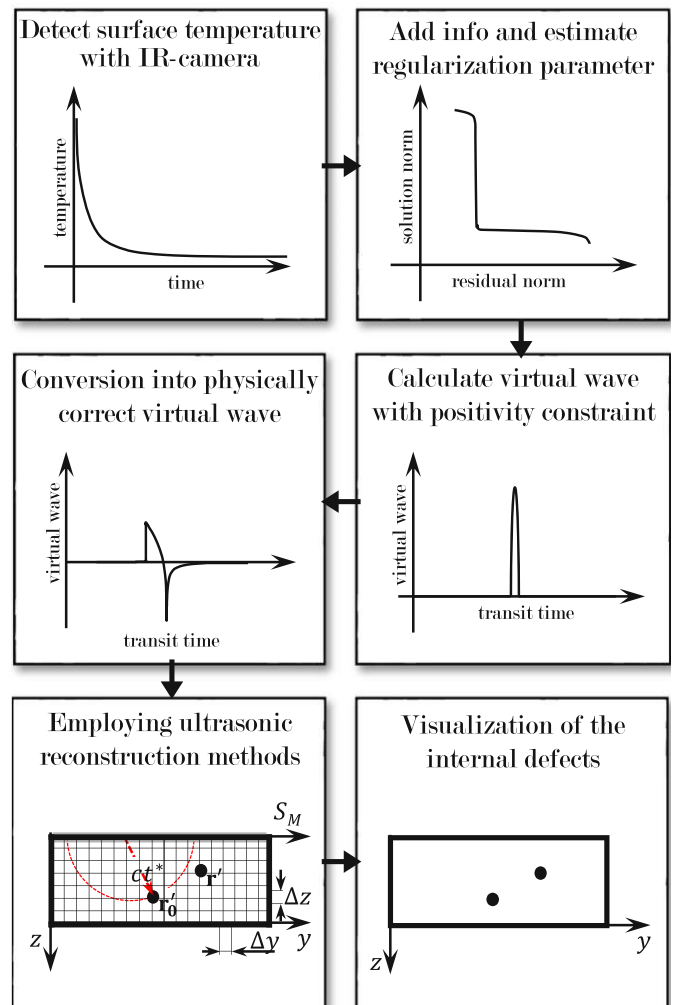


Fig. 1. Overview of the process steps using VWC for a 2D problem incorporating additional information.

and virtual speed of sound c , which describes the speed of heat and virtual wave propagation.

2.1. Incorporating positivity as prior information

Thermal diffusion causes entropy production and hence information loss. In contrast to the 1D virtual wave field [24], the 2D and 3D virtual wave fields contains negative data points. To increase the information content in the regularization process, the data set is projected via spherical or circular means onto positive data points.

In this work we consider 2D photothermal temperature data of an opaque material with embedded slots. Thermal waves are introduced at the sample surface. Simultaneously, the data is recorded on the observation plane that correspond to the sample surface. The thermal waves propagate through the solid until their flow is perturbed by the slots. Consequently, secondary thermal wave sources are introduced at the boundaries of the slots [25]. Due to the fact that the superposition principle is valid for both heat and wave equation, we can imagine the secondary thermal wave sources as accumulation of point scatterers that introduce heat in the semi infinite body. According to VWC we transform these point scatterers into an “acoustic” virtual wave. Consequently, the secondary thermal waves sources exhibit the bimodal characteristic of a 2D photoacoustic wave form (see Fig. 1 middle-left box) [26]. As one can see the 2D photoacoustic wave exhibits negative data points. In this section, we show how the bimodal virtual waves can

be projected onto a positive data set in order to incorporate positivity in the regularization process. We consider a 2D data set. The corresponding virtual wave field $T_{\text{virt}}(x, y, t)$ is described by the 2D photoacoustic wave equation:

$$\left[\Delta_{2D} - \frac{1}{c^2} \frac{\partial^2}{\partial t^2} \right] T_{\text{virt}}(x, y, t) = -\frac{1}{c^2} \frac{\partial}{\partial t} T_0(x, y) \delta(t), \quad (2)$$

where $T_0(x, y)$ is an initial temperature distribution. The solution of the wave equation is given by Ref. [27]:

$$T_{\text{virt}}(x, y, t) = \frac{\partial}{\partial t} \left[\frac{1}{2\pi c} \iint_{\sqrt{(x-x')^2 + (y-y')^2} < ct} \frac{T_0(x', y') dx' dy'}{\sqrt{c^2 t^2 - (x-x')^2 - (y-y')^2}} \right]. \quad (3)$$

Now let us consider a finite number of $n = 1, 2, \dots, N$ detection points (x^n, y^n) which are positioned on a closed or open detector curve outside the specimen. According to Ref. [28] we can write:

$$T_{\text{virt}}(x^n, y^n, t) = \frac{\partial}{\partial t} \left[\frac{1}{c} \int_0^{ct} \frac{r(M_n T_0)(x^n, y^n, r) dr}{\sqrt{c^2 t^2 - r^2}} \right]$$

with

$$(M_n T_0)(x^n, y^n, r) = \frac{1}{2\pi r} \oint_{\sqrt{(x^n-x')^2 + (y^n-y')^2} = r} T_0(x', y') dC', \quad (4)$$

where $(M_n T_0)(x^n, y^n, r)$ are the circular means of T_0 at detection point (x^n, y^n) with radius r . Eq. (4) is of Abel-type and can be written as

$$T_{\text{virt}}(x^n, y^n, t) = \frac{\partial}{\partial t} \frac{1}{c} \mathcal{A}\{(M_n T_0)(x^n, y^n, r)\} \quad (5)$$

$$\text{with } \mathcal{A}\{(M_n T_0)(x^n, y^n, r)\} = \int_0^{ct} \frac{r(M_n T_0)(x^n, y^n, r) dr}{\sqrt{c^2 t^2 - r^2}}$$

Herein, $\mathcal{A}\{\cdot\}$ is the Abel transformation operator. Based on the inverse Abel transformation the circular means $(M_n T_0)(x^n, y^n, r)$ can be calculated explicitly [22,28]:

$$(M_n T_0)(x^n, y^n, r) = \frac{2c}{\pi} \int_0^{r/c} \frac{T_{\text{virt}}(x^n, y^n, t') dt'}{\sqrt{r^2 - c^2 t'^2}}. \quad (6)$$

Due to Eq. (5) we can see that the projection onto positive data points (the circular means) and the virtual wave field, which fulfils the 2D wave equation, are connected by the Abel transformation. The Abel transformation relates the computed virtual wave signals, that are a function of time, to its circular projection and consequently to the circular integrals of a photothermal source with radius r and center point (x^n, y^n) .

2.2. Discrete data

Let us consider the *Fredholm* integral of the first kind, shown Eq. (2). Due to the fact that thermography data is discrete in time and space, Eq. (2) is first discretized:

$$\mathbf{T} = \mathbf{K} \mathbf{T}_{\text{virt}}. \quad (7)$$

The aim is to calculate \mathbf{T}_{virt} based on the measured temperature field \mathbf{T} . This is a severely ill-posed inverse problem. To incorporate additional information the inverse problem must be reformulated. Therefore, we compute the circular projections of the virtual wave \mathbf{T}_{virt} with respect to Eq. (5) with the inverse *Abel*-trafo matrix \mathbf{A}^{-1} in the following manner [22]:

$$\mathbf{M}_{\text{virt}} = \mathbf{A}^{-1} \mathbf{T}_{\text{virt}}. \quad (8)$$

Consequently, we can substitute \mathbf{T}_{virt} by $\mathbf{A} \mathbf{M}_{\text{virt}}$ in Eq. (7). This yields

the new inverse problem

$$\mathbf{T} = \mathbf{K} \mathbf{A} \mathbf{M}_{\text{virt}} = \bar{\mathbf{K}} \mathbf{M}_{\text{virt}} \quad (9)$$

with $\bar{\mathbf{K}} = \mathbf{K} \mathbf{A}$.

Note, the discrete *Abel*-trafo matrix already respects the time derivative $\frac{\partial}{\partial t}$ in Eq. (5).

2.3. Solve the inverse problem

Computing the circular projection \mathbf{M}_{virt} with positivity constraint based on the linear matrix equation Eq. (9) is a severely ill posed inverse problem. Therefore, we need some kind of regularization to get an appropriate solution for \mathbf{M}_{virt} . Basically, one can distinguish direct and iterative regularization methods. Here we use the alternating direction method of multipliers (ADMM) [29,30], that is an iterative regularization scheme to incorporate the additional information sparsity. The intention of ADMM is to split the objective function and to introduce a constraint. The following objective function is minimized [21].

$$\frac{1}{2} \left\| \bar{\mathbf{K}} \mathbf{M}_{\text{virt}} - \mathbf{T} \right\|_2^2 + \lambda \left\| \mathbf{M}_{\text{virt}} \right\|_1 \quad (10)$$

subject to $\mathbf{M}_{\text{virt}} - \mathbf{z} = 0$

In Eq. (10) the 2-norm represents the residual norm and the 1-norm represents the solution norm. The 1-norm incorporates sparsity, so we assume that the solution matrix is sparse. λ is a regularization parameter, that can be determined e.g. by the *L-curve*-method [31]. To get an iterative procedure we form the *Lagrangian* using the objective function and the constraint. The optimization of the dependent variables yields the subsequent iteration steps [21]:

$$\begin{aligned} \mathbf{M}_{\text{virt}}^{k+1} &:= (\bar{\mathbf{K}}^T \bar{\mathbf{K}} + \rho \mathbf{I})^{-1} [\bar{\mathbf{K}}^T \mathbf{T} + \rho(\mathbf{z}^k - \mathbf{u}^k)] \\ \mathbf{z}^{k+1} &:= S_{\lambda/\rho}(\mathbf{M}_{\text{virt}}^{k+1} + \mathbf{u}^k) \\ \mathbf{u}^{k+1} &:= \mathbf{u}^k + \mathbf{M}_{\text{virt}}^{k+1} - \mathbf{z}^{k+1}. \end{aligned} \quad (11)$$

In Eq. (11) ρ is a penalty parameter, that makes the algorithm faster and more robust. $S_{\lambda/\rho}$ is a soft-threshold operator. The thresholding is applied only onto positive entries. Negative entries are set to zero, hence positivity is enforced. The \mathbf{u} vector contains the *Lagrangian* multipliers.

2.4. Image reconstruction

The use of image reconstruction techniques is intended to simplify the interpretation of the measurement result and to increase the signal-to-noise (SNR) ratio. This makes inner structures visible, which cannot be found in the classic B-scan image. To improve the sensitivity and resolution of the virtual wave field, we use the synthetic aperture focusing technique (SAFT) [32,33]. The principle of time domain (T)-SAFT is depicted in Fig. 2.

Thermography allows the simultaneous acquisition of a large number of signals (up to 10^6) over the surface of a test specimen, which is equivalent to a large aperture. In the case of optically excited pulsed thermography the generation and detection of the virtual waves are focused on the same location on the surface ($z = 0$). The virtual wave field originates from every point of the surface simultaneously as a plane wave. A diffraction source, e.g. the tip of a defect, is located at a position \mathbf{r}' inside the specimen (Fig. 2). This disturbance re-radiates the virtual wave field originating from the specimen surface with a time delay. The theoretical scattering hyperbola can be calculated for each voxel with the coordinates (x', y', z') if the speed of sound c is known. Along this curve, an integration of the scalar measurement data T_{virt} is then carried out:

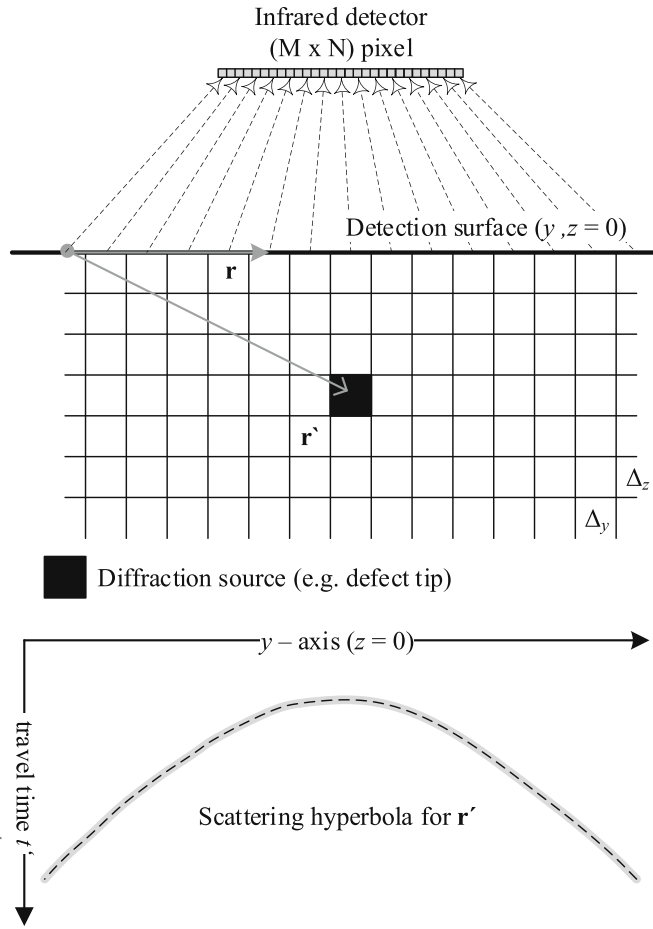


Fig. 2. Principle of T-SAFT.

$$T_0(x', y', z') = \iint_{S_M} T_{\text{virt}}(x, y, 0, t') dx dy \quad (12)$$

with $t' = 2 \frac{\sqrt{(x-x')^2 + (y-y')^2 + (z-z')^2}}{c}$.

In principle T-SAFT is a trial and error method [34]. The assumption is that any defect consists of a number of independent (discrete) point diffraction sources. So, in the first step, the reconstruction space (sample volume) is discretized with $\Delta_y = \Delta_z$. We prescribe any discrete point \mathbf{r}' . If this point is equal to \mathbf{r} , the integral of Eq. (12), or in discrete cases, the sum yields a high value. Otherwise the value is low. Performing this operation for each point \mathbf{r}' gives the final reconstruction image. In this work we apply frequency domain (F)-SAFT. Here, the virtual wave field is transferred into Fourier domain for time and space. The F-SAFT procedure gives the same results as T-SAFT [34], but the F-SAFT method is much faster than T-SAFT [35].

3. Numerical simulation

To test the virtual wave concept with noisy temperature data by respecting prior information, numerical simulation with the FEM are carried out. To do this we consider the 2D model, depicted in Fig. 4 a). The specimen has a length of 100 mm and a height of 10 mm. All boundaries have adiabatic conditions. The slots of the investigated specimen have a width of 3 mm and a height of 0.5 mm with a horizontal distance of $\Delta_y = 10$ mm. The vertical distances with respect to the inspected surface ($z = 0$) are $z_i = (1.75 + i)$ mm ($i = 0, 1, \dots, 6$). The corresponding defect width-to-depth ratios are sketched in Fig. 4 a). The objective of the FEM simulations is the solution of the direct problem to

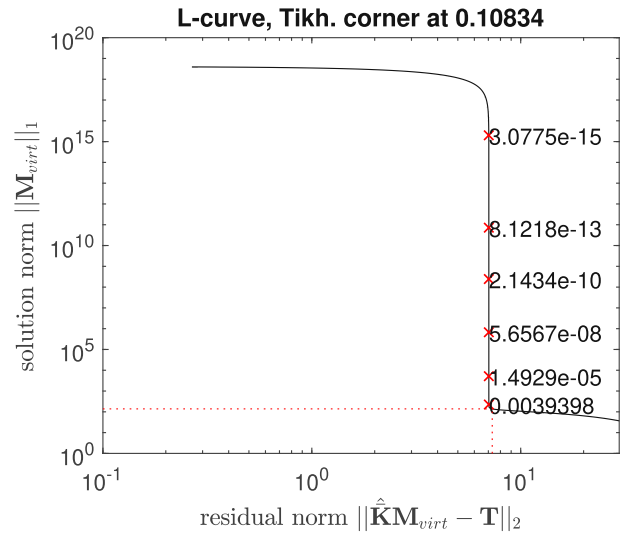


Fig. 3. The regularization parameter λ is found at the edge of the L-Curve. At the edge the best trade off between solution norm and residual norm is located [37]. For the preparation of the L-curve, the Toolbox of [36] was used.

determine the transient temperature field $T(y, z, t)$ in the region of the slots. The initial temperature $T(y, z, t = 0)$ is zero. The plane $z = 0$ is heated with an instantaneous and locally uniform pulse. An appropriate simulation time was estimated by $t_{\text{end}} = L^2/\alpha$. The physical parameters are listed in Table 1. Since the virtual speed of sound c can be chosen arbitrarily, we prescribed the dimensionless virtual speed of sound with $\tilde{c} = 1$.

The time resolution Δ_t was $2e-3$ s. The temperature data \mathbf{T} that is depicted in 4 a), was evaluated at $z = 0$ with an equidistant grid and $N_y = 564$ data points. Additionally, the surface temperature was superposed by white Gaussian noise with a standard deviation of $\sigma_0 = 0.0097$ K in order to achieve the same signal to noise ratio $\text{SNR} = \max(\mathbf{T})/\sigma_0$ as for the experimental temperature field. Referring to Fig. 1, the \mathbf{K} -matrix is set up using the physical parameters listed in Table 1 and the corresponding spatial and temporal resolution. This matrix has to be multiplied by the Abel trafo matrix \mathbf{A} in order to incorporate the additional information positivity. Next, the regularization parameter λ has to be estimated based on the observed temperature data. Therefore, the L-curve method, Fig. 3, is applied. For the preparation of the L-curve the toolbox of [36] was used. For the regularization process applying ADM, we prescribe the penalty term ρ with 0.0039. Subsequently, the linear severely ill posed problem, namely the calculation of the virtual wave field based on temporal surface temperature data, is solved.

The solution of the inverse problem yields the circular projection \mathbf{M}_{virt} of the 2D virtual wave field \mathbf{T}_{virt} . Due to this, \mathbf{M}_{virt} is multiplied by the Abel-trafo matrix \mathbf{A} to obtain the physically correct 2D virtual wave. The resulting virtual wave field is illustrated in Fig. 4 b). The illustration can be interpreted as superposition of point scatterers. A point scatterer yields a characteristic hyperbola (see Fig. 2), that is rudimentary visible for the first three slots with the highest width-to-depth ratios. In Fig. 5 A-Scans, where virtual waves for different slot positions are represented as a function of depth $z = c \cdot t'$, are shown. The graphs exhibit a good approximation of the typical 2D wave form.

Referring to Eq. (12), \mathbf{T}_{virt} is the input for the image reconstruction tool F-SAFT. Since the heat was introduced at $z = 0$, the heat or virtual wave travels to the defect where it is reflected to the surface. Hence, to obtain the correct position of the defect we have to halve the distance or the dimensionless speed of sound $\tilde{c} = 0.5$ for F-SAFT. Fig. 4 d) shows the final image. Let us compare the processed images using the virtual wave concept Fig. 4 c) and the image reconstruction Fig. 4 d). It is visible that F-SAFT improves both sensitivity and the lateral resolution and slots with a defect width-to-depth ratio of 0.52 are detectable. The defect

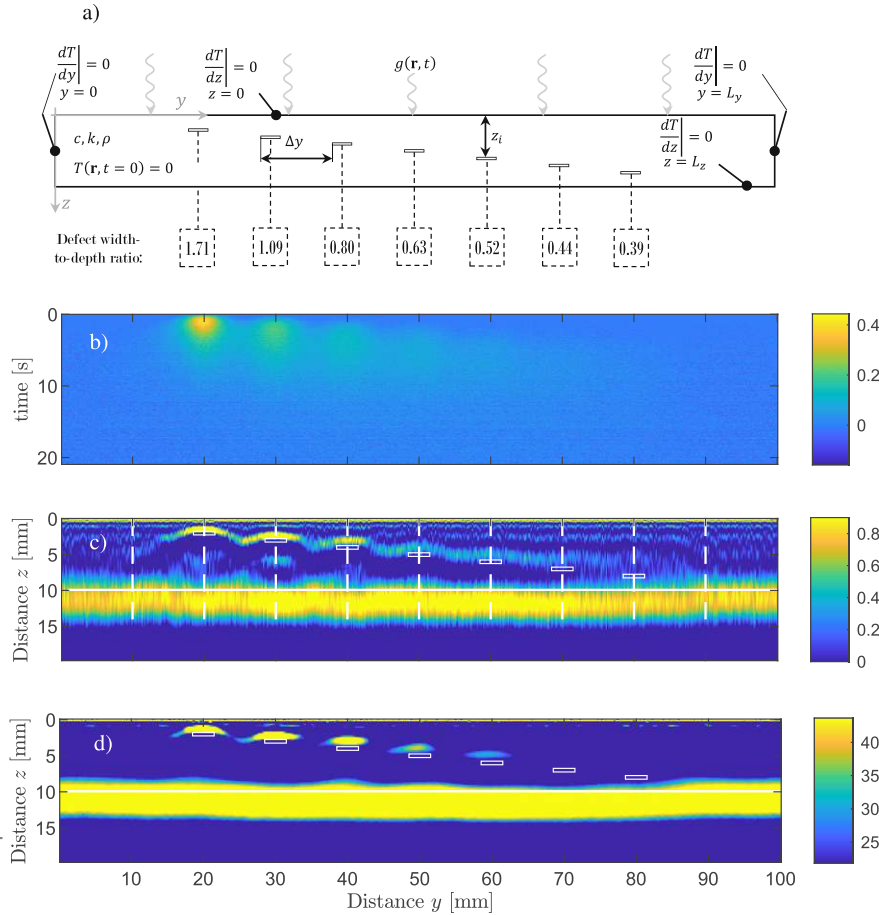


Fig. 4. a) Image reconstruction based on simulated data. Model of the examined specimen with the corresponding boundary conditions. b) Running temperature contrast [1] based on simulated temperature data that is superposed with white Gaussian noise (standard deviation $\sigma = 0.0097$). c) Dimensionless virtual wave field (B-Scan) computed using ADMM and the Abel transformation related to the maximal data point as function of spatial coordinates y, z . d) Reconstructed field computed applying F-SAFT as function of spatial coordinates y, z . The colorbars have the unit Kelvin.

Die approbierte gedruckte Originalversion dieser Dissertation ist an der TU Wien Bibliothek verfügbar. The approved original version of this doctoral thesis is available in print at TU Wien Bibliothek.

TU BIBLIOTHEK
WIEN
Your knowledge hub

Table 1
Physical parameters for FEM simulation.

Parameter	Value	Unit
thermal conductivity k	15	$\text{W m}^{-1} \text{K}^{-1}$
density ρ_M	7800	kg m^{-3}
specific heat capacity c_p	500	$\text{J kg}^{-1} \text{K}^{-1}$
thermal diffusivity α	$3.85\text{e-}06$	$\text{m}^2 \text{s}^{-1}$

depths were estimated using an A-Scan based on circular projection (Fig. 5 a). For the estimation of the defect depths the local maxima after the front-wall echo was evaluated, because these maxima correspond to the reflection at the slot boundaries. The corresponding virtual wave field is shown in Fig. 5 b).

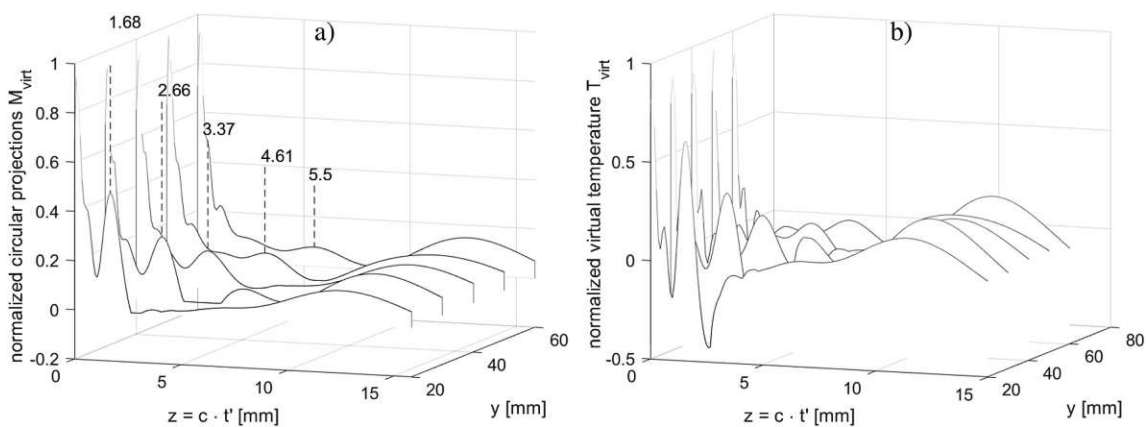


Fig. 5. a) Waterfall plot of the circular projections based on simulated temperature data for different slot positions according to the white dashed line in Fig. 7 b). The numerical markers show the estimated position of the slots. b) Waterfall plot of the Abel transformed circular means or virtual wave field. At $z = 0$ the initial pulse and at $z = L$ the back-wall echo occurs that is denoted by a raise of amplitude. For a defect (slot) an additional virtual wave amplitude occurs at different depths $z = c \cdot t'$.

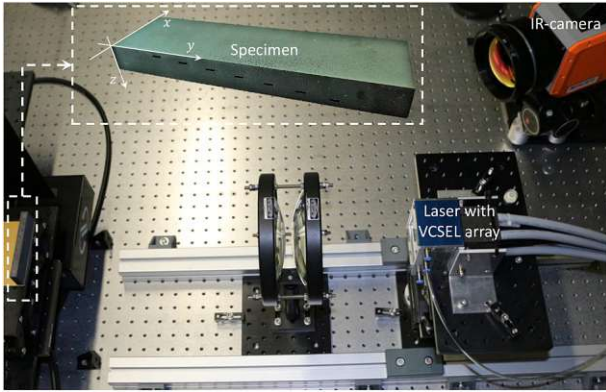


Fig. 6. Metallic specimen (100 mm × 30 mm × 10 mm) with rectangular slots representing defects.

4. Experimental results

4.1. Experimental setup

In order to test the virtual wave concept for pulsed thermography data, we have prepared a metallic specimen with slots representing defects (Fig. 6). The [100 mm × 30 mm × 10 mm] specimen was produced using a cobalt-chromium alloy powder for metal additive manufacturing, also known as metal 3D printing. Additionally, the specimen was coated by diamond-like carbon (DLC). Due to this, the absorption of the flash light radiation and the emissivity is increased. The coating thickness is approximately 7 μm. Therefore, we can assume that the optical material properties of the specimen are homogeneous and isotropic.

In addition to the sample, the experimental setup (see Fig. 6) essentially consists of a laser array for heating and an infrared thermography camera for surface temperature measurement. The laser array is a VCSEL (Vertical-Cavity Surface-Emitting Laser) array with a nominal output power of 2.4 kW [38]. The emitting aperture was imaged onto the sample ($x - y$ plane @ $z = 0$) using a pair of lenses (distance

laser lens approx. 155 mm, distance lens sample approx. 398 mm). The image was slightly defocused to achieve a homogeneous irradiance of $14 \pm 1 \text{ W/cm}^2$ of the entire sample surface, the magnification corresponds to approximately 2.3. The laser was controlled by Labview with pulse lengths of 50 ms. The actual pulse shape was measured using a photodiode and was 50 ms. It was stored frame synchronously in the additional A/D channels of the camera. The temperature-calibrated infrared thermography camera used (InSb-based, 2.5–5.5 μm spectral sensitivity, 100 mm lens, 200 μs integration time) was triggered by the laser pulse with a pretrigger of 1000 frames via the photodiode. In each measurement, 21000 frames were recorded at a frame rate of 1000 Hz, i.e. 1 s before the laser pulse and 20 s after it. The image was taken in full frame mode of 640×512 pixels with a spatial resolution of approx. 177 μm per pixel.

4.2. Experimental results

In Fig. 7 a) the measured transient surface temperature is depicted. For the image reconstruction, the mean of 100 surface temperature slices between the pixels 46:145 in x-direction (see Fig. 6) was calculated in order to improve the signal-to-noise ratio. The data set was then temporally downsampled, yielding an evaluation frequency of 500 Hz. The spatial resolution, the physical parameters and the signal to noise ratio $\text{SNR} = \max(\mathbf{T})/\sigma_M$, where σ_M is the standard deviation of the measurement data, are equal to the simulated data set (Table 1). The process steps listed in Fig. 1 were then applied again. The corresponding virtual wave field T_{virt} is illustrated in Fig. 7 b). Fig. 8 a) illustrates the circular means of the virtual waves for the different slot positions, indicated in Fig. 7 b) by white dashed lines. Fig. 8 b) shows the corresponding virtual waves. At $z = c \cdot t' = 0$ the characteristic initial pulse and at $z = L$ the back-wall echo occur. In the center position of the slots $y = \{20, 30, 40, 50, 60\}$ mm an additional peak occurs in the A-Scan. This is because the virtual wave is diffracted at the slot boundaries. The nominal and estimated slot depths using VWC, based on simulated and measurement data, are visible in Fig. 9. The black-dashed line shows the nominal values and is a guide for the eyes. This representation shows, that the slot positions can be detected well, for both simulated and measurement data. For the slot reconstruction based on simulated data,

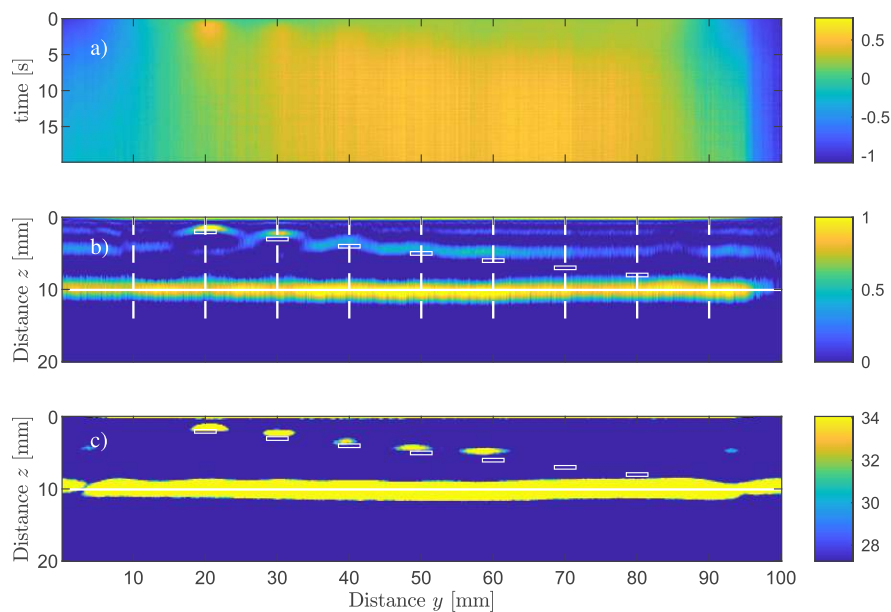


Fig. 7. Image reconstruction based on experimental data. Running temperature contrast based on measured temperature data a), calculated virtual wave field b) using ADMM and reconstructed field applying F-SAFT c). The colorbars have the unit Kelvin.

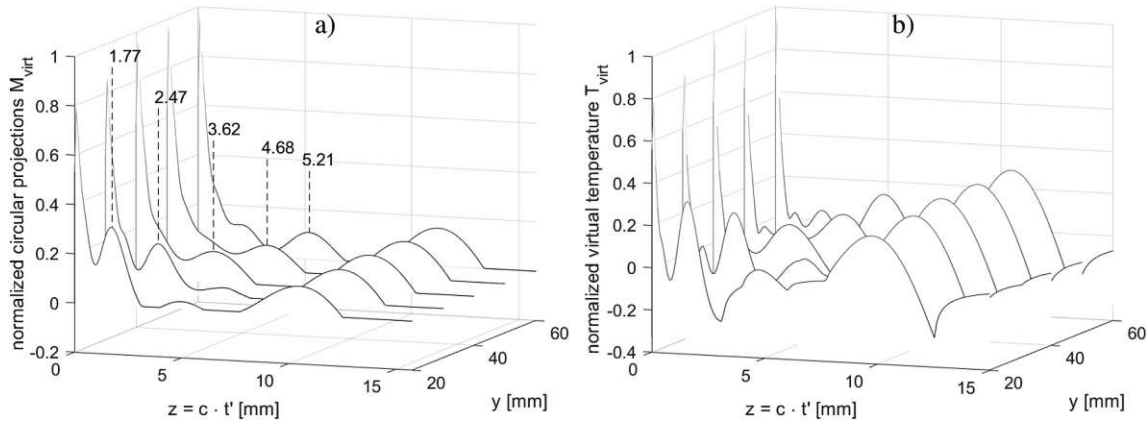


Fig. 8. a) Waterfall plot of the circular projections based on experimental temperature data for different slot positions according to the white dashed line in Fig. 7 b). The numerical markers show the estimated position of the slots. b) Waterfall plot of the Abel transformed circular means or virtual wave field. At $z = 0$ the initial pulse and at $z = L$ the back-wall echo occurs that is denoted by a raise of amplitude. For a defect (slot) an additional virtual wave amplitude occurs at different depths $z = c \cdot t'$.

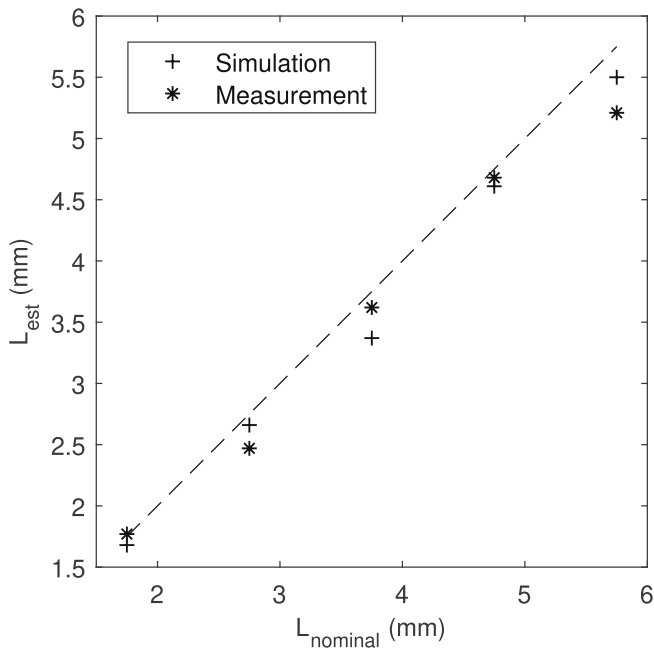


Fig. 9. Nominal positions versus estimated positions for the detectable slots. The black-dashed line indicates the nominal values and is a guide for the eyes. The plus sign exhibits the estimation for simulated data and the asterisk represents the estimated values for the measurement.

we can see a lower intensity of the secondary heat sources for deeper lying defects. The reason for this might result from the growing influence of the back-wall, more precisely from the corresponding boundary. Considering the simulated data we have adiabatic boundaries, which cause a stronger reflection at the back-wall than for measurement data were the boundaries slightly differ from adiabatic boundaries because of heat convection. Consequently, in contrast to the measurement data, the heat flow in the domain of the deeper lying slots of the simulated data is more affected by the back-wall reflection. We can detect the slots (defects) with a defect width-to-depth ratio of 0.52. Fig. 7 c) depicts the final reconstruction applying F-SAFT to the virtual wave field 7 b). In contrast to the transient virtual wave field the final reconstruction exhibits a much better localization of the slots (defects).

5. Conclusion

In this paper, we have shown an application of the virtual wave concept for 2D pulsed thermography data in reflection mode. Heat diffusion causes entropy production and hence information loss. To compensate the information loss partly, we have incorporated additional information for the regularization process. For the incorporation of positivity as additional information, we have applied the Abel transformation. Here the 2D virtual wave is projected onto a positive data set. Due to this, the inverse problem was reformulated, which yields a new ill-posed inverse problem.

The thermal waves were locally transformed into virtual waves which obey the photoacoustic wave equation. Based on this so called virtual waves, the depth of the slots are detectable by the application of the time of flight method (TOF). Further, we can apply image reconstruction methods from ultrasonic testing. Especially, the F-SAFT algorithm was used for defect reconstruction. The 2D heat diffusion in the region of the slot is respected by the integration along the scattering hyperbolas of the superposed point scatterers. The modified VWC reconstruction based on simulated data was validated with a reconstruction based on experimental data.

Declaration of competing interest

The authors declare that there is no conflict of interest.

CRediT authorship contribution statement

G. Thummerer: Conceptualization, Methodology, Software, Formal analysis, Validation, Investigation, Writing - original draft, Visualization. **G. Mayr:** Conceptualization, Methodology, Writing - original draft, Writing - review & editing, Visualization, Project administration, Funding acquisition. **P.D. Hirsch:** Validation, Investigation, Writing - original draft. **M. Ziegler:** Writing - review & editing. **P. Burgholzer:** Writing - review & editing, Supervision.

Acknowledgement

The financial support by the Austrian Federal Ministry of Science, Research and Economy and the National Foundation for Research, Technology and Development is gratefully acknowledged. Furthermore, this work has been supported by the project "multimodal and in-situ characterization of inhomogeneous materials" (MiCi), by the federal government of Upper Austria and the European Regional Development Fund (EFRE) in the framework of the EU-program IWB2020.

Gefördert durch die Deutsche Forschungsgemeinschaft (DFG) - German Research Foundation) - 400857558.
400857558, funded by the Deutsche Forschungsgemeinschaft (DFG),

Appendix. 1. Forward problem

The aim of the subsequent steps is to solve the forward problem in two dimensions and free space (without boundaries), based on the 3D virtual Greens function $G_{\text{virt}}^{3D}(\mathbf{r}, t)$, in order to get a deeper insight how the virtual wave concept works. Therefore, we use the Greens function solution equation (GFSE) for both, diffusion and wave equation [39]. Inserting the respective GFSEs into Eq. (1), yields for the same position vector \mathbf{r} in 3D

$$G^{3D}(\mathbf{r}, t) = \int_{-\infty}^{\infty} K(t, t') G_{\text{virt}}^{3D}(\mathbf{r}, t') dt' \quad (1)$$

and

$$G^{2D}(\boldsymbol{\rho}, t) = \int_{-\infty}^{\infty} K(t, t') G_{\text{virt}}^{2D}(\boldsymbol{\rho}, t') dt' \quad (2)$$

in 2D with position vector $\boldsymbol{\rho}$. To calculate $G^{2D}(\boldsymbol{\rho}, t)$ we need the 2D virtual Greens function $G_{\text{virt}}^{2D}(\boldsymbol{\rho}, t')$. Hence, we start from the 3D virtual Greens function

$$G_{\text{virt}}^{3D}(\mathbf{r}, t' | \mathbf{r}', \tau') = \frac{1}{4c\pi} \frac{\partial}{\partial t'} \frac{\delta[c(t' - \tau') - |\mathbf{r} - \mathbf{r}'|]}{|\mathbf{r} - \mathbf{r}'|}. \quad (3)$$

To get the 2D Greens function we carry out the integration with respect to z' :

$$\begin{aligned} G_{\text{virt}}^{2D}(\boldsymbol{\rho}, t' | \boldsymbol{\rho}', \tau') &= \int_{-\infty}^{\infty} G_{\text{virt}}^{3D}(\mathbf{r}, t' | \mathbf{r}', \tau') dz' \\ &= \frac{1}{4c\pi} \frac{\partial}{\partial t'} \int_{-\infty}^{\infty} \frac{\delta[c(t' - \tau') - \sqrt{|\boldsymbol{\rho} - \boldsymbol{\rho}'|^2 + z'^2}]}{\sqrt{|\boldsymbol{\rho} - \boldsymbol{\rho}'|^2 + z'^2}} dz' \end{aligned} \quad (4)$$

$$\text{with } |\boldsymbol{\rho} - \boldsymbol{\rho}'| = \sqrt{(x - x')^2 + (y - y')^2}$$

Now substitute $\mu = \sqrt{|\boldsymbol{\rho} - \boldsymbol{\rho}'|^2 + z'^2}$ and use symmetry with respect to the z' axes yields:

$$G_{\text{virt}}^{2D}(\boldsymbol{\rho}, t' | \boldsymbol{\rho}', \tau') = \frac{1}{2c\pi} \frac{\partial}{\partial t'} \int_{|\boldsymbol{\rho} - \boldsymbol{\rho}'|}^{\infty} \frac{\delta[c(t' - \tau') - \mu]}{\sqrt{\mu^2 - |\boldsymbol{\rho} - \boldsymbol{\rho}'|^2}} d\mu = \frac{1}{2c\pi} \frac{\partial}{\partial t'} \frac{1}{\sqrt{c^2(t' - \tau')^2 - |\boldsymbol{\rho} - \boldsymbol{\rho}'|^2}} = \frac{-c^2(t' - \tau')}{2c\pi [c^2(t' - \tau')^2 - |\boldsymbol{\rho} - \boldsymbol{\rho}'|^2]^{3/2}} \text{ for } t' > \tau' - \frac{1}{c} |\boldsymbol{\rho} - \boldsymbol{\rho}'| = \gamma. \quad (5)$$

Inserting Eq. (5) into Eq. (2) gives:

$$G^{2D}(\boldsymbol{\rho}, t | \boldsymbol{\rho}', \tau') = \frac{\pi^{-3/2}}{2\sqrt{at}} \int_{\gamma}^{\infty} \frac{\exp\left(-\frac{c^2(t' - \tau')^2}{4at}\right) c^2(\tau' - t') dt'}{[c^2(t' - \tau')^2 - |\boldsymbol{\rho} - \boldsymbol{\rho}'|^2]^{3/2}} = -\frac{\exp\left(\frac{-|\boldsymbol{\rho} - \boldsymbol{\rho}'|^2}{4at}\right)}{2\pi^{3/2}\sqrt{at}} \int_{\gamma}^{\infty} \frac{\exp\left(\frac{-c^2(t' - \tau')^2 + |\boldsymbol{\rho} - \boldsymbol{\rho}'|^2}{4at}\right) c^2(\tau' - t') dt'}{[c^2(t' - \tau')^2 - |\boldsymbol{\rho} - \boldsymbol{\rho}'|^2]^{3/2}}. \quad (6)$$

Now we substitute $\xi^2 = c^2(t' - \tau')^2 - |\boldsymbol{\rho} - \boldsymbol{\rho}'|^2$:

$$G^{2D}(\boldsymbol{\rho}, t | \boldsymbol{\rho}', \tau') = -\frac{\exp\left(\frac{-|\boldsymbol{\rho} - \boldsymbol{\rho}'|^2}{4at}\right)}{2\pi^{3/2}\sqrt{at}} \int_0^{\infty} \frac{\exp\left(\frac{-\xi^2}{4at}\right) d\xi}{\xi^2} = -A \int_0^{\infty} \frac{\exp\left(\frac{-\xi^2}{4at}\right) d\xi}{\xi^2}. \quad (7)$$

Integration by parts yields:

$$\frac{G^{2D}(\boldsymbol{\rho}, t | \boldsymbol{\rho}', \tau')}{A} = 2 \int_0^{\infty} \frac{\exp\left(\frac{-\xi^2}{4at}\right)}{4at} d\xi = \sqrt{4\pi at} \operatorname{erf}\left(\frac{\xi^2}{\sqrt{4at}}\right) \Big|_0^{\infty} = \frac{\sqrt{\pi}}{\sqrt{4at}} \quad (8)$$

Replacing A in Eq. (8) gives:

$$G^{2D}(\boldsymbol{\rho}, t | \boldsymbol{\rho}', \tau') = A \frac{\sqrt{\pi}}{\sqrt{4at}} = \frac{\exp\left(\frac{-|\boldsymbol{\rho} - \boldsymbol{\rho}'|^2}{4at}\right)}{2\pi^{3/2}\sqrt{at}} \frac{\sqrt{\pi}}{\sqrt{4at}} = \frac{1}{4\pi at} \exp\left(\frac{-|\boldsymbol{\rho} - \boldsymbol{\rho}'|^2}{4at}\right) \quad (9)$$

This is exactly the Greens function for a 2D body with infinite extension [40]. We note, that the Greens function for heat conduction in 2D and free space is deductible by VWC. Applying the method of images, Eq. (9) is readily extended for Dirichlet and Neumann boundaries or a mix of them [41].

References

- [1] Maldague XPV. *Theory and practice of infrared technology for nondestructive testing*. New York and Chichester: A Wiley-Interscience publication, Wiley; 2001.
- [2] Vavilov VP, Burleigh DD. Review of pulsed thermal ndt: physical principles, theory and data processing. *NDT E Int* 2015;73:28–52. <https://doi.org/10.1016/j.ndteint.2015.03.003>.
- [3] Burgholzer P. Thermodynamic limits of spatial resolution in active thermography. *Int J Thermophys* 2015;36(9):2328–41. <https://doi.org/10.1007/s10765-015-1890-7>.
- [4] Almond DP, Pickering SG. An analytical study of the pulsed thermography defect detection limit. *J Appl Phys* 2012;111(9):093510. <https://doi.org/10.1063/1.4704684>.
- [5] Oswald-Tranta B. Time and frequency behaviour in tsr and ppt evaluation for flash thermography. *Quant InfraRed Thermogr J* 2017;14(2):164–84. <https://doi.org/10.1080/17686733.2017.1283743>.
- [6] Ranjit S, Choi M, Kim W. Quantification of defects depth in glass fiber reinforced plastic plate by infrared lock-in thermography. *J Mech Sci Technol* 2016;30(3):1111–8. <https://doi.org/10.1007/s12206-016-0215-5>.
- [7] Liu JY, Gong JL, Qin L, Guo B, Wang Y. Three-dimensional visualization of subsurface defect using lock-in thermography. *Int J Thermophys* 2015;36(5–6):1226–35. <https://doi.org/10.1007/s10765-014-1717-y>.
- [8] Kaipravil S, Mandelis A. Truncated-correlation photothermal coherence tomography for deep subsurface analysis. *Nat Photon* 2014;8(8):635–42. <https://doi.org/10.1038/NPHOTON.2014.111>.
- [9] Tavakolian P, Sivagurunathan K, Mandelis A. Enhanced truncated-correlation photothermal coherence tomography with application to deep subsurface defect imaging and 3-dimensional reconstructions. *J Appl Phys* 2017;122(2):023103. <https://doi.org/10.1063/1.4992807>.
- [10] Orlande HRB. *Thermal measurements and inverse techniques*, Heat transfer. Boca Raton, FL: CRC Press; 2011.
- [11] Richter R, Maierhofer C, Kreutzbruck M. Numerical method of active thermography for the reconstruction of back wall geometry. *NDT E Int* 2013;54:189–97. <https://doi.org/10.1016/j.ndteint.2012.10.010>.
- [12] Dizeu FBD, Laurendeau D, Bendada A. Non-destructive testing of objects of complex shape using infrared thermography: rear surface reconstruction by temporal tracking of the thermal front. *Inverse Probl* 2016;32(12):125007. <https://doi.org/10.1088/0266-5611/32/12/125007>.
- [13] Pawar SS, Vavilov VP. Applying the heat conduction-based 3d normalization and thermal tomography to pulsed infrared thermography for defect characterization in composite materials. *Int J Heat Mass Tran* 2016;94:56–65. <https://doi.org/10.1016/j.ijheatmasstransfer.2015.11.018>.
- [14] Mendioroz A, Martínez K, Celorrio R, Salazar A. Characterizing the shape and heat production of open vertical cracks in burst vibrothermography experiments. *NDT E Int* 2019;102:234–43. <https://doi.org/10.1016/j.ndteint.2018.12.006>.
- [15] Holland SD, Schiefelbein B. Model-based inversion for pulse thermography. *Exp Mech* 2019;59(4):413–26. <https://doi.org/10.1007/s11340-018-00463-2>.
- [16] Burgholzer P, Thor M, Gruber J, Mayr G. Three-dimensional thermographic imaging using a virtual wave concept. *J Appl Phys* 2017;121(10):105102. <https://doi.org/10.1063/1.4978010>.
- [17] Lee KH, Liu G, Morrison HF. A new approach to modeling the electromagnetic response of conductive media. *Geophysics* 1989;54(9):1180–92. <https://doi.org/10.1190/1.1442753>.
- [18] Lee KH, Xie G. A new approach to imaging with low-frequency electromagnetic fields. *Geophysics* 1993;58(6):780–96. <https://doi.org/10.1190/1.1443464>.
- [19] Gershenson M. Simple interpretation of time-domain electromagnetic sounding using similarities between wave and diffusion propagation. *Geophysics* 1997;62(3):763–74. <https://doi.org/10.1190/1.1444186>.
- [20] Hansen PC. *Rank-deficient and discrete ill-posed problems: numerical aspects of linear inversion*/Per Christian Hansen, SIAM monographs on mathematical modeling and computation. Philadelphia, Pa.: SIAM; 1998.
- [21] Aster RC, Borchers B, Thurber CH. *Parameter estimation and inverse problems*. third ed. Edition. Amsterdam: Elsevier; 2018.
- [22] Burgholzer P, Bauer-Marschallinger J, Grün H, Haltmeier M, Paltauf G. Temporal back-projection algorithms for photoacoustic tomography with integrating line detectors. *Inverse Probl* 2007;23(6):S65–80. <https://doi.org/10.1088/0266-5611/23/6/S06>.
- [23] Finch D, Haltmeier M, Rakesh. Inversion of spherical means and the wave equation in even dimensions. *SIAM J Appl Math* 2007;68(2):392–412. <https://doi.org/10.1137/070682137>.
- [24] Mayr G, Stockner G, Plasser H, Hendorfer G, Burgholzer P. Parameter estimation from pulsed thermography data using the virtual wave concept. *NDT E Int* 2018;100:101–7. <https://doi.org/10.1016/j.ndteint.2018.09.003>.
- [25] Almond D, Patel P. *Photothermal science and techniques*, Vol. 10 of Physics and its applications. London: Chapman & Hall; 1996.
- [26] Wang LV. *Photoacoustic imaging and spectroscopy*, Vol. 144 of Optical science and engineering. Boca Raton: CRC Press; 2009.
- [27] Paltauf G, Nuster R, Passler K, Haltmeier M, Burgholzer P. Optimizing image resolution in three-dimensional photoacoustic tomography with line detectors. In: SPIE proceedings. SPIE; 2008. p. 685621. <https://doi.org/10.1117/12.763161>.
- [28] Paltauf G, Nuster R, Haltmeier M, Burgholzer P. Experimental evaluation of reconstruction algorithms for limited view photoacoustic tomography with line detectors. *Inverse Probl* 2007;23(6):S81–94. <https://doi.org/10.1088/0266-5611/23/6/S07>.
- [29] Boyd S. Distributed optimization and statistical learning via the alternating direction method of multipliers. *Found Trends® Mach Learn* 2010;3(1):1–122. <https://doi.org/10.1561/22000000016>.
- [30] Parikh N. Proximal algorithms. *Found Trends® Optim* 2014;1(3):127–239. <https://doi.org/10.1561/24000000003>.
- [31] Hansen PC. The L-curve and its use in the numerical treatment of inverse problems. IMM-REP, IMM, Department of Mathematical Modelling, Technical University of Denmark; 1999. D. T. U. I. f. M. Modelling, T. U. o. D. o. M. Modelling, DTU, <https://books.google.at/books?id=Ge-cXwAACAAJ>.
- [32] Mayer K, Marklein R, Langenberg KJ, Kreutter T. Three-dimensional imaging system based on fourier transform synthetic aperture focusing technique. *Ultrasonics* 1990;28(4):241–55. [https://doi.org/10.1016/0041-624X\(90\)90091-2](https://doi.org/10.1016/0041-624X(90)90091-2).
- [33] Busse LJ. Three-dimensional imaging using a frequency-domain synthetic aperture focusing technique. *IEEE Trans Ultrason Ferroelectrics Freq Contr* 1992;39(2):174–9. <https://doi.org/10.1109/58.139112>.
- [34] Langenberg K-J, Marklein R, Mayer K. *Ultrasonic nondestructive testing of materials: theoretical foundations*/Karl-Jorg Langenberg, Rene Marklein, Klaus Mayer. Boca Raton: Taylor & Francis; 2012.
- [35] Marklein R, Mayer K, Hannemann R, Krylow T, Balasubramanian K, Langenberg KJ, Schmitz V. Linear and nonlinear inversion algorithms applied in nondestructive evaluation. *Inverse Probl* 2002;18(6):1733–59. <https://doi.org/10.1088/0266-5611/18/6/319>.
- [36] Hansen PC. Regularization tools version 4.0 for matlab 7.3. Numer Algorithm 2007;46(2):189–94. <https://doi.org/10.1007/s11075-007-9136-9>.
- [37] Hansen PC. *Discrete inverse problems: insight and algorithms*, Fundamentals of algorithms. Philadelphia: Society for Industrial and Applied Mathematics; 2010.
- [38] Ziegler M, Thiel E, Studemund T. Thermography using a 1d laser array – from planar to structured heating. *Mater Test* 2018;60(7–8):749–57. <https://doi.org/10.3139/120.111209>.
- [39] Hahn DW. *Heat conduction*. third ed. Hoboken N.J.: Wiley; 2012.
- [40] Cole KD. *Heat conduction using Green's functions*, 2nd Edition, Series in computational and physical processes in mechanics and thermal sciences. Boca Raton: CRC Press; 2011.
- [41] Morse PM, Feshbach H. *Methods of theoretical physics*, International series in pure and applied physics. Boston Mass.: McGraw-Hill; 1953.

5.3 Photothermal testing of composite materials: Virtual wave concept with prior information for parameter estimation and image reconstruction

In this study, the VWC was extended for 3D defect reconstruction and visualization in anisotropic media. In contrast to the isotropic VWC procedure, where the virtual sound velocities in the principal direction can be specified arbitrarily, the anisotropic VWC procedure requires knowledge of the anisotropic material properties for the second reconstruction step. To make the VWC applicable to anisotropic materials, a mathematical relationship between the thermal diffusivity tensor and the virtual speed of sound tensor was derived. This relationship yields a novel parameter estimation procedure for the determination of the anisotropic thermal diffusivity tensor. As in Papers 5.1 and 5.2, ADMM was used for regularization and prior information in the form of positivity and sparsity was incorporated by computing the spherical projections of the virtual wave signal. Simulations and thermographic experiments were performed in the transmission configuration to verify and validate the proposed procedure. For the estimation of the thermal diffusivity tensor, the anisotropic sample was thermally excited with a laser with finite laser spot diameter to initiate a 3D thermal wave signal. UD CFRP samples with different thicknesses were analyzed for experimental validation. The samples were considered at the macroscopic length scale and therefore effective material parameters were estimated for the reconstruction of the initial temperature signal. Finally, the performance of the proposed VWC method was demonstrated for 3D image reconstruction in the transmission configuration for the UD CFRP samples.

The results clearly show that the proposed procedure allows the rectification of the anisotropic thermal diffusion process and thus the accurate reconstruction of the initial temperature signal.


Authorship contribution statement

G. Thummerer: Conceptualization, Methodology, Software, Formal analysis, Validation, Investigation, Writing - original draft, Visualization. **G. Mayr:** Conceptualization, Writing - review & editing, Project administration, Funding acquisition. **P. Burgholzer:** Writing - review & editing, Supervision.

Photothermal testing of composite materials: Virtual wave concept with prior information for parameter estimation and image reconstruction F

Cite as: J. Appl. Phys. **128**, 125108 (2020); <https://doi.org/10.1063/5.0016364>

Submitted: 03 June 2020 . Accepted: 30 August 2020 . Published Online: 24 September 2020

G. Thummerer , G. Mayr , and P. Burgholzer 

COLLECTIONS

Note: This paper is part of the Special Topic on Photothermics.

F This paper was selected as Featured

SCI This paper was selected as Scilight



View Online



Export Citation



CrossMark



New

SHFQA
Quantum Analyzer
8.5GHz

Zurich Instruments

Your Qubits. Measured.

Meet the next generation of quantum analyzers

- Readout for up to 64 qubits
- Operation at up to 8.5 GHz, mixer-calibration-free
- Signal optimization with minimal latency

[Find out more](#)



Photothermal testing of composite materials: Virtual wave concept with prior information for parameter estimation and image reconstruction



Cite as: J. Appl. Phys. 128, 125108 (2020); doi: 10.1063/5.0016364
Submitted: 3 June 2020 · Accepted: 30 August 2020 ·
Published Online: 24 September 2020



G. Thummerer,^{1,a)} G. Mayr,^{1,b)} and P. Burgholzer^{2,c)}

AFFILIATIONS

¹Josef Ressel Centre for Thermal NDE of Composites, University of Applied Sciences Upper Austria, 4600 Wels, Austria
²RECENDT—Research Centre for Nondestructive Testing, 4040 Linz, Austria

Note: This paper is part of the Special Topic on Photothermics.

^{a)}Author to whom correspondence should be addressed: gregor.thummerer@fh-wels.at

^{b)}Electronic mail: guenther.mayr@fh-wels.at

^{c)}Electronic mail: peter.burgholzer@recendt.at

ABSTRACT

In this paper, we propose a new parameter estimation and image reconstruction approach for the photothermal testing of composite materials. Therefore, the full multidimensional evaluation method, virtual wave concept, is extended to estimate the orthotropic thermal diffusivity tensor and to reconstruct the initial temperature distribution after a laser spot heating in an orthotropic material. We establish a formal relationship between the virtual speed of sound tensor and the thermal diffusivity tensor. Furthermore, we show how prior information in the form of positivity and sparsity can be incorporated in the regularization process to improve the solution of the inverse imaging problem. In a second step, the initial temperature distribution is reconstructed by applying ultrasonic imaging methods on the calculated 3D bimodal virtual wave field. This new approach is validated on simulation and experimental data of a unidirectional carbon fiber reinforced polymer. The information loss that results from entropy production during heat diffusion can be partly compensated by including prior information. This allows an accurate parameter estimation and a high-resolution image reconstruction.

Published under license by AIP Publishing. <https://doi.org/10.1063/5.0016364>

I. INTRODUCTION

In recent decades, the application of active thermography, especially photothermal testing with an infrared (IR) camera, has significantly grown because it is a contactless non-destructive testing (NDT) method and the focal plane array of the IR camera enables a large measurement throughput.^{1,2} Nowadays, research work in the field of thermographic testing shows a trend from qualitative defect detection to multidimensional defect imaging. Commonly, an inverse heat conduction problem (IHCP) is solved for parameter estimation or defect reconstruction.^{3,4} Mendioroz *et al.*,⁵ e.g., used vibrothermography for 2D defect shape and depth estimation of planar cracks. Holland and Schiefelbein⁶ formulated a model-based inversion for composite materials based on Green's functions that results in a computationally expensive large-scale problem. For this reason, they developed a sophisticated reflector model adapted from the method of images.

Kaipilavil and Mandelis⁷ introduced another approach, the so-called truncated-correlation photothermal coherence tomography (TC-PCT), which allows a 3D visualization of subsurface features based on the match filtering technique that was further enhanced by Tavakolian *et al.*⁸ to obtain higher contrast and resolution images.

A novel approach for the full multidimensional evaluation of temperature data was introduced by Burgholzer *et al.*,⁹ called the Virtual Wave Concept (VWC). A formal relationship between a diffusive electromagnetic field and a wave field was originally published by Lee *et al.* and Gershenson.^{10,11} In addition to these previous studies, VWC is intended to combine the advantages of the NDT methods, active thermography, and ultrasonic testing. In contrast to IHCPs, the VWC is a two-step inverse problem. In a first step, the surface temperature data are transformed locally (pixelwise) into an "acoustic" virtual wave signal. Then, well-developed ultrasonic

reconstruction methods, such as time of flight (TOF) and the frequency domain synthetic aperture focusing technique (F-SAFT), can be applied on photothermal data to reconstruct the initial temperature distribution and the corresponding mirror sources.^{12,13} In addition, defects and boundaries can be detected by ultrasonic reconstruction methods because they introduce secondary wave sources. Due to the local transformation, the computation of the virtual wave signal can be readily parallelized. The second reconstruction step is performed in the frequency domain using F-SAFT.¹⁴ Consequently, the reconstruction of defects using VWC is very efficient. Our recent work is based on isotropic bodies where we have incorporated prior information in the form of positivity and sparsity in the temperature to virtual wave inversion in order to overcome the diffusion-based information loss.¹⁵ This approach was validated on a metallic test specimen with rectangular notches, where 2D defects with a defect width-to-depth ratio of 0.52 were detectable.¹⁶

The aim of the present work is to extend the virtual wave concept for application to materials with an anisotropic thermal diffusivity tensor, such as composite materials. In an anisotropic material, heat diffuses faster, e.g., parallel to the direction of carbon fibers than perpendicular to their orientation. On a macroscopic length scale, an anisotropic thermal diffusivity tensor can describe the heat propagation in the composite material, which can be treated as an effective medium without any internal interfaces.¹⁷ For the virtual wave concept, according to the varying heat conductivity in different directions, the virtual sound speed varies in different directions. Again, we incorporate in the first inversion step prior information in the form of positivity and sparsity to improve the quality of the regularized solution. We assume that the orientation of the coordinate system is parallel to the three mutually perpendicular preferred heat diffusion directions.¹⁸ Therefore, the presented approach is limited to applications where the thermal diffusivity tensor is in the main axis of anisotropy. As stated by Burgholzer *et al.*,⁹ the virtual speed of sound for an isotropic material can be chosen arbitrarily. In the case of orthotropic virtual wave propagation, only one entry of the orthotropic speed of sound tensor can be prescribed. The others are unknown and must be determined to enable a correct second reconstruction step with F-SAFT for defect detection. As derived in this paper, there are two possibilities to determine the unknown entries of the virtual speed of sound tensor:

- calculating the unknown entries based on a known thermal diffusivity tensor or
- determining the unknown entries in a preceding step using the virtual wave field.

The first possibility is valid for some standard materials, where literature values or material models are available.^{19,20} In the industrial manufacturing, however, the thermal diffusivity tensor differs for each component due to production tolerances and, therefore, the tensor has to be determined for each component separately to ensure the precise application of F-SAFT. There are various photothermal evaluation techniques for estimating the anisotropic thermal diffusivity tensor. Krapez *et al.*²¹ introduced thermal ellipsometry to determine the thermal diffusivity components. This approach was extended by Gavérina *et al.*²² for applications where the thermal diffusivity tensor is out of the main axes of anisotropy. Salazar *et al.*^{23,24} studied different photothermal

methods such as infrared radiometry, photothermal reflectance, and optical beam deflection. Due to theoretical considerations, they introduced the quantity “resistivity to heat diffusion” to emphasize that the anisotropic thermal diffusivity tensor is only equal to the inverse of the thermal resistivity if they lie within the main axes of anisotropy. Tralshawala *et al.*²⁵ determined the thermal diffusivity components based on the creation of thermal time of flight images with the benefit of avoiding any sort of curve fitting.

In this paper, we propose a new method for parameter estimation to determine the unknown entries of the speed of sound tensor based on the virtual wave field. Therefore, we estimate the unknown virtual speeds of sound by fitting the scattering hyperbolas at the symmetry cross sections of the computed scattering hyperboloid, which result from a point-like laser heating. Due to the estimation of the unknown entries of the virtual speed of sound tensor, we can reconstruct the initial temperature distribution and secondary wave sources caused by defects using F-SAFT. As mentioned before, we derive a formal link between the orthotropic virtual speed of sound and the orthotropic thermal diffusivity tensor. Hence, it is possible to determine the thermal diffusivity tensor based on the virtual speed of sound tensor. The paper is organized as follows: in Sec. II, we introduce the mathematical framework and derive the link between the thermal diffusivity tensor and the virtual speed of sound tensor. Herein, we show how prior information in the form of positivity and sparsity can be incorporated for 3D bimodal virtual wave propagation. In Sec. III, we introduce the parameter estimation procedure to determine the virtual speed of sound and thermal diffusivity tensor. Then, the extended VWC is validated on simulated measurement data with different signal to noise ratios (SNRs). Finally, we verify the approach on experimental photothermal data.

II. THEORY

The virtual wave concept is characterized by a two-step inversion problem. In the first step, we compute a virtual wave signal for each detection point based on simulated or measured surface temperature data. In a second step, especially for the reconstruction of internal defects, we apply ultrasonic reconstruction methods, like F-SAFT. The evaluation of an orthotropic composite material requires the knowledge of the virtual speed of sound in each principal direction. In the subsequent steps, we establish a relationship between the orthotropic temperature field and the virtual wave field. Therefore, we transform the orthotropic heat equation and wave equation into isotropic partial differential equations (PDEs). In addition, we derive the relationship between the thermal diffusivity tensor α and the virtual speed of sound tensor c .

A. Orthotropic heat equation

The heat conduction in an orthotropic solid, is described by the following heat equation:

$$\left[(\mathbf{k}\nabla) \cdot \nabla - \rho c_p \frac{\partial}{\partial t} \right] T(\mathbf{r}, t) = -\rho c_p T_0(\mathbf{r}) \delta(t),$$

$$\text{with } \mathbf{k} = \begin{pmatrix} k_{11} & 0 & 0 \\ 0 & k_{22} & 0 \\ 0 & 0 & k_{33} \end{pmatrix}. \quad (1)$$

Herein, $T(\mathbf{r}, t)$ is the temperature as a function of position vector $\mathbf{r} = (x, y, z)$ and time t , \mathbf{k} is the thermal conductivity tensor, ρ is the density, and c_p is the specific heat capacity of the material. ∇ is the spatial Nabla operator. The right-hand side of Eq. (1) contains the source term, where $T_0(\mathbf{r})$ denotes the initial temperature distribution and the Dirac delta distribution in the time domain $\delta(t)$ arranges that the heat is introduced spontaneously at $t = 0$. We assume that the orientation of the coordinate system is parallel to the three mutually perpendicular preferred heat conduction directions. Consequently, the coordinate system is orientated along the principal axes of heat conduction. Hence, we can transform the heat conduction equation from an orthotropic problem into an isotropic problem by stretching the coordinate axes in the following manner:²⁶

$$\bar{x} = x \left(\frac{k}{k_{11}} \right)^{1/2}; \quad \bar{y} = y \left(\frac{k}{k_{22}} \right)^{1/2}; \quad \bar{z} = z \left(\frac{k}{k_{33}} \right)^{1/2}. \quad (2)$$

Respecting these formal relationships in Eq. (1) yields the heat equation similar to the isotropic body,

$$\left(k \nabla^2 - \rho c_p \frac{\partial}{\partial t} \right) T(\bar{\mathbf{r}}, t) = -\rho c_p T_0(\bar{\mathbf{r}}) \delta(t). \quad (3)$$

The thermal conductivity k is related to the thermal conductivities in the principal directions in the following manner:

$$k = (k_{11} k_{22} k_{33})^{1/3}. \quad (4)$$

By introducing the thermal diffusivity $\alpha = k/(\rho c_p)$ into Eq. (3), we have

$$\left(\nabla^2 - \frac{1}{\alpha} \frac{\partial}{\partial t} \right) T(\bar{\mathbf{r}}, t) = -\frac{1}{\alpha} T_0(\bar{\mathbf{r}}) \delta(t), \quad (5)$$

$$\text{with } \alpha = (\alpha_{11} \alpha_{22} \alpha_{33})^{1/3}. \quad (6)$$

B. Orthotropic wave equation

The wave equation for virtual wave propagation is given by Ref. 15,

$$\left[(\mathbf{c}^T \mathbf{c} \nabla) \cdot \nabla - \frac{\partial^2}{\partial t'^2} \right] T_{\text{virt}}(\mathbf{r}, t') = -\frac{\partial}{\partial t'} T_0(\mathbf{r}) \delta(t'), \quad \text{with}$$

$$\mathbf{c}^T \mathbf{c} = \begin{pmatrix} c_{11} & 0 & 0 \\ 0 & c_{22} & 0 \\ 0 & 0 & c_{33} \end{pmatrix} \begin{pmatrix} c_{11} & 0 & 0 \\ 0 & c_{22} & 0 \\ 0 & 0 & c_{33} \end{pmatrix} = \begin{pmatrix} c_{11}^2 & 0 & 0 \\ 0 & c_{22}^2 & 0 \\ 0 & 0 & c_{33}^2 \end{pmatrix}. \quad (7)$$

Herein, ∇ is the spatial Nabla operator and $T_{\text{virt}}(\mathbf{r}, t')$ is the orthotropic virtual wave field as a function of the position vector \mathbf{r} and the time scale t' for virtual wave propagation. The tensor \mathbf{c} contains the virtual speed of sound in the principal directions. The right-hand side of Eq. (7) characterizes the source term, where the initial temperature field $T_0(\mathbf{r})$ is spontaneously introduced due to the Dirac delta distribution in virtual time domain $\delta(t')$. Similar

to the orthotropic heat equation, we can stretch the coordinate axes in Eq. (7) to transform the orthotropic wave equation into an isotropic PDE. This yields

$$\bar{x} = x \frac{c}{c_{11}}; \quad \bar{y} = y \frac{c}{c_{22}}; \quad \bar{z} = z \frac{c}{c_{33}}. \quad (8)$$

The speed of sound c is related to the speed of sound in the principal directions in the following manner:

$$c = (c_{11} c_{22} c_{33})^{1/3}. \quad (9)$$

Using Eqs. (7) and (8), the isotropic wave equation can be written as

$$\left(\nabla^2 - \frac{1}{c^2} \frac{\partial^2}{\partial t'^2} \right) T_{\text{virt}}(\bar{\mathbf{r}}, t') = -\frac{1}{c^2} \frac{\partial}{\partial t'} T_0(\bar{\mathbf{r}}) \delta(t'). \quad (10)$$

C. Relation between heat and virtual wave propagation

According to Burgholzer *et al.*⁹ the virtual wave concept relates the thermal wave to an ‘‘acoustic’’ virtual wave for the same position vector $\bar{\mathbf{r}}$ but different time scales, t and t' ,

$$T(\bar{\mathbf{r}}, t) = \int_{-\infty}^{\infty} T_{\text{virt}}(\bar{\mathbf{r}}, t') K(t, t') dt', \quad (11)$$

$$\text{with } K(t, t') = \frac{c}{\sqrt{\pi \alpha t}} \exp\left(-\frac{c^2 t'^2}{4 \alpha t}\right). \quad (12)$$

The kernel $K(t, t')$ contains the thermal diffusivity $\alpha = (\alpha_{11} \alpha_{22} \alpha_{33})^{1/3}$ and the virtual speed of sound $c = (c_{11} c_{22} c_{33})^{1/3}$, which are the characteristic parameters for heat and virtual wave propagation. The Fredholm integral of the first kind, Eq. (11), is valid for a temporal Dirac-Delta like heating and describes a local 1D transformation between the temperature field and the virtual wave field. Because the virtual wave concept is valid for the same position vector $\bar{\mathbf{r}}$ or \mathbf{r} , we can establish the subsequent relationships based on Eqs. (2) and (8),

$$\frac{c}{\sqrt{k}} = \frac{c_{11}}{\sqrt{k_{11}}} = \frac{c_{22}}{\sqrt{k_{22}}} = \frac{c_{33}}{\sqrt{k_{33}}} \quad (13)$$

or

$$\frac{c}{\sqrt{\alpha}} = \frac{c_{11}}{\sqrt{\alpha_{11}}} = \frac{c_{22}}{\sqrt{\alpha_{22}}} = \frac{c_{33}}{\sqrt{\alpha_{33}}}. \quad (14)$$

In our study, we are not interested in c and α but in the speed of sound and thermal diffusivity in the principal directions. Because the VWC is a 1D transformation with respect to the axis perpendicular to the evaluation surface ($x - y$ plane), we substitute the ratio $c/\sqrt{\alpha}$ in Eq. (12) by $c_{33}/\sqrt{\alpha_{33}}$,

$$K(t, t') = \frac{c_{33}}{\sqrt{\pi \alpha_{33} t}} \exp\left(-\frac{c_{33}^2 t'^2}{4 \alpha_{33} t}\right). \quad (15)$$

Using Eq. (14), prescribing c_{33} and assuming the thermal diffusivity tensor is known, we can compute the remaining unknown components of the virtual speed of sound tensor and vice versa,

$$\mathbf{c} = \begin{pmatrix} c_{11} & 0 & 0 \\ 0 & c_{22} & 0 \\ 0 & 0 & c_{33} \end{pmatrix} = \begin{pmatrix} c_{33} \sqrt{\frac{\alpha_{11}}{\alpha_{33}}} & 0 & 0 \\ 0 & c_{33} \sqrt{\frac{\alpha_{22}}{\alpha_{33}}} & 0 \\ 0 & 0 & c_{33} \end{pmatrix}. \quad (16)$$

1. Discrete data

Because the thermographic data is discrete in time and space, we must discretize the Fredholm integral [Eq. (11)]. With $t_k = (k - 1)\Delta_t$ and $t_j = (j - 1)\Delta_t$, we obtain a linear matrix equation for one spatial cross section of the surface temperature field \mathbf{T} ,

$$\mathbf{T} = \mathbf{K}\mathbf{T}_{\text{virt}}. \quad (17)$$

The dimensions of the matrices are $\mathbf{T} \in \mathbb{R}^{m \times q}$, $\mathbf{K} \in \mathbb{R}^{m \times n}$, and $\mathbf{T}_{\text{virt}} \in \mathbb{R}^{n \times q}$. The components of the kernel matrix \mathbf{K} are given by

$$K_{kj} = \frac{\eta}{\sqrt{\pi(k-1)}} \exp\left(-\frac{\eta^2(j-1)^2}{4(k-1)}\right). \quad (18)$$

Herein, the dimensionless number $\eta = \tilde{c}/\sqrt{\Delta_{F0}}$ is defined as the ratio of the dimensionless virtual speed of sound $\tilde{c} = c\Delta_t/\Delta_x$ and the discrete Fourier number $\Delta_{F0} = \alpha\Delta_t/\Delta_x^2$. Δ_x is the spatial resolution that is equal in each considered spatial direction.

2. Inverse problem respecting prior information

Our goal is to calculate a virtual wave signal based on a measured temperature signal. This is a severely ill-posed inverse problem because of the entropy produced during heat diffusion, which is equal to information loss. To enhance the quality of the inverse solution, we incorporate prior information in the form of positivity and sparsity. A 3D heat diffusion field causes a 3D virtual wave field where the bimodal characteristic is visible in the A-scan in the form of the N-shaped function (Fig. 1). To incorporate the prior information positivity, we project the negative data points of the 3D virtual wave field onto a positive data set.¹⁶ This is feasible by integrating the 3D virtual wave field with respect to time, which yields the spherical projections \mathbf{M}_{virt} of \mathbf{T}_{virt} .²⁷ In discrete form we apply the time integral operator matrix \mathbf{R} . Hence, the formal relationship between virtual wave field and spherical projections is given by

$$\mathbf{M}_{\text{virt}} = \mathbf{R}\mathbf{T}_{\text{virt}}, \quad \text{with } \mathbf{R} = \begin{pmatrix} 1 & 0 & \cdots & 0 \\ 1 & 1 & \cdots & 0 \\ \vdots & \vdots & \ddots & \vdots \\ 1 & 1 & \cdots & 1 \end{pmatrix} \in \mathbb{R}^{n \times n}. \quad (19)$$

Substituting Eq. (19) in Eq. (17) yields

$$\mathbf{T} = \mathbf{K}\mathbf{T}_{\text{virt}} = \mathbf{K}\mathbf{R}^{-1}\mathbf{M}_{\text{virt}} = \bar{\mathbf{K}}\mathbf{M}_{\text{virt}}. \quad (20)$$

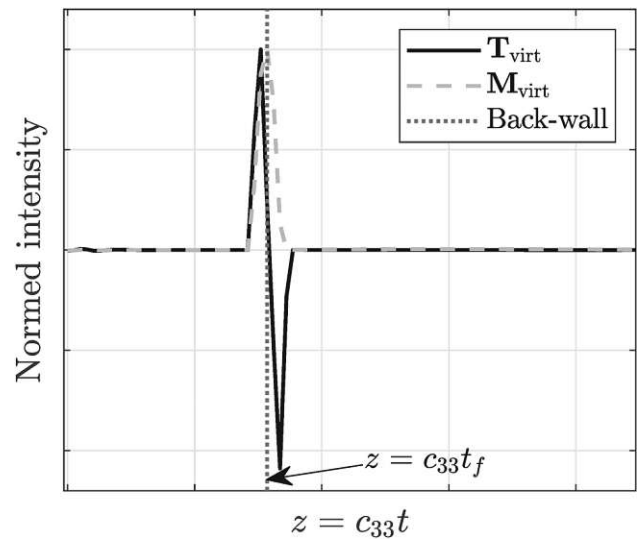


FIG. 1. A-scans of the virtual wave field, where the intensity of the virtual wave is plotted vs the propagation distance z . To incorporate the prior information positivity, we project the bimodal virtual wave \mathbf{T}_{virt} onto its spherical means \mathbf{M}_{virt} .

The inverse of the integral operator matrix \mathbf{R}^{-1} is the differential operator. Multiplication of a discretized signal matrix in time with this operator results in a discretized version of the time derivative of this signal. The introduction of the spherical projections results in a new inverse but also severely ill-posed inverse problem. To solve this inverse problem, we apply the iterative regularization method Alternating Direction Method of Multipliers (ADMM).^{28,29} We minimize the subsequent objective function to compute an appropriate solution for \mathbf{M}_{virt} ,

$$\frac{1}{2} \|\bar{\mathbf{K}}\mathbf{M}_{\text{virt}} - \mathbf{T}\|_2^2 + \lambda \|\mathbf{M}_{\text{virt}}\|_1. \quad (21)$$

To enforce positivity in this iteration scheme, we apply soft-thresholding only on positive entries and set the negative values to zero.¹⁵ In addition to the threshold value as one regularization parameter, the second regularization parameter λ describes a trade-off between the data fitting term, which is the first term in Eq. (21), and the L1-norm of the spherical projection \mathbf{M}_{virt} . This second term in Eq. (21) introduces sparsity, which can be assumed, as the absorbed short laser pulse results in a delta-like spherical projection for \mathbf{M}_{virt} (see also Fig. 1).

III. PARAMETER ESTIMATION

Let us consider the thermographic experiment depicted in Fig. 2. The sample is heated by a short laser pulse, where the corresponding heat source term $g(\mathbf{r}, t) = T_0(\mathbf{r})\delta(t)$ consists of a spatial temperature distribution $T_0(\mathbf{r})$ and a temporal heating function $h(t) = \delta(t)$. The laser beam with a diameter a is absorbed at the sample surface $z = 0$, which causes a

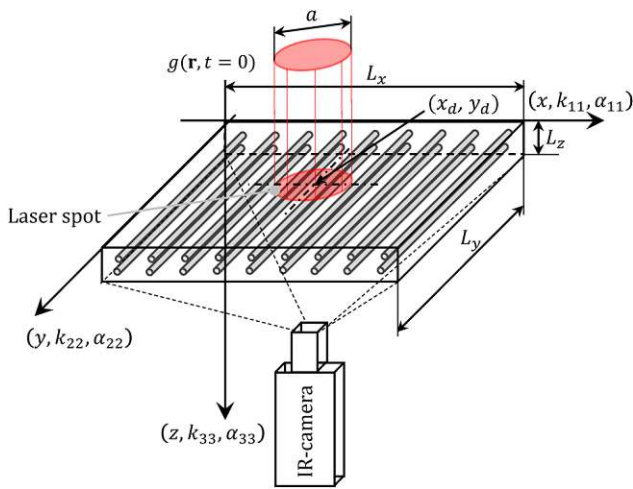


FIG. 2. Principal sketch of the experiment. The gray cylinders represent the orientation of the individual fibers (e.g., carbon or glass fibers) in a homogeneous and isotropic matrix (e.g., thermosets or thermoplastics).

multidimensional heat flux in the specimen. The temperature field is measured at $z = L_z$ which corresponds to the back wall of the sample. Figure 3(a) shows a cross section at $x_d = L_x/2$ of the measured surface temperature field $T(\mathbf{r}, t)$. Based on the measured temperature data, we compute the virtual wave field that corresponds to a B-scan [Fig. 3(b)]. For the 3D case, we obtain a characteristic scattering hyperboloid (Fig. 4) for a point-like source. Based on the B- and C-scan, we can obtain the unknown parameters c_{11} and c_{22} for the reconstruction of the initial temperature distribution $T_0(\mathbf{r})$.

A. Modification of F-SAFT

Using the estimated speed of sound in the principal directions, we can reconstruct the initial temperature distribution using F-SAFT. Because we consider an orthotropic composite material, we must modify the standard F-SAFT algorithm. Therefore, we consider the homogeneous PDE of the wave equation for virtual wave propagation:

$$c_{11}^2 \frac{\partial^2 T_{\text{virt}}(\mathbf{r}, t')}{\partial x^2} + c_{22}^2 \frac{\partial^2 T_{\text{virt}}(\mathbf{r}, t')}{\partial y^2} + c_{33}^2 \frac{\partial^2 T_{\text{virt}}(\mathbf{r}, t')}{\partial z^2} - \frac{\partial^2 T_{\text{virt}}(\mathbf{r}, t')}{\partial t'^2} = 0. \quad (22)$$

The spatial Fourier transform in x, y and the temporal Fourier transform in t' of Eq. (22) yields,

$$\left[\frac{c_{11}^2}{c_{33}^2} \xi_x^2 + \frac{c_{22}^2}{c_{33}^2} \xi_y^2 - \frac{1}{c_{33}^2} \omega^2 \right] \Theta(\xi_x, \xi_y, z, \omega) = \frac{\partial^2 \Theta(\xi_x, \xi_y, z, \omega)}{\partial z^2}, \quad (23)$$

wherein ξ_x and ξ_y are the spatial frequencies and ω is the temporal

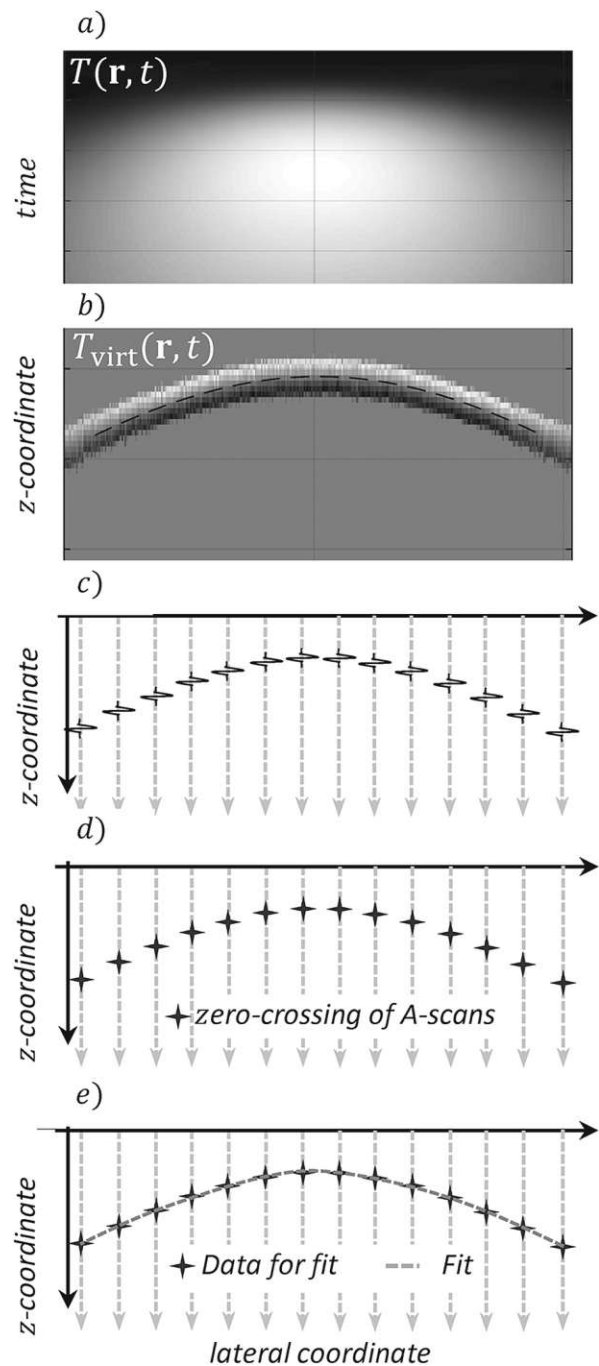


FIG. 3. Process steps for parameter estimation: (a) cross section of the simulated or measured surface temperature field. Based on the temperature signal, an “acoustic” virtual wave field is calculated, which exhibits the characteristic B-scan (b) for a point-like source. (c) shows that the B-scan is composed of A-scans. (d) We search for the zero crossing of the A-scans to obtain the data for parameter fitting and (e) shows the fitting data and the corresponding least square fit.

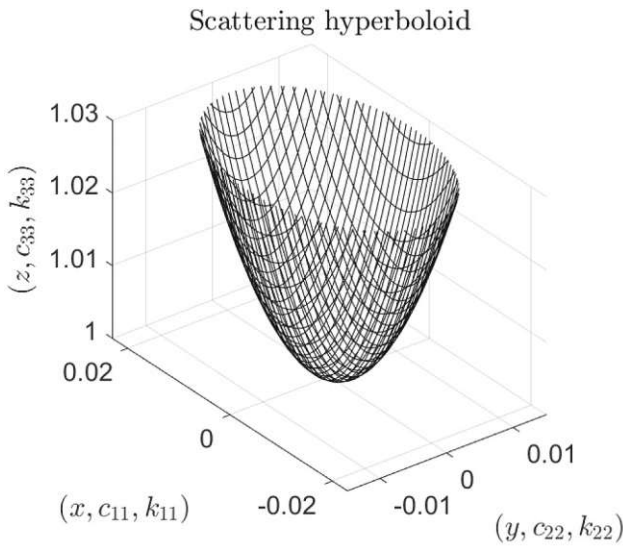


FIG. 4. Scattering hyperboloid obtained by a point-like source.

frequency. $\Theta(\xi_x, \xi_y, z, \omega)$ is defined in the following manner:

$$\Theta(\xi_x, \xi_y, z, \omega) = \iiint_{-\infty}^{\infty} T_{\text{virt}}(\mathbf{r}, t') e^{-i(\xi_x x + \xi_y y + \omega t')} dx dy dt. \quad (24)$$

Solving the ordinary differential equation (ODE), Eq. (23), with the exponential approach yields,

$$\Theta(\xi_x, \xi_y, z, \omega) = \Theta_0 \exp\left(-iz \sqrt{\frac{1}{c_{33}^2} \omega^2 - \frac{c_{11}^2}{c_{33}^2} \xi_x^2 - \frac{c_{22}^2}{c_{33}^2} \xi_y^2}\right). \quad (25)$$

In our case, $\Theta(\xi_x, \xi_y, z, \omega)$ is given by the calculated virtual wave field and Eq. (24). Hence, we must backpropagate the virtual wave field to obtain the initial temperature distribution Θ_0 or T_0 . Compared to the isotropic F-SAFT backpropagation, we need only scale the axes in the principal directions for orthotropic materials.

B. The thermal scattering hyperbola

Figure 3(c) shows that the scattering hyperbola visible in the B-scan consists of A-scans. Our goal is to estimate the unknown components of the speed of sound tensor, c_{11} and c_{22} by fitting the scattering hyperbolas

$$\begin{aligned} z_{11}(x) &= \frac{c_{33}}{c_{11}} \sqrt{c_{11}^2 t_f^2 + (x - x_d)^2} \quad \text{and} \\ z_{22}(y) &= \frac{c_{33}}{c_{22}} \sqrt{c_{22}^2 t_f^2 + (y - y_d)^2}. \end{aligned} \quad (26)$$

With $c_{11} = \tilde{c}_{11} \Delta x / \Delta t$ and $c_{22} = \tilde{c}_{22} \Delta x / \Delta t$ we can write Eq. (26) in discrete form,

$$\begin{aligned} z_{11}(x) &= \tilde{c}_{33} \sqrt{\left(\frac{\Delta x}{\Delta t}\right)^2 t_f^2 + \frac{(x - x_d)^2}{c_{11}^2}} \quad \text{and} \\ z_{22}(y) &= \tilde{c}_{33} \sqrt{\left(\frac{\Delta x}{\Delta t}\right)^2 t_f^2 + \frac{(y - y_d)^2}{c_{22}^2}}. \end{aligned} \quad (27)$$

The unknown parameters in Eq. (27) are \tilde{c}_{11} , \tilde{c}_{22} , and the time of flight t_f and, if the center of excitation is unidentified, x_d and y_d . As mentioned before, according to VWC, we prescribe the dimensionless virtual speed of sound \tilde{c}_{33} perpendicular to the measurement surface. Reconsidering Eq. (15), we see that the axial thermal diffusivity α_{33} has to be known before the speeds of sound, c_{11} and c_{22} , can be calculated. For the calculation of α_{33} , we measure the thickness L_m of the observed specimen mechanically. Using the VWC, we determine α_{33} by the following steps:

1. Prescribe a starting value for the thermal diffusivity $\hat{\alpha}_{33}$, e.g., from the literature.
2. Then, calculate the virtual wave signal based on the maximum temperature pixel, which corresponds to the center of excitation, and evaluate the time of flight t_f between the front and the back wall.
3. The thickness is calculated by the relationship $c_{33} t_f = \tilde{c}_{33} \Delta x / \Delta t t_f = \hat{L}_z$.
4. If the measured thickness L_m is equal to the estimated thickness \hat{L}_z , the proposed thermal diffusivity is correct.
5. Otherwise, we must correct for the thermal diffusivity $\hat{\alpha}_{33}$ by $\hat{\alpha}_{33}^{\text{cor}} = \alpha_{33} = \hat{\alpha}_{33} (L_m / \hat{L}_z)^2$ (detailed derivation in Appendix B).

To obtain the fitting data for c_{11} and c_{22} , we search for the zero crossings of the N-shaped function, as depicted in Figs. 3(c) and 3(d). They correspond to the maxima of the spherical means (Fig. 1). Finally, the unknown parameters are estimated by a least square (LS) fit of the data points, as illustrated in Fig. 3(e). We use symmetry from the scattering hyperboloid and evaluate the cross section at y_d for the estimation of c_{11} and the cross section at x_d for the estimation of c_{22} . Then, as visible in Eq. (16), we can calculate the thermal diffusivity tensor based on the speed of sound tensor,

$$\boldsymbol{\alpha} = \frac{\alpha_{33}}{c_{33}^2} \begin{pmatrix} c_{11}^2 & 0 & 0 \\ 0 & c_{22}^2 & 0 \\ 0 & 0 & c_{33}^2 \end{pmatrix} = \frac{\alpha_{33}}{c_{33}^2} \begin{pmatrix} \tilde{c}_{11}^2 & 0 & 0 \\ 0 & \tilde{c}_{22}^2 & 0 \\ 0 & 0 & \tilde{c}_{33}^2 \end{pmatrix} = \frac{\alpha_{33}}{c_{33}^2} \tilde{\mathbf{c}}^T \tilde{\mathbf{c}}. \quad (28)$$

In the penultimate step, the virtual speed of sound tensor is written in discrete form.

C. Respecting finite laser spot diameter

The point source is not an ideal point, but can be imagined as a superposition of point sources as depicted in Fig. 5. This is valid because both heat equation and virtual wave equation are linear

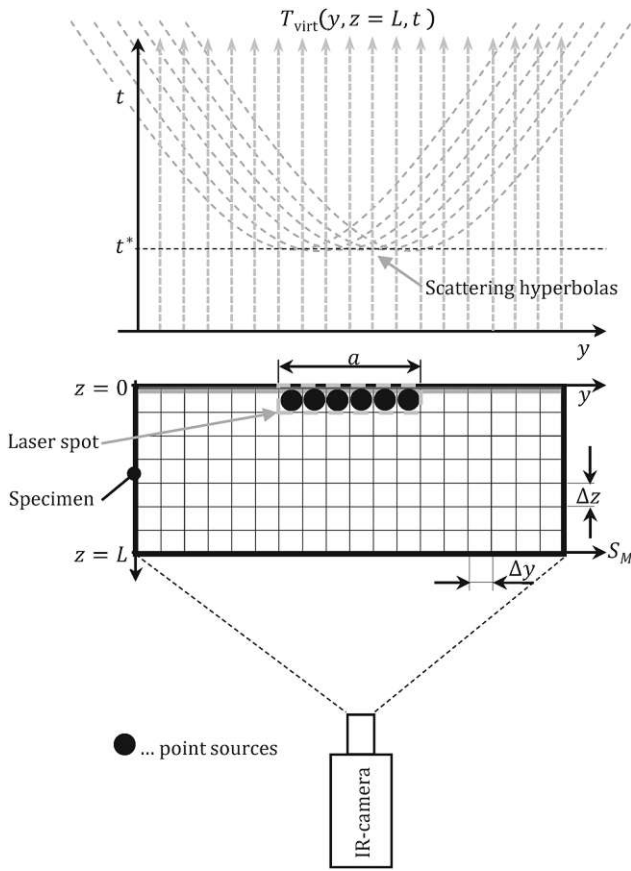


FIG. 5. Superposition of point scatterers.

PDEs. Consequently, Eq. (27) becomes

$$z_{11}(x) = \sum_{i=-N_x/2}^{N_x/2-1} \tilde{c}_{33} \sqrt{\left(\frac{\Delta_x}{\Delta_t}\right)^2 t_f^2 + \frac{(x-x_d+i\Delta_x)^2}{c_{11}^2}} \quad \text{and} \quad (29)$$

$$z_{22}(y) = \sum_{j=-N_y/2}^{N_y/2-1} \tilde{c}_{33} \sqrt{\left(\frac{\Delta_x}{\Delta_t}\right)^2 t_f^2 + \frac{(y-y_d+j\Delta_y)^2}{c_{22}^2}}.$$

The sum limits $N_x = N_y = a/\Delta_x$ can be calculated by the laser spot diameter a and the spatial resolution Δ_x .

D. Validation on simulated data

In this section, we validate the novel approach for virtual speed of sound and, consequently, for thermal diffusivity tensor estimation using simulated data. For practical applications, we must limit the laser power because otherwise the sample under test can be damaged. This limits the signal amplitude measured by the IR camera. The noise of the camera is given by the noise equivalent

TABLE I. Simulation and evaluation parameters.

Property	Unit	Value
Radial extensions	L_x, L_y	m
Sample thickness	L_z	m
Laser spot diameter	a	m
Thermal diffusivities	α	$\begin{pmatrix} 0.7 & 0 & 0 \\ 0 & 3.8 & 0 \\ 0 & 0 & 0.32 \end{pmatrix} \times 10^{-6}$
Temporal resolution	Δ_t	s
Spatial resolution	$\Delta_x, \Delta_y, \Delta_z$	m
		$L_z/30$

temperature difference (NETD). These practical conditions result in a limited signal to noise ratio (SNR). For this reason, we apply the VWC for parameter estimation on simulated data with different SNRs, where the SNR is defined as the ratio of maximum temperature T_{\max} and the corresponding standard deviation σ .

The model is described in principle by Fig. 2. We apply adiabatic boundary conditions in each spatial dimension, whereby the radial extensions L_x and L_y are large compared to the laser spot diameter and the sample thickness L_z . Consequently, the boundaries in lateral direction do not affect the heat flow. We introduce a short laser pulse with laser spot diameter a and a top-hat beam. The chosen geometrical and thermophysical parameters, as well as the temporal and spatial resolution correspond to the parameters of the experiment and are listed in Table I. The prescribed thermal diffusivity tensor contains typical values for carbon fiber reinforced polymers (CFRPs).

The simulated temperature field is evaluated at the back wall ($z = L_z$) and is divided by the maximum temperature T_{\max} . For the simulated measurement data, ten different noise levels are added to obtain a SNR with $\text{SNR} = 8\ell$ and $\ell = \{1, 2, \dots, 10\}$.

1. Estimation of the axial thermal diffusivity

In this section, we focus on the estimation of the axial thermal diffusivity α_{33} for discrete simulated measurement data. According to Sec. III B, the corrected axial thermal diffusivity is calculated by

$$\hat{\alpha}_{33}^{\text{cor}} = \hat{\alpha}_{33} \left(\frac{L_m}{\hat{L}_z}\right)^2 = \hat{\alpha}_{33} \left(\frac{L_m}{c_{33} t_f}\right)^2 = \hat{\alpha}_{33} \left(\frac{L_m}{\tilde{c}_{33} N_{t_f} \Delta_z}\right)^2. \quad (30)$$

The index N_{t_f} indicates the zero crossing of the virtual wave signal (see Fig. 1). Figure 6 shows the influence of the discretization. Herein, the estimated thickness \hat{L}_z with spatial resolution Δ_z is plotted against different assumptions for $\hat{\alpha}_{33} = \hat{\alpha}_{33}^{\text{cor}} \cdot 0.9; \hat{\alpha}_{33}^{\text{cor}}/200; \hat{\alpha}_{33}^{\text{cor}} \cdot 1.1$. Due to the discretization, the resulting curve is not smooth but indicates a stepwise change in the estimated thickness \hat{L}_z . Consequently, an infinite set of assumed $\hat{\alpha}_{33}$ will give the correct thickness L_m . This results in a significant error for the estimation of α_{33} . At this point, Eq. (30) provides a good but improvable estimation of α_{33} denoted as $\hat{\alpha}_{33}^{\text{cor}}$. To obtain a more precise estimation for α_{33} , the following steps are taken:

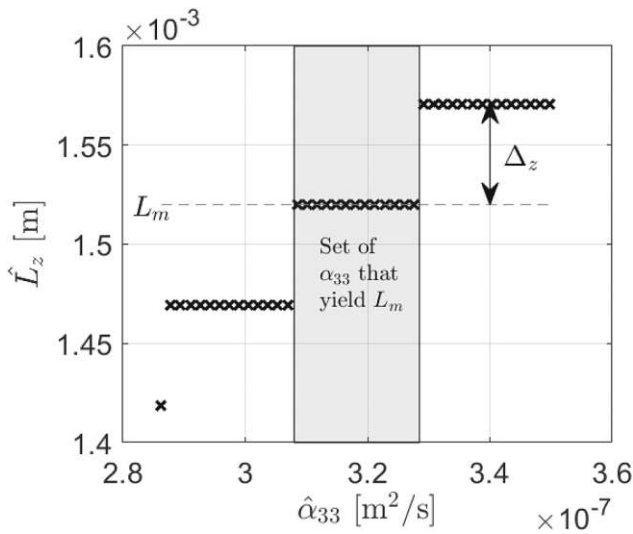


FIG. 6. Estimated thickness \hat{L}_z vs the vector of estimations for the axial thermal diffusivity $\hat{\alpha}_{33}^{cor} \cdot 0.9; \hat{\alpha}_{33}^{cor} / 200; \hat{\alpha}_{33}^{cor} \cdot 1.1$ for SNR=8.

- $\hat{\alpha}_{33}^{cor}$ is estimated according to Sec. III B.
- Then, a vector of estimations $\hat{\alpha}_{33}^{cor} \cdot 0.9; \hat{\alpha}_{33}^{cor} / 200; \hat{\alpha}_{33}^{cor} \cdot 1.1$ is set up and the points listed in Sec. III B are repeated for each entry until step 4 is reached.
- The mean value of thermal diffusivities, which give the correct thickness L_m (Fig. 6, gray background) is taken in order to

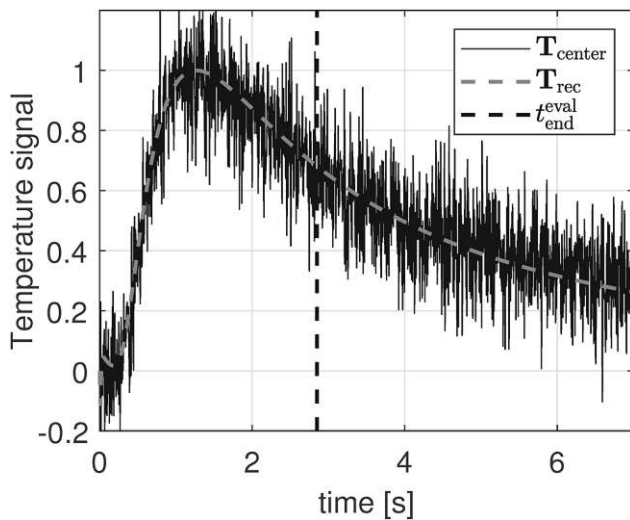


FIG. 7. Visualization of the simulated temperature at the center point (x_d, y_d) with SNR = 8 and the corresponding reconstructed temperature slope $T_{rec} = KT_{virt}$. For the estimation of α_{33} , temperature values until t_{end}^{eval} were used (dashed line).

obtain the final estimation of α_{33} . This is reasonable because Fig. 6 shows a linear approximation of the quadratic sample thickness to thermal diffusivity relationship due to the limited range of estimation values for α_{33} .

For the improved estimation of the axial thermal diffusivity, we truncated the initial simulation time L_m^2/α_{33} according to Appendix A. Figure 7 shows a simulated temperature curve with SNR = 8, the corresponding reconstructed temperature slope $T_{rec} = KT_{virt}$, and the end time t_{end}^{eval} for the final evaluation of α_{33} .

Because we have a finite laser spot diameter a , we can perform the above-mentioned evaluation for 25 pixels which proves the repeatability of this method.

2. Estimation of speed of sound and thermal diffusivity tensor

Due to the estimation of α_{33} , we can calculate the scattering hyperboloid that results from a point-like heating. Then, we evaluate the symmetry cross sections at $x_d = L_x/2$ and $y_d = L_y/2$.

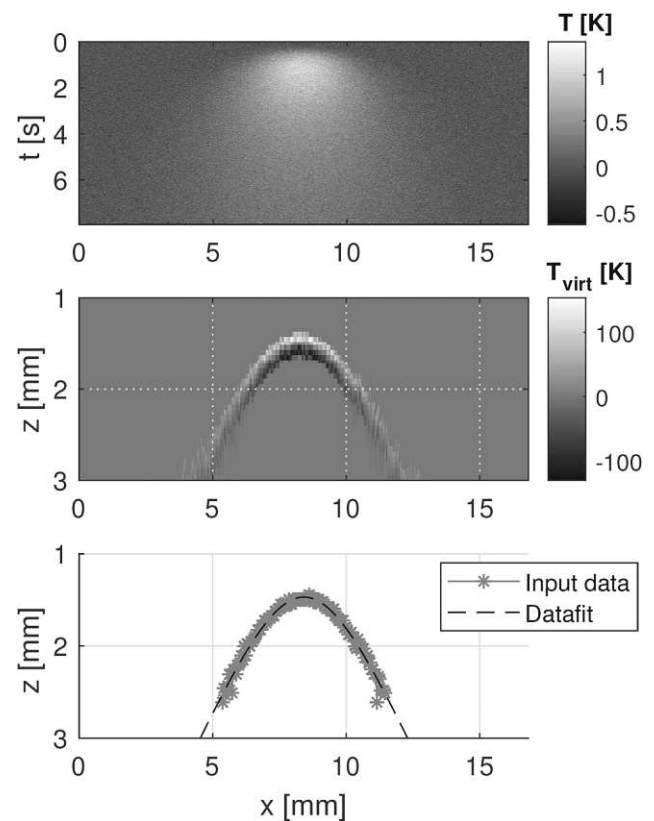


FIG. 8. Top: Cross section of the simulated temperature field at $y_d = L_y/2$ with SNR = 8. Middle: Corresponding cross section of the computed virtual wave field. Bottom: Extracted data points of the virtual wave field to estimate the dimensionless virtual speed of sound \tilde{c}_{11} . The black dashed line is the fitted curve.

As described in Sec. III B, we search for the zero crossings of the B-scan that consists of A-scans. Based on these data points, we can perform a data fit to estimate the unknown speeds of sound \tilde{c}_{11} and \tilde{c}_{22} . For both data fits, the data points until a depth of $z = c_{33}t' = 2.5$ mm were used. Consequently, according to the findings in Appendix A and Fig. 7, we considered data points until $(2.5 \times 10^{-3}/L_m)^2 t_{\text{end}}^{\text{eval}}$. Figures 8 and 9 illustrate the procedure. The top image shows the temperature field, while the image in the middle depicts the corresponding virtual wave field and the bottom graph exhibits the extracted data points and the corresponding fitted curve for both evaluated cross sections. Based on the estimated dimensionless speed of sound tensor, we calculated the initial temperature distribution T_0 and the unknown thermal diffusivities α_{11} and α_{22} .

3. Results based on simulated data

Figure 10 shows error plots representing the mean value and standard deviation of (a) the estimated speed of sound tensor and

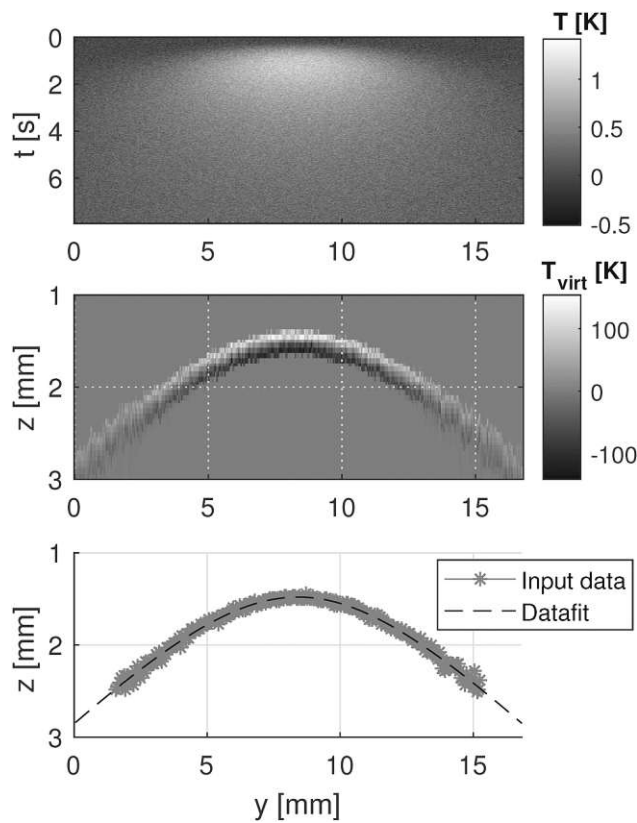


FIG. 9. Top: Cross section of the simulated temperature field at $x_y = L_x/2$ with SNR = 8. Middle: Corresponding cross section of the computed virtual wave field. Bottom: Extracted data points of the virtual wave field to estimate the dimensionless virtual speed of sound \tilde{c}_{22} . The black dashed line is the fitted curve.

(b) the computed thermal diffusivity tensor, for different SNRs and nine repetitions. As visible in plot (a), the virtual speed of sound in the axial direction exhibits no error because it was prescribed. Furthermore, the thermal diffusivity in the axial direction α_{33} can be determined very well for all SNRs, except SNR= 8 for which the mean error is smaller than $\pm 0.5\%$. For each SNR, the starting value for the axial thermal diffusivity was $\hat{\alpha}_{33} = 2.3 \times 10^{-6} \text{ m}^2/\text{s}$. The mean errors of \tilde{c}_{11} and \tilde{c}_{22} for the different SNRs lie in the error bounds of $\pm 1.0\%$ for each SNR. Moreover, we can see that the standard deviation for each estimated parameter decreases with increasing SNR. Equation (28) shows that α_{11} and α_{22} are calculated by the product of α_{33} and \tilde{c}_{11}^2 and \tilde{c}_{22}^2 , respectively. It is important to note that the quantities α_{33} , \tilde{c}_{11} , and \tilde{c}_{22} are correlated. From a theoretical point of view, an overestimation of α_{33} yields an underestimation of \tilde{c}_{11} and \tilde{c}_{22} . Hence, according to the law of error propagation, we have in the worst case a sum of the relative errors of these quantities. However, Fig. 10(a) depicts an overestimation for \tilde{c}_{11} and an underestimation of \tilde{c}_{22} . As visible, the accuracy of the estimations for α_{11} and α_{22} mainly depends on the accuracy of \tilde{c}_{11} and \tilde{c}_{22} . Figure 11(a) depicts the reference initial temperature curve T_0 and the reconstructed temperature distribution evaluated at $z = 0$ and the centerline in the x - and y -direction, by applying F-SAFT and the estimated dimensionless virtual speed of sound tensor \tilde{c} on the computed 3D virtual wave field. Figure 11(b) shows an isosurface representation of the initial temperature distribution. Due to the well estimated tensor \tilde{c} , we have a circular area, which represents the laser spot heating.

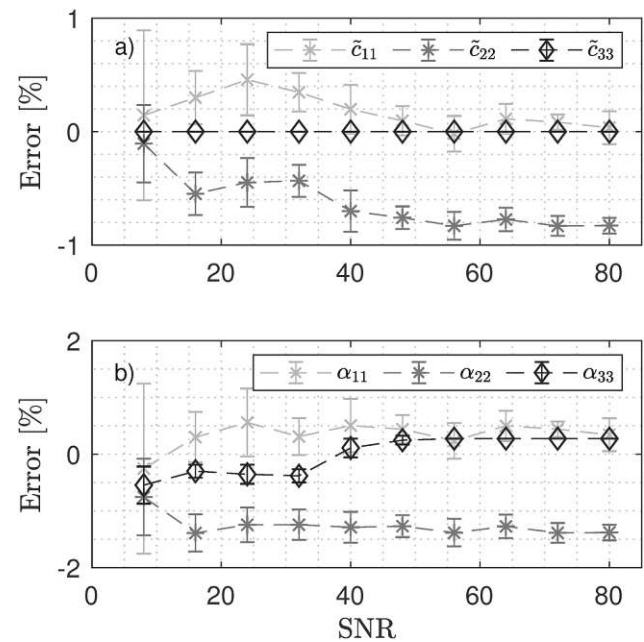


FIG. 10. (a) Error plots representing the mean value and standard deviation of the estimated dimensionless speed of sound tensor \tilde{c} , and (b) the corresponding thermal diffusivity tensor α .

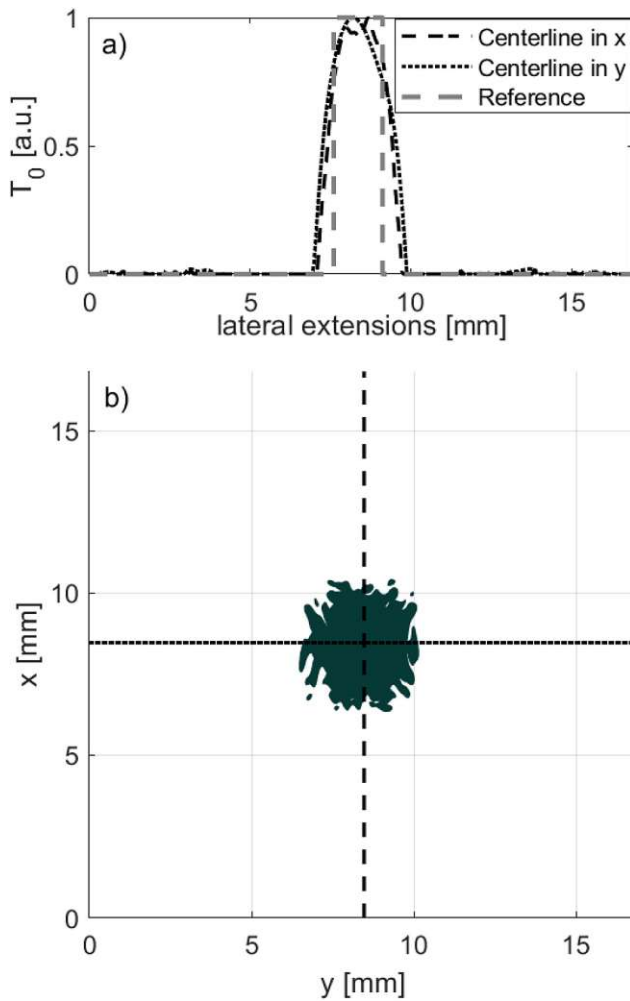


FIG. 11. (a) Line plot of the reference initial temperature distribution T_0 and the reconstructed initial temperature distribution evaluated at $z = 0$ and the centerline in the x - and y -direction. (b) Corresponding isosurface representation of T_0 . These representations are based on simulated surface temperature data with $\text{SNR} = 8$, by applying F-SAFT and the estimated speed of sound tensor \mathbf{c} on the computed virtual wave field.

E. Experiment

For the experimental investigations, we consider two carbon fiber reinforced polymer (CFRP) specimens with a unidirectional fiber matrix. The lateral extensions for both specimens are $L_x = 100$ mm and $L_y = 100$ mm. One specimen has 8 layers (UD8) and a thickness of $L_z = 1.65$ mm, the other specimen has 16 layers (UD16) and a thickness of $L_z = 3.27$ mm. The thicknesses were measured with a micrometer. Figure 2 depicts a sketch of the specimens. Figure 12 shows the experimental setup. The setup consists of a laser system, optical lenses, specimen, dichroic mirror, and the IR camera. The raise time of the diode laser is smaller than $10 \mu\text{s}$

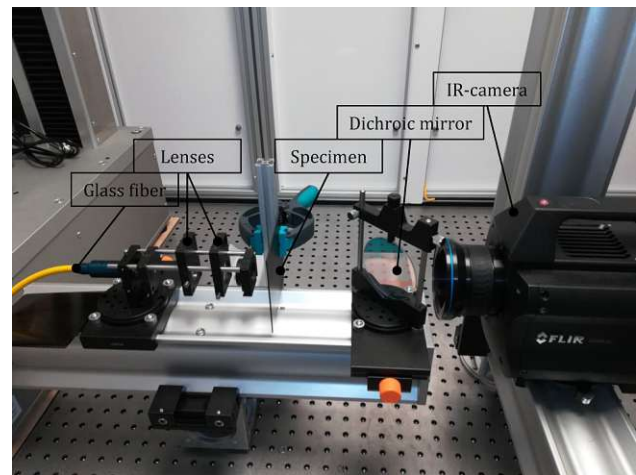


FIG. 12. Experimental setup.

and the bandwidth is greater than 50 kHz. The maximum power is 250 W and the numerical aperture is 0.22. The IR camera has a NEDT smaller than 25 mK. It has a cooled indium antimony (InSb) sensor that is sensitive in the spectral range of $3.0\text{--}5.1 \mu\text{m}$. The laser power for the different measurements of the UD8 sample was 25 W and the heating time in the experiment was $t_h = \{0.01, 0.02, 0.03\}$ s with a laser-spot diameter of approximately 1.5 mm. For the UD16 sample, the laser power was again

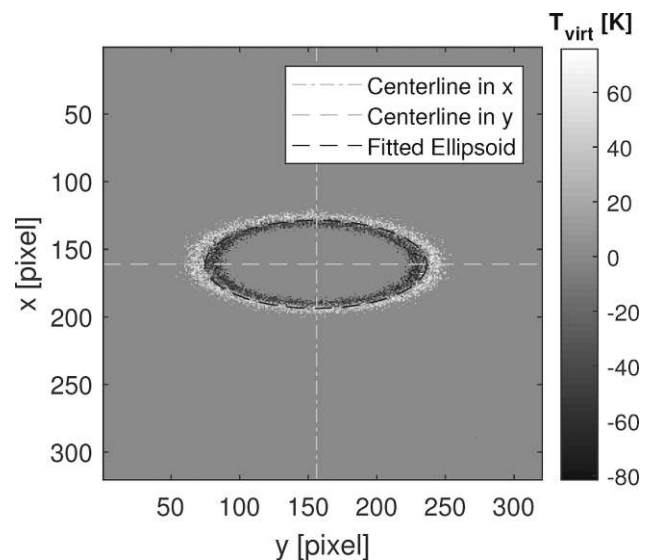


FIG. 13. Visualization of virtual wave field at $z^* = c_{33}t^* = 2.32$ mm. For the ellipse fit, the function in Ref. 30 was used.

25 W, the heating time t_h was 0.04 s, and the laserspot diameter was approximately 2.5 mm. Due to the laser heating, the specimen was thermally stimulated. Simultaneously, the temperature signal was recorded in transmission mode. For the UD8 sample, the image frequency of the IR camera was 227 Hz and the spatial resolution was $\Delta_x = 56.6 \mu\text{m}$. For the UD16 sample, the image frequency was 57 Hz and the spatial resolution was $\Delta_x = 91.6 \mu\text{m}$.

1. Parameter estimation and image reconstruction

For the estimation of the thermal diffusivity in axial direction α_{33} , the data evaluation was equal to the procedure for simulated data. Furthermore, we make use of an effective medium approximation for the estimation of the thermal diffusivity. The assumption is that the UD samples have no distinctive interfaces between the single plies, because the orientation of the layers does not change. The starting value for the axial thermal diffusivity was prescribed with $\hat{\alpha}_{33} = 0.31 \times 10^{-6} \text{ m}^2/\text{s}$ for each evaluation. Then, we

calculated the scattering hyperboloid using c_{33} and α_{33} . Because this approach and formalism is only valid if the main axes of the coordinate system lie in the principal directions of heat conduction, we checked the orientation of the main axes. For the verification, we observed the computed scattering hyperbola at the depth $z^* = c_{33}t^* = 2.32 \text{ mm}$. The shape of the cross section is described by an ellipse, as shown in Fig. 13. Hence, we can perform an ellipse fit to check if the main axes are in the principle thermal diffusivity direction. Furthermore, especially for experimental data, we can determine the center of the ellipsoid and, hence, the symmetry cross sections of the hyperboloid. Figures 14 and 15 show the evaluation of the dimensionless virtual speeds of sound \tilde{c}_{11} and \tilde{c}_{22} for the UD8 sample. The top image shows the temperature signal at the symmetry cross section. In the middle, the corresponding virtual wave field is illustrated. The bottom graph shows the extracted fitting data and the fitted curve. For the estimation of \tilde{c}_{11} and \tilde{c}_{22} , data points until a depth of $z = c_{33}t^* = 2.5 \text{ mm}$ were used. For the evaluation of the UD16 sample, data points until a depth of

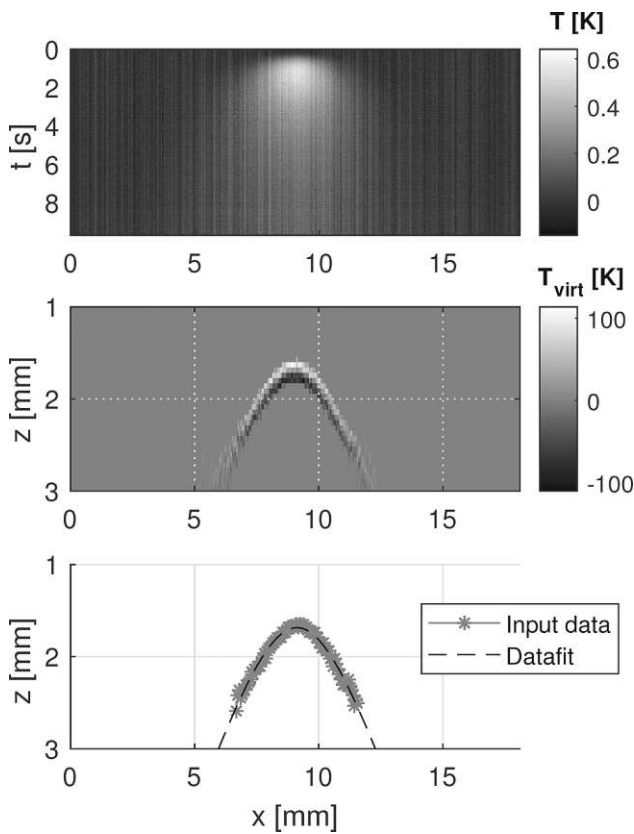


FIG. 14. Top: Cross section of the measured temperature field, with $t_h = 0.02 \text{ s}$, at the centerline of y . Middle: Corresponding cross section of the computed virtual wave field. Bottom: Extracted data points of the virtual wave field to estimate the dimensionless virtual speed of sound \tilde{c}_{11} . The black dashed line is the fitted curve.

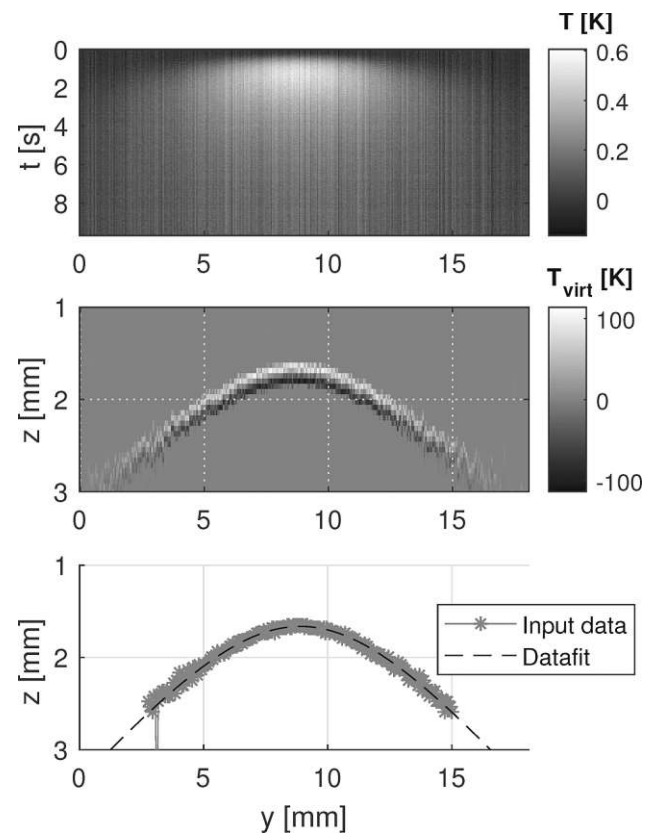
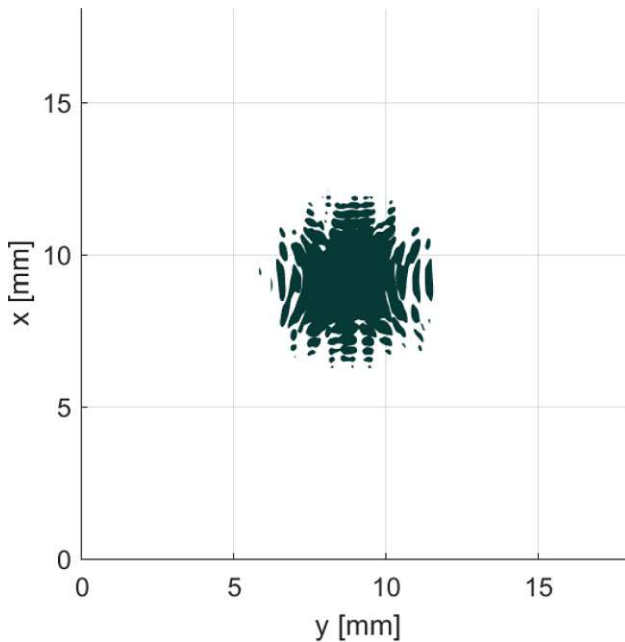


FIG. 15. Top: Cross section of the measured temperature field, with $t_h = 0.02 \text{ s}$, at the centerline of x . Middle: Corresponding cross section of the computed virtual wave field. Bottom: Extracted data points of the virtual wave field to estimate the dimensionless virtual speed of sound \tilde{c}_{22} . The black dashed line is the fitted curve.

TABLE II. Estimated parameters based on experimental data consisting of mean value and standard deviation.

Sample	UD8		UD16		Unit
	0.01	0.02	0.03	0.04	
\tilde{c}_{11}	...	1.25 ± 0.03	1.21 ± 0.04	1.23 ± 0.09	(...)
\tilde{c}_{22}	...	3.10 ± 0.04	3.11 ± 0.08	3.12 ± 0.16	(...)
α_{11}	...	0.58 ± 0.03	0.54 ± 0.04	0.55 ± 0.07	(mm ² /s)
α_{22}	...	3.55 ± 0.07	3.56 ± 0.17	3.55 ± 0.31	(mm ² /s)
α_{33}	0.37 ± 0.00	0.37 ± 0.00	0.37 ± 0.00	0.36 ± 0.01	(mm ² /s)

$z = c_{33}t' = 5$ mm were used. Table II lists the results for different heating times t_h and equal laser power and consequently different SNRs. For each heating time, five measurements were performed. Hence, the listed results consist of a mean value and the corresponding standard deviation. The kernel for a Dirac–Delta like heating K was temporally convolved with the corresponding heating function to account for the different heating times.¹³ As visible in Table II, the estimated values match well. Due to the low SNR, only α_{33} was evaluable for $t_h = 0.01$. Figure 16 exhibits the reconstructed initial temperature field T_0 based on measured surface temperature data by applying F-SAFT and the estimated dimensionless speed of sound tensor \tilde{c} on the computed virtual wave field. As expected, the reconstruction shows a circular area as

**FIG. 16.** Isosurface representation of the reconstructed initial temperature field T_0 , based on measured surface temperature data with $t_h = 0.02$ s, by applying F-SAFT and the estimated speed of sound tensor \tilde{c} on the computed virtual wave field.

a consequence of the point-like laser heating with finite laser spot diameter. Furthermore, the estimated values of the UD8 and UD16 sample match well, which proves that the application of an effective medium approximation is valid for this type of specimen. For the axial thermal diffusivity estimations, we carried out reference evaluations with the linear diffusivity fit (LDF)-method, which also bases on measurements in transmission mode. The LDF method bases on a 1D solution of heat equation for a semi-infinite body and a temporal Dirac–Delta heating.^{31,32} Using this method and the same evaluation domain, we obtained for the UD8 sample a axial thermal diffusivity of $\alpha_{33} = 3.68 \times 10^{-7}$ m²/s and for the UD16 sample $\alpha_{33} = 3.65 \times 10^{-7}$ m²/s. These results match the values obtained via VWC very well, which proves the new evaluation method additionally.

IV. CONCLUSIONS

In this work, we have extended the VWC for the 3D image reconstruction of composite materials with an orthotropic heat conduction tensor. The extension includes a new approach for the estimation of the orthotropic thermal diffusivity tensor based on the virtual scattering hyperbolas.

For this purpose, we transformed the orthotropic heat equation and wave equation into isotropic PDEs to establish a formal relationship between the virtual speed of sound \mathbf{c} and the thermal diffusivity tensor $\boldsymbol{\alpha}$. To increase the accuracy for parameter estimation and image reconstruction, we incorporated prior information in the form of positivity and sparsity. The 3D bimodal virtual wave signal resulting from a 3D temperature field is projected onto a positive dataset to incorporate the prior information positivity. We can also assume a sparse reconstruction matrix \mathbf{T}_{virt} due to the spatial point-like and temporal short laser excitation. Based on the calculated virtual scattering hyperboloid, we proposed an evaluation procedure for the virtual speed of sound tensor. The virtual speed of sound tensor enables a high-resolution image reconstruction of composite materials and a precise parameter estimation of the thermal diffusivity tensor. To validate the presented approach, we carried out finite element evaluations. In addition, we made reference evaluations based on the LDF method to check if the axial thermal diffusivity values obtained via VWC are plausible. The circular reconstruction of the initial temperature distribution shows that the estimations of the thermal diffusivities in plane are meaningful.

The benefits of the proposed procedure are:

- 3D visualization of the orthotropic/anisotropic thermal diffusion based on the computed scattering hyperboloid.
- The initial temperature distribution and the thermal diffusivity tensor can be computed with the same method.
- Better defect detectability is possible because of the incorporation of prior information positivity and sparsity and the rectification of the anisotropic thermal diffusion.
- Due to the local transformation between temperature and virtual wave signal, the method can be readily parallelized yielding a computationally efficient reconstruction method.

In future work, the potential of the VWC for composite materials should be tested on complex shaped industrial manufactured

components. In addition, the determination of the thermal diffusivity tensor should be adapted for applications, in which the coordinate system is not parallel to the three mutually perpendicular preferred thermal diffusion directions. Furthermore, the VWC for parameter estimation and image reconstruction should be applied for different heating functions, e.g., a sequence of temporal rectangular pulses. In contrast to an illumination with a single pulse, this allows a higher energy input for a certain limited maximum illumination power, and thus to increase the SNR.

ACKNOWLEDGMENTS

The financial support by the Austrian Federal Ministry of Science, Research and Economy and the National Foundation for Research, Technology and Development is gratefully acknowledged. Furthermore, this work has been supported by the project multimodal and *in situ* characterization of inhomogeneous materials (MiCi), by the Federal Government of Upper Austria and the European Regional Development Fund (EFRE) in the framework of the EU-program IWB2020. Signal and data processing was funded by the Austrian Science Fund (FWF) (Project No. P 33019-N).

APPENDIX A: ESTIMATION OF EVALUATION TIME

To decrease the computational cost for the estimation of the thermal diffusivity in axial direction α_{33} , we propose a cut-off criterion regarding the observation time for simulated and measured temperature data. For this purpose, we solve the direct problem respecting an orthotropic material. As mentioned in Sec. II, the orthotropic heat conduction problem can be transformed into an isotropic heat conduction problem, with the thermal diffusivity $\alpha = (\alpha_{11}\alpha_{22}\alpha_{33})^{1/3}$, by scaling the principle axes. For the solution of the forward problem, we reconsider Fig. 2. In the x - y plane, the sample is assumed to be extended to infinity, because the laser spot is small compared to the lateral dimensions. In the depth direction, we assume adiabatic boundary conditions and the sample thickness L_z . The corresponding Green's functions are³³

$$G_{XY00}(\bar{x}, \bar{y}, t|\bar{x}', \bar{y}', \tau) = \frac{1}{4\pi\alpha(t-\tau)} \times \exp\left[-\frac{(\bar{x}-\bar{x}')^2 + (\bar{y}-\bar{y}')^2}{4\alpha(t-\tau)}\right] \quad (A1)$$

and

$$G_{Z22}(\bar{z}, t|\bar{z}', \tau) = \frac{1}{L} \left[1 + 2 \sum_{m=1}^{\infty} \exp\left[-\frac{m^2\pi^2\alpha(t-\tau)}{\bar{L}_z^2}\right] \times \cos\left(\frac{m\pi\bar{z}}{\bar{L}_z}\right) \cos\left(\frac{m\pi\bar{z}'}{\bar{L}_z}\right) \right]. \quad (A2)$$

Due to the rectangular coordinate system and the assumed boundary conditions (zeroth and second kind), we can multiply Eqs. (A1) and (A2) to obtain Green's function for the 3D heat conduction case. The heat source term $g(\bar{x}, \bar{y}, \bar{z}, t) = q_0\Theta(\sqrt{\bar{x}^2 + \bar{y}^2})\delta(\bar{z})\delta(t)$ is modeled with a temporal Dirac-Delta pulse (short laser pulse) $\delta(t)$, a lateral rectangular pulse $\Theta(\sqrt{\bar{x}^2 + \bar{y}^2})$ and a Dirac-Delta pulse in depth direction $\delta(\bar{z})$. The laser spot has radius η and q_0 [J/m²] denotes the heat flux. For the sake of simplicity, we shifted the coordinate system into the center of excitation ($x_d = 0$ and $y_d = 0$). For the estimation of the evaluation time, we observe the temporal temperature signal at the center point $\bar{x} = x\sqrt{\alpha/\alpha_{11}} = 0$ and $\bar{y} = y\sqrt{\alpha/\alpha_{22}} = 0$. Applying Green's function solution equation (GFSE)²⁶ gives the corresponding temperature signal,

$$T(\bar{x} = 0, \bar{y} = 0, \bar{z}, t) = \frac{\alpha}{k} \int_0^t \int_{-\eta}^{\eta} \int_{-\sqrt{\eta^2 - \bar{x}^2}}^{\sqrt{\eta^2 - \bar{x}^2}} \int_0^{\bar{L}_z} G_{XY00}(0, 0, t|\bar{x}', \bar{y}', \tau) \times G_{Z22}(\bar{z}, t|\bar{z}', \tau)g(\bar{x}', \bar{y}', \bar{z}', \tau) d\bar{z}' d\bar{y}' d\bar{x}' d\tau. \quad (A3)$$

The dimensionless temperature solution $V(\bar{z}, t) = T(\bar{z}, t)\rho c_p \bar{L}_z / q_0$ of Eq. (A3) is given by

$$V(\bar{z}, t) = \left[1 - \exp\left(-\frac{\eta^2}{4\alpha t}\right) \right] \times \left[1 + 2 \sum_{m=1}^{\infty} \exp\left[-\frac{m^2\pi^2\alpha t}{\bar{L}_z^2}\right] \cos\left(\frac{m\pi\bar{z}}{\bar{L}_z}\right) \right]. \quad (A4)$$

In our experiment, we collect the temperature in transmission mode. Hence, we evaluate Eq. (A4) at the stretched depth \bar{L}_z ,

$$V(\bar{z} = \bar{L}_z, t) = \left[1 - \exp\left(-\frac{\eta^2}{4\alpha t}\right) \right] \times \left[1 + 2 \sum_{m=1}^{\infty} \exp\left[-\frac{m^2\pi^2\alpha t}{\bar{L}_z^2}\right] (-1)^m \right]. \quad (A5)$$

Furthermore, we can substitute for $\bar{L}_z = L_z\sqrt{\alpha/\alpha_{33}}$ and introduce the dimensionless time $u = \pi^2\alpha_{33}t/L^2$ that enables us to split the radial from the axial temperature component,

$$V(\bar{z} = \bar{L}_z, u) = \underbrace{\left[1 - \exp\left(-\frac{\eta^2\pi^2}{4\bar{L}_z^2 u}\right) \right]}_{\text{radial component } V_r} \underbrace{\left[1 + 2 \sum_{m=1}^{\infty} \exp[-m^2 u] (-1)^m \right]}_{\text{axial component } V_a}. \quad (A6)$$

Figure 17 shows the radial temperature signal V_r , the axial temperature signal V_a , and the resulting temperature curve $V_r \times V_a$ as a function of u for the laser-spot radius $\eta = 0.75$ mm. It is visible that with increasing time, the influence of the axial component $V_a \approx 1$ decreases, and the resulting temperature signal is approximately V_r . Therefore, at a certain point in time u^* , the resulting temperature signal has no significance for the estimation of the axial thermal diffusivity. Hence, the evaluation domain is defined as $\{0, u^*\}$ (Fig. 17, gray background). We define the characteristic point u^* as the time step that corresponds to the local

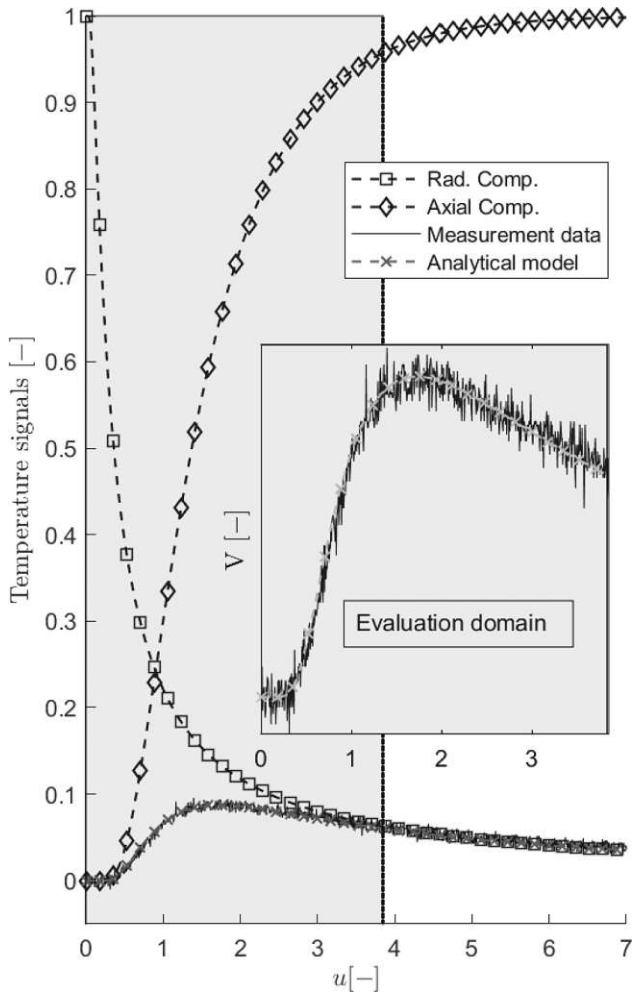


FIG. 17. Illustration of the radial component, the axial component, and the resulting temperature signal at the center point ($x = 0, y = 0$) due to a short laser pulse with laser spot diameter η following Ref. 34. The gray background shows the evaluation time for the estimation of the axial thermal diffusivity. In the exploded area, the analytical and measured temperature slopes are plotted. The measured temperature slope corresponds to a heating time of $t_h = 0.02$ s. The analytical slope was plotted with the estimated parameters listed in Table II ($t_h = 0.02$ s.). As visible, the analytical model fits the measurement data well.

maximum of the second derivative in the cooling domain. The benefit of this definition is that u^* can be determined without the prior knowledge of α_{33} . At this point, the influence of V_a to the resulting temperature curve is lower than 5%. Due to the noisy temperature data, we use the filtered temperature signal $T_{\text{rec}} = \mathbf{K}T_{\text{virt}}$ obtained during calculation of $\hat{\alpha}_{33}^{\text{cor}}$ to calculate the observation time u^* .

APPENDIX B: ANALYTICAL 3D VIRTUAL WAVE SIGNAL

In this section, we deduce the analytical relationship between temperature signal and virtual wave signal based on the same model that is described in Appendix A. The aim of the subsequent steps is to provide a deeper insight into the analytical temperature to virtual wave transformation, while on the other hand, the proof of the formal relationship $\alpha_{33} = \hat{\alpha}_{33}(L_z/\bar{L}_z)^2$ claimed in Sec. III B that may not be straightforward for anisotropic thermal diffusion. For the sake of simplicity and in contrast to Appendix A, we consider a point-like thermal source $g(\bar{r}, t) = q_0\delta(\bar{r})\delta(t)$ and in axial direction, the adiabatic Green's function obtained via the method of images.³³ The unit of the instantaneous point source q_0 is W s. The corresponding temperature function is

$$T(\bar{r}, t) = \frac{2q_0}{(4\pi\alpha t)^{3/2}} \frac{\alpha}{k} \sum_{n=-\infty}^{\infty} \exp\left[-\frac{\bar{x}^2 + \bar{y}^2 + (2n\bar{L}_z + \bar{z})^2}{4\alpha t}\right]. \quad (\text{B1})$$

Again, we have $\alpha = (\alpha_{11}\alpha_{22}\alpha_{33})^{1/3}$. In the next steps, we determine the corresponding virtual wave field $T_{\text{virt}}(\bar{r}, t')$ based on Eqs. (11) and (15). Further, we take into account the property

$$\int_{-\infty}^{\infty} f(t') \frac{\partial}{\partial t'} \delta(t' - a) dt' = -\frac{\partial}{\partial t'} f(a) \quad (\text{B2})$$

of the Dirac-Delta distribution.³⁵ We assume the correct thermal diffusivity α_{33} is unknown. For this reason, we bring in an estimation $\hat{\alpha}_{33}$ for the thermal diffusivity to Eq. (15). Substituting this into Eq. (11) yields,

$$\begin{aligned} & \frac{2q_0}{(\pi\alpha t)^{3/2}} \frac{\alpha}{k} \sum_{n=-\infty}^{\infty} \exp\left[-\frac{\bar{x}^2 + \bar{y}^2 + (2n\bar{L}_z + \bar{z})^2}{4\alpha t}\right] \\ &= \int_{-\infty}^{\infty} T_{\text{virt}}(\bar{r}, t') \frac{c_{33}}{\sqrt{\pi\hat{\alpha}_{33}t'}} \exp\left(-\frac{c_{33}^2 t'^2}{4\hat{\alpha}_{33}t}\right) dt'. \end{aligned} \quad (\text{B3})$$

From Eqs. (B2) and (B3), we can deduce the corresponding virtual wave field,

$$\begin{aligned} T_{\text{virt}}(\bar{r}, t') &= \frac{1}{2} \frac{q_0 \hat{\alpha}_{33}}{k \pi c_{33}} \sum_{n=-\infty}^{\infty} \frac{\partial}{\partial t'} \\ &\times \frac{\delta\left[c_{33}t' - \sqrt{\bar{x}^2 + \bar{y}^2 + (2n\bar{L}_z + \bar{z})^2} \sqrt{\frac{\hat{\alpha}_{33}}{\alpha}}\right]}{\sqrt{\bar{x}^2 + \bar{y}^2 + (2n\bar{L}_z + \bar{z})^2}}. \end{aligned} \quad (\text{B4})$$

For the estimation of α_{33} , we consider the virtual wave field at $\bar{x} = x\sqrt{\alpha/\alpha_{11}} = 0$, $\bar{y} = y\sqrt{\alpha/\alpha_{22}} = 0$ and rescale the z -axes,

$$T_{\text{virt}}(0, 0, z, t') = \frac{1}{2} \frac{q_0 \hat{\alpha}_{33}}{k\pi c_{33}} \sum_{n=-\infty}^{\infty} \frac{\partial}{\partial t'} \delta \left[c_{33} t' - (2nL_z + z) \sqrt{\frac{\alpha}{\alpha_{33}}} \sqrt{\frac{\hat{\alpha}_{33}}{\alpha}} \right] \times \frac{1}{(2nL_z + z) \sqrt{\frac{\alpha}{\alpha_{33}}}}. \quad (\text{B5})$$

For the estimation of α_{33} , we evaluate the first mirror source. Due to this fact, we only evaluate the term $n = 0$ at $z = L_z$ in Eq. (B5),

$$T_{\text{virt}}(0, 0, L_z, t') = \frac{1}{2} \frac{q_0 \hat{\alpha}_{33}}{k\pi c_{33}} \frac{\partial}{\partial t'} \frac{\delta \left[c_{33} t' - L_z \sqrt{\frac{\hat{\alpha}_{33}}{\alpha_{33}}} \right]}{L_z \sqrt{\frac{\alpha}{\alpha_{33}}}}. \quad (\text{B6})$$

Using the time-of-flight method, we estimate the thickness $\hat{L}_z = c_{33} t_f$ of the sample, where t_f is the time of flight. If $\hat{\alpha} = \alpha$, the estimated thickness is equal to the correct thickness L_z . Otherwise, as obvious in the argument of the Dirac-Delta distribution, we must correct the thermal diffusivity in the following manner:

$$\alpha_{33}^{\text{cor}} = \alpha_{33} = \hat{\alpha}_{33} \left(\frac{L_z}{\hat{L}_z} \right)^2. \quad (\text{B7})$$

DATA AVAILABILITY

The data that support the findings of this study are available from the corresponding author upon reasonable request.

REFERENCES

- V. P. Vavilov and D. D. Burleigh, "Review of pulsed thermal NDT: Physical principles, theory and data processing," *NDT E Int.* **73**, 28–52 (2015).
- P. Tavakolian and A. Mandelis, "Perspective: Principles and specifications of photothermal imaging methodologies and their applications to non-invasive biomedical and non-destructive materials imaging," *J. Appl. Phys.* **124**, 160903 (2018).
- H. R. B. Orlande, *Thermal Measurements and Inverse Techniques, Heat Transfer* (CRC Press, Boca Raton, FL, 2011).
- M. N. Ozisik and H. R. Orlande, *Inverse Heat Transfer: Fundamentals and Applications* (Routledge, Boca Raton, FL, 2018).
- A. Mendioroz, K. Martínez, R. Celorrio, and A. Salazar, "Characterizing the shape and heat production of open vertical cracks in burst vibrothermography experiments," *NDT E Int.* **102**, 234–243 (2019).
- S. D. Holland and B. Schiefelbein, "Model-based inversion for pulse thermography," *Exp. Mech.* **59**, 413–426 (2019).
- S. Kaipilavil and A. Mandelis, "Truncated-correlation photothermal coherence tomography for deep subsurface analysis," *Nat. Photonics* **8**, 635–642 (2014).
- P. Tavakolian, K. Sivagurunathan, and A. Mandelis, "Enhanced truncated-correlation photothermal coherence tomography with application to deep subsurface defect imaging and 3-dimensional reconstructions," *J. Appl. Phys.* **122**, 023103 (2017).
- P. Burgholzer, M. Thor, J. Gruber, and G. Mayr, "Three-dimensional thermographic imaging using a virtual wave concept," *J. Appl. Phys.* **121**, 105102 (2017).

- K. H. Lee, G. Liu, and H. F. Morrison, "A new approach to modeling the electromagnetic response of conductive media," *Geophysics* **54**, 1180–1192, (1989).
- M. Gershenson, *Simple Interpretation of Time Domain Electromagnetic Sounding Using Similarities Between Wave and Diffusion Propagation* (SPIE, 1995), pp. 942–947.
- G. Mayr, G. Stockner, H. Plasser, G. Hendorfer, and P. Burgholzer, "Parameter estimation from pulsed thermography data using the virtual wave concept," *NDT E Int.* **100**, 101–107 (2018).
- P. Burgholzer, G. Stockner, and G. Mayr, "Acoustic reconstruction for photo-thermal imaging," *Bioengineering* **5**, 70 (2018).
- L. J. Busse, "Three-dimensional imaging using a frequency-domain synthetic aperture focusing technique," *IEEE Trans. Ultrason. Ferroelectr. Freq. Control* **39**, 174–179 (1992).
- G. Thummerer, G. Mayr, M. Haltmeier, and P. Burgholzer, "Photoacoustic reconstruction from photothermal measurements including prior information," *Photoacoustics* **19**, 100175 (2020).
- G. Thummerer, G. Mayr, P. D. Hirsch, M. Ziegler, and P. Burgholzer, "Photothermal image reconstruction in opaque media with virtual wave backpropagation," *NDT E Int.* **112**, 102239 (2020).
- S. Torquato, in *Random Heterogeneous Materials: Microstructure and Macroscopic Properties/Salvatore Torquato*, Interdisciplinary Applied Mathematics. Mechanics and Materials Vol. 15 (Springer, New York, 2002).
- H. S. Carslaw and J. C. Jaeger, *Conduction of Heat in Solids*, 2nd ed. (Oxford Science Publications, Oxford, 1986).
- M. R. Kulkarni and R. P. Brady, "A model of global thermal conductivity in laminated carbon/carbon composites," *Compos. Sci. Technol.* **57**, 277–285 (1997).
- A. N. Salazar, "On thermal diffusivity," *Eur. J. Phys.* **24**, 351–358 (2003).
- J. C. Krapez, G. Gardette, and D. Balageas, "Thermal ellipsometry in steady-state or by lock-in thermography. Application for anisotropic materials characterization," in *Proceedings of the 1996 International Conference on Quantitative InfraRed Thermography* (QIRT Council, 1996).
- L. Gavérina, J. C. Batsale, D. Mourand, and C. Pradere, "Estimation of the thermal diffusivities tensor out of the main axes of anisotropy with a pulsed laser spot method," in *Proceedings of the 2016 International Conference on Quantitative InfraRed Thermography* (QIRT Council, 2016).
- A. Salazar, A. Sánchez-Lavega, A. Ocariz, J. Guitonny, J. C. Pandey, D. Fournier, and A. C. Boccara, "Novel results on thermal diffusivity measurements on anisotropic materials using photothermal methods," *Appl. Phys. Lett.* **67**, 626–628 (1995).
- A. Salazar, A. Sánchez-Lavega, A. Ocariz, J. Guitonny, G. C. Pandey, D. Fournier, and A. C. Boccara, "Thermal diffusivity of anisotropic materials by photothermal methods," *J. Appl. Phys.* **79**, 3984 (1996).
- N. Tralshawala, D. R. Howard, B. Knight, Y. Plotnikov, and H. I. Ringermacher, "Lateral heat flow method for thickness independent determination of thermal diffusivity," *J. Appl. Phys.* **102**, 083522 (2007).
- D. W. Hahn and M. N. Özisik, *Heat Conduction*, 3rd ed. (Wiley, Hoboken, NJ, 2012).
- P. Burgholzer, J. Bauer-Marschallinger, H. Grün, M. Haltmeier, and G. Paltauf, "Temporal back-projection algorithms for photoacoustic tomography with integrating line detectors," *Inverse Probl.* **23**, S65–S80 (2007).
- S. Boyd, "Distributed optimization and statistical learning via the alternating direction method of multipliers," *Found. Trendsx24C7; Mach. Learn.* **3**, 1–122 (2010).
- R. C. Aster, B. Borchers, and C. H. Thurber, *Parameter Estimation and Inverse Problems*, 3rd ed. (Elsevier, Amsterdam, 2018).
- Ohad Gal, "fit_ellipse," see https://www.mathworks.com/matlabcentral/fileexchange/3215-fit_ellipse, MATLAB Central File Exchange (last accessed May 26, 2020).
- G. Hendorfer, G. Mayr, G. Zauner, M. Haslhofer, and R. Pree, "Quantitative determination of porosity by active thermography," *AIP Conf. Proc.* **894**, 702–708 (2007).

³²G. Mayr, B. Plank, J. Sekelja, and G. Hendorfer, "Active thermography as a quantitative method for non-destructive evaluation of porous carbon fiber reinforced polymers," *NDT E Int.* **44**, 537–543 (2011).

³³K. D. Cole, J. V. Beck, A. Haji-Sheikh, and B. Litkouhi, in *Heat Conduction Using Green's Functions*, 2nd ed., Series in Computational and Physical Processes in Mechanics and Thermal Sciences (CRC Press, Boca Raton, FL, 2011).

³⁴M. A. Sheikh, S. C. Taylor, D. R. Hayhurst, and R. Taylor, "Measurement of thermal diffusivity of isotropic materials using a laser flash method and its validation by finite element analysis," *J. Phys. D Appl. Phys.* **33**, 1536–1550 (2000).

³⁵G. B. Arfken and H.-J. Weber, *Mathematical Methods for Physicists*, 6th ed. (Elsevier Academic Press, Amsterdam, 2008).

5.4 3D photothermal imaging of subsurface defects in composite materials

In this study, a fast, easily interpretable, and efficient 3D photothermal "pulse-echo" defect imaging tool for nondestructive testing of anisotropic materials is presented. Here, the findings of Paper 5.3 are applied to CFRP specimens with artificial subsurface defects. The artificial defects are represented by flat bottom holes with varying defect-diameter-to-depth ratios. To optimize the computation time of the VWC procedure without affecting the reconstruction quality, a discretization criterion was proposed by a parameter study and physical-based considerations. To obtain the evaluation data, the observed CFRP specimens were thermally excited with flash lamps and the surface temperature signal was measured simultaneously in the pulse-echo configuration. A source and sink model was proposed to explain the characteristics of the virtual wave signal due to the disturbed thermal diffusion caused by a defect. As in the previous papers the iterative regularization tool ADMM was used for the temperature-to-virtual wave signal transformation.

The results of the source and sink explanation suggest that for highly anisotropic samples, positivity as prior information can not be incorporated by calculating the spherical projection of the virtual wave signal. In addition, the results show that when the signal-to-noise ratio is high enough, the FBH diameter can be reconstructed well, but the depth of the FBH interfaces can not be localized exactly. Due to the finding that subsurface defects yield a source and sink in the virtual wave signal, their depth can be estimated. The proposed multi-dimensional reconstruction procedure is fast and the results are easy to interpret, since the same visualization techniques as for ultrasonic reconstructions (A-scan, B-scan C-scan) can be used.

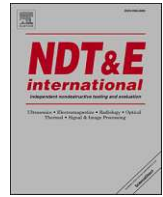
Authorship contribution statement

G. Thummerer: Conceptualization, Methodology, Software, Formal analysis, Validation, Investigation, Writing - original draft, Visualization. **G. Mayr:** Conceptualization, Writing - review & editing, Project administration, Funding acquisition. **P. Burgholzer:** Writing - review & editing, Supervision, Funding acquisition.



Contents lists available at ScienceDirect

NDT and E International

journal homepage: www.elsevier.com/locate/ndteint

3D photothermal imaging of subsurface defects in composite materials

G. Thummerer^{a,*}, G. Mayr^a, P. Burgholzer^b

^a Josef Ressel Centre for Thermal NDE of Composites, University of Applied Sciences Upper Austria, Wels, Austria

^b RECENDT - Research Centre for Nondestructive Testing, Linz, Austria

ARTICLE INFO

Keywords:

Active thermography
Photothermal technique
Virtual wave concept
Image reconstruction
Carbon fiber reinforced polymer

ABSTRACT

In this work, we show the application of the virtual wave concept for 3D “pulse-echo” photothermal defect imaging in anisotropic materials. We consider a woven and a unidirectional carbon fiber reinforced material including flat bottom holes with varying diameter-to-depth ratios. We discuss the characteristics of the virtual wave signal due to disturbed heat diffusion caused by a defect and the resulting consequences for our defect reconstruction method regarding the incorporation of prior information. In addition, we optimize the virtual wave concept in terms of computation time by performing a parameter study and a physical-based derivation that suggest reasonable values for the temporal and spatial discretization, respectively. The paper presents a very fast, easily interpretable and efficient 3D reconstruction tool for active thermography testing of anisotropic materials.

1. Introduction

Large, thin-wall monolithic components made from carbon fiber reinforced polymers (CFRP) used in the aerospace and automotive industries are predestined for non-destructive testing (NDT) with active thermography (AT) [1,2]. Using this contactless and fast thermal NDT method, the sample under test (SUT) can be subjected to an arbitrary heating that varies in time and space. Simultaneously, the resulting surface temperature signal can be recorded with an infrared (IR) camera in reflection (“pulse-echo”) or transmission mode. In industrial applications, the reflection mode is of particular interest because the components are often only accessible from one side [3,4]. The crucial challenge with AT testing is the diffusive nature of thermal waves [5,6]. Heat diffusion causes entropy production that is equal to information loss and hence leads to blurred images for deeper lying structures [7]. The surface temperature signal and the noise equivalent temperature difference (NETD) from the IR camera result in a certain signal-to-noise ratio (SNR). This is in principle the limiting factor for maximum defect depth or back wall resolution and defect separation. This limitation can be overcome with enhanced signal processing methods including prior information of the experiment [8–10]. The near surface defect resolution limit depends only on the camera frame rate [9]. The surface temperature signal contains information about possible defects or irregularities in the sample, which can be partially and qualitatively revealed by standard post processing methods such as the pulse phase

thermography (PPT) [11] and the thermographic signal reconstruction (TSR) [12,13]. Mulaveesala and Tuli [14,15] proposed another data-based approach, called frequency-modulated thermal wave imaging, for non-destructive detection of subsurface defects, which uses a temporal frequency modulated thermal excitation signal. Later, Kiplavil and Mandelis [16] introduced the truncated-correlation photothermal coherence tomography (TC-PCT). This approach uses a matched filtering technique to improve the lateral and axial resolution which enables a 3D visualization of subsurface features. Tavakolian et al. [17] enhanced TC-PCT by an optimized evaluation system and reconstruction algorithm. These 1D methods do not take into account a lateral heat flow and thus making a precise defect sizing difficult or impossible especially when testing highly anisotropic materials, like CFRP.

Recent multidimensional approaches, which use the fundamental solution of heat conduction, count for the lateral heat flow in composite materials. For example, Groz et al. [18] introduced a model-based inversion procedure for an infinite body and internal heat sources, where a reasonable discretization of AT data was discussed in detail. Holland and Schiefelbein [19] proposed an inversion for thermographic data with a temporal short excitation pulse in reflection mode. Their model is constructed with multiple reflectors which are set in different depths with different lateral resolutions in the reconstruction domain. Both approaches end in a large scale problem which is in general computationally very expensive.

Burgholzer et al. [20] introduced an alternative two step

* Corresponding author.

E-mail address: gregor.thummerer@fh-wels.at (G. Thummerer).

<https://doi.org/10.1016/j.ndteint.2021.102476>

Received 31 December 2020; Received in revised form 30 April 2021; Accepted 20 May 2021

Available online 2 June 2021

0963-8695/© 2021 The Author(s). Published by Elsevier Ltd. This is an open access article under the CC BY license (<http://creativecommons.org/licenses/by/4.0/>).

reconstruction method, the so-called virtual wave concept (VWC). In a first step, the measured surface temperature signal is transformed locally (pixelwise) into a virtual wave signal. This virtual wave signal obeys the wave equation and hence, in a second step, well known ultrasonic reconstruction methods like the frequency domain synthetic aperture focusing technique (F-SAFT) [21] can be applied for defect reconstruction. This reconstruction step accounts for the lateral heat flow and improves the SNR by integrating along scattering hyperbolas and can be interpreted as a matched filter method. VWC is inexpensive because the local surface temperature-to-virtual wave signal transformation can be readily parallelized and the second inversion step is performed without explicit regularization in the frequency domain. In a previous work, we have extended this method and introduced a fully multidimensional image reconstruction and parameter estimation procedure that enables the rapid and robust defect detection of composite materials [22]. This work applies the VWC to woven and unidirectional (UD) composite materials with flat bottom holes (FBHs) with varying diameter-to-depth ratios. Furthermore, we deduce a discretization criterion which can be used to optimize the evaluation performance of the virtual wave concept. The paper is organized as follows: In the first section, we introduce the mathematical framework of the virtual wave concept and an optimization approach by a parameter study and analytical considerations. We discuss the characteristics of the virtual wave signal due to disturbed heat diffusion, caused by a defect. In the second section we show the results obtained from the FBH sample for both woven and UD composite material.

2. Virtual wave concept

In this section, we formulate a discretization criterion for the virtual wave concept (VWC) in order to speed up the evaluation procedure and to increase the defect detection capability. For the multidimensional reconstruction of defects, the following evaluation steps are performed:

1. The change of the surface temperature signal due to the thermal stimulation of the SUT is recorded with an IR camera.
2. The measured surface temperature signal is transformed into a so-called virtual wave signal which obeys the wave equation.
3. Finally, ultrasonic reconstruction methods are applied for the defect sizing and the rectification of the anisotropic heat flow.

In this section, we focus on the second evaluation step - the transformation between the surface temperature signal $T(\mathbf{r}, t)$ and virtual wave signal $T_{\text{virt}}(\mathbf{r}, t')$. The corresponding mathematical formulation is given by Ref. [20].

$$T(\mathbf{r}, t) = \int K(t, t') T_{\text{virt}}(\mathbf{r}, t') dt' \quad (1)$$

with $K(t, t') = \frac{c}{\sqrt{\pi \alpha t}} \exp\left(-\frac{c^2 t'^2}{4 \alpha t}\right)$

Herein α denotes the thermal diffusivity and c is the virtual speed of sound. Eq. (1) shows that the kernel K is independent of the position vector $\mathbf{r} = (x, y, z)$. Therefore, Eq. (1) describes a local transformation between surface temperature and virtual wave signal. The Fredholm integral of the first kind, Eq. (1), is valid for a temporal Dirac-Delta thermal stimulation. Because the experimental data is discrete in space and time, we discretize the Fredholm integral which yields a linear matrix equation. Especially for one spatial cross section of the 3D SUT, with pixel number q , we can write:

$$\mathbf{T} = \mathbf{K} \mathbf{T}_{\text{virt}} \quad (2)$$

The dimensions of these matrices are $\mathbf{T} \in \mathbb{R}^{N_t \times q}$, $\mathbf{K} \in \mathbb{R}^{N_t \times N_{\text{tv}}}$ and $\mathbf{T}_{\text{virt}} \in \mathbb{R}^{N_{\text{tv}} \times q}$, where N_t and N_{tv} are the number of time steps for the surface temperature signal and the virtual wave signal. With the running variables $k = \{0, 1, 2, \dots, N_t-1\}$ and $j = \{0, 1, 2, \dots, N_{\text{tv}}-1\}$ and the

corresponding discrete time steps $t_k = k \Delta_t$ and $t'_j = j \Delta_t$, the component notation of the kernel K is given by

$$K(k, j) = \frac{c \sqrt{\Delta_t}}{\sqrt{\pi \alpha k}} \exp\left(-\frac{c^2 \Delta_t j^2}{4 \alpha k}\right) = \frac{\eta}{\sqrt{\pi k}} \exp\left(-\frac{\eta^2 j^2}{4 k}\right) \quad (3)$$

Here, we introduced the dimensionless number $\eta = c \sqrt{\Delta_t} / \sqrt{\alpha}$, which depends on the propagation parameters c and α and on the temporal resolution Δ_t . Our goal is to compute a virtual wave signal \mathbf{T}_{virt} based on a known surface temperature signal \mathbf{T} . Due to the diffusive nature of heat propagation, we deal with a severely ill-posed inverse problem and, hence, Eq. (2) cannot be inverted directly. Thus, we need regularization tools and the corresponding regularization parameters [23].

2.1. Parameter study

As visible in Eq. (3), \mathbf{K} depends only on the dimensionless number η and the number of time steps N_t and N_{tv} . To reduce the computational cost for the inversion of Eq. (2) it is desirable to keep N_t and N_{tv} small, whereby their minimum is given by the geometrical and physical parameters of the SUT. If η is poorly selected, the solution of the inverse problem becomes worse. To determine the appropriate parameter configurations, we perform a parameter study and a singular value decomposition (SVD) of \mathbf{K} in order to evaluate the number of significant singular values n_ϕ . Fig. 1 visualizes the singular values of \mathbf{K} for exemplary parameters N_b , N_{tv} and η . This figure shows that the singular values s decrease until the value of machine accuracy is reached. At this point the singular values do not contain significant information for the inverse solution and hence, they are truncated according to Fig. 1 [18].

In the next step, we vary the parameters $\eta = \{0 : 0.004 : 10\}$ and $N_{\text{tv}} = \{10 : 20 : 3000\}$ for a) $N_t = 100$ and b) $N_t = 200$ and evaluate for each parameter configuration the corresponding number of significant singular values n_ϕ of \mathbf{K} . Fig. 2 shows the result of the parameter study. Herein, it is visible that, for a good choice of η and N_{tv} and a specific N_t , the number of significant values n_ϕ can be increased. Furthermore, n_ϕ is constant for a large region of N_{tv} even in the domain of small η values. Therefore, N_{tv} can be strongly reduced without decreasing the quality of the inverse solution. The red dashed and dotted lines show the result of a physical-based consideration of the minimum and maximum number of η , which are deduced in the next section. The results of the parameter study offers valuable hints for good parameter configurations but is only valid for a specific number of time steps N_t . This parameter was limited because otherwise the computational cost of the parameter study becomes unmanageable.

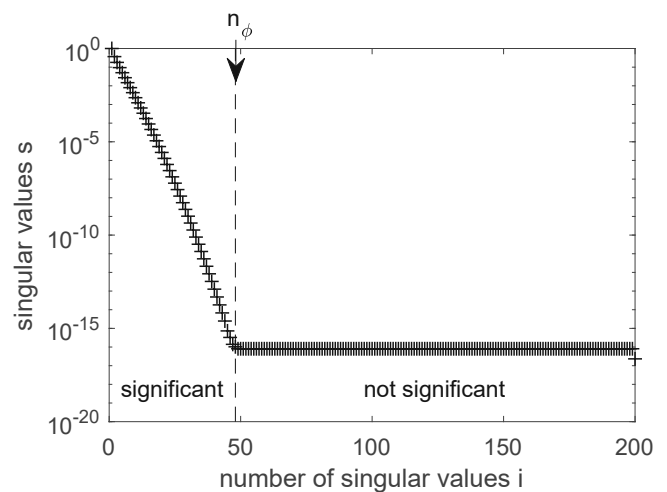


Fig. 1. Semi-log plot of the singular values s as function of the number of singular values i . The black dashed line separates the significant singular values n_ϕ from not significant singular values.

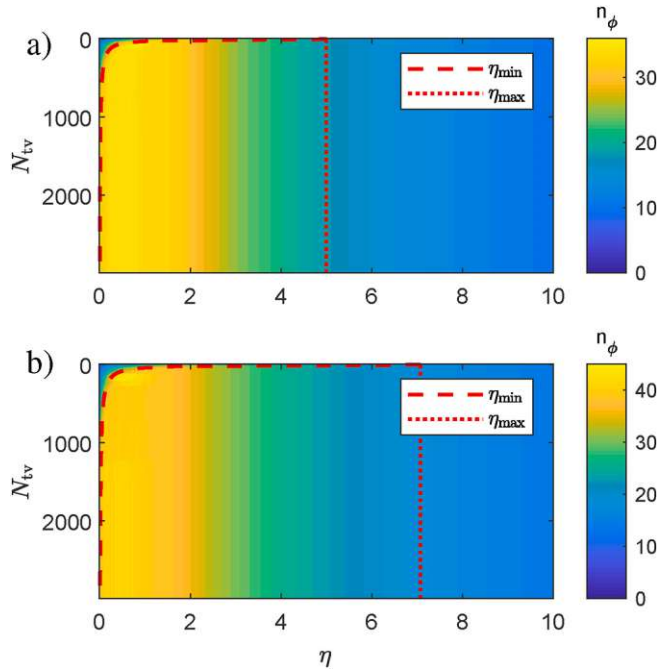


Fig. 2. Parameter study: The color-bars show the number of significant singular values n_ϕ as a function of η and N_{tv} for a) $N_t = 100$ and b) $N_t = 200$. The red dashed and dotted lines are described by Eqs. (11) and (13). These lines indicate the limits of the minimum and maximum number of η for a defect-free SUT. (For interpretation of the references to color in this figure legend, the reader is referred to the Web version of this article.)

2.2. Physical-based limitation of η

To circumvent the high computational cost due to high numbers of N_t or N_{tv} and consequently very large matrices \mathbf{K} , we deduce a physical-based limitation for the parameter η . We reformulate $\eta = c\sqrt{\Delta_t}/\sqrt{\alpha}$, because c is a virtual speed of sound which is not physically based and, therefore, unknown. For this reason, we expand η by the axial spatial resolution Δ_z

$$\eta = \frac{c\sqrt{\Delta_t}}{\sqrt{\alpha}} \frac{\Delta_z}{\Delta_z} = \frac{\tilde{c}}{\sqrt{\Delta_{Fo}}}, \quad (4)$$

which yields the dimensionless virtual speed of sound $\tilde{c} = c\Delta_t/\Delta_z$ and the discrete Fourier number $\Delta_{Fo} = \alpha\Delta_t/\Delta_z^2$. As in previous studies, we prescribe $\tilde{c} = 1$ instead of c and, in accordance with the time of flight method (TOF), we can relate the time t to the depth coordinate z in the following manner:

$$z = ct = \frac{\tilde{c}\Delta_z}{\Delta_t} j\Delta_t = \tilde{c}\Delta_z j. \quad (5)$$

On the one hand, we claim for a minimum value of $\eta = \eta_{\min}$ that the reconstruction domain $\tilde{c}\Delta_z N_{tv}$ is large enough to detect the back wall of the observed sample. On the other hand we claim, for a maximum value of $\eta = \eta_{\max}$, that the axial spatial resolution Δ_z is small enough to resolve a defect at a certain depth or at least the back wall.

2.2.1. Minimum value of η

To ensure a reliable detection of the back wall, in reflection mode, we must claim that the detection domain is at least:

$$3L \stackrel{!}{=} ct = \tilde{c} \frac{\Delta_z}{\Delta_t} N_{tv} \Delta_t = \tilde{c} \Delta_z N_{tv}, \quad (6)$$

whereby L is the thickness of the SUT. For the reconstruction of the back wall in reflection mode, an evaluation domain of $2L$ would be large enough, but we have to solve a discrete, severely ill-posed inverse

problem and the back wall echo may occur on a wrong position due to a bad assumption of the thermal diffusivity α . Note, to find the back wall echo and the mirror source of the front wall, we consider an A-scan of the virtual wave [24]. Both are characterized by a local maximum in the A-scan, and the estimated amplitude position can be wrong in the size of the spatial resolution. Furthermore, for a plate the thermal diffusivity can vary for each pixel location. Consequently, the minimum evaluation domain is chosen with three times the sample thickness L . Based on the postulation in Eq. (6), we want to derive the minimum number of η that ensures a reasonable estimation of the back wall and the mirror source of the front wall. Assuming that \tilde{c} is prescribed, we can relate η to the spatial resolution Δ_z :

$$\eta = \frac{\tilde{c}}{\sqrt{\Delta_{Fo}}} = \frac{\tilde{c}\Delta_z}{\sqrt{\alpha\Delta_t}} \rightarrow \Delta_z = \frac{\eta}{\tilde{c}} \sqrt{\alpha\Delta_t}. \quad (7)$$

Substituting Eq. (7) in Eq. (6) yields:

$$3L \stackrel{!}{=} \frac{\tilde{c}\eta}{\tilde{c}} \sqrt{\alpha\Delta_t} N_{tv} = \eta \sqrt{\alpha\Delta_t} N_{tv}. \quad (8)$$

In the next step, we reformulate Eq. (8) to obtain the minimum value for η :

$$\eta_{\min} = \frac{3}{N_{tv}} \frac{L}{\sqrt{\alpha\Delta_t}}. \quad (9)$$

In addition, we can substitute the term $\alpha\Delta_t$ based on the measurement time t_{end} . The temporal resolution Δ_t and the measurement time t_{end} are defined in the following manner:

$$\Delta_t = \frac{t_{\text{end}}}{N_t} \quad \wedge \quad t_{\text{end}} = \frac{L^2}{\alpha} \quad \rightarrow \quad \alpha\Delta_t = \frac{L^2}{N_t}, \quad (10)$$

wherein N_t are the time steps of the measurement data. The definition of t_{end} ensures the detection of the back wall signal. Respecting this relationship in Eq. (9) yields the minimum number of η :

$$\eta_{\min} = \frac{3}{N_{tv}} \frac{L}{\sqrt{\alpha\Delta_t}} = \frac{3}{N_{tv}} \frac{L\sqrt{N_t}}{\sqrt{L^2}} = 3 \frac{\sqrt{N_t}}{N_{tv}}. \quad (11)$$

Eq. (11) reveals that η_{\min} depends only on the numbers of time steps N_t and N_{tv} .

2.2.2. Maximum value of η

To define the maximum value of η , we claim that a defect at a certain depth ζ or at least the back-wall should be detected. To avoid any overlapping of the minimum and maximum values of η we limit the value of ζ in the following manner:

$$\zeta_{\min} < \zeta \leq \zeta_{\max} \quad (12)$$

with $\zeta_{\min} = 2\Delta_{z,\min} = 2 \frac{\eta_{\min}}{\tilde{c}} \sqrt{\alpha\Delta_t} \quad \wedge \quad \zeta_{\max} = \frac{L}{2}$.

ζ_{\max} ensures that at least two spatial discretization points are available to detect the back-wall at position L . Using Eq. (12), the maximum value of η is given by:

$$\eta_{\max} = \begin{cases} \frac{\zeta}{2\sqrt{\alpha\Delta_t}} \tilde{c} & \text{SUT with defects} \\ \frac{L}{2\sqrt{\alpha\Delta_t}} \tilde{c} = \frac{\tilde{c}}{2} \sqrt{N_t} & \text{defect-free SUT.} \end{cases} \quad (13)$$

Herein, we have used the relations in Eq. (10) for the last step.

2.3. Reduction of computational cost

Using the defect depth ζ , we can compute the minimum number of N_{tv} . To sample the defect at a certain depth ζ , we claim that the spatial resolution is at least $\Delta_z = \zeta/2$, which is predefined by the user. The reformulation of Eq. (6) yields then the minimum number of time steps:

$$N_{iv, \min} = 6 \frac{L}{\tilde{c}\zeta} = 3 \frac{L}{\tilde{c}\Delta_z} \quad (14)$$

Eq. (7) shows that based on Δ_z the temporal resolution Δ_t or the frame rate (frames per second) of the IR-camera can be computed

$$\Delta_z = \frac{\eta}{\tilde{c}} \sqrt{\alpha \Delta_t} \rightarrow \Delta_t = \frac{1}{\alpha} \left(\frac{\Delta_z \tilde{c}}{\eta} \right)^2, \quad (15)$$

As mentioned before, $\tilde{c} = 1$ is predefined and we suppose that the thermal diffusivity in axial direction α is known. The η -value between η_{\min} and η_{\max} is unknown. The likely easiest and most efficient approach to select a reasonable η -value for the calculation of Δ_t is given by the following iteration steps:

1. Define $\hat{\eta}$ as an estimator for η .
2. Compute Δ_t from Eq. (15) and calculate $t_{\text{end}} = L^2/\alpha$.
3. Calculate $N_t = t_{\text{end}}/\Delta_t$.
4. Based on N_t calculate η_{\min} and η_{\max} .
5. If $\hat{\eta}$ is between these values then $\hat{\eta} \rightarrow \eta$ and we can use the computed frame rate from iteration step 2.
6. Else select a new $\hat{\eta}$ and repeat the above steps.

The calculated frame rate must at least cover the physical correct temporal surface temperature signals. For noiseless surface temperature signals, the limiting factors for defect detection are the maximum camera frame rate and the minimal lateral spatial resolution $\Delta_{x,\min}$ which are specified by the IR camera. We want to emphasize that Δ_z is independent of Δ_x because we have a local (pixelwise) transformation between surface temperature and virtual wave signal. Hence, the limiting camera property for one pixel is only the frame rate or temporal resolution Δ_t .

2.4. Application on analytical solution

To observe the influence of the dimensionless number η on the solution of the inverse problem, we consider an analytical solution for a 1D heat conduction problem with adiabatic boundaries in reflection mode ($z = 0$). Before the thermal excitation, we assume that the SUT has equilibrium temperature. At time $t = 0$, the SUT is subjected to a short laser pulse. Moreover, the penetration depth of the heat source is very small. Therefore, the heat source can be mathematically modelled with a Dirac-Delta excitation both temporally and spatially. Using the corresponding Greens function and the Greens function solution equation [25], we obtain the spatial and temporal temperature distribution:

$$T(z=0, t) = \frac{2\hat{T}_0}{\sqrt{4\pi\alpha t}} \sum_{n=-\infty}^{\infty} \exp\left(-\frac{(2nL)^2}{4\alpha t}\right), \quad (16)$$

with $\hat{T}_0 = q_0/(\rho c_p)$. The parameter q_0 denotes the absorbed heat energy density, ρ is the density and c_p is the specific heat capacity. In a previous work [24], we demonstrated that the corresponding virtual wave signal can be directly deduced from Eq. (16) and is given by

$$T_{\text{virt}}(z=0, t) = \frac{\hat{T}_0}{c} \sum_{n=-\infty}^{\infty} \left[\delta\left(t + \frac{2nL}{c}\right) + \delta\left(t - \frac{2nL}{c}\right) \right] \quad (17)$$

This equation yields the characteristic front-wall echo and the first mirror source at $z = 2L$. Furthermore, Eq. (17) reveals that the boundary echoes occur $2L$ periodically, but for the present considerations only the first mirror sources are of interest, because they describe the back wall. Hence, the number of sum terms was limited to $n = \{-2, -1, \dots, 2\}$. Based on Eq. (16), we calculated the surface temperature signal for the reflection mode. The temperature signal is visualized in Fig. 3a) on the double logarithmic scale. Fig. 3b) shows the corresponding virtual wave signal related to its maximum as function of dimensionless depth $z/(2L) = c \cdot t/(2L)$ and different η values. Due to the double way diffusion we respected the factor two in the dimensionless depth. The vertical black

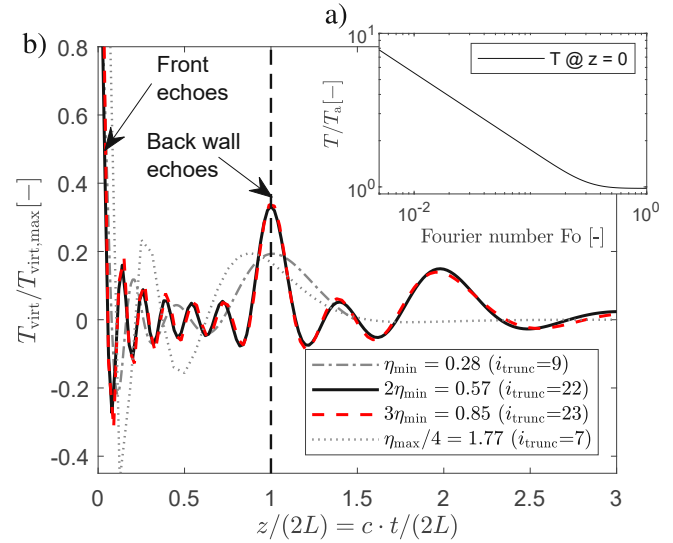


Fig. 3. a) Temporal temperature signal at $z = 0$ (reflection mode) as a function of the Fourier number $Fo = at/L^2$ related to the adiabatic temperature T_a . The thermal diffusivity was $\alpha = 0.39 \cdot 10^{-6} \text{ m}^2/\text{s}$. The temporal resolution $\Delta_t = 0.46 \text{ s}$ was constantly maintained and the spatial resolution Δ_z was calculated according to Eq. (15) with the corresponding η value. b) Influence of different η values on the virtual wave signal calculated using a). The virtual wave signals as function of dimensionless depth $z/(2L)$ were related to the maximum signal amplitudes. η_{\min} ensures a reconstruction domain which is large enough to find the back wall but is not the best choice, because for $2\eta_{\min}$ and $3\eta_{\min}$ the back wall amplitude increases and the corresponding full half-width decreases. Therefore, the back wall is easier detectable. The legend shows the corresponding truncation values i_{trunc} for the T-SVD. The numbers of time steps are $N_t = 200$ and $N_{iv} = 150$.

dashed line at $z/(2L) = 1$ represents the back wall position. For the inversion, we used the truncated singular value decomposition (T-SVD) [26]. Due to the different η values, we obtained different truncation or regularization parameters i_{trunc} which were estimated with the Picard-plot. They are listed in the legend of Fig. 3b). As visible in Fig. 3b) the minimal value of η ensures a reconstruction domain that is large enough to find the back wall but compared to $2\eta_{\min}$ and $3\eta_{\min}$ the amplitude of the mirror source is smaller and the corresponding full half width is broader and hence might not be the best choice for the inversion. For $\eta_{\max}/4$ the poor spatial resolution leads to the false positioning of the back wall amplitude. Furthermore, the trend of the different truncation parameters i_{trunc} reflects the trend of Fig. 2 and, hence, the result can be summarized as follows: A good choice of the dimensionless number η , increases the number of significant singular values that correspond to the truncation parameter i_{trunc} and hence improves the quality of the inverse solution.

3. Multidimensional defect reconstruction

In Section 2, we have introduced a discretization criterion which enables a fast and robust temperature to virtual wave signal inversion and, hence, a very efficient defect detection. In this section we analyze the virtual wave signal evaluated on samples with artificial defects represented by FBHs. This defect approximation is meaningful, because:

- FBHs are a standard defect approximation in the aerospace industry,
- they have well defined geometries,
- they have well defined reflection coefficients at the defect interfaces,
- and hence the results are well reproducible.

The FBHs in the samples have varying aspect ratios γ between defect diameter D and the remaining wall thickness (RWT) ζ (see Table 1). We

Table 1

Geometrical parameters of the FBHs: γ [-] denotes the aspect ratio of FBH diameter D [mm] and the RWT ζ [mm] of the woven a) and the UD sample b).

Parameter	aD	ζ	γ	bD	ζ	γ
FBH ₁	4.00	1.50	2.67	4.00	1.45	2.76
FBH ₂	8.30	1.50	5.53	8.30	1.50	5.53
FBH ₃	11.60	1.75	6.63	11.60	2.00	5.80
FBH ₄	4.00	2.95	1.36	4.00	2.65	1.51
FBH ₅	8.30	3.15	2.63	8.30	2.90	2.86
FBH ₆	11.60	3.10	3.74	11.60	3.10	3.74

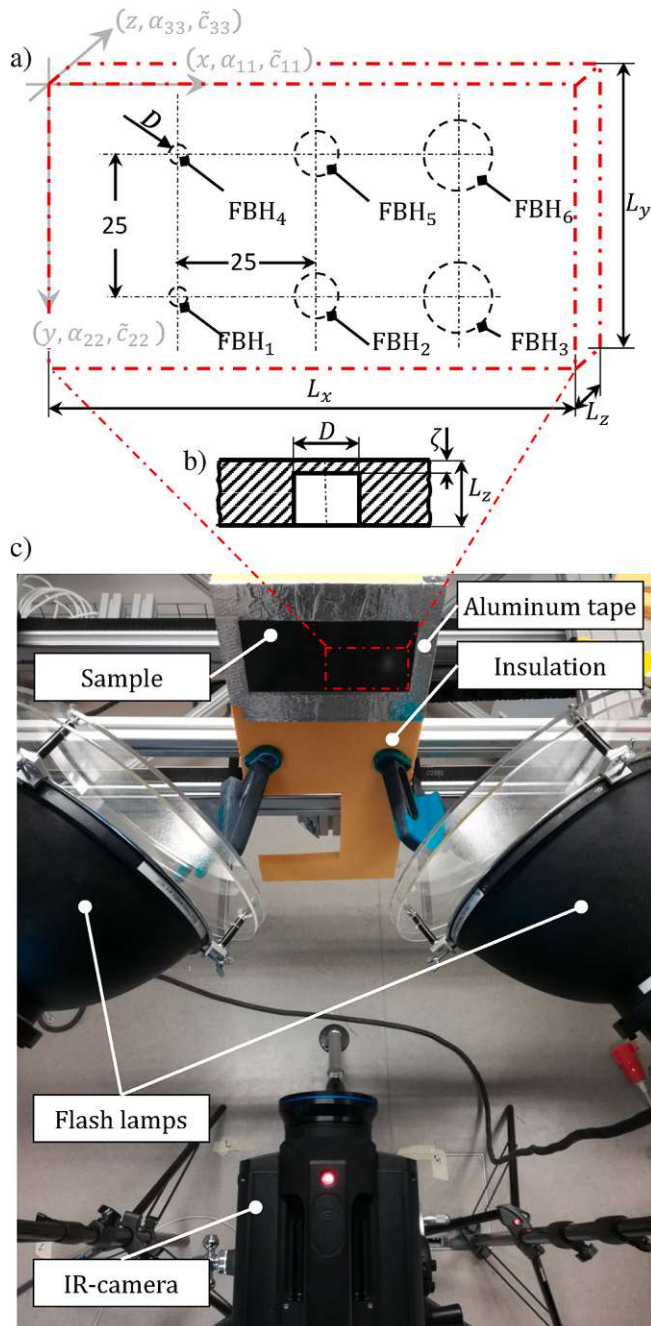


Fig. 4. Experimental details: a) Observed region which shows the arrangement of the FBHs (all dimensions are in mm), b) Cross section of FBH₃ and c) photo of the measurement set up.

apply and verify the findings on a woven and a UD CFRP test sample which have different values of thermal diffusivity and hence different virtual speeds of sound in the principal directions. A sketch of the samples, which have the same hole pattern, is shown in Fig. 4a). In contrast to Section 2, we consider anisotropic 3D samples with different thermal diffusivities in the principal directions. According to Ref. [22], we can reformulate the ratio $c/\sqrt{\alpha}$ by $c_{33}/\sqrt{\alpha_{33}}$, where c_{33} and α_{33} are the axial virtual speed of sound and axial thermal diffusivity, respectively. Hence, for the anisotropic heat diffusion, the dimensionless number η can be reformulated by $\eta = \tilde{c}_{33}/\sqrt{\Delta F_0}$ with $\Delta F_0 = \alpha_{33}\Delta t/\Delta z^2$. At this point we want to remind and emphasize that the VWC is a two-step reconstruction procedure. In the first step we locally transform (pixel by pixel) the surface temperature signal into a virtual wave signal. The virtual wave signal obeys the wave equation and therefore in the second step we can use ultrasound reconstruction techniques such as F-SAFT for defect imaging. In the second step, we also consider the anisotropic heat flow by the virtual speeds of sound, which are related to the thermal diffusivities in the principal directions. Furthermore, we discuss the applicability of prior information in the form of positivity, due to the perturbed virtual wave propagation in the regularization process.

3.1. Materials

For the experimental investigations we consider a woven and a UD CFRP sample. The woven fabric sample consists of 28 plain weave prepreg layers (CYCOM 970/HMF 5-322/70C) and the total sample thickness is $L_z = 5.95$ mm. For the layup, the plain weave prepregs were laid alternately in the 0-degree and 45-degree orientations. The UD sample consists of 42 unidirectional prepreg layers (CYCOM 5276-1/G40-800 Tape) and the total sample thickness is $L_z = 5.95$ mm.

We want to emphasize that for the evaluations the composite materials are considered at the macroscopic length scale. Therefore, we use an effective medium approximation and thus effective thermophysical parameters are applied for the reconstructions. The effective material parameters which are necessary for the defect reconstruction were estimated using the procedure described in Ref. [22] and are listed in Table 2.

3.2. Experimental setup

In this section, we discuss the generation of surface temperature data by a thermography experiment. The measurement set up is visualized in Fig. 4c). The SUTs were insulated at the edges to avoid a decrease in the defect detection capability due to lateral heat flows. To avoid heating of the insulation it was covered by aluminum tape. Each SUT was subjected to a short flash lamp pulse on the surface where the FBHs are invisible. The heating time was $t_h \approx 2$ ms and the electrical energy input was approximately 12 kJ. The resulting change in the surface temperature signal was measured in the “pulse-echo” configuration. The IR camera used has a cooled indium antimony (InSb) sensor and is sensitive in the spectral range of 3.0–5.1 μm . The NETD of this camera is smaller than 25 mK. For both samples, the axial resolution of $\Delta_z = 120$ μm was chosen, while the lateral resolution that depends on the IR camera was $\Delta_x = \Delta_y = 157$ μm and the temporal resolution was $\Delta_t = 0.04$ s. The measurement time was estimated with L_z^2/α_{33} . The mean sample thickness for both samples is $L_z = 5.95$ mm.

Table 2

Virtual speeds of sound in the principal directions and axial thermal diffusivities α_{33} of the observed samples. The parameters were estimated according to Ref. [22].

Parameter	\tilde{c}_{11} [-]	\tilde{c}_{22} [-]	\tilde{c}_{33} [-]	α_{33} [m ² /s]
Woven	2.12	2.14	1.00	$0.403 \cdot 10^{-6}$
UD	3.71	1.14	0.99	$0.434 \cdot 10^{-6}$

3.3. Perturbed heat and virtual wave propagation

In this section, we focus on the discussion regarding the perturbed virtual wave propagation due to a perturbed heat flow caused by a defect. We observe one surface temperature pixel at the center point of FBH₃. Fig. 4b) shows a sketch of this FBH, where D denotes the diameter of the FBH and ζ is the RWT of the FBH. Using the recorded temporal surface temperature signal, we calculate a virtual wave signal. We use the iterative regularization scheme ADMM (see e.g. Refs. [27,28]) in order to incorporate prior information in the form of sparsity. We can expect a sparse virtual wave signal due to the temporal short heating and the limited number of defect interfaces. The necessary parameters for defect reconstruction for both woven and UD sample are listed in Table 2 and were estimated according to Ref. [22]. The geometrical and physical parameters yield a dimensionless number of $\eta = 0.95$ with $\eta_{\min} = 0.72$ and $\eta_{\max} = 5.91$ for the woven and $\eta = 0.91$ with $\eta_{\min} = 0.72$ and $\eta_{\max} = 5.70$ for the UD sample. The number of respected time steps for the surface temperature signal is $N_t = 2300$ and the number of time steps for the virtual wave signal was prescribed with $N_{tv} = 200$. Fig. 5a) shows the corresponding surface temperature signal at the FBH center and in a defect-free region as function of time on the double logarithmic scale for the woven sample. As one can see, the FBH forms three characteristic regions, marked with arrows. These characteristic regions may be more easily interpreted with the corresponding A-Scan or virtual wave signal, Fig. 5b). A positive signal amplitude corresponds to a source and a negative signal amplitude corresponds to a sink. The first region, shows

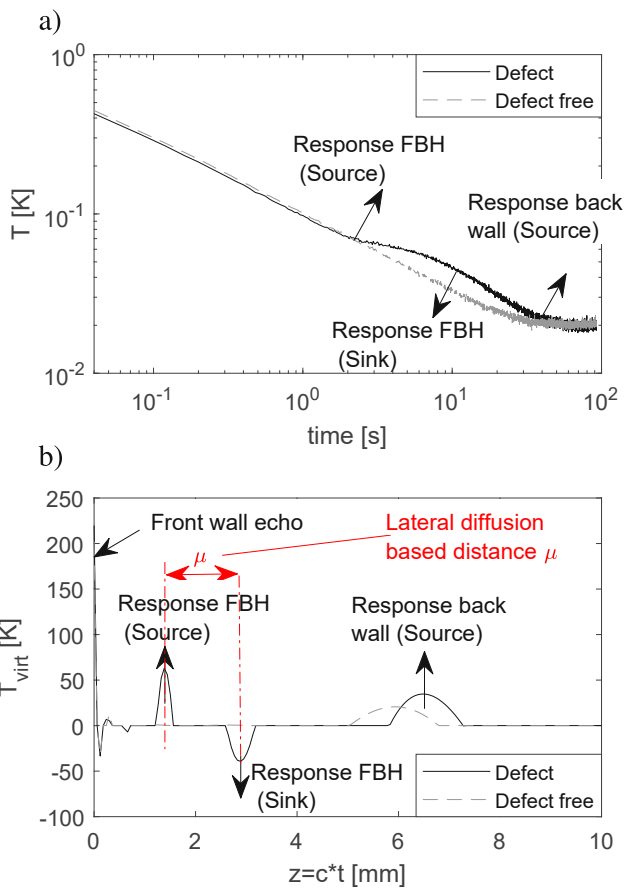


Fig. 5. a) Double logarithmic surface temperature signal of the woven sample as function of time at the center of FBH₃ compared to a defect-free surface temperature signal. b) Corresponding virtual wave signals (A-Scan) as function of depth $z = ct$. As visible in the A-Scans, the perturbed temperature signal causes a heat source and a heat sink with a certain distance μ , which is caused by lateral heat diffusion.

a source due to trapped heat caused by the FBH. As described by Almond et al. [29–31], this heat source causes a heat sink for equilibrium, which is marked by the second arrow and a negative signal amplitude in the virtual wave signal.

The defect source and sink have a certain distance μ , which is caused by the lateral heat flow. The distance μ depends on the ratio of lateral thermal diffusivity and axial thermal diffusivity, the defect diameter D and the defect depth ζ . The distance μ has an important influence on our defect reconstruction procedure, because in contrast to prior studies [22] we cannot use positivity by computing the spherical projection. The spherical projection is only applicable when the distance μ is very small, which can be achieved, e.g. by a point-like defect. Furthermore, the third arrow shows a source at the back wall. Here it is visible that for the perturbed signal the back wall echo is displaced compared to the defect-free signal because the heat has to “flow around” the FBH.

In prior studies, we have shown, that the virtual wave signal can be computed based on the kernel $K(t, t')$ and a surface temperature signal which was obtained by the method of images [24]. Here, we want to reverse this approach and model the temporal temperature signal of Fig. 5a) using the virtual wave signal of Fig. 5b) in order to substantiate the above source and sink explanations for adiabatic boundaries. We assume that the virtual wave signal yields the exact position of the sources and sinks discussed above. We recall Eq. (16) at position $z = 0$, which covers the front and back wall signal. Due to this we limit the sum terms by $n = \{-1, 0, 1\}$. We denote the back wall position with L^* , because the FBH causes a lateral heat flow and, hence, a shift of the back wall position in the A-scan. Furthermore, we introduce a heat source at the FBH source position ζ^+ and a sink at ζ^- with reflection amplitudes T_{ζ^+} and T_{ζ^-} . In this model and in contrast to Ref. [31], it is not necessary to introduce an anisotropy factor, because the anisotropy is covered by the positions of the sources and sinks and the mathematical model is given by

$$T(z=0, t) = \frac{\hat{T}_0}{\sqrt{\pi\alpha_{33}t}} \sum_{n=-1}^1 \exp\left(-\frac{(2nL^*)^2}{4\alpha_{33}t}\right) + \frac{T_{\zeta^+}}{\sqrt{\pi\alpha_{33}t}} \exp\left(-\frac{(2\zeta^+)^2}{4\alpha_{33}t}\right) - \frac{T_{\zeta^-}}{\sqrt{\pi\alpha_{33}t}} \exp\left(-\frac{(2\zeta^-)^2}{4\alpha_{33}t}\right) \quad (18)$$

Fig. 6 shows the defect surface temperature signal of Fig. 5a), a reconstructed defect temperature signal using Eq. (2) and the model-based least squares fit using Eq. (18) with fitting parameters \hat{T}_0 , T_{ζ^+}

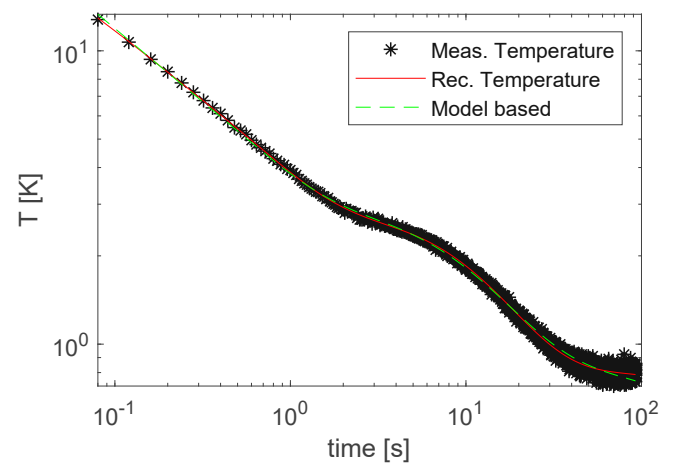


Fig. 6. Double logarithmic surface temperature signal of the woven sample as function of time in reflection mode and at the center of FBH₃ (asterisk), a reconstructed defect temperature signal (red line) using Eq. (2) and the model based least squares fit using Eq. (18) (green dashed line). (For interpretation of the references to color in this figure legend, the reader is referred to the Web version of this article.)

and T_c^- . As visible, the modelled surface temperature signal represents the measured surface temperature signal very well and hence substantiates the source/sink explanation. This result may be improved by considering more sum terms n but, for the sake of simplicity we skipped this here because the shown result is already plausible. A similar behaviour was obtained for the UD sample.

3.3.1. FBH detection of the woven sample

With the findings of the previous sections, we are able to perform a fast and robust 3D defect reconstruction. The evaluation domain is marked in Fig. 4c) by a rectangle with a red dot-dashed line. The length and the width of the evaluation domain are $L_x = 100$ mm and $L_y = 50$ mm, respectively. Figs. 7a) and 8a) show exemplary thermograms at $t = 9.28$ s and $t = 17.76$ s from FBH₁ to FBH₃ and from FBH₄ to FBH₆, respectively. Using the recorded temporal surface temperature signal, we calculate a virtual wave signal. Again, we use the iterative regularization scheme ADMM in order to incorporate prior information in the form of sparsity. Figs. 7b) and 8b) show the corresponding top view of the calculated virtual wave signals. Using the calculated virtual wave signals, the estimated dimensionless speeds of sound in the principal directions (see Table 2) and the ultrasonic reconstruction method F-SAFT we can reconstruct, in a second inversion step, the front wall, the back wall and the FBH interfaces. The reconstructed FBH interfaces from FBH₁ to FBH₃ and FBH₄ to FBH₆ are shown in Figs. 7c) and 8c). Figs. 9a) and 10a) show cross sections of the measured surface temperature signal along the center lines of FBH₁ to FBH₃ and FBH₄ to FBH₆. In Figs. 9b) and 10b) the corresponding virtual wave signals are visualized which show the characteristic hyperbolas. The defect reconstruction of the cross section is shown in Figs. 9c) and 10c). The black and white dashed lines indicate the correct FBH position. In Fig. 11, a 3D representation of the reconstructed signal along the center line FBH₁ to FBH₃ is visible. At $z = 0$ we see the front wall echo of the woven sample. The back wall echo was hidden to enable the visualization of the defect interfaces. Again, sources and sinks of the FBHs are visible. Due to the well estimated virtual speeds in the principal directions we have a rectification of the lateral heat flow. Furthermore, the reconstructed source interfaces met the FBH diameters very well.

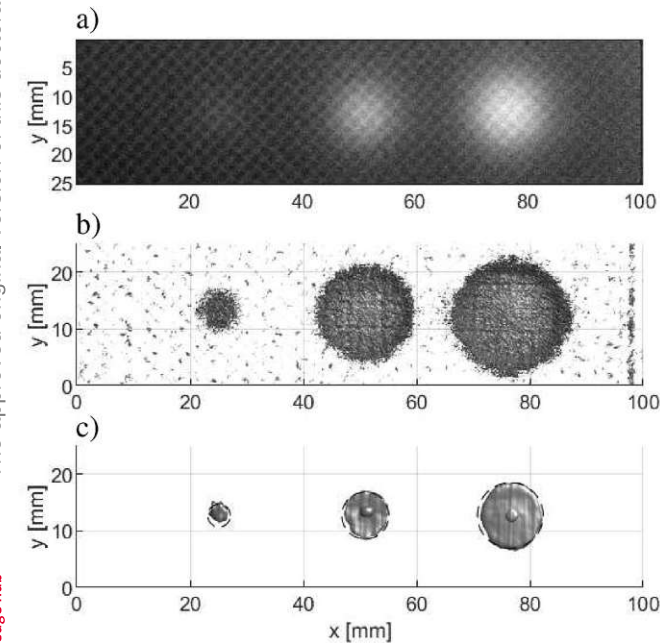


Fig. 7. a) Thermogram at $t = 9.28$ s, b) top view of the virtual wave signal and c) top view of the corresponding reconstructed defect signal from FBH₁ to FBH₃ of the woven sample. The black dashed lines show the correct defect diameter. The subfigures b) and c) are isosurface plots.

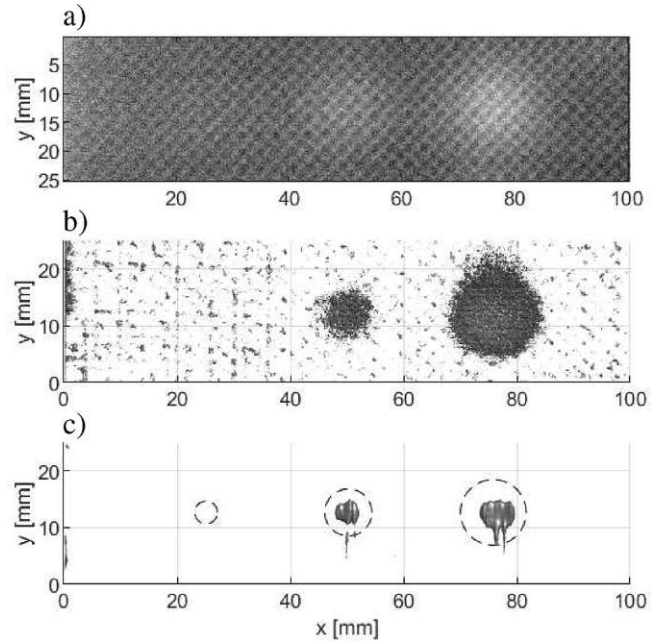


Fig. 8. a) Thermogram at $t = 17.76$ s, b) top view of the virtual wave signal and c) top view of the corresponding reconstructed defect signal from FBH₄ to FBH₆ of the woven sample. The black dashed lines show the correct defect position. The subfigures b) and c) are isosurface plots.

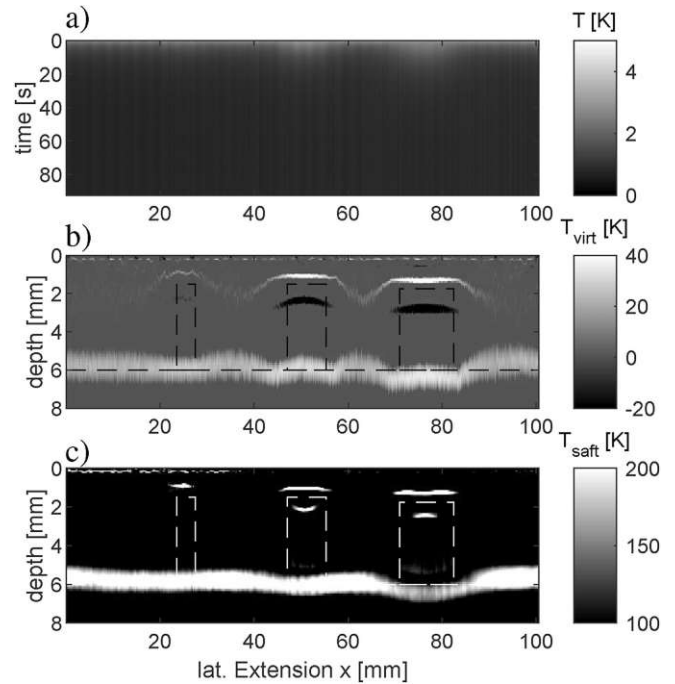


Fig. 9. a) Cross section of the temporal surface temperature signal and b) cross section of the virtual wave signal along the center line FBH₁ to FBH₃ of the woven sample. The black dashed and white dashed lines show the correct defect size and position.

3.3.2. FBH detection of the UD sample

For the UD sample, we performed the same evaluation steps and used the same evaluation domain size as for the woven sample. Figs. 12a) and 13a) show exemplary thermograms at $t = 7.64$ s and $t = 11.20$ s from FBH₁ to FBH₃ and from FBH₄ to FBH₆, respectively. Using the recorded temporal surface temperature signal, we calculate a virtual wave signal.

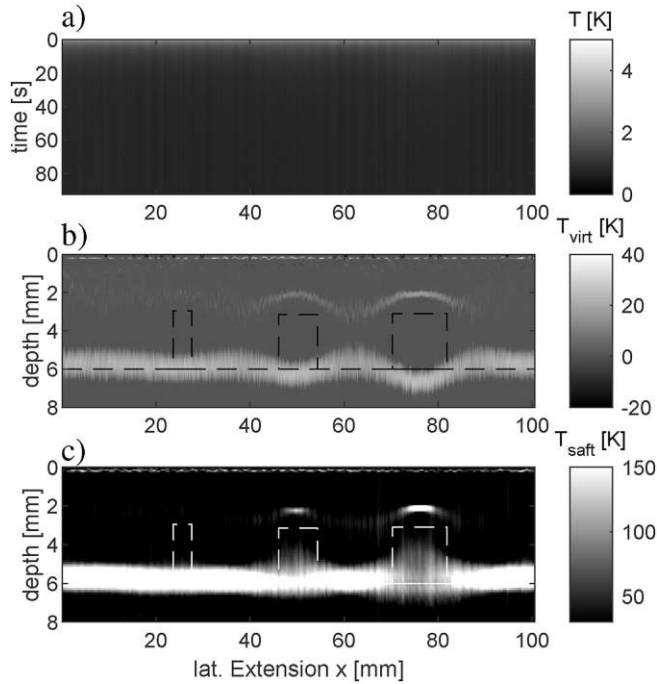


Fig. 10. a) Cross section of the temporal surface temperature signal and b) cross section of the virtual wave signal along the center line FBH₄ to FBH₆ of the woven sample. The black dashed and white dashed lines show the correct defect size and position.

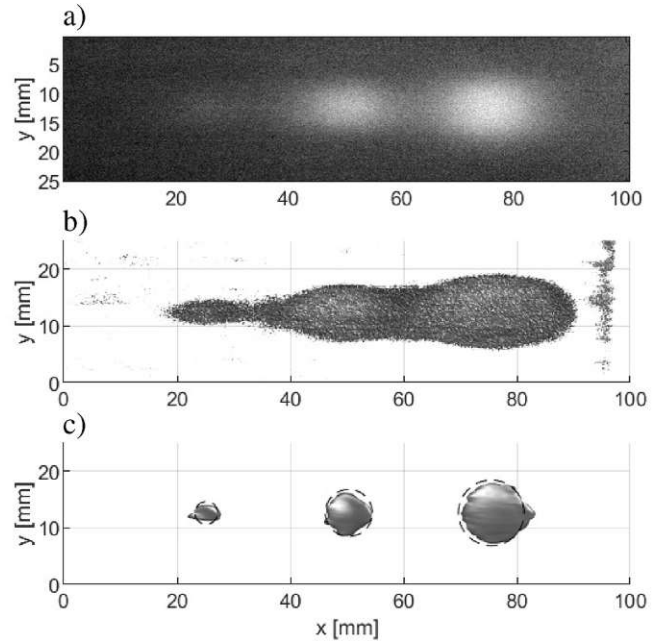


Fig. 12. a) Thermogram at $t = 7.64$ s, b) top view of the virtual wave signal and c) top view of the corresponding reconstructed defect signal from FBH₁ to FBH₃ of the UD sample. The black dashed lines show the correct defect diameter. The subfigures b) and c) are isosurface plots.

Die approbierte gedruckte Originalversion dieser Dissertation ist an der TU Wien Bibliothek verfügbar. The approved original version of this doctoral thesis is available in print at TU Wien Bibliothek.

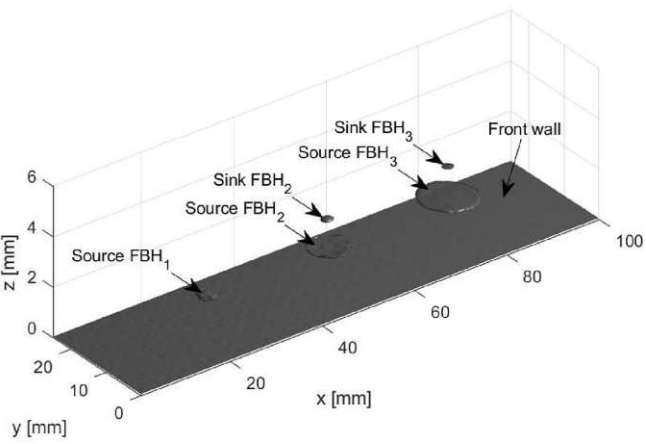


Fig. 11. 3D representation of the reconstructed defect signal from FBH₁ to FBH₃ of the woven sample.

Figs. 12b) and 13b) show the top view of the calculated virtual wave signals from FBH₁ to FBH₃ and from FBH₄ to FBH₆. Using the calculated virtual wave signal, the estimated dimensionless speeds of sound in the principal directions (see Table 2) and the ultrasonic reconstruction method F-SAFT we can reconstruct, in a second inversion step, the corresponding front wall, the back wall and the FBH interfaces. In Figs. 12c) and 13c) the front and back wall were hidden.

3.4. Discussion

The reconstruction results for both the woven and UD sample show that, even for samples with strongly varying thermal diffusivities in the principal direction, the FBH interfaces can be reconstructed at least for FBH₁ to FBH₃ very well. For row FBH₄ to FBH₆ the reconstruction becomes worse because the FBH interfaces lie deeper and the FBH row

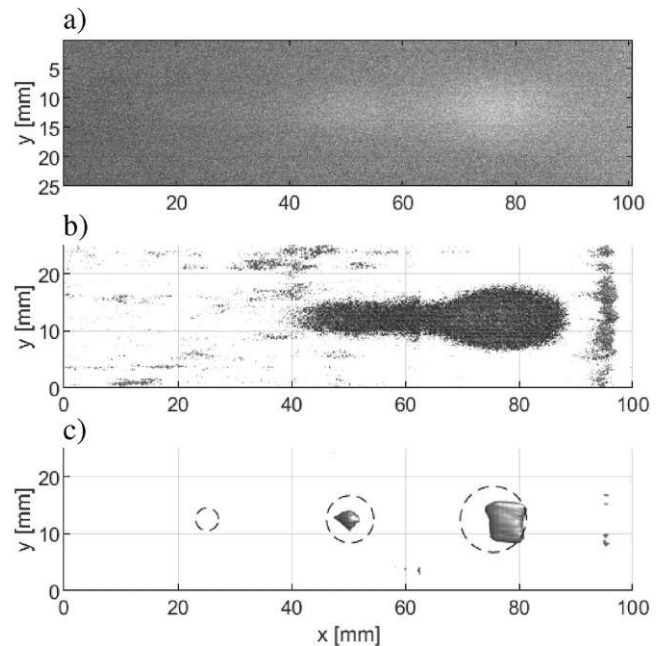


Fig. 13. a) Thermogram at $t = 11.20$ s, b) top view of the virtual wave signal and c) top view of the corresponding reconstructed defect signal from FBH₄ to FBH₆ of the UD sample. The black dashed lines show the correct defect diameter. The subfigures b) and c) are isosurface plots.

FBH₁ to FBH₃ cause lateral heat flows which decreases the defect detection capability. For both samples FBH₄ cannot be detected. Furthermore, the reconstruction results indicate that the FBH defect surfaces parallel to the measurement surface introduce sources and sinks as described in Section 3.3. Therefore, we can not accurately determine the defect depth, but we can locate the defect position ζ between the sources and sinks caused by the FBH. The F-SAFT algorithm respects the lateral heat flows and increases the SNR by integrating along the

scattering hyperbolas which introduces a spatial noise filtering and hence improves the defect size estimation considerable. A very attractive feature of the presented two-step reconstruction approach is the very low computational cost for defect reconstruction. Due to the findings in Section 2, we are able to limit the number of time steps $N_{TV} = 200$ and $N_t = 2300$, which strongly reduces the computational cost without affecting the reconstruction quality. The computation time for both inversion steps and one FBH row with an evaluation domain of $100 \times 25 \text{ mm}^2$ and 50 ADMM iterations is only 53s. The computations were performed on a standard computer with RAM = 32 GB and a processor with 4 cores and 8 threads.

4. Conclusions

In this paper, we presented a very fast, well interpretable and efficient reconstruction procedure for composite materials with strongly differing thermal diffusivities in the principal directions. We introduced a physical-based discretization criterion which ensures reliable and fast defect reconstruction. Furthermore, we discussed the features of a perturbed virtual wave signal caused by a perturbed heat flow due to an artificial defect and the findings are:

- we cannot incorporate the prior information positivity in our reconstruction procedure and
- we cannot accurately detect the defect depth position, but we can locate it because it lies in between the source and sink amplitude.

In future work, we will apply heating that varies in time and space, to increase the defect detection capability of deeper lying defects. Moreover, we will also consider foreign object inclusions (e.g. foil, paper) that have a finite lateral and axial extension and varying reflection coefficients at the defect interfaces and, hence, better representing real defects, such as delaminations.

CRedit authorship contribution statement

G. Thummerer: Conceptualization, Methodology, Software, Formal analysis, Validation, Investigation, Writing – original draft, Visualization. **G. Mayr:** Conceptualization, Methodology, Writing – review & editing, Project administration, Funding acquisition. **P. Burgholzer:** Writing – review & editing, Supervision, Funding acquisition.

Declaration of competing interest

The authors declare that they have no known competing financial interests or personal relationships that could have appeared to influence the work reported in this paper.

Acknowledgements

The financial support by the Austrian Federal Ministry of Science, Research and Economy and the National Foundation for Research, Technology and Development is gratefully acknowledged. Furthermore, this work has been supported by the project multimodal and in-situ characterization of inhomogeneous materials (MiCi), by the Federal Government of Upper Austria and the European Regional Development Fund (EFRE) in the framework of the EU-program IWB2020. Signal and data processing was funded by the Austrian Science Fund (FWF), project P 33019-N.

References

- [1] Meola C, Boccardi S, Carlomagno G. Infrared thermography in the evaluation of aerospace composite materials: infrared thermography to composites. Elsevier Science; 2016.
- [2] Vavilov V, Burleigh D. Infrared thermography and thermal nondestructive testing. 2020.

- [3] Maldague XPV, Moore PO, editors. Infrared and thermal testing, 3rd Edition, Nondestructive testing handbook. Columbus, Ohio: American Society for Nondestructive Testing; 2001.
- [4] Vavilov VP, Burleigh DD. Review of pulsed thermal ndt: physical principles, theory and data processing. NDT E Int 2015;73:28–52. <https://doi.org/10.1016/j.ndteint.2015.03.003>.
- [5] Almond D, Patel P. of Physics and its applications. Photothermal science and techniques, vol. 10. London: Chapman & Hall; 1996.
- [6] Mandelis A. Diffusion-wave fields: mathematical methods and green functions. New York: Springer; 2013.
- [7] Burgholzer P, Hendorfer G. Limits of spatial resolution for thermography and other non-destructive imaging methods based on diffusion waves. Int J Thermophys 2013;34:1617–32. <https://doi.org/10.1007/s10765-013-1513-0>.
- [8] Shepard SM, Lhota JR, Ahmed T. Flash thermography contrast model based on ir camera noise characteristics. Nondestruct Test Eval 2007;22(2–3):113–26. <https://doi.org/10.1080/10589750701448662>.
- [9] Shepard SM, Lhota JR, Ahmed T. Measurement limits in flash thermography. In: Burleigh DD, Dinwiddie RB, editors. Thermosense XXXI, vol. 7299. SPIE: International Society for Optics and Photonics; 2009. p. 209–15. <https://doi.org/10.1117/12.820062>.
- [10] Burgholzer P, Mayr G, Thummerer G, Haltmeier M. Linking information theory and thermodynamics to spatial resolution in photothermal and photoacoustic imaging. J Appl Phys 2020;128(17):171102. <https://doi.org/10.1063/5.0023986>.
- [11] Maldague X, Galmiche F, Ziadi A. Advances in pulsed phase thermography. Infrared Phys Technol 2002;43(3–5):175–81. [https://doi.org/10.1016/S1350-4495\(02\)00138-X](https://doi.org/10.1016/S1350-4495(02)00138-X).
- [12] Shepard SM, Freundberg Beemer M. Advances in thermographic signal reconstruction. In: SPIE proceedings. SPIE; 2015. 94850R. <https://doi.org/10.1117/12.2176748>.
- [13] Balageas DL, Roche J-M, Leroy F-H, Liu W-M, Gorbach AM. The thermographic signal reconstruction method: a powerful tool for the enhancement of transient thermographic images. Biocybernetics and Biomedical Engineering 2015;35(1): 1–9. <https://doi.org/10.1016/j.bbe.2014.07.002>.
- [14] Mulaveesala R, Tuli S. Theory of frequency modulated thermal wave imaging for nondestructive subsurface defect detection. Appl Phys Lett 2006;89(19):191913. <https://doi.org/10.1063/1.2382738>.
- [15] Tuli S, Mulaveesala R. Defect detection by pulse compression in frequency modulated thermal wave imaging. Quantitative InfraRed Thermography Journal 2005;2(1):41–54. <https://doi.org/10.3166/qirt.2.41-54>.
- [16] Kaipilavil S, Mandelis A. Truncated-correlation photothermal coherence tomography for deep subsurface analysis. Nat Photonics 2014;8(8):635–42. <https://doi.org/10.1038/NPHOTON.2014.111>.
- [17] Tavakolian P, Sivagurunathan K, Mandelis A. Enhanced truncated-correlation photothermal coherence tomography with application to deep subsurface defect imaging and 3-dimensional reconstructions. J Appl Phys 2017;122(2):023103. <https://doi.org/10.1063/1.4992807>.
- [18] Groz M-M, Abisset-Chavanne E, Mezziane A, Sommier A, Pradère C. Three-dimensional reconstruction of thermal volumetric sources from surface temperature fields measured by infrared thermography. Appl Sci 2019;9(24):5464. <https://doi.org/10.3390/app9245464>.
- [19] Holland SD, Schiefelbein B. Model-based inversion for pulse thermography. Exp Mech 2019;59(4):413–26. <https://doi.org/10.1007/s11340-018-00463-2>.
- [20] Burgholzer P, Thor M, Gruber J, Mayr G. Three-dimensional thermographic imaging using a virtual wave concept. J Appl Phys 2017;121(10):105102. <https://doi.org/10.1063/1.4978010>.
- [21] Langenberg K-J, Marklein R, Meyer K. Ultrasonic nondestructive testing of materials: theoretical foundations. Boca Raton: CRC Press, Taylor et Francis; 2017.
- [22] Thummerer G, Mayr G, Burgholzer P. Photothermal testing of composite materials: virtual wave concept with prior information for parameter estimation and image reconstruction. J Appl Phys 2020;128(12):125108. <https://doi.org/10.1063/5.0016364>.
- [23] Hansen PC. Rank-deficient and discrete ill-posed problems: numerical aspects of linear inversion/Per Christian Hansen, SIAM monographs on mathematical modeling and computation. Philadelphia, Pa.: SIAM; 1998.
- [24] Mayr G, Stockner G, Plasser H, Hendorfer G, Burgholzer P. Parameter estimation from pulsed thermography data using the virtual wave concept. NDT E Int 2018; 100:101–7. <https://doi.org/10.1016/j.ndteint.2018.09.003>.
- [25] Cole KD, Beck JV, Haji-Sheikh A, Litkouhi B. Heat conduction using Green's functions, 2nd Edition, Series in computational and physical processes in mechanics and thermal sciences. Boca Raton, Fla: CRC Press; 2011.
- [26] Hansen PC. Discrete inverse problems: insight and algorithms, Fundamentals of algorithms. Philadelphia: Society for Industrial and Applied Mathematics; 2010.
- [27] Thummerer G, Mayr G, Hirsch PD, Ziegler M, Burgholzer P. Photothermal image reconstruction in opaque media with virtual wave backpropagation. NDT E Int 2020;112:102239. <https://doi.org/10.1016/j.ndteint.2020.102239>.
- [28] Thummerer G, Mayr G, Haltmeier M, Burgholzer P. Photoacoustic reconstruction from photothermal measurements including prior information. Photoacoustics 2020;19:100175. <https://doi.org/10.1016/j.pacs.2020.100175>.

- [29] Almond DP, Lau SK. Edge effects and a method of defect sizing for transient thermography. *Appl Phys Lett* 1993;62(25):3369–71. <https://doi.org/10.1063/1.109074>.
- [30] Almond DP, Lau SK. Defect sizing by transient thermography. i. an analytical treatment. *J Phys Appl Phys* 1994;27(5):1063–9. <https://doi.org/10.1088/0022-3727/27/5/027>.
- [31] Almond DP, Pickering SG. An analytical study of the pulsed thermography defect detection limit. *J Appl Phys* 2012;111(9):093510. <https://doi.org/10.1063/1.4704684>.

5.5 3D photothermal imaging of real subsurface defects in anisotropic media

This manuscript uses the findings of Paper 5.4 and presents an application to 3D photothermal imaging of real subsurface defects represented by a delamination in an anisotropic media, where temperature signals were recorded in the pulse-echo configuration. The delamination was caused by a defined impact that introduced microcracks, macrocracks, and delaminations. In this preprint, only the delamination is considered for defect imaging.

In addition, an alternative temperature contrast imaging approach based on the VWC was presented. In contrast to state-of-the-art temperature contrast imaging techniques such as differentiated absolute contrast (DAC) and corrected DAC, the VWC provides a temporally noise-free representation of the temperature contrast signal. Due to the feature extraction capability of the temperature-to-virtual wave signal transformation, the front wall feature and the back wall feature can be separated from the defect features.

Furthermore, the reconstruction results of 3D photothermal imaging using VWC with F-SAFT, were compared with those of X-ray computed tomography (XCT). In general, the results for the spatial cross-sectional images evaluated perpendicular to the observation plane agree well. However, the defect images obtained with XCT show that the impact caused a non-planar observation surface for thermographic inspection. In addition, the special prepreg stacking of the observed CFRP specimen requires a depth adaptation of the virtual speed of sound tensor.

However, when using F-SAFT for 3D photothermal testing, a flat observation surface is required and the virtual speed tensor cannot be adopted for different depths. Therefore, in future work, it is planned to use alternative ultrasound reconstruction tools such as the time reversal algorithms to overcome these issues.

Authorship contribution statement

G. Thummerer: Conceptualization, Methodology, Software, Formal analysis, Validation, Investigation, Writing - original draft, Visualization. **L. Gahleitner:** Methodology, Writing - original draft, Visualization. **G. Mayr:** Writing - review & editing, Project administration, Funding acquisition. **P. Burgholzer:** Writing - review & editing, Supervision, Funding acquisition.

3D photothermal imaging of real subsurface defects in anisotropic media

G. Thummerer^a, L. Gahleitner^a, G. Mayr^a and P. Burgholzer^b

^aJosef Ressel Center of Thermal NDE of Composites, Stelzhamerstrasse 23, 4040 Wels, Austria

^bResearch Center for Non-Destructive Testing, Altenbergerstrasse 69, 4020 Linz, Austria

ARTICLE INFO

Keywords:

Virtual wave concept
Photothermal reconstruction
Parameter estimation
Thermography

ABSTRACT

In this paper, we present a 3D photothermal imaging tool to detect subsurface defects in anisotropic media using the virtual wave concept. In addition, we propose a novel approach to compute the temperature contrast using a virtual wave signal, which enables a temporal noise-free representation of the contrast temperature signal. The results obtained with the proposed imaging tool are compared with those obtained using computed tomography for a carbon fiber reinforced polymer sample containing a delamination caused by a defined impact. To sum up, this work presents a fast, easily interpretable and efficient 3D photothermal defect reconstruction and visualization tool.

1. Introduction

The increasing replacement of metal-based aircraft components with structures made of carbon fiber-reinforced polymers (CFRP) has boosted the use of active infrared thermography (IRT) for nondestructive testing (NDT) in the aerospace industry. Active IRT requires heating or cooling of the specimen under test (SUT) to obtain information about potential defects below the specimen surface, which can be detected with an infrared (IR) camera [1, 2, 3]. In this work, we use a subcategory of active IRT, called pulsed thermography (PT), in which a short temporal heating pulse (Dirac Delta-like) thermally excites the SUT.

The principle limits for near-surface and maximum-depth defect or back-wall detection from PT data were investigated by Shepard et al. [4] based on a 1D heat diffusion process in a finite body. Another principal limitation, the defect separability of PT data, was discussed by Burgholzer et al. [5]. These studies show, for a Dirac Delta-like heating in time, that the near-surface defect detection limit depends on the camera frame rate and the maximum defect depth detection limit as well as the defect separation limit depend on the noise equivalent temperature difference (NETD) of the IR camera and the introduced heating energy.

The major challenge with active IRT is entropy production during heat diffusion, which leads to blurred images for deeper defect structures [6, 7]. This effect is even more amplified for materials with a large ratio of in-plane to through-plane thermal diffusivity, such as anisotropic CFRP materials. Therefore, active IRT data requires further processing to improve defect imaging. One of the most computationally favorable methods to improve the quality of defect imaging are thermal contrast techniques such as running temperature contrast and differential absolute contrast (DAC) [1, 8]. Another prominent post-processing tool is the thermal signal reconstruction (TSR), which provides temporal noise filtering of the measured transient temperature signal [9, 10]. Using

the TSR, for example with a polynomial fit, the original data cube can be greatly reduced since each pixel can be represented by the estimated polynomials. Pulsed phase thermography (PPT) is also commonly applied to compensate for the blurring caused by heat diffusion by using a transient Fourier transform and surface temperature signals obtained via a PT experiment [11, 12].

Due to the heterogeneous material composition of CFRP materials, subsurface defects such as delaminations occur, which are a great concern for their mechanical integrity [13]. The anisotropic material properties make it difficult to correctly size subsurface defects using the above mentioned thermographic post-processing tools, because they do not take into account the lateral heat flow. In particular, for small defect diameter-to-depth ratios and high in-plane to through-plane thermal diffusivity ratios, the ability to correctly size defects decreases.

The conventional way to account for lateral heat flow is to solve an inverse heat transfer problem (IHTP), which requires regularization or stabilization to compute a useful inverse solution and allow 3D visualization of subsurface defects [14, 15]. Mendioroz et al. proposed, for example, an inversion procedure for a one-way heat diffusion process initiated by mechanical friction at defect interfaces in isotropic samples to reconstruct subsurface defects [16, 17]. Another inversion method for anisotropic samples and a one-way heat diffusion process that can be modeled by the fundamental solution of heat conduction and the method of images was discussed by Groz et al. [18]. Holland and Schiefelbein [19] modeled and tackled an IHTP for anisotropic samples and PT data acquired in the pulse-echo configuration (two-way heat diffusion process). Their approach requires the solution of a large-scale problem and therefore they proposed a depth-adapted discretization to reduce the computational cost of their inversion procedure.

Burgholzer et al. [20] suggested an alternative approach, the so-called virtual wave concept (VWC), which involves two reconstruction steps to account for the multidimensional heat diffusion process. In the first step, the measured sur-

✉ Gregor.Thummerer@fh-wels.at (G. Thummerer)

ORCID(s):

face temperature is transformed locally (pixel by pixel) into an "acoustic" virtual wave signal. The virtual wave signal obeys the wave equation and therefore ultrasound reconstruction methods such as time of flight (TOF) [21, 22] or frequency domain synthetic aperture focusing technique (F-SAFT) [23, 24] can be used in the second reconstruction step. In recent work, the VWC has been extended for application to anisotropic materials, the properties of the virtual wave signal due to a perturbed surface temperature signal have been discussed, and the computational cost has been significantly reduced [25, 26].

In this paper, we present results of 3D photothermal imaging based on the virtual wave concept for real subsurface defects such as delaminations embedded in composite materials. In addition, we propose an alternative method for calculating the temperature contrast based on the VWC, which has the advantage that it can be used for arbitrary excitation signals. Moreover, the proposed method enables a temporal noise-free representation of the contrast temperature signal. To sum up, this work presents a fast, easily interpretable and efficient multi-dimensional reconstruction method.

The paper is organized as follows: Section 2 discusses the materials, methods and parameters used. Also, the thermal contrast calculation using VWC are introduced. In Section 3, the imaging results are presented and discussed.

2. Materials and Methods

2.1. Materials

The observed carbon fiber reinforced polymer (CFRP) sample consists of 18 unidirectional prepreg layers (CY-COM G40-800/5276-1) with the stacking sequence

$$[0_3/90_4/+45/-45]_{s=1}. \quad (1)$$

It was cured at 350 °F for 120 min. The sample is depicted in Fig. 1 and has a thickness of $L_z = 2.6$ mm. The specimen has an impact damage caused by a steel ball with an imprint on the front side reaching a diameter of approximately 3.5 mm. The impact introduced micro- and macrocracks as well as delaminations into the specimen.

In this work, only interlaminar delaminations are observed, since the test setup is unsuitable for the detection of intralaminar cracks.

2.2. Photothermal testing

To obtain information about the internal structure of the observed sample, it was heated with flash lamps and the corresponding surface temperature signal was recorded in pulse-echo configuration. The corresponding experimental setup is shown in Fig. 1. The sample was insulated to ensure lateral adiabatic boundary conditions. In addition, the insulation was covered by aluminum tape to avoid lateral heat fluxes due to thermal excitation of the insulation material. Each flash lamp provides 6 kJ of electrical energy with a heating time of approximately 2 ms. The used IR camera is sensitive in the spectral range of 3.0-5.1 μm and the noise

equivalent temperature difference (NETD) is approximately 25 mK. The lateral resolution was $\Delta_x = 141 \mu\text{m}$ and the temporal resolution was $\Delta_t = 0.01$ s. Fig. 1 shows also the observed region of the sample and the impact damage schematically. The observed region is $(100 \times 25) \text{ mm}^2$.

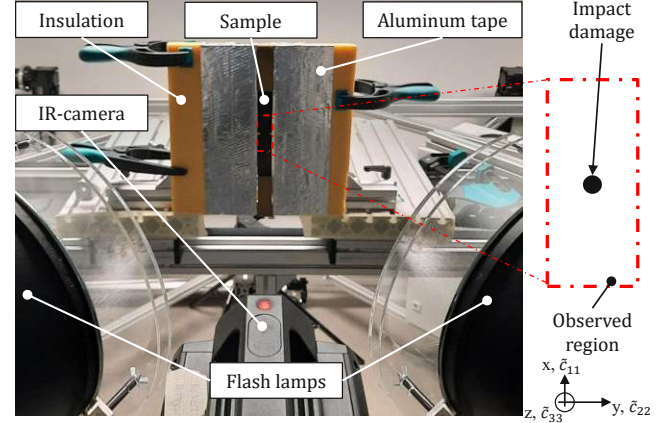


Figure 1: Experimental active IRT setup for the detection of the subsurface delamination in the CFRP sample.

2.2.1. Virtual wave concept

The aim of this work is to present an alternative method for calculating thermal contrast images and to present 3D photothermal defect images calculated based on VWC. Therefore the following steps are necessary:

1. Record the change of the surface temperature signal caused by thermal stimulation with an IR camera.
2. Then transform the surface temperature signal into a virtual wave signal in the first reconstruction step.
3. The virtual wave signal obeys the wave equation, thus ultrasonic reconstruction methods can be applied in the second reconstruction step.

The transformation between surface temperature $T(\mathbf{r}, t)$ and virtual wave signal $T_{\text{virt}}(\mathbf{r}, t')$ is given by:

$$T(\mathbf{r}, t) = \int K(t, t') T_{\text{virt}}(\mathbf{r}, t') dt' \quad (2)$$

$$\text{with } K(t, t') = \frac{c}{\sqrt{\pi\alpha t}} \exp\left(-\frac{c^2 t'^2}{4\alpha t}\right).$$

Herein α denotes the thermal diffusivity and c is the virtual speed of sound. Since the measured surface temperature signal is discrete in space and time, Eq. 2 is discretized. The transformation between surface temperature $T(\mathbf{r}, t)$ and virtual wave signal $T_{\text{virt}}(\mathbf{r}, t')$ for one spatial cross-section of the 3D SUT with pixel number q is given in discrete form by:

$$\mathbf{T} = \mathbf{K} \mathbf{T}_{\text{virt}}, \quad (3)$$

with the discrete temperature signal $\mathbf{T} \in \mathbb{R}^{N_t \times q}$, the discrete kernel $\mathbf{K} \in \mathbb{R}^{N_t \times N_{t'}}$ and the discrete virtual wave signal

$\mathbf{T}_{\text{virt}} \in \mathbb{R}^{N_{\text{iv}} \times q}$. With $t_k = k\Delta_t$ and $t'_j = j\Delta_t'$, the component notation of the discrete kernel \mathbf{K} is given by [26]:

$$K(k, j) = \frac{\tilde{c}}{\sqrt{\pi\Delta_{\text{Fo}}k}} \exp\left(-\frac{\tilde{c}^2 j^2}{4\Delta_{\text{Fo}}k}\right) \quad (4)$$

$$= \frac{\eta}{\sqrt{\pi k}} \exp\left(-\frac{\eta^2 j^2}{4k}\right),$$

with the dimensionless speed of sound $\tilde{c} = c\Delta_t/\Delta_z$, the discrete Fourier number $\Delta_{\text{Fo}} = \alpha\Delta_t/\Delta_z^2$, the dimensionless number $\eta = \tilde{c}/\sqrt{\Delta_{\text{Fo}}}$, the axial spatial resolution Δ_z and the temporal resolution $\Delta_t = \Delta_t'$. To compute a useful virtual wave signal based on a surface temperature signal, we must solve a severely ill-posed inverse problem. Hence, we need stabilization or regularization methods [27]. In this work we use the alternating direction method of multipliers (ADMM) for regularization [28, 29].

2.2.2. Estimation of speed of sound tensor

Because we deal with an anisotropic composite material, we have different thermal diffusivities and virtual speeds of sound in the principal directions. Therefore, we must estimate a virtual speed of sound tensor. This is necessary for the application of the F-SAFT procedure in the second reconstruction step. The dimensionless speed of sound tensor

$$\tilde{\mathbf{c}} = \begin{pmatrix} \tilde{c}_{11} & 0 & 0 \\ 0 & \tilde{c}_{22} & 0 \\ 0 & 0 & \tilde{c}_{33} \end{pmatrix} = \begin{pmatrix} 2.99 & 0 & 0 \\ 0 & 2.56 & 0 \\ 0 & 0 & 1.00 \end{pmatrix}. \quad (5)$$

was estimated by applying the procedure proposed in Ref. [25]. Also the thermal diffusivity in axial direction $\alpha_{33} = 4.47 \cdot 10^{-7} \text{ m}^2/\text{s}$ was estimated with this procedure. For the estimation of α_{33} , the temporal resolution was $\Delta_t = 0.01 \text{ s}$ and the axial spatial resolution was $\Delta_z = 70 \mu\text{m}$. For the estimation of the dimensionless virtual sound velocities \tilde{c}_{11} and \tilde{c}_{22} , the temporal resolution was $\Delta_t = 0.02 \text{ s}$ and the spatial resolutions were $\Delta_x = \Delta_y = \Delta_z = 161 \mu\text{m}$. The diameter of the laser spot was approximately 2.7 mm.

We want to emphasize that the estimation procedure from Ref. [25] only allows an approximate estimation of the virtual sound velocity tensor for the specific stacking configuration of the observed sample. Using this estimation procedure the observed sample is considered as an effective medium.

2.2.3. Temperature contrast imaging with VWC

In this section we propose a procedure to compute a temporal noise-free representation of the temperature contrast signal based on the VWC. Therefore, we compute in the first step the virtual wave signal \mathbf{T}_{virt} using the measured surface temperature signal \mathbf{T}_{meas} . For this reason we calculate the inverse of the subsequent linear matrix equation:

$$\mathbf{T}_{\text{meas}} = \mathbf{K}\mathbf{T}_{\text{virt}}. \quad (6)$$

Exemplary measured surface temperature signals in the defect region $(x, y) = (336, 86) \text{ px}$ and defect-free region

as well as the corresponding A-scans are represented in Figs. 2a) and 2b), respectively. The axial spatial resolution was $\Delta_z = 50 \mu\text{m}$. Based on Δ_z the temporal resolution $\Delta_t = (\Delta_z \tilde{c}_{33})^2 / (\alpha_{33} \eta^2) = 0.02 \text{ s}$ was calculated according to Ref. [26] with $\eta = 0.5267$. The evaluation time $t_{\text{eval}} = 15.68 \text{ s}$ was estimated with L_z^2 / α_{33} , which results in $N_t = 784$ time steps for the temperature signal. The number of time steps for the virtual wave signal was $N_{\text{iv}} = 350$. As visible in Fig. 2b) the delamination interface causes a source and a sink in the A-scan. In addition, the A-scan shows a source at $z = 0 \text{ mm}$, which represents the observation plane, and a source at $z \approx 2.6 \text{ mm}$, which represents the back-wall echo.

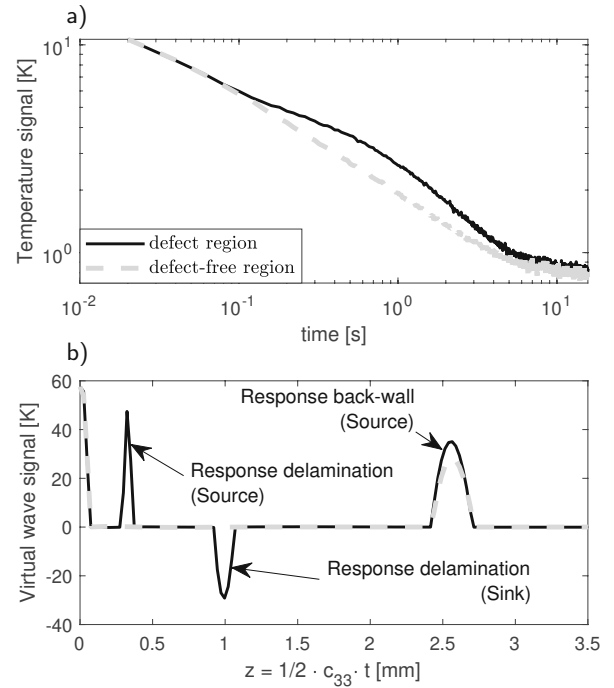


Figure 2: a) Measured surface temperature signals in the defect region $(x, y) = (336, 86) \text{ px}$ and defect-free region $(x, y) = (85, 20) \text{ px}$. b) Corresponding virtual wave signals computed with the regularization tool ADMM. The temporal resolution and the axial spatial resolution was $\Delta_t = 0.02 \text{ s}$ and $\Delta_z = 50 \mu\text{m}$, respectively. Note, the product $c_{33} \cdot t$ was halved due to the double-way heat diffusion.

Consequently, the virtual wave signal allows to distinguish between observation plane feature, defect features and back-wall feature, which enables the calculation of the temporal noise-free temperature contrast for both defect features plus back-wall feature $\mathbf{T}_{\text{c,VWC}}^{\text{db}}$ and the defect feature $\mathbf{T}_{\text{c,VWC}}^{\text{d}}$. Mathematically, the computation of the temperature contrasts, using Eq. 6, can be expressed in the following manner:

$$\mathbf{T}_{\text{c,VWC}}^{\text{db}} = \mathbf{K}\mathbf{T}_{\text{virt,c}}^{\text{db}} \quad \text{and} \quad \mathbf{T}_{\text{c,VWC}}^{\text{d}} = \mathbf{K}\mathbf{T}_{\text{virt,c}}^{\text{d}}, \quad (7)$$

where $\mathbf{T}_{\text{virt,c}}^{\text{db}}$ includes the defect source and sink as well as the back-wall source and $\mathbf{T}_{\text{virt,c}}^{\text{d}}$ only includes the defect

source and sink. This means that for the computation of both temperature contrast images the source due to the observation plane is set equal to zero.

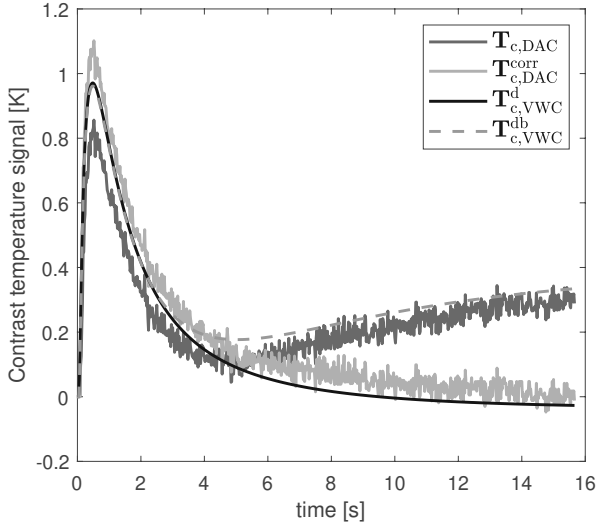


Figure 3: Contrast surface temperature signals $T_{c,DAC}$ and $T_{c,DAC}^{corr}$ obtained by using the DAC and the corrected DAC method, respectively computed according to Ref. [30]. Also the temporal noise-filtered contrast temperatures signals computed with VWC are shown. While $T_{c,VWC}^{db}$ includes the defect source and sink as well as the back-wall source, $T_{c,VWC}^d$ only respects the defect source and sink. The temporal resolution and the axial spatial resolution was $\Delta_t = 0.02$ s and $\Delta_z = 50$ μm , respectively.

Fig. 3 shows exemplary temperature contrast signals for the same defect pixel-position as in Fig. 2. To allow a comparison, temperature contrast signals $T_{c,DAC}$ and $T_{c,DAC}^{corr}$ were computed with DAC and the corrected DAC, respectively. These contrast temperature signals were calculated according to Ref. [30]. In contrast to DAC, the corrected DAC accounts for the sample thickness L_z . Fig. 3 clearly shows that $T_{c,DAC}$ follows the curve of $T_{c,VWC}^{db}$ and $T_{c,DAC}^{corr}$ follows the curve of $T_{c,VWC}^d$, but the curves computed with VWC allow for a temporal noise-free representation of the contrast temperature signals. Therefore, this representation enables proper additional evaluation steps such as differentiation.

3. Imaging results

In this section, we compare the imaging results obtained with the proposed thermal contrast method with the results obtained with the state-of-the-art thermal contrast calculation method DAC. In addition, we apply VWC for multidimensional defect imaging and compare the obtained results with those obtained with 3D-X-ray computed tomography (XCT). For the computation of the virtual wave signal from the measured surface temperature signal, the same parameters as in Sec. 2.2.3 were used.

3.1. Thermal contrast imaging

Fig. 4 compares a maximum defect thermogram and XCT evaluations with thermal contrast images. The maximum defect thermogram was evaluated from the offset corrected measured surface temperature signal T_{meas} at $\tau = 0.54$ s and is shown in Fig. 4a). Fig. 4b) shows the mean thermal contrast image that was computed with DAC and evaluated in the time sequence $\Delta_t : \Delta_t : \tau$. The time t_{DAC} which describes the time between flash pulse and the time where the delamination becomes visible, was determined according to Ref. [30]. Fig. 4c) shows the mean thermal contrast image that was computed with VWC and evaluated in the time sequence $\Delta_t : \Delta_t : \tau$. The defect image resulting from XCT measurements is shown in Fig. 4d). The temporal resolution of the measured surface temperature signal was $\Delta_t = 0.02$ s and the axial spatial resolution for the VWC evaluation was $\Delta_z = 50$ μm . For the XCT measurements a Phoenix/X-Ray Nanotom 180 computer tomograph, equipped with a 180 kV nanofocus X-ray source and a 2300 PX \times 2300 PX array Hamamatsu detector was utilized. The tube voltage was 60 kV, the tube amperage was 350 μA , the integration time was 700 ms and the spatial resolution was 15 μm .

Each defect image clearly shows the delamination. However, compared to the XCT evaluations, the results obtained based on photothermal data indicate a distortion of the defect due to the anisotropic heat flow. Comparing the contrast images from Figs. 4 b) and c) the contrast image obtained using VWC is less blurry than the contrast image obtained via DAC. However, both evaluations do not allow a depth feature extraction for a multi-dimensional visualization of the delamination.

3.2. Multi-dimensional defect imaging

To enable a 3D visualization of the delaminations for the measured surface temperature signal, we compute the contrast temperature signal $T_{c,VWC}^{db}$ using VWC and the procedure proposed in sec. 2.2.3. Using $T_{c,VWC}^{db}$, we calculate the contrast virtual wave signal $T_{virt,c}^{db}$, which shows now only sources and sinks due to the delamination and the back-wall in the defect region, because the source due to observation plane was eliminated.

Fig. 5 shows a comparison of the thermal contrast image obtained via VWC, the virtual wave signal, and the reconstructed defect signal calculated with F-SAFT. The thermal contrast image from Fig. 5a) was evaluated like the contrast signal in Fig. 4c). To obtain a defect image from the virtual wave signal the mean value of the depth-sequence (400 : Δ_z : 950) μm was evaluated and the result is represented in Fig. 5b). For the evaluation of the saft-image the mean of the depth-sequence (400 : Δ_z : 950) μm of the reconstructed defect signal T_{saft} was evaluated. For the calculation of T_{saft} the dimensionless speed of sound tensor from Eq. 5 was used to rectify the anisotropic heat flow and the absolute value of the reconstructed signal was taken to improve the defect visualization.

Each visualization clearly indicates the delamination.

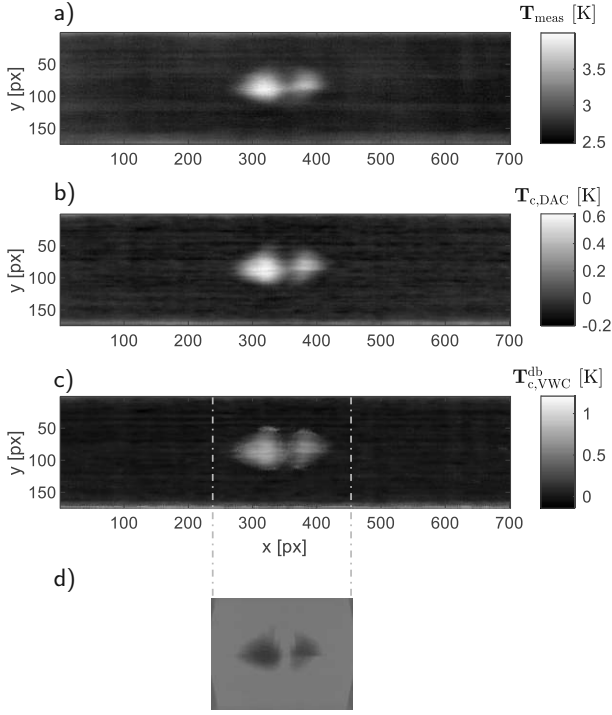


Figure 4: a) Maximum defect thermogram evaluated at $\tau = 0.54$ s. b) Mean thermal contrast image computed with DAC and evaluated for the time sequence $\Delta_t : \Delta_t : \tau$. c) Mean thermal contrast image computed with VWC and evaluated for the time sequence $\Delta_t : \Delta_t : \tau$. The axial spatial resolution was $\Delta_z = 50 \mu\text{m}$. d) Defect image reconstructed using XCT data.

However, the $\mathbf{T}_{c,VWC}^{db}$ image and the $\mathbf{T}_{virt,c}^{db}$ image clearly show a distortion caused by the lateral anisotropic heat flow. Due to F-SAFT, that respects the speeds of sound in the principal direction of heat diffusion or virtual wave propagation, the defect image can be rectified.

Fig. 6 shows a comparison between $\mathbf{T}_{c,VWC}^{db}$, $\mathbf{T}_{virt,c}^{db}$, \mathbf{T}_{saft} and the defect image reconstructed using XCT data for the cross-sections at $x = 336$ px and at $y = 86$ px. The corresponding cross-sections positions are also indicated in Fig. 5 by red-dashed lines. For the $\mathbf{T}_{c,VWC}^{db}$ images the subsurface defect depth and the sample thickness cannot be extracted. The $\mathbf{T}_{virt,c}^{db}$ images clearly show the defect and depth feature extraction capability of the VWC. In the \mathbf{T}_{saft} image that was computed with F-SAFT and the virtual speeds of sound in the principle direction, the lateral anisotropic heat flow was respected, which significantly rectifies the anisotropic heat flow.

Figs. 7 and 8 show 3D isosurface representations of the reconstructed defect signal \mathbf{T}_{saft} which clearly show the delamination.

As discussed in Sec. 2.2.3, the delamination introduces a source and a sink and hence the defect can be localized and the source due to the defect interface is in accordance with the correct depth that is indicated by a white dashed line in Fig. 6. The correct defect depth can be extracted

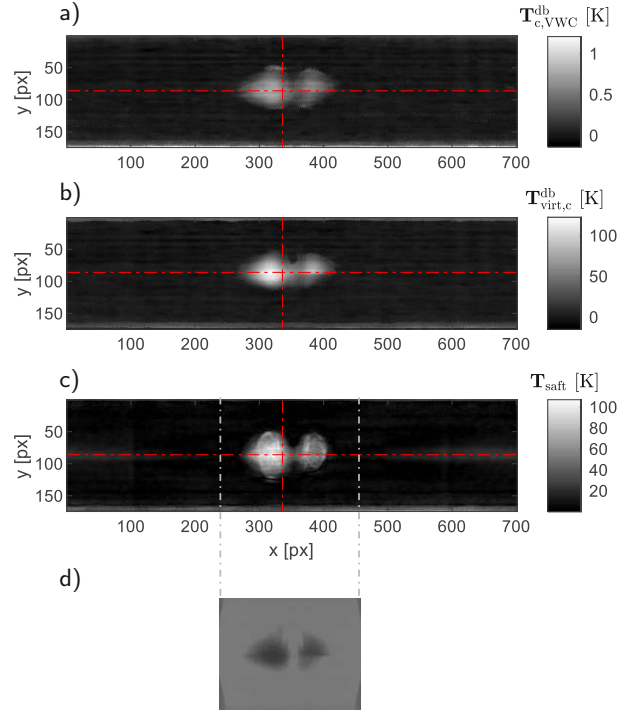


Figure 5: a) Mean thermal contrast image computed with VWC and evaluated for the time sequence $\Delta_t : \Delta_t : \tau$. b) Mean virtual wave image evaluated for the depth sequence $(400 : \Delta_z : 950) \mu\text{m}$. c) Mean saft-image evaluated for the depth sequence $(400 : \Delta_z : 950) \mu\text{m}$. The axial spatial resolution is $\Delta_z = 50 \mu\text{m}$. d) Defect image reconstructed using XCT data. The red-dashed lines indicate the position of the cross section, which are presented in Fig. 6.

from the XCT images, where the delamination occurs between prepreg layer three and four. Furthermore, a correct application of F-SAFT requires a plane observation surface. As can be seen in the XCT images, the observed sample surface deviates from this requirement in the delamination area, which degrades the reconstruction quality, however the reconstruction quality is still good. The observed sample and its stacking sequence indicates another limitation for the application of F-SAFT and the parameter estimation procedure proposed in Ref. [25]. Due to the stacking sequence the virtual speeds of sound in the principal directions depends on depth position and therefore the estimation of the speed of sound tensor in Sec. 2.2.2 is an approximate estimation.

4. Conclusion and Outlook

In this work we presented an alternative approach to calculate thermal contrast images using the VWC. In contrast to state-of-the-art methods the proposed contrast method can be applied for arbitrary heating patterns, because the patterns can be readily respected by a temporal convolution with the transformation kernel \mathbf{K} . However, the computation using, for example, DAC is faster because only basic computer operations are required. But the defect visualization is less accurate than visualization obtained with the proposed con-

3D photothermal imaging

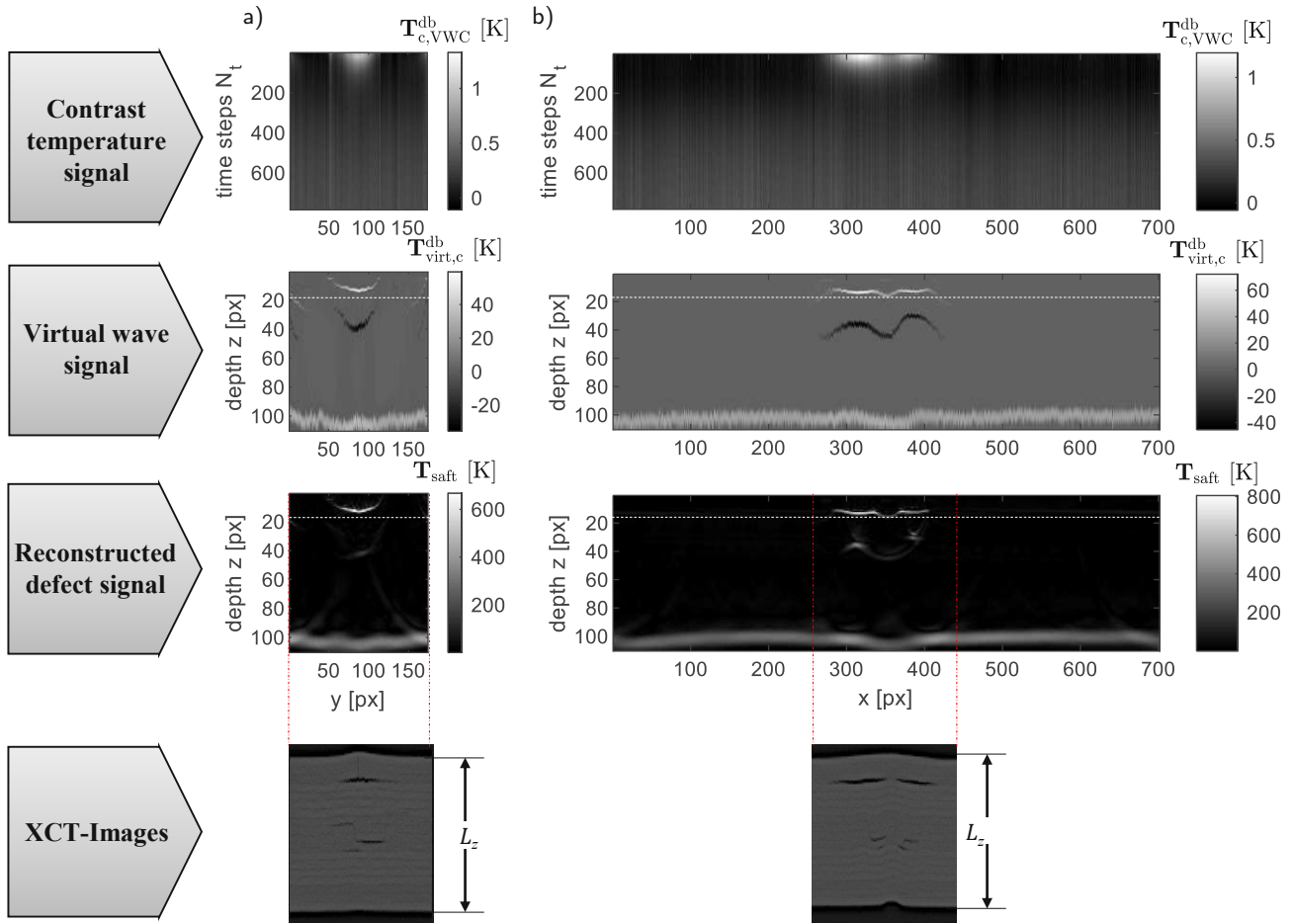


Figure 6: a) Cross-section images of $T_{c,VWC}^{db}$, $T_{virt,c}^{db}$, T_{saft} at $x = 322$ px compared with the corresponding XCT image. b) Cross-section images of $T_{c,VWC}^{db}$, $T_{virt,c}^{db}$, T_{saft} at $y = 84$ px compared with the corresponding XCT image. The temporal resolution was $\Delta_t = 0.02$ s, the lateral axial resolution was $\Delta_x = \Delta_y = 141$ μm and the axial lateral resolution was $\Delta_z = 50$ μm for the VWC reconstruction. The voxel size for the XCT results is 15 μm .

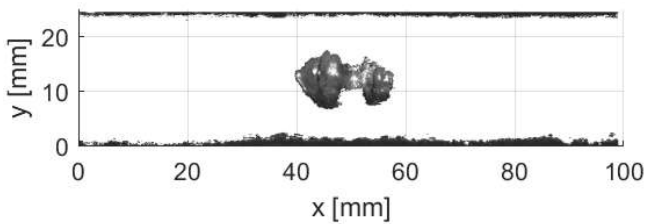


Figure 7: T_{saft} (top view) showing the isosurface representation of the delamination.

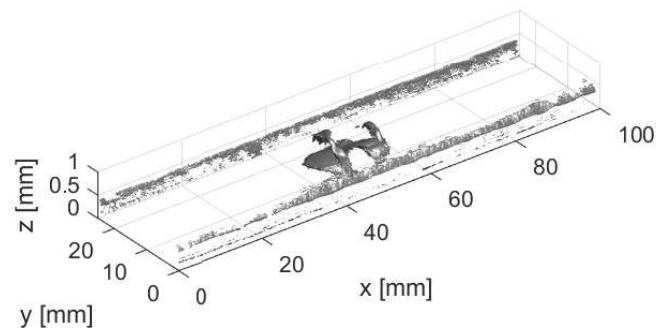


Figure 8: T_{saft} (isometric view) showing the isosurface representation of the delamination.

trast method and the proposed method allows for a temporal noise-free representation of the thermal contrast signal.

In addition we performed 3D photothermal imaging of a real subsurface defect represented by a delamination. F-SAFT was used for the rectification of the anisotropic heat flow. It turned out that the use of F-SAFT allows only for approximate defect estimations because:

- the observation surface is not plane due to the impact and
- the virtual speed of sound tensor depends on sample depth due to the stacking sequence of the sample.

To overcome these issues it is planned to use alternative ultrasonic reconstruction method such as time reversal algorithms, that allow a prepreg and layer related definition of the virtual speed of sound, in future research work. In addition, the proposed thermal contrast method will be applied for different heating patterns.

Acknowledgements

The financial support by the Austrian Federal Ministry of Science, Research and Economy and the National Foundation for Research, Technology and Development is gratefully acknowledged. Furthermore, this work has been supported by the project multimodal and in-situ characterization of inhomogeneous materials (MiCi), by the Federal Government of Upper Austria and the European Regional Development Fund (EFRE) in the framework of the EU-program IWB2020. Signal and data processing was funded by the Austrian Science Fund (FWF), project P 33019-N.

References

- [1] X. P. V. Maldague, P. O. Moore (Eds.), *Infrared and thermal testing*, 3rd Edition, *Nondestructive testing handbook*, American Society for Nondestructive Testing, Columbus, Ohio, 2001.
- [2] C. Meola, S. Boccardi, G. Carlomagno, *Infrared Thermography in the Evaluation of Aerospace Composite Materials: Infrared Thermography to Composites*, Elsevier Science, 2016.
- [3] V. Vavilov, D. Burleigh, *Infrared Thermography and Thermal Non-destructive Testing*, 2020.
- [4] S. M. Shepard, J. R. Lhota, T. Ahmed, Measurement limits in flash thermography, in: D. D. Burleigh, R. B. Dinwiddie (Eds.), *Thermosense XXXI*, Vol. 7299, International Society for Optics and Photonics, SPIE, 2009, pp. 209 – 215. doi:10.1117/12.820062.
- [5] P. Burgholzer, Thermodynamic limits of spatial resolution in active thermography, *International journal of thermophysics* 36 (9) (2015) 2328–2341. doi:10.1007/s10765-015-1890-7.
- [6] P. Burgholzer, G. Hendorfer, Limits of spatial resolution for thermography and other non-destructive imaging methods based on diffusion waves, *International journal of thermophysics* 34 (2013) 1617–1632. doi:10.1007/s10765-013-1513-0.
- [7] P. Burgholzer, G. Mayr, G. Thummerer, M. Haltmeier, Linking information theory and thermodynamics to spatial resolution in photothermal and photoacoustic imaging, *Journal of Applied Physics* 128 (17) (2020) 171102. doi:10.1063/5.0023986.
- [8] M. Klein, A. Bendada, M. Pilla, C. Ibarra-Castanedo, X. Maldague, Enhancing infrared images contrast for pulsed thermography, 2008. doi:10.21611/qirt.2008.08_02_03.
- [9] S. M. Shepard, J. R. Lhota, B. A. Rubadoux, D. Wang, T. Ahmed, Reconstruction and enhancement of active thermographic image sequences, *Optical Engineering* 42 (5) (2003) 1337 – 1342. doi:10.1117/1.1566969.
- [10] D. L. Balageas, J.-M. Roche, F.-H. Leroy, W.-M. Liu, A. M. Gorbach, The thermographic signal reconstruction method: A powerful tool for the enhancement of transient thermographic images, *Biocybernetics and Biomedical Engineering* 35 (1) (2015) 1 – 9. doi:10.1016/j.bbe.2014.07.002.
- [11] X. c. S. Marinetti, Pulse phase infrared thermography, *Journal of Applied Physics* 79 (5) (1996) 2694–2698. doi:10.1063/1.362662.
- [12] X. Maldague, F. Galmiche, A. Ziadi, *Advances in pulsed phase thermography*, *Infrared Physics Technology* 43 (3) (2002) 175–181. doi:10.1016/S1350-4495(02)00138-X.
- [13] F. C. Campbell, *Structural composite materials*, ASM Internat, Materials Park, Ohio, 2010.
- [14] J. V. Beck, B. Blackwell, C. R. St. Clair, *Inverse heat conduction: Ill-posed problems* / James V. Beck, Ben Blackwell, Charles R. St. Clair, Jr, Wiley, New York, 1985.
- [15] H. R. B. Orlande, *Thermal measurements and inverse techniques*, Heat transfer, CRC Press, Boca Raton, FL, 2011.
- [16] A. Mendioroz, A. Castelo, R. Celorrio, A. Salazar, Characterization and spatial resolution of cracks using lock-in vibrothermography, *NDT & E International* 66 (1) (2014) 8–15. doi:10.1016/j.ndteint.2014.04.004.
- [17] A. Mendioroz, K. Martínez, R. Celorrio, A. Salazar, Characterizing the shape and heat production of open vertical cracks in burst vibrothermography experiments, *NDT & E International* 102 (2019) 234–243. doi:10.1016/j.ndteint.2018.12.006.
- [18] M.-M. Groz, E. Abisset-Chavanne, A. Meziane, A. Sommier, C. Pradère, Three-dimensional reconstruction of thermal volumetric sources from surface temperature fields measured by infrared thermography, *Applied Sciences* 9 (24) (2019) 5464. doi:10.3390/app9245464.
- [19] S. D. Holland, B. Schiefelbein, Model-based inversion for pulse thermography, *Experimental Mechanics* 59 (4) (2019) 413–426. doi:10.1007/s11340-018-00463-2.
- [20] P. Burgholzer, M. Thor, J. Gruber, G. Mayr, Three-dimensional thermographic imaging using a virtual wave concept, *Journal of Applied Physics* 121 (10) (2017) 105102. doi:10.1063/1.4978010.
- [21] J. P. Charlesworth, J. Temple, *Engineering Applications of Ultrasonic Time-of-flight Diffraction*, Ultrasonic inspection in engineering series, Research Studies Press, 2001.
- [22] G. Mayr, G. Stockner, H. Plasser, G. Hendorfer, P. Burgholzer, Parameter estimation from pulsed thermography data using the virtual wave concept, *NDT & E International* 100 (2018) 101–107. doi:10.1016/j.ndteint.2018.09.003.
- [23] K.-J. Langenberg, R. Marklein, K. Meyer, *Ultrasonic nondestructive testing of materials: Theoretical foundations*, CRC Press, Taylor et Francis, Boca Raton, 2017.
- [24] D. Lévesque, A. Blouin, C. Néron, J.-P. Monchalain, Performance of laser-ultrasonic f-saft imaging, *Ultrasonics* 40 (10) (2002) 1057–1063. doi:10.1016/S0041-624X(02)00256-1.
- [25] G. Thummerer, G. Mayr, P. Burgholzer, Photothermal testing of composite materials: Virtual wave concept with prior information for parameter estimation and image reconstruction, *Journal of Applied Physics* 128 (12) (2020) 125108. doi:10.1063/5.0016364.
- [26] G. Thummerer, G. Mayr, P. Burgholzer, 3d photothermal imaging of subsurface defects in composite materials, *NDT & E International* 122 (2021) 102476. doi:10.1016/j.ndteint.2021.102476.
- [27] P. C. Hansen, *Rank-deficient and discrete ill-posed problems: Numerical aspects of linear inversion* / Per Christian Hansen, SIAM monographs on mathematical modeling and computation, SIAM, Philadelphia, Pa., 1998.
- [28] S. Boyd, Distributed optimization and statistical learning via the alternating direction method of multipliers, *Foundations and Trends® in Machine Learning* 3 (1) (2010) 1–122. doi:10.1561/22000000016.
- [29] R. C. Aster, B. Borchers, C. H. Thurber, *Parameter estimation and inverse problems*, third edition Edition, Elsevier, Amsterdam, 2018.
- [30] H. D. Benítez, C. Ibarra-Castanedo, A. Bendada, X. Maldague, H. Loaiza, E. Caicedo, Definition of a new thermal contrast and pulse correction for defect quantification in pulsed thermography, *Infrared Physics Technology* 51 (3) (2008) 160–167. doi:10.1016/j.infrared.2007.01.001.

5.6 Summary

CFRP structures are increasingly replacing metal-based aircraft structures. This, in turn, boosts the application of active infrared thermography (IRT) for non-destructive testing of aircraft structures, as it is a fast and non-contact measurement technique, thus enabling economical testing of highly integrated composite components. Active IRT requires thermal excitation of the specimen under test, and the excitation pattern can vary in space and time. A major issue and challenge with active IRT data is multidimensional defect reconstruction and visualization. For this task, an inverse heat conduction problem (IHCP) can be tackled. IHCPs are severely ill-posed inverse problems, due to the strong attenuation of the thermal waves, and therefore regularization and stabilization methods are required to compute a useful inverse solution.

In this doctoral thesis, the virtual wave concept (VWC), a promising multidimensional defect reconstruction method, has been extended for application to anisotropic materials such as composites and for photothermal data acquired in the pulse-echo configuration. VWC represents an IHCP and therefore requires the solution of a severely ill-posed inverse problem for defect reconstruction. To compensate for the degradation of spatial resolution that leads to blurred images of deeper structures and to improve the quality of the inverse solution, the iterative regularization technique alternating direction method of multipliers (ADMM) was implemented that allows the incorporation of prior information in the form of positivity and sparsity. The inclusion of sparsity is reasonable because samples usually have few defects, resulting in a sparse inverse solution or virtual wave signal. Only for adiabatic boundary conditions, 1D thermal diffusion, and defect-free samples a direct incorporation of positivity is possible. One possible application under these conditions is to estimate the thermal diffusion time perpendicular to the observation plane. Otherwise, the bi-modal virtual wave signal must be projected onto a positive data set using the circular projections in 2D and the spherical projections in 3D to incorporate the prior information positivity. The use of these projections works well for samples with internal heat sources and boundary point sources. However, for highly anisotropic samples containing defects with lateral extension at a certain depth, it was found that the circular and spherical projections are not applicable, especially for the pulse-echo configuration.

Moreover, a mathematical relationship of the thermal diffusivity tensor and the virtual speed of sound tensor was derived to enable the rectification of the anisotropic heat flow. Using this relationship, a novel method for estimating the thermal diffusivity tensor was proposed. To account for the different virtual speeds of sound in the principal directions, the second recon-

struction step was modified. Using the findings from Paper 5.3, the modified VWC was applied to anisotropic samples with artificial defects and photothermal data acquired in the pulse-echo configuration. To speed up the defect reconstruction, the reconstruction domain was significantly reduced based on parameter studies and physical-based considerations. In addition, the properties of a virtual wave signal resulting from a perturbed defect temperature signal were discussed in detail. The discussions show that using the VWC together with ADMM one can properly distinguish between front-wall feature, back-wall feature and defect feature. Finally, the modified VWC method was applied to 3D photothermal imaging of real defects represented by delaminations in a CFRP sample. It was found that the application of frequency-synthetic aperture focusing technique (F-SAFT) is inappropriate for accurate defect reconstruction due to the specific stacking sequence of the sample. Therefore, the use of alternative ultrasonic reconstruction methods such as the time reversal algorithm was suggested. In this context, VWC was adopted for thermal contrast imaging, which allows the calculation of temporally noise-free thermal contrast images for different heating patterns. In summary, this doctoral thesis presents a rapid, easily interpretable, and efficient 3D photothermal imaging tool for anisotropic media.

5.7 Outlook

To date, only 3D photothermal surface temperature signals acquired in the pulse-echo configuration and based on a temporal Dirac Delta-like, temporally rectangular or spatially homogeneous heating pulse have been converted into a virtual wave signal. To improve the signal-to-noise ratio of the transient temperature signal and to comply with the maximum allowable exposure of the observed sample, time-varying heating, such as a linear frequency-modulated excitation signal, will be used in future research. The defect detection capability for cracks oriented perpendicular to the excitation surface could also be improved by spatially varying heating pulses in combination with the VWC reconstruction procedure.

Another future research aspect related to the VWC reconstruction procedure is the investigation of the influence of non-adiabatic boundary conditions, e.g. due to convective heat losses, on the reconstruction quality.

The current state of research of VWC in conjunction with F-SAFT requires an approximately flat observation surface. Moreover, only global propagation parameters can be included with F-SAFT for defect reconstruction. However, some stacking sequences of CFRP samples require depth adjustment of the propagation parameters. Therefore, another research focus could be to complement VWC for non-planar, complex-shaped anisotropic specimen geometries and arbitrary stacking sequences, by alternative ultrasound reconstruction methods such as time reversal algorithms.

Another possible research direction could be the application of Deep Learning approaches to a virtual wave signal obtained from a 3D photothermal temperature signal recorded in the pulse-echo configuration.

Curriculum Vitae

Name: Gregor Thummerer (né Stockner)
Address: Sonnenstraße 6, 3340 Waidhofen/Ybbs
Phone: 0680/2301756
E-Mail: Gregor.Stockner@gmx.at

Education

10/2018 - present	Technical University Vienna, AT Mechanical Engineering, PhD study
10/2013 - 09/2018	University of Applied Science Upper Austria, AT Mechanical Engineering, Dipl.-Ing., BSc
01/2012 - 09/2012	Institute for Economic Promotion (WIFI), AT Examination for the master craftsman's certificate in metal and mechanical engineering
2010 - 2012	Adult education center (VHS), AT Berufsreifepprüfung
09/2005 - 02/2009	Apprenticeship at Seisenbacher GmbH, AT Metal technician

Research and professional experience

10/2018 - present	FH OÖ Forschung & Entwicklung GmbH, AT Research Associate
03/2009 - 05/2014	Seisenbacher GmbH, AT Metal technician

- [1] **G. Thummerer**, G. Mayr, P. Burgholzer, 3D photothermal imaging of subsurface defects in composite materials, *NDT & E International*, Volume 122, 2021, 102476, doi:10.1016/j.ndteint.2021.102476.
- [2] S. Ahmadi, **G. Thummerer**, S. Breitwieser, G. Mayr, J. Lecompanon, P. Burgholzer, P. Jung, G. Caire, M. Ziegler, Multi-dimensional reconstruction of internal defects in additively manufactured steel using photothermal super resolution combined with virtual wave based image processing, *IEEE Transactions on Industrial Informatics*, 2021, doi:10.1109/TII.2021.3054411.
- [3] P. Kovács, B. Lehner, **G. Thummerer**, G. Mayr, P. Burgholzer, M. Huemer, Deep learning approaches for thermographic imaging, *Journal of Applied Physics*, Volume 128, 2020, 155103, doi:10.1063/5.0020404.
- [4] H. Plasser, G. Mayr, **G. Thummerer**, G. Hendorfer, P. Burgholzer, Z. Major, Photothermal porosity estimation in cfrp by the time-of-flight of virtual waves, *Journal of Nondestructive Evaluation*, Volume 39, 2020, 509, doi:10.1007/s10921-020-00722-0.
- [5] P. Burgholzer, G. Mayr, **G. Thummerer**, M. Haltmeier, Linking information theory and thermodynamics to spatial resolution in photothermal and photoacoustic imaging, *Journal of Applied Physics*, Volume 128, 2020, 171102, doi:10.1063/5.0023986.
- [6] **G. Thummerer**, G. Mayr, P. Burgholzer, Photothermal testing of composite materials: Virtual wave concept with prior information for parameter estimation and image reconstruction, *Journal of Applied Physics*, Volume 128, 2020, 125108, doi:10.1063/5.0016364.
- [7] **G. Thummerer**, G. Mayr, M. Haltmeier, P. Burgholzer, Photoacoustic reconstruction from photothermal measurements including prior information, *Photoacoustics*, Volume 19, 2020, 100175, doi:10.1016/j.pacs.2020.100175.
- [8] **G. Thummerer**, G. Mayr, P.D. Hirsch, M. Ziegler, P. Burgholzer, Photothermal image reconstruction in opaque media with virtual wave backpropagation, *NDT & E International*, Volume 112, 2020, 102239, doi:10.1016/j.ndteint.2020.102239.
- [9] G. Mayr, **G. Stockner**, H. Plasser, G. Hendorfer, P. Burgholzer, Parameter estimation from pulsed thermography data using the virtual wave concept, *NDT & E International*, Volume 100, 2018, Pages 101-107, doi:10.1016/j.ndteint.2018.09.003.
- [10] P. Burgholzer, **G. Stockner**, G. Mayr, Acoustic reconstruction for photothermal imaging, *Bioengineering*, Volume 5, 2018, doi:10.3390/bioengineering5030070.
- [11] P. Burgholzer, G. Mayr, J. Gruber, **G. Stockner** (2018). Thermografische Rekonstruktion von internen Wärmequellen mittels virtueller Schallwellen. *Materials Testing*, Volume 60, 2018, Pages 600-606. doi:10.3139/120.111192

- [1] P. Burgholzer, **G. Thummerer**, G. Mayr, P. Kovacs, M. Haltmeier, Iterative methods for thermographic reconstruction using the virtual wave concept, Quantitative Infrared Thermography (QIRT) Conference – short paper, 2020, doi:10.21611/qirt.2020.056
- [2] P. Kovacs, B. Lehner, **G. Thummerer**, G. Mayr, P. Burgholzer, M. Huemer, A hybrid approach for thermographic imaging with deep learning, in: ICASSP 2020 - 2020 IEEE International Conference on Acoustics, Speech and Signal Processing (ICASSP), IEEE, 2020, pp. 4277–4281, doi:10.1109/ICASSP40776.2020.9053411.
- [3] H. Plasser, G. Mayr, **G. Thummerer**, G. Hendorfer, P. Burgholzer, Photothermal porosity estimation in carbon fiber reinforced plastics based on the virtual wave concept. In B. Oswald-Tranta, & J. N. Zalameda (Eds.), *Thermosense: Thermal Infrared Applications XLII* [114090P] (Proceedings of SPIE - The International Society for Optical Engineering; Vol. 11409), SPIE, 2020, doi:10.1117/12.2557353

- [1] P. Burgholzer, **G. Thummerer**, G. Mayr, P. Kovacs, M. Haltmeier, Iterative methods for thermographic reconstruction using the virtual wave concept, 15th Quantitative InfraRed Thermography conference (QIRT2020, Porto), Videoconference, 2020
- [2] **G. Thummerer**, G. Mayr, P. Burgholzer, 3D Thermographic Reconstruction of Defects in Composite Materials, 15th International Symposium on Nondestructive Characterization of Materials, Portoroz (Slovenia), 2019
- [3] **G. Thummerer**, G. Mayr, P. Burgholzer, Virtual Wave Concept for Thermographic Reconstruction using Inverse Wave Propagation Methods, 2019 International Congress on Ultrasonics (ICU), Bruegge (Belgium), 2019